

**Green and Durable Geopolymer Composites for
Sustainable Civil Infrastructure**

by

Motohiro Ohno

A dissertation submitted in partial fulfillment
of the requirements for the degree of
Doctor of Philosophy
(Civil Engineering)
in The University of Michigan
2017

Doctoral Committee:

Professor Victor C. Li, Chair

Professor Gregory A. Keoleian

Assistant Professor Aaron R. Sakulich, Worcester Polytechnic Institute

Associate Professor Jeffrey T. Scruggs

Motohiro Ohno

motoohno@umich.edu

ORCID iD: [0000-0002-4995-2366](https://orcid.org/0000-0002-4995-2366)

© Motohiro Ohno 2017

ACKNOWLEDGMENTS

This dissertation would not have been completed without the guidance and support from many individuals. My gratitude to them is beyond description but I will try to express it here.

First and foremost, I would like to express my deepest gratitude to Professor Victor Li. I am deeply indebted to him for his mentorship, encouragement, and patience throughout my doctoral research. I would also like to thank Professor Gregory Keoleian, Assistant Professor Aaron Sakulich, and Associate Professor Jeffery Scruggs for their valuable inputs, encouragement, and kind words.

I would like to extend my gratitude to other professors and staff in the department. Especially, experimental work in this doctoral study was possible thanks to technical advice and support from our lab technicians – Bob Spence, Bob Fischer, and Jan Pantolin.

My gratitude also goes to my colleagues at the ACE-MRL. I have enjoyed working, discussing, and chatting with them during my time at the University of Michigan. I would like to give special thanks to Taeho Kim, who helped experimental studies for Chapters 5 and 6.

Finally, I am very grateful to my wife, Eunkyung, and my daughter, Hinami. Eunkyung has always believed in me even when I did not believe in myself. The love and support of my beloved family are always essential for my life.

After all, words alone are not enough to express my gratitude to you all.

TABLE OF CONTENTS

ACKNOWLEDGMENTS	ii
LIST OF TABLES	viii
LIST OF FIGURES	xi
LIST OF APPENDICES.....	xvii
ABSTRACT.....	xviii
CHAPTER	
PART I: INTRODUCTION.....	1
CHAPTER 1: Introduction	1
1.1 Background and motivation	1
1.2 Problem statement	4
1.3 Research objectives	7
1.4 Research approach and thesis organization.....	8
PART II: DEVELOPMENT OF EGC.....	12
CHAPTER 2: Review of Green and Durable Concretes	12
2.1 Geopolymer	12
2.1.1 History of development.....	13
2.1.2 Previous studies for geopolymer design	17
2.1.3 Unsolved problems	22
2.2 Engineered Cementitious Composite	24

2.2.1 History of development.....	24
2.2.2 Previous studies for ECC design.....	28
2.2.3 Unsolved problems	33
2.3 Challenges for development of Engineered Geopolymer Composite	34
CHAPTER 3: Integrated Design Method	45
3.1 Framework of proposed design method	45
3.2 Matrix development.....	49
3.2.1 Orthogonal array	49
3.2.2 Analysis of Variance.....	52
3.2.3 Main-effect plot and optimum conditions.....	56
3.2.4 Confirmation experiment	58
3.3 Composite Design	60
3.3.1 Experimental characterization	60
3.3.2 Analytical model.....	68
3.3.3 Analytical simulation	75
3.3.4 Confirmation experiment	78
3.4 Environmental assessment.....	79
3.5 Summary.....	82
CHAPTER 4: Application of Integrated Design Method.....	87
4.1 Preliminary study.....	87
4.2 Matrix development.....	90
4.2.1 Materials and testing methods	90
4.2.2 Design of Experiment	92
4.2.3 Results and discussion	95
4.2.4 Optimum conditions.....	98

4.2.5 Verification experiment for compressive strength.....	99
4.3 Composite design	101
4.3.1 Experimental and analytical methods	101
4.3.2 Results and discussion	103
4.3.3 Verification experiment for tensile ductility.....	105
4.4 Environmental performance comparison	110
4.4.1 Materials and methods	110
4.4.2 Results and discussion	112
4.5 Summary and conclusions.....	114
PART III: CHARACTERIZATION OF EGC DURABILITY	121
CHAPTER 5: Cracking Characteristics and Water Permeability of EGC	121
5.1 Introduction	121
5.2 Materials and methods.....	123
5.2.1 Materials and mix design	123
5.2.2 Specimen preparation.....	123
5.2.3 Preloading and crack width measurement	125
5.2.4 Permeability testing	126
5.3 Results and discussion.....	129
5.3.1 Crack patterns of EGC.....	129
5.3.2 Water permeability.....	133
5.3.3 Sealed cracks and reduction in permeability	139
5.4 Summary and conclusions.....	141
CHAPTER 6: Feasibility Study of Self-healing EGC	145
6.1 Introduction	145
6.2 Materials and methods.....	147

6.2.1 Mix design and specimen preparation	147
6.2.2 Mechanical testing	148
6.2.3 SEM observation and EDS analysis	150
6.3 Results and discussion.....	151
6.3.1 Visual appearance of sealed crack	151
6.3.2 Stiffness recovery.....	152
6.3.3 Observation and elemental analysis on self-healing products	155
6.4 Summary and conclusions.....	161
CHAPTER 7: Sulfuric Acid Resistance of EGC	165
7.1 Introduction	165
7.2 Material and methods	167
7.2.1 Materials and mix designs	167
7.2.2 Specimen preparation.....	168
7.2.3 Sulfuric acid exposure.....	170
7.2.4 Test procedures	171
7.3 Results and discussion.....	172
7.3.1 Visual appearance and weight change	172
7.3.2 Compressive strength degradation.....	174
7.3.3 Flexural strength and deflection capacity at 28 days	177
7.3.4 Crack patterns in preloading	178
7.3.5 Residual flexural strength and deflection capacity	179
7.3.6 Residual bending stiffness	181
7.4 Summary and conclusions.....	183
PART IV: APPLICATION OF EGC.....	187
CHAPTER 8: Application and Environmental Life Cycle Assessment.....	187

8.1 Introduction	187
8.2 Target Market	189
8.3 Technical advantage analysis	190
8.4 Life cycle environmental assessment	193
8.4.1 LCA methodology	193
8.4.2 Goal and scope definition	194
8.4.3 Inventory analysis	200
8.4.4 Impact assessment and interpretation	204
8.5 Summary and conclusions.....	208
PART V: CONCLUSION.....	213
CHAPTER 9: Concluding Remarks	213
9.1 Research impacts and contributions	213
9.2 Research findings	215
9.3 Recommendations for future work.....	219
APPENDICES	222

LIST OF TABLES

Table 2.1: Summary of previous studies on material durability and structural resilience of ECC.	27
Table 3.1: L9 standard orthogonal array. Underlined tabulated values represent the coded factor levels.	50
Table 3.2: Example data set of measured compressive strength.	53
Table 3.3: ANOVA results on the example problem.	56
Table 3.4: Pooled ANOVA results on the example problem.	58
Table 3.5: 100-year GWP values of greenhouse gasses.	81
Table 3.6: Life-cycle inventory data of EGC ingredients.	81
Table 3.7: Mix design and computed energy- and carbon-MSI of preliminary EGC.	82
Table 4.1: Mechanical properties of preliminary EGC.	88
Table 4.2: Number of cracks and crack width of preliminary EGC at various strain levels.	88
Table 4.3: Mix proportion of preliminary EGC matrix (by mass).	91
Table 4.4: Chemical compositions (mass %) and physical properties of fly ash.	91
Table 4.5: L18 orthogonal array for EGC-matrix development.	93
Table 4.6: Compressive strength of 18 EGC mixtures with 3 samples each (in MPa).	95
Table 4.7: ANOVA results on six design variables of EGC matrix (unpooled).	96

Table 4.8: Mix proportion of optimum EGC matrix (by mass).	99
Table 4.9: Pooled ANOVA results on six design variables of EGC matrix.	100
Table 4.10: Measured and predicted compressive strengths of optimum EGC matrix (in MPa).	101
Table 4.11: Micromechanical parameters used as model input.	103
Table 4.12: Measured micromechanical parameters of optimum EGC matrix.	104
Table 4.13: Mechanical properties of EGC with three different fiber volume fractions.	108
Table 4.14: Life-cycle inventories of raw ingredients of concrete, ECC and EGC materials.	111
Table 4.15: Mixture proportions of EGC, concrete, and ECC materials (in kg/m ³).	112
Table 5.1: Mix designs of EGC used in this study (by mass).	123
Table 5.2: Residual-crack patterns of EGC.	130
Table 5.3: Change in permeability coefficients of EGC with time.	140
Table 6.1: Mix design of EGC used in this study (by mass).	148
Table 6.2: Initial and residual stiffness and stiffness ratio for the range of 0.5 – 2.0 MPa.	153
Table 6.3: Initial and residual stiffness and stiffness ratio for the range of 0.5 – 1.0 MPa.	155
Table 7.1: Mixture proportions of cement concrete, ECC, and EGC (in kg/m ³).	168
Table 7.2: Crack patterns of preloaded beam specimens.	179
Table 7.3: Flexural properties of RC, ECC, and EGC at 28 days and after acid exposure.	180
Table 8.1: Summary of assumptions and simplifications for LCA.	196
Table 8.2: Summary of inputs for life-cycle inventory analysis.	204

Table 8.3: Energy use of RC, ECC, and EGC pipes for each LCA phase in Scenario II (in MJ).

207

Table 8.4: GWI of RC, ECC, and EGC pipes for each LCA phase in Scenario II (in kg CO₂-eq).

207

Table A-1: L4 standard orthogonal array.

223

LIST OF FIGURES

- Fig. 1.1: Nonfuel material consumption in the US, 1900-2010. Construction of large-scale civil infrastructure is the largest user of raw materials. Continuous repair activities consume additional energy and materials over the long lifespan. 2
- Fig. 1.2: Typical tensile stress-strain curve and average crack-width development of ECC. The high ductility and tight cracking provide enhanced resilience and durability of infrastructure. 5
- Fig. 1.3: Green and durable fiber-reinforced geopolymer composites through combination of geopolymer and ECC technologies. 6
- Fig. 2.1: Schematic model for geopolymer structure. Geopolymers consist of three-dimensional aluminosilicate chains with charge-balancing alkali cations (typically Na^+ or K^+), unlike layered structure of calcium-silicate-hydrates (CSH) in portland cement-based binders. 13
- Fig. 2.2: Purdon demonstrated in 1940 that alkali-activated slag using various combinations of activator compounds could achieve strength comparable to OPC-based concrete. 14
- Fig. 2.3: Residential building made of alkali-activated slag concrete in Mariupol, Ukraine, 1960. The alkali-activation technology found various applications in the former Soviet Union. 15
- Fig. 2.4: Estimated CO_2 reduction of geopolymers compared to OPC, as a function of dissolved solids content of the activating solution. Fly ash-based geopolymers typically offer higher CO_2 reduction than metakaoline-derived ones. 17
- Fig. 2.5: (a) Conceptual model of geopolymerization for low-Ca alkali-activated systems. (b) More detailed model including Ca-rich systems such as alkali-activated slag. 20
- Fig. 2.6: Example of proposed mix-design methods for geopolymers. 22

Fig. 2.7: Schematic illustration of brittle concrete, tension-softening FRC, and strain-hardening HPFRCC.	25
Fig. 2.8: Examples of various ECC applications: (a) structural repair of concrete dam, (b) surface repair of retaining wall, (c) bridge-deck link slab, (d) bridge-deck overlay, (e)(f) structural dampers for high-rise buildings.	27
Fig. 2.9: Two required conditions for steady-state multiple cracking. Violation of either criterion results in oval-shaped Griffith-type crack propagation where fibers away from the crack tip are mostly pulled-out or broken. When both conditions are satisfied, the steady-state crack propagation takes place maintaining the constant crack opening and load-carrying capacity.	29
Fig. 2.10: Schematic illustration of a bridging fiber.	31
Fig. 3.1: Design scheme of the proposed integrated design method. Three design techniques for matrix, composite, and sustainability design phases are utilized, working synergistically to guide the optimization.	46
Fig. 3.2: Mean compressive strength at each trial, and the total and group means.	53
Fig. 3.3: Main-effect plots showing mean compressive strength at each level of factors.	57
Fig. 3.4: (a) Specimen geometry and (b) test setup for JSCE dog bone testing.	61
Fig. 3.5: Specimen geometry for matrix fracture-toughness test.	63
Fig. 3.6: (a) Specimen geometry and (b) test setup for single-fiber pullout test.	64
Fig. 3.7: Typical single-fiber pullout curve with slip-hardening.	65
Fig. 3.8: (a) One-way pullout case; only the short-embedment side enters the pullout stage, while the other side remains in the debonding stage. (b) Two-way pullout case; the long-embedment side also undergo the pullout stage for $\delta = u_L + u_S$ such that $u_S > u_{0S}$ and $u_L > u_{0L}$.	70
Fig. 3.9: Proposed hysteresis of the debonding curve for a standard ECC (M45).	72
Fig. 3.10: Schematic illustration of matrix micro-spalling.	74

Fig. 3.11: Schematic illustration of Cook-Gordon effect. (a) Matrix crack approaching an embedded fiber triggers debonding of the premature fiber/matrix interface, (b) which results in additional crack opening δ_{cg} .	75
Fig. 3.12: Flow chart of numerical simulation of σ - δ curve.	76
Fig. 3.13: Simulated σ - δ curve of ECC M45. Three-dimensional uniform fiber distribution was assumed, and both matrix micro-spalling and Cook-Gordon effect were included.	77
Fig. 3.14: Singe-crack test: (a) specimen geometry, (b) test setup, and (c) fracture plane after testing.	78
Fig. 4.1: Stress-strain curves of preliminary EGC specimens under uniaxial tension.	88
Fig. 4.2: Strain maps obtained from the DIC analysis. Multiple-crack formation at progressively increased imposed strain was visualized.	89
Fig. 4.3: Plots of mean responses at each level of factors to visualize the main factor effects.	97
Fig. 4.4: Computed (a) fiber-bridging capacity and (b) complementary energy with their PSH indices. Dashed lines indicate recommended PSH values for practical design.	105
Fig. 4.5: Tensile stress-strain curves of all EGC series show strain hardening with high ductility.	107
Fig. 4.6: (a) Embodied energy and (b) global warming potential for EGC, concrete, and ECC materials. CO ₂ equivalent emissions of EGC-1.5% are about half of regular concrete.	114
Fig. 5.1: Design of prism mold.	124
Fig. 5.2: Curing conditions for intact and cracked EGC specimens prior to permeability testing.	125
Fig. 5.3: Permeability-testing apparatus developed by Lepech and Li.	127
Fig. 5.4: Modified permeability-testing setup used in this study.	128

Fig. 5.5: Tensile stress-strain curves of EGC specimens under preloading.	130
Fig. 5.6: Density histograms of EGC crack width and their fitted lognormal distributions.	132
Fig. 5.7: Comparison between fitted probability distributions of $V_f1.5$ and $V_f2.0$ series.	133
Fig. 5.8: Permeability coefficient of EGC versus applied tensile strain.	134
Fig. 5.9: Comparison of permeability coefficients for EGC, ECC and reinforced cement mortar.	135
Fig. 5.10: Permeability coefficient versus maximum crack width (after unloading) for cement concrete, reinforced cement mortar, ECC, and EGC (outliers included).	136
Fig. 5.11: Permeability coefficient versus average crack width of EGC.	139
Fig. 6.1: Test schedule and curing condition for each series of EGC.	148
Fig. 6.2: Images of EGC microcracks right after preloading and after water curing: (a)(b) a completely-sealed microcrack; and (c)(d) a partially-sealed microcrack.	152
Fig. 6.3: Portions of stress-strain curves at preloading and reloading and chord modulus for reloading.	154
Fig. 6.4: (a) SEM image of a microcrack and self-healing products sealing the crack; and (b) magnified view of the healing products.	156
Fig. 6.5: EDS line-scan analysis was performed on the line that crosses a microcrack sealed with white precipitates, including the uncracked region of the geopolymer matrix.	157
Fig. 6.6: Elemental compositions along the scanned line. The presence of efflorescence products (Na_2CO_3) and calcite (CaCO_3) is not confirmed. The healing products are Si- and Al-rich substance.	159
Fig. 6.7: EDS mapping. Regions of higher concentration are shown in higher brightness. Higher concentration of Si and Al, and lower concentration of Ca in the sealed crack can be clearly seen.	160

Fig. 7.1: RC beam design and testing setup of four-point bending.	169
Fig. 7.2: Test conditions of sulfuric acid exposure. Five cycles (35-day exposure) correspond to average corrosion damage observed in 20-year-old ordinary concrete sewer pipes.	171
Fig. 7.3: Typical appearances of specimen surface with various acid exposure periods.	173
Fig. 7.4: Slight weight gain is observed for both concrete and ECC in the first two cycles (i.e. 14 days), but the rate of subsequent weight loss is three times that of EGC.	174
Fig. 7.5: Compressive strength of concrete, ECC, and EGC before and after sulfuric acid exposure. All the series show strength increase even after the acid attack, compared to their 28-day compressive strength (i.e. “0d”).	175
Fig. 7.6: Strength increase due to continuous hydration is extracted by normalizing the raw compressive strength data by those of control specimens cured in water. Continuous strength degradation due to the acid attack is observed in concrete, while there is no significant effect on ECC and EGC.	176
Fig. 7.7: Typical flexural stress–mid deflection curves of RC, ECC, and EGC beams. Due to relatively high reactive fly ash, ECC beams show lower deflection capacities than expected, with a few multiple cracks.	178
Fig. 7.8: (a) RC beam shows significant reduction in bending stiffness due to the preloading and subsequent acid attack. The smallest stiffness reduction of (b) ECC beam is suggested to be a result of recovery due to self-healing.	182
Fig. 8.1: Large-diameter pipe demand in the US (a) by material and (b) by application, 2011.	190
Fig. 8.2: Predicted concrete-pipe lifespan by Ohio Department of Transportation (ODOT). Years for the pipe to reach a poor condition (based on ODOT classification) highly depend on pH of the stream.	191
Fig. 8.3: (a) Precast geopolymer sewer pipes of 1.8 m diameter, commercially available in Australia; (b) repair of deteriorated concrete sewer pipes in the US by spray-applied geopolymer.	192

Fig. 8.4: Schematic illustrations of comparison between RC and EGC sewer pipes.	193
Fig. 8.5: System boundary of the sewer pipe system. Use and disposal phases are omitted because of the low contribution to the life-cycle environmental impacts.	196
Fig. 8.6: Service-life estimation procedure.	199
Fig. 8.7: Linear regressions for weight loss-exposure time relationship for acid-exposed concrete, ECC and EGC. For concrete and ECC, the constant rate was assumed for data after 35 days.	199
Fig. 8.8: Trench design for circular RC pipe. The total trench volume for this study is 1.22 m ³ .	203
Fig. 8.9: Life-cycle energy use and GWI values of RC, ECC, and EGC pipes in Scenario I.	206
Fig. B-1: (a) Model of fiber debonding process; (b) a small fiber segment of the debonded zone.	225
Fig. B-2: Force equilibrium in the debonded fiber and surrounding matrix.	227
Fig. B-3: Model of fiber pullout process.	231
Fig. C-1: Pullout-debonding phase of single-fiber pullout.	234
Fig. C-2: Simulated σ - δ relations of ECC M45 by using the original and modified models.	236
Fig. C-3: Simulated fiber status at each crack opening.	236
Fig. C-4: Simulated σ - δ relations with high chemical bond of 10 J/m ² and fiber strength of 2000 MPa.	237
Fig. C-5: Simulated fiber status with high chemical bond and fiber strength.	238
Fig. D-1: Modified permeability-testing setup used in this study.	239

LIST OF APPENDICES

APPENDIX

A. Confounding of interaction effects.	223
B. Derivation of P-u relations for debonding and pullout stages.	225
C. Derivation and analysis of the proposed hysteresis for fiber debonding load.	234
D. Derivation of the modified formula for permeability coefficient.	239

ABSTRACT

Green concrete, which incorporates industrial byproducts to partially/fully replace portland cement in normal concrete, is not as sustainable as many would like to believe. Like conventional cement concrete, it is a brittle material with low tensile strength and ductility, and therefore susceptible to cracking. Extensive cracking causes many types of deterioration in concrete structures, significantly reducing their service life. Even if the structure is made of more “environmentally-friendly” materials, the short lifespan makes it unsustainable. For establishing sustainable infrastructure systems, a new material technology that combines high material greenness and durability in one concrete needs to be developed.

This dissertation is focused on green and durable fiber-reinforced geopolymer composites – Engineered Geopolymer Composites (EGCs) – for civil infrastructure applications. EGCs combine two emerging technologies: geopolymer, which is a cement-free binder material, and Engineered Cementitious Composite (ECC), which is a strain-hardening fiber-reinforced cement composite with high tensile ductility and multiple-microcracking characteristics. This research covers three aspects: development, characterization, and application of EGC.

First, a new design method for ductile fiber-reinforced geopolymer composites is proposed to facilitate the development of EGC. It integrates three material-design techniques – Design of Experiment (DOE), micromechanical modeling, and Material Sustainability Indices (MSI) – each of which assists the geopolymer-matrix development, composite design, and environmental

performance assessment. With the aid of the integrated design method, an optimized EGC with good compressive strength, high tensile ductility, and enhanced material greenness is systematically developed.

Second, fundamental durability properties of the developed EGC are experimentally characterized. Specifically, cracking characteristics, water permeability, self-healing functionality, and sulfuric acid resistance are investigated. Extensive crack-width measurement and water-permeability testing on cracked EGC demonstrate the tightly-controlled multiple cracks and higher water tightness than cracked reinforced concrete (RC). The permeability test also observes a white substance formed inside microcracks of EGC, providing the recovery in water tightness. Subsequent experiments also confirm the stiffness recovery, which demonstrates the self-healing functionality of EGC. In the case of sulfuric acid resistance, acid-exposed EGC specimens show limited surface erosion compared to cement concrete and ECC. Further, no significant degradation in mechanical properties of EGC is observed.

Finally, this dissertation explores a promising infrastructure application of EGC. Combined with the characterized durability properties, brief market research and technical-advantage analysis suggest that EGC is promising for large-diameter sewer pipes. In addition, an environmental life cycle analysis (LCA) is conducted to verify and quantify the enhanced sustainability of EGC pipes, in comparison with RC and ECC pipes. The comparative LCA shows the 13% lower greenhouse gas emissions of EGC than RC. Further, it is estimated that, if service life of EGC pipes is more than 1.3 times that of RC pipes, EGC performs best in both energy consumption and greenhouse gas emissions.

PART I: INTRODUCTION

CHAPTER 1: Introduction

1.1 Background and motivation

Human life is full of manufactured goods today. Manufactured goods are designed and manufactured to improve our quality of life, but their production has some adverse impact on the environment we live in. The same is true for civil infrastructure. However, infrastructure systems – transportation, power, water and wastewater, and communication systems, for instance – are different from most other products in two aspects: *size* and *longevity*. The large scale of civil infrastructure implies huge consumption of material resources and energy in their construction (Fig. 1.1); the long lifespan is linked to continuous repair and retrofit, which also cause environmental impacts. Because of the large and long-lasting impacts on the environment, sustainable design of civil infrastructure is crucial for us and future generations. This raises the question: *what does truly sustainable infrastructure look like?*

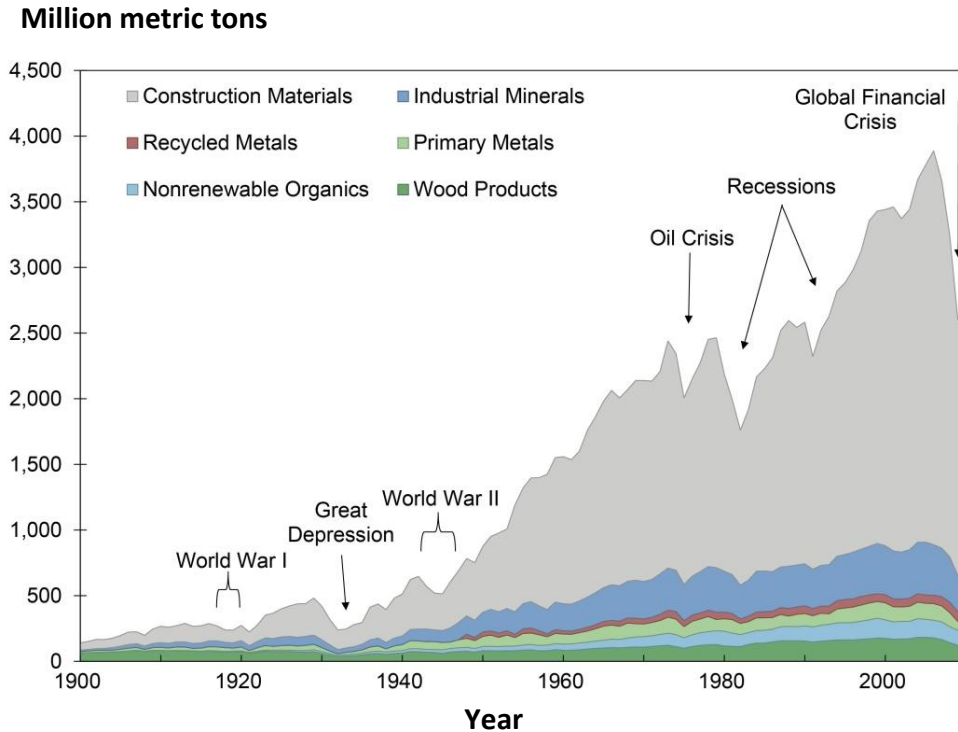


Fig. 1.1: Nonfuel material consumption in the US, 1900-2010 [1]. Construction of large-scale civil infrastructure is the largest user of raw materials. Continuous repair activities consume additional energy and materials over the long lifespan.

As with many other manufactured goods, the use of green materials – i.e. materials with low environmental impacts regarding energy use, greenhouse gas emissions, etc. – is a typical approach in civil infrastructure for improving sustainability. A particular focus has been placed on cement concrete, which is the most widely-used construction material today, and has high carbon intensity. Ordinary Portland Cement (OPC) is a primary ingredient in cement concrete and the largest contributor to the carbon footprint. During OPC production, carbon dioxide (CO₂) is generated from both fossil fuel combustion in the cement kiln operation and the chemical reactions involved in calcination of limestone. The former can be improved by enhancing the thermal efficiency of kiln and cooler systems, but the latter is inherent to cement manufacturing. Indeed, studies have estimated that, despite good progress in switching to highly optimized kilns,

OPC production accounts for 5-8% of the global man-made CO₂ emissions [2–5]. As a consequence of the high carbon intensity of OPC, much effort has been made in developing *green concrete* that incorporates industrial wastes to partially/fully replace OPC.

However, such concrete with lower environmental impacts does not always provide true infrastructure sustainability. Like conventional concrete, green concrete is a brittle material with low tensile strength and ductility, and therefore susceptible to cracking. Steel reinforcement is typically placed in concrete structures, but often insufficient to fully control cracking under combined mechanical and environmental loads in field applications. Cracking causes many types of deterioration in concrete structures: it directly lowers mechanical properties of concrete, and also accelerates the degradation by serving as pathways for aggressive agents, which penetrate the structure and attack the concrete and steel reinforcement. The resultant poor durability of the structure leads to frequent and/or intensive repair activities, consuming a large amount of energy and raw materials. In the worst case scenario, full replacement of the structure is needed much earlier than the designed service life. Thus, the approach of using green materials is inadequate in the context of minimizing life-cycle environmental impacts of civil infrastructure.

Truly sustainable infrastructure materials should be not only green but also durable. However, current research and development activities on sustainable construction materials are often focused on only one aspect of the two, with little emphasis on the other. For enhancing sustainability of infrastructure systems, a new material technology that combines high material greenness and durability in one concrete needs to be developed. This is the motivation behind the present doctoral research.

1.2 Problem statement

Recently, the research community has begun to explore green and durable concrete materials. A promising approach is to integrate existing technologies developed for either green or durable concrete. Out of various available ones, *geopolymer* and *Engineered Cementitious Composite* (ECC) are emerging material technologies that have gained increasing interest in the past few decades.

Geopolymer is a family of alkali-activated binder materials that shows promise as a green alternative to OPC [6–8]. Geopolymer paste is formed from solid aluminosilicate sources activated by alkaline solution. The fresh geopolymer has similar rheological and hardening properties to those of cement binders, and can be used to produce geopolymer mortar or concrete. Among various types of geopolymer materials, fly ash-based geopolymer is one of the most promising candidates; it utilizes fly ash – an industrial byproduct from coal-fired power plants – as the aluminosilicate source and relies on no OPC. Indeed, geopolymer binders have been estimated to offer 80% or greater reduction in CO₂ emissions than OPC [9]. However, geopolymer concrete is by its nature a brittle material like cement concrete. The low ductility of geopolymer causes cracking and corresponding performance degradation, which limits its durability as in cement concrete.

Engineered Cementitious Composite (ECC), on the other hand, is a material technology that imparts high tensile ductility – and therefore enhanced durability – to brittle cement concrete [10–12]. ECC consists of OPC-based cement mortar and randomly-oriented short fibers with moderate volume fraction (typically less than 2% by volume). Through systematic optimization of matrix, fiber, and fiber/matrix interface properties, ECC exhibits the tensile strain-hardening behavior with high ductility of 3-5%. Further, multiple cracking occurs in the strain-hardening

stage and the crack width is controlled to be as tight as a human hair (Fig. 1.2). These unique features are beneficial in infrastructure applications; both laboratory and field studies have demonstrated that the high ductility and tight cracking of ECC provide improved durability of civil infrastructure [13–15]. However, compared to regular cement concrete, ECC has higher carbon and energy footprints due to its use of a larger amount of OPC and petroleum-based synthetic fibers with high embodied energy. Thus, the low material greenness of ECC is a technical challenge to overcome for achieving true sustainability of civil infrastructure.

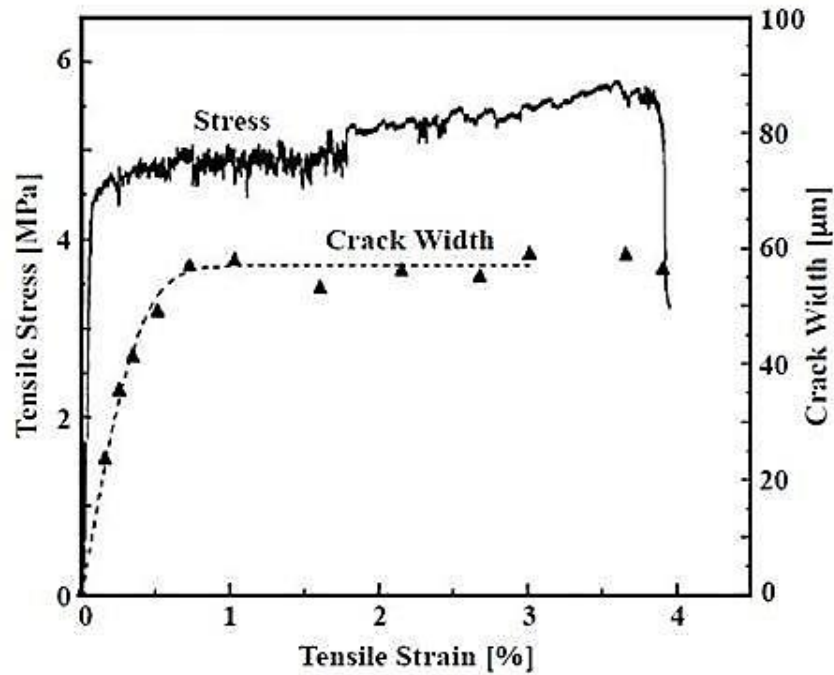


Fig. 1.2: Typical tensile stress-strain curve and average crack-width development of ECC [16]. The high ductility and tight cracking provide enhanced resilience and durability of infrastructure.

It is considered that combination of geopolymer and ECC technologies is a promising solution for developing green and durable concrete materials: that is, a family of fiber-reinforced geopolymer composites that has high tensile ductility and multiple-microcracking characteristics (Fig. 1.3). Indeed, there has been a growing interest in such materials since the 1990s [17].

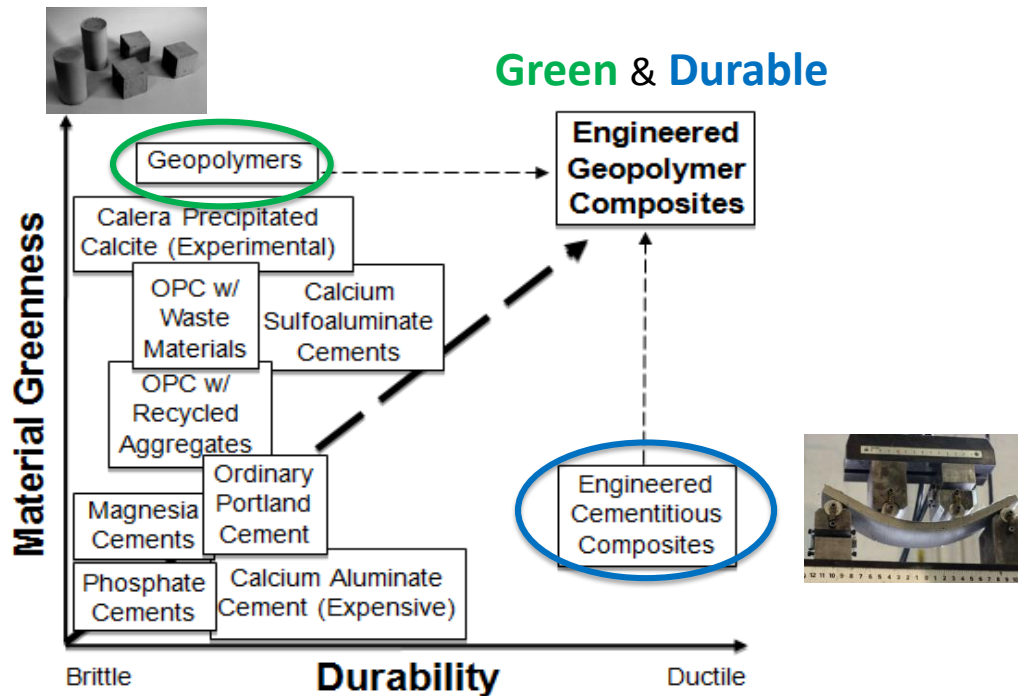


Fig. 1.3: Green and durable fiber-reinforced geopolymer composites through combination of geopolymer and ECC technologies (diagram adapted from [17]).

While much research effort has been taken so far, scientific and technical knowledge of ductile geopolymer composites is still in the early stage of development. Specifically, the following major challenges remain today:

- No comprehensive design method of fiber-reinforced geopolymers has been developed yet.
- High tensile ductility and multiple-microcracking characteristics comparable to ECC have not yet been achieved in such types of materials.
- Much remains unknown about their durability properties.
- As a result, it is difficult to quantitatively assess their sustainability in the context of infrastructure applications throughout their service life.

In particular, the lack of a systematic design methodology for ductile fiber-reinforced geopolymers is a key issue; currently, time- and cost-intensive trial-and-error approaches are often taken in the research community, which slows overall progress on the subject.

1.3 Research objectives

This doctoral study aims to develop a novel class of ductile fiber-reinforced geopolymer composites – named *Engineered Geopolymer Composite* (EGC) – for a variety of large-scale infrastructure applications. The cement-free geopolymer matrix of EGC offers substantial reduction in energy and carbon footprints; the enhanced durability through optimized fiber reinforcement contributes to less repair/maintenance and longer service life of civil infrastructure. This next-generation infrastructure material will open a new window toward establishing truly sustainable infrastructure systems.

Specific objectives of this research are detailed below, which covers three aspects: development, characterization, and application of the material.

- Develop a comprehensive design method of EGC that facilitate the research and development.
- Achieve high tensile ductility and self-controlled microcracking in EGC, while minimizing energy and carbon intensities of the material.
- Characterize fundamental durability properties of the developed EGC.
- Explore promising applications of EGC in which the high material greenness and durability can be fully utilized.

- Conduct a case study on life-cycle environmental impacts of the example EGC application, in comparison with conventional cement concrete and ECC.

1.4 Research approach and thesis organization

A broad range of multidisciplinary research methods are used in this thesis, including statistics, fracture mechanics, micromechanics, materials science, and industrial ecology. The research approach and structure of the thesis are outlined below:

Following this introductory part, Part II containing three chapters is focused on development of green and ductile – and therefore durable – EGC materials. Chapter 2 outlines previous research and development of both geopolymer and ECC, and also presents technical challenges in combining the two materials technologies. Chapter 3 then proposes a new design methodology for EGC that integrates three design techniques: Design of Experiment (DOE), micromechanical modeling, and Material Sustainability Indices (MSI). The systematic design method enables simultaneous optimization of multiple responses such as strength, tensile ductility (often inversely related to strength), and energy/carbon footprints. The application of the proposed design method is presented in Chapter 4, which systematically develops an optimized version of EGC.

Part III describes experimental characterization on durability properties of the developed EGC, throughout three chapters. In Chapter 5, cracking characteristics and water tightness of the developed EGC are evaluated. Residual-crack patterns of EGC are first determined with respect to the maximum and average crack widths, and the probability density function of crack width. The permeability coefficients of both intact and cracked EGC are then measured by using a

newly-developed test setup and a formula derived based on the Darcy's law. The effect of EGC microcracks on the water permeability is discussed based on the measured crack patterns and permeability coefficients. Chapter 6 focuses on the feasibility of self-healing EGC. Stiffness recovery of EGC specimens that are preloaded to create cracks and then cured in water is measured by uniaxial tension testing. Self-healing products are also observed by using a Scanning Electron Microscope (SEM) equipped with an Energy Dispersive Spectroscopy (EDS) analyzer. Chapter 7 examines the sulfuric acid resistance of EGC. Weight loss and degradation of mechanical properties in acid-exposed EGC specimens are reported, as well as those of regular cement concrete and ECC.

Part IV explores promising infrastructure applications of EGC. In particular, large-diameter sewer pipes are considered in Chapter 8. The market demand, existing technology, and technical challenges of sewer concrete pipes are first outlined. Then, a Life Cycle Assessment (LCA) on environmental impacts of EGC sewer pipes is conducted, in comparison with reinforced-concrete and ECC pipes.

Chapter 9 in Part V is the concluding chapter. Scientific contributions and impacts to the research field of this dissertation are first highlighted. Major research findings are then summarized, and recommendations for future work of this subject are provided.

References

- [1] Center for Sustainable Systems, University of Michigan, “U.S. Material Use Factsheet,” Pub. No. CSS05-18 , 2016.
- [2] C. Chen, G. Habert, Y. Bouzidi, and A. Jullien, “Environmental impact of cement production: detail of the difference processes and cement plant variability evaluation,” *J. Cleaner Production*, vol. 18, pp. 478–485, 2010.
- [3] E. Benhelal, G. Zahedi, E. Shamsaei, and A. Bahadori, “Global strategies and potential to curb CO₂ emissions in cement industry,” *J. Cleaner Production*, vol. 51, pp. 142–161, 2013.
- [4] WBCSD, “Cement Industry Energy and CO₂ Performance: Getting the Numbers Right” [Online]. Available: <http://www.wbcscement.org/pdf/GNR%20dox.pdf>. [Accessed: 29-August-2017].
- [5] WBCSD, “Cement Sustainability Initiative Progress Report 2005,” [Online]. Available: https://www.wbcscement.org/pdf/csi_progress_report_2005.pdf. [Accessed: 05-May-2017].
- [6] J. Davidovits, *Geopolymer Chemistry and Applications*, Third ed. Saint-Quentin (France): Institut Geopolymere, 2008.
- [7] P. Duxson, A. Fernández-Jiménez, J. L. Provis, G. C. Lukey, A. Palomo, and J. S. J. Van Deventer, “Geopolymer technology: The current state of the art,” *J. Mater. Sci.*, vol. 42, no. 9, pp. 2917–2933, Dec. 2007.
- [8] J. L. Provis and J. S. J. van Deventer, *Geopolymers-Structure, processing, properties and industrial applications*. Cambridge (UK): Woodhead Publishing, 2009.
- [9] P. Duxson, J. L. Provis, G. C. Lukey, and J. S. J. van Deventer, “The role of inorganic polymer technology in the development of ‘green concrete,’” *Cem. Concr. Res.*, vol. 37, no. 12, pp. 1590–1597, Dec. 2007.
- [10] V. C. Li, “Engineered Cementitious Composites (ECC) – Tailored Composites through Micromechanical Modeling,” in *Fiber reinforced concrete: present and future*, N. Banthia, A. Bentur, and A. A. Mufti, Eds. Montreal (Canada): Canadian Society for Civil Engineering, 1998, pp. 64–97.
- [11] V. C. Li, “On engineered cementitious composites (ECC). A review of the material and its applications,” *J. Adv. Concr. Technol.*, vol. 1, no. 3, pp. 215–230, 2003.
- [12] V. C. Li, “Engineered Cementitious Composites (ECC) – Material , Structural , and Durability Performance,” in *Concrete Construction Engineering Handbook*, E. G. Nawy, Ed. CRC Press, 2008, pp. 1–40.
- [13] M. D. Lepech and V. C. Li, “Long Term Durability Performance of Engineered Cementitious Composites,” *Restor. Build. Monum.*, vol. 2, no. 2, pp. 119–132, 2006.

- [14] M. Şahmaran and V. C. Li, “Durability properties of micro-cracked ECC containing high volumes fly ash,” *Cem. Concr. Res.*, vol. 39, no. 11, pp. 1033–1043, Nov. 2009.
- [15] M. Kunieda and K. Rokugo, “Recent Progress on HPFRCC in Japan Required Performance and Applications,” *J. Adv. Concr. Technol.*, vol. 4, no. 1, pp. 19–33, 2006.
- [16] S. Wang, “Micromechanics based matrix design for engineered cementitious composites,” University of Michigan, Ann Arbor, 2005.
- [17] A. R. Sakulich, “Reinforced geopolymer composites for enhanced material greenness and durability,” *Sustainable Cities and Society*, vol. 1, no. 4. Elsevier B.V., pp. 195–210, Dec-2011.

PART II: DEVELOPMENT OF EGC

CHAPTER 2: Review of Green and Durable Concretes

This chapter provides a literature review on two material technologies: *geopolymer* and *Engineered Cementitious Composite* (ECC). The historical development, previous research findings, and unsolved problems of each material are outlined, with emphasis on the material design. Based on the review, challenges in combining the two technologies are considered.

2.1 Geopolymer

In the context of this dissertation, “geopolymer” is defined as an aluminosilicate binder material that is formed from an aluminosilicate precursor (typically supplied in a powdered form) activated by an alkali hydroxide, alkali carbonate, and/or alkali silicate activator. As such, there are many types of geopolymers with various physical and chemical properties, depending on the types of precursors and activators. In general, geopolymers have three-dimensional polymeric structure of cross-linked silicate (SiO_4) and aluminate (AlO_4^-) tetrahedra, coupled with charge-balancing alkali cations (Fig. 2.1).

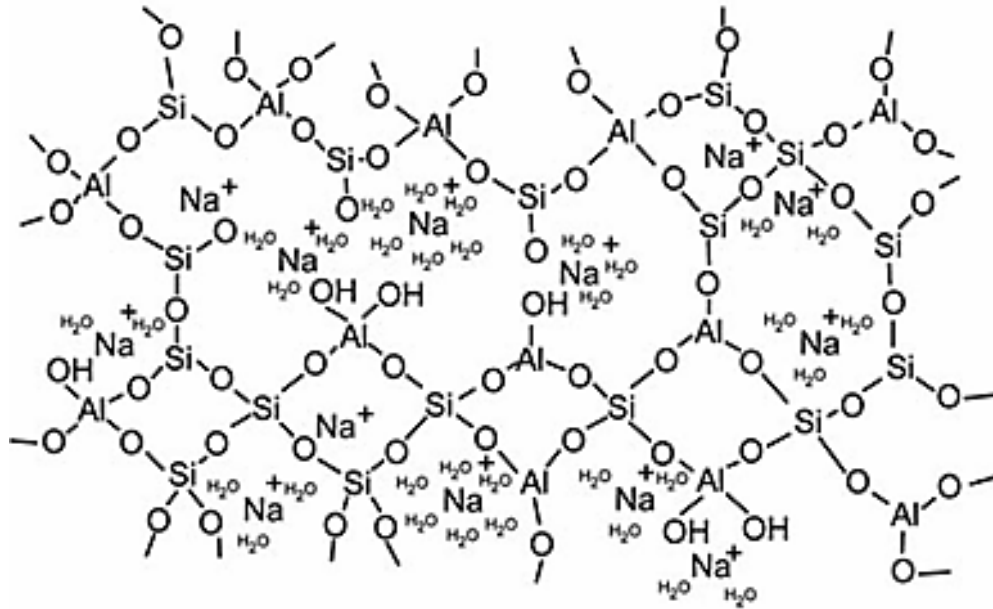


Fig. 2.1: Schematic model for geopolymer structure [1]. Geopolymers consist of three-dimensional aluminosilicate chains with charge-balancing alkali cations (typically Na^+ or K^+), unlike layered structure of calcium-silicate-hydrates (CSH) in portland cement-based binders.

2.1.1 History of development

The first literature on alkali-activated binder materials dates back to the early 1900s: a German chemist Kühl reported a study on reactions of a metallurgical slag with alkaline components to form a binder, which was patented in the US in 1908 [2]. Following his initial investigation, the detailed scientific basis on such binders for construction purposes was developed in Belgium by Purdon, who published a landmark paper in 1940 [3]. His extensive laboratory study demonstrated that alkali-activated slag could achieve good strength, moderate shrinkage, and low water permeability comparable to OPC concrete (Fig. 2.2). Nevertheless, research on the alkali-activation technology was limited in the Western world until the 1980s [4]; in those days, the primary focus in the research community remained in production and optimization of portland cement and cement concrete [5]. In general, a strong driving force is needed for intensive research and development of a technology.

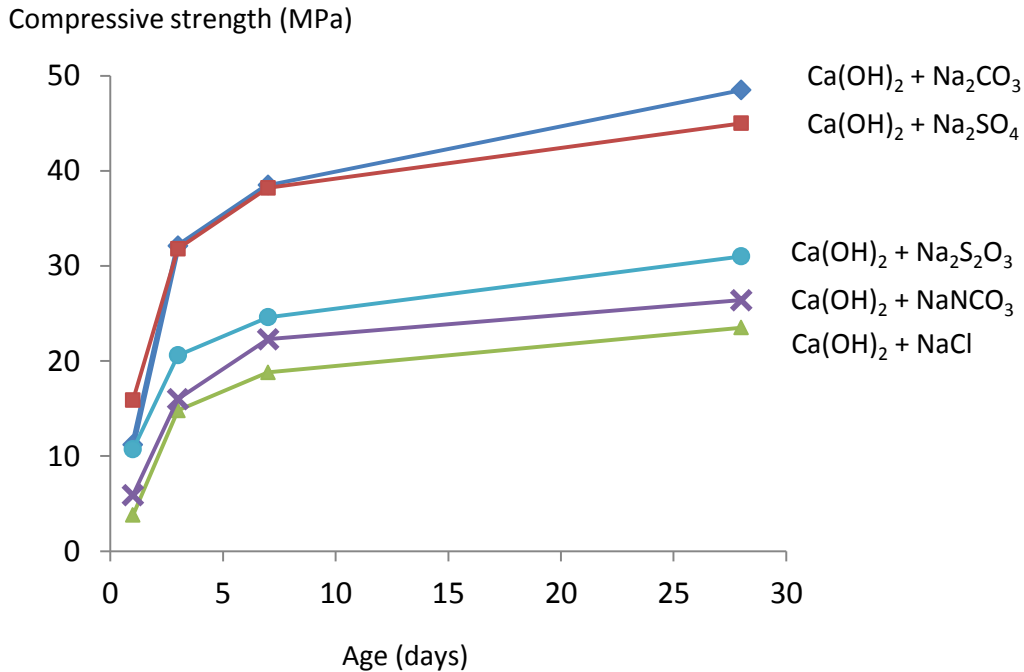


Fig. 2.2: Purdon demonstrated in 1940 that alkali-activated slag using various combinations of activator compounds could achieve strength comparable to OPC-based concrete (data from [3]).

The former Soviet Union had a dominant economic driver: along with a massive construction program undertaken in the mid-20th century, the Eastern-bloc country faced a serious cement shortage. There was an urgent need for low-cost alternatives to cement that can utilize materials at hand. Meanwhile, in the mid-1950s, Glukhovsky began to study ancient concrete structures in Rome and Egypt. He discovered that ancient cements with superior durability were typically low in calcium (*Ca*) and rich in alkalis, *Al* and *Si* [6]. Based on the investigation, he proposed a general mechanism for alkali activation of aluminosilicate materials, and developed alkaline aluminosilicate cementitious systems, called “soil cements” [7]. Active researches on such materials were then carried out in the Eastern world, boosted by the cement demand outstripping its supply.

The invention by Glukhovsky also found a wide range of applications: the research institute in Kiev, Ukraine used alkali-activated blast furnace slag (BFS) in construction of apartment buildings, railway sleepers, road sections, pipes, drainage and irrigation channels, flooring for dairy farms, pre-cast slabs and blocks [8] (Fig. 2.3). Until 1989, more than 3 hm³ (cubic hectometers) of alkali-activated concrete had been poured in the former Soviet Union [9]. High durability of those alkali-activated slag concrete structures has been reported in recent studies [10, 11].



Fig. 2.3: Residential building made of alkali-activated slag concrete in Mariupol, Ukraine, 1960 [12]. The alkali-activation technology found various applications in the former Soviet Union.

In the past few decades, the major driver for the alkali-activated binders has shifted from economic aspects to technical advantages, and to environmental concerns.

In the late 1970s, Davidovits developed a series of alkali-activated binders based on metakaolin, which is calcined kaolin clay [13]. He patented many aluminosilicate-based formulations and

coined the term “geopolymer” for his products. The material technology was originally developed for fire-resistant applications; shortly afterward, its high early-strength development attracted attention from the US Army for military applications [14]. From the 1980s onwards, research and development activities on alkali-activation technologies began to expand worldwide because of their technical advantages such as rapid strength gain, fire resistance, chemical and dimensional stabilities, and low permeability. However, primary use of metakaolin-based geopolymers has been limited to small-scale niche applications to date; metakaolin is expensive to produce in large volumes and is energy intensive due to its calcination process.

Another breakthrough came in 1993 when Wastiels *et al.* published the first paper on alkali-activated binders using fly ash, which is an industrial byproduct from coal-fired power plants [15]. Since then, research into fly ash-based geopolymers (FAGP) has been growing dramatically because of their significant environmental benefits. Particularly, considerably lower carbon footprints of FAGP than OPC-based binders have been highlighted in many studies (e.g. [16–19]) (Fig. 2.4). In addition, FAGP can increase the recycling rate of fly ash; while a huge volume of fly ash is generated around the world, most of it is just disposed of in landfills. For instance, 1.03 billion tons of fly ash was produced in the US from 2000 to 2015, but only 40% of it has been utilized so far [20]. The same problem of fly ash disposal is true in both China and India, which are the top users of OPC and large contributors to the global CO₂ emissions, as well as the US. Driven by worldwide concerns of global warming, resource depletion, and waste disposal, utilization of FAGP for large-scale construction applications is now an important subject in both academic and industrial research institutions [16].

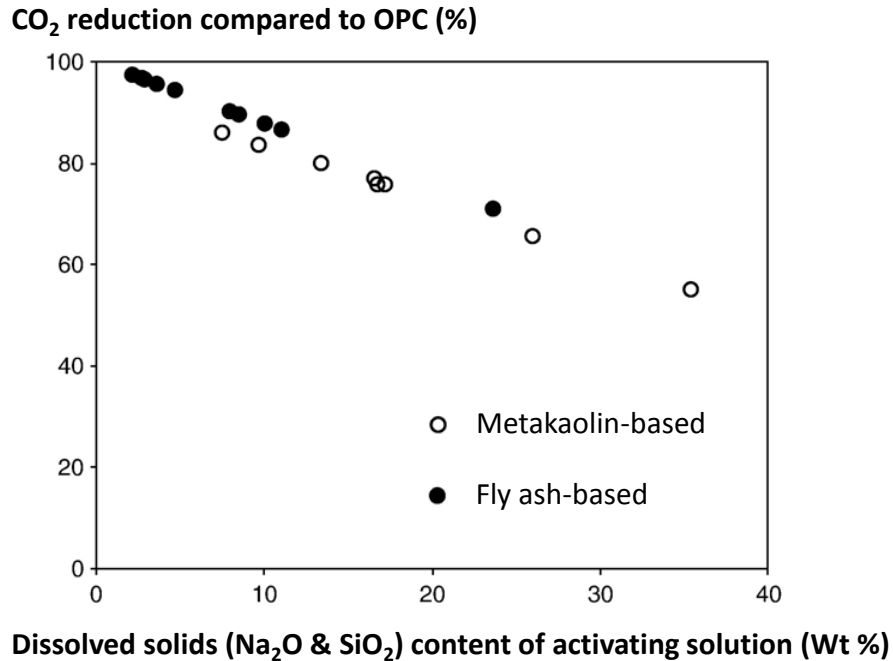


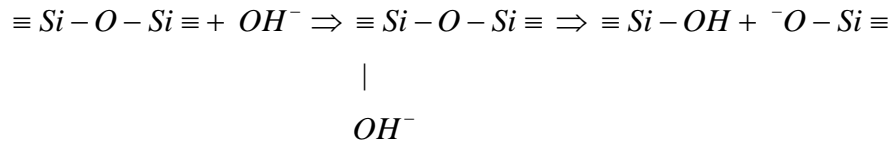
Fig. 2.4: Estimated CO₂ reduction of geopolymers compared to OPC, as a function of dissolved solids content of the activating solution (adapted from [16]). Fly ash-based geopolymers typically offer higher CO₂ reduction than metakaoline-derived ones.

2.1.2 Previous studies for geopolymer design

With the support of economic, technical, and environmental driving forces, alkali-activated binder materials have been actively studied since 1960s. The subjects of investigation include, but are not limited to, reaction mechanisms and processes involved in alkali activation of aluminosilicate precursors, setting behavior and workability of the fresh paste, and chemical structure, microstructure, and macroscopic engineering properties of the hardened matrix. Among many previous investigations, studies of the reaction mechanisms and processes are particularly important for material design of geopolymers: understanding of the chemistry is essential to predict physical and chemical properties of the material at multiple length and time scales. The present literature review focuses on this subject.

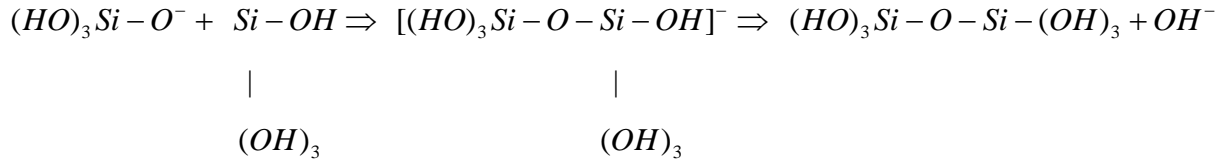
Glukhovsky was the first to propose a general reaction mechanism of alkali-activation of aluminosilicate minerals [7], which has served as a basis for subsequent studies on the chemistry of “geopolymerization”. His model divides the reaction processes into three stages: (i) destruction–coagulation, (ii) coagulation–condensation, and (iii) condensation–crystallization.

The first destruction process is initiated by hydroxide ions (OH^-) in the alkaline activator that sever covalent bonds of $Si-O-Si$ and $Al-O-Si$ in the solid aluminosilicate precursor [21]. The severance of $Si-O-Si$ bonds, for instance, can be expressed as:



Silanol ($\equiv Si-OH$) and sialate ($\equiv Si-O^-$) species are produced in this reaction, and the negative charge of $\equiv Si-O^-$ groups is instantly neutralized by the alkali cations (most commonly Na^+) provided from the activator. The resultant $\equiv Si-O^- - Na^+$ complexes are chemically stable in the alkaline media, suppressing the reverse reaction to form $Si-O-Si$ bonds. Then, the stability creates suitable conditions for diffusion of disaggregated units from the particle surface to the inter-particle space, and for their subsequent coagulation. The OH^- ions affect the $Al-O-Si$ and $Al-O-Al$ bonds in the same way.

Following the dissolution of the solid aluminosilicate, accumulation of the disaggregated products forms a coagulated structure that favors polycondensation. The monomer $-Si(OH)_4$ in the case of the silanol species – reacts with another monomer to form the following dimer:



This is followed by formation of trimers and more condensed oligomers. Aluminate species also participate in the polycondensation process, replacing the silicate tetrahedra.

In the third stage, polymerization of silicate-aluminate species grow in all directions, producing colloids. Lastly, the colloidal particles progressively precipitate to reconsolidate, supported by particles in the initial solid phase working as nuclei.

The initial conceptual model developed by Glukhovsky has been extended and refined by many other researchers (e.g. [22–29]). Based on those contributions, Duxson *et al.* presented an often-reproduced schematic illustration of geopolymerization processes (Fig. 2.5-a) in their “state of the art” review paper [30]. The illustrated reaction mechanism outlines the key processes of dissolution, rearrangement, condensation, and re-solidification. Those processes do not proceed fully linearly, but rather are coupled reactions occurring concurrently. The proposed process of particle-to-gel conversion has been confirmed in subsequent studies [31–34], with advances in experimental and analytical methods. More recently, Provis and Bernal pointed out that their conceptual model was highly simplified and inappropriate to be used for Ca-rich alkali-activated systems such as alkali-activated slag [35]. It does not include the formation of CSH-type structure, which is actually the main binder phase in slag-derived alkali-activated systems. A more detailed conceptual diagram was provided by Provis and Bernal in [36] (Fig. 2.5-b).

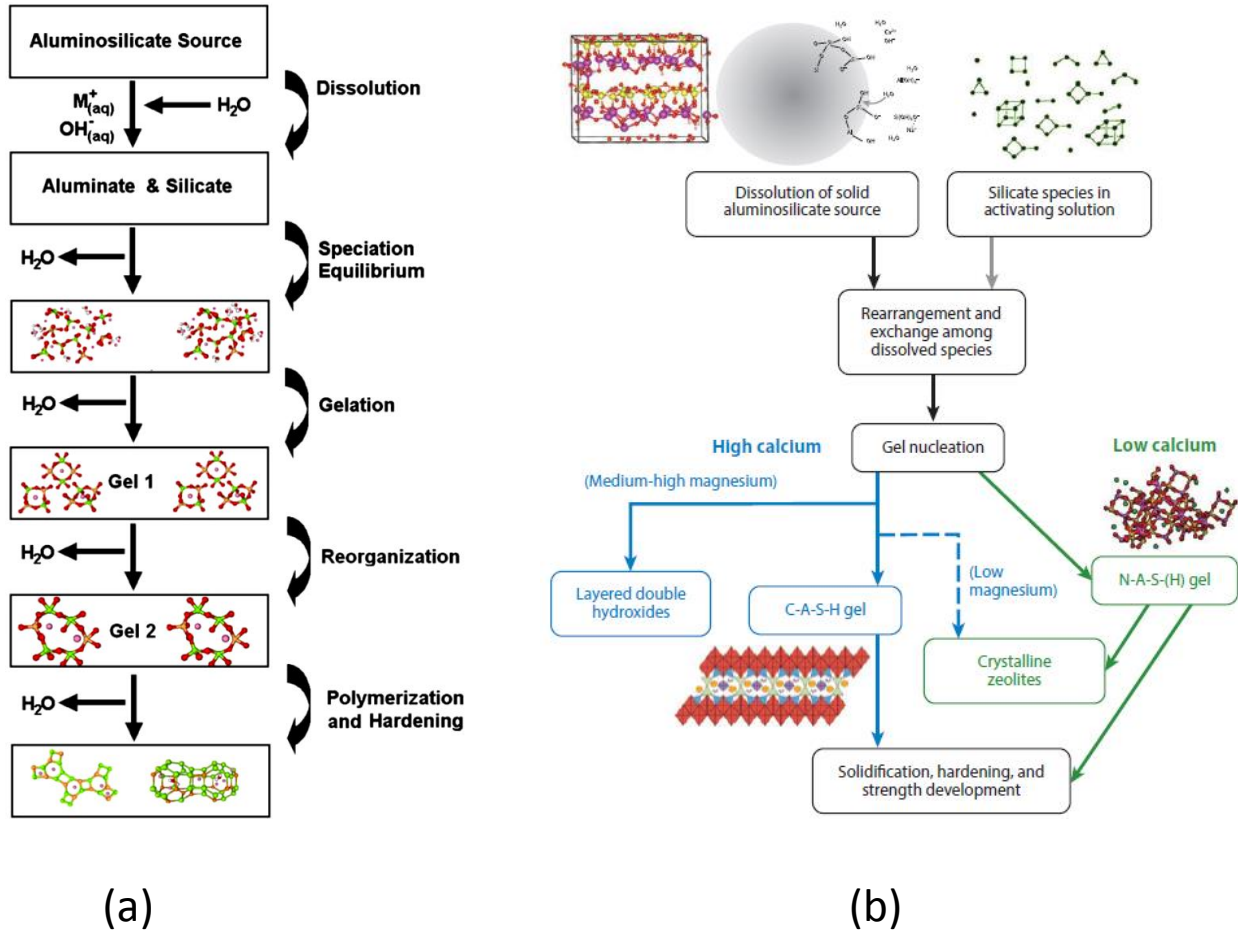


Fig. 2.5: (a) Conceptual model of geopolymerization for low-Ca alkali-activated systems [30]. (b) More detailed model including Ca-rich systems such as alkali-activated slag [36].

The model of the reaction mechanism and processes offered valuable insights in the material design of geopolymers; a great deal of research has been conducted on what factors promote/hinder each process, when each reaction is initiated and terminated, and how the composition and structure of the final product are determined. Obtained knowledge and findings from numerous previous investigations are well documented in review papers [4, 12, 16, 30, 37, 38] and books [13, 39, 40]. From those previous studies, the following essential ideas can be drawn:

- The dissolution process plays a critical role in controlling all subsequent reactions and the resultant workability, setting characteristics, mechanical properties, microstructure, and chemical stability of geopolymers.
- The rate and extent of dissolution (and those of the following precipitation and polymerization steps) depend on many factors, including temperature, pH, alkali-cation type and soluble-silicon concentration of the alkaline activator, and particle size, morphology, crystallinity, and chemical compositions of the solid aluminosilicate precursor.
- Secondary elements in the aluminosilicate precursor (i.e. other than *Si* and *Al* – especially *Ca*) can cause side reactions during geopolymerization that significantly affect material properties of the fresh and hardened geopolymer.
- Hardened geopolymers are typically X-ray amorphous, but the amorphous phase is converted into crystalline zeolite-type structure with time. This conversion could be either beneficial or detrimental for long term durability of geopolymers; increased compressive strength due to the formation of crystalline zeolites has been demonstrated in some studies [21, 41], but decreased tensile strength has been also reported in another study [42].

Building on the accumulated knowledge, recent studies proposed some practical design methods based on “alkaline liquid-to-fly ash ratio” (Fig. 2.6), “water-to-geopolymer solids ratio” [43–45] (both are analogous to the water-to-cement ratio of OPC-based concrete), and/or other parameters including properties of aggregate [46, 47]. More recently, a computer-aided machine learning method has been developed to predict compressive strength of geopolymers based on ample data available from the literature [48–50].

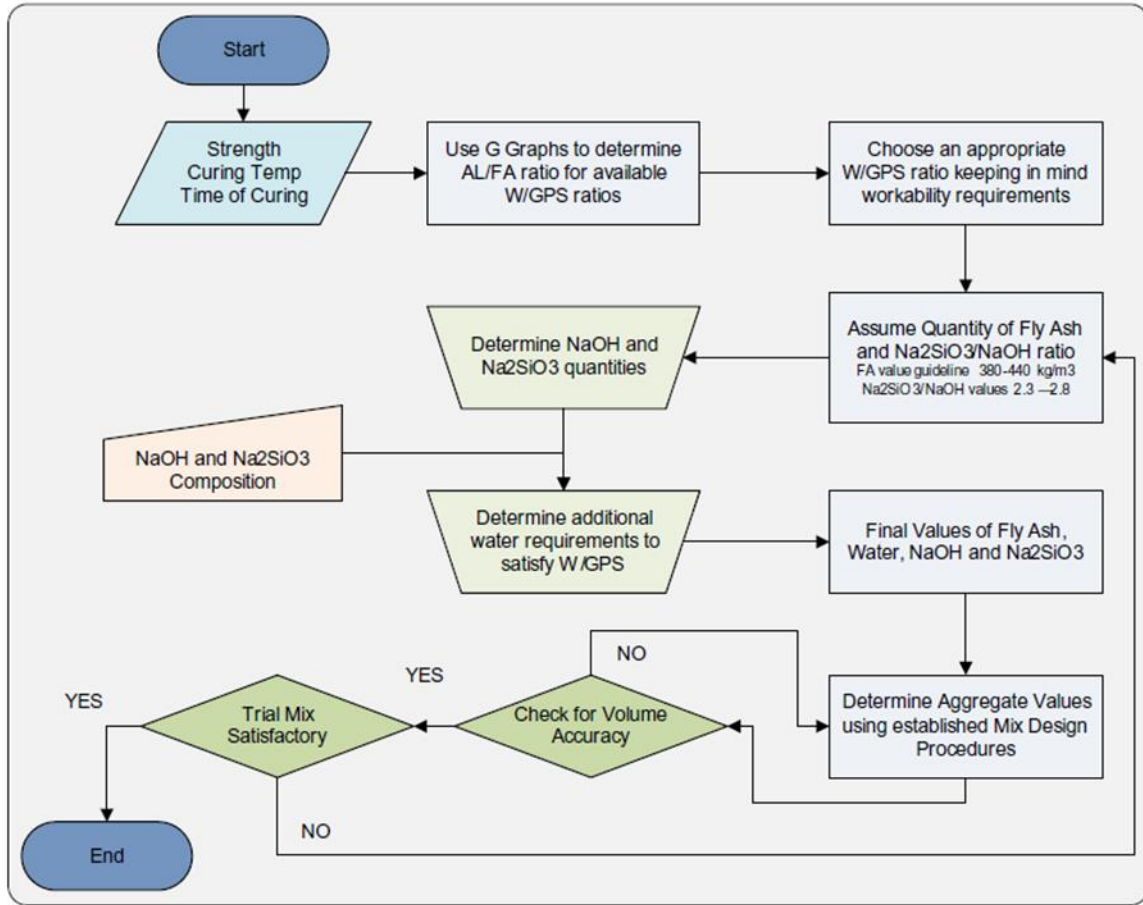


Fig. 2.6: Example of proposed mix-design methods for geopolymers [45].

2.1.3 Unsolved problems

Much work has been done on the reaction mechanism/processes and their influential factors of geopolymerization; yet much still remains unknown. Particularly, fly ash-based geopolymers (FAGP) are the most complex system for which further understanding is needed. Indeed, contradictory results have been sometimes reported among different studies, even when using similar ingredients, mix proportions, and processing methods.

One of the biggest technical challenges of FAGP is large variability in fly ash properties. First of all, since fly ash is still regarded as an industrial waste in many countries, its quality control is not considered, unlike with blast furnace slag and metakaolin. However, the particle size,

morphology, composition, and reactivity of fly ash can vary to a large extent, depending on the size and elemental compositions of feed coal, combustion conditions, and collection methods at power plants. Even when using the same source and processing methods, a plant can produce fly ash with a composition that varies significantly from day to day [51]. Further, crystallinity of fly ash also affects the geopolymerization: relative amounts of crystalline and amorphous phases in fly ash determine the dissolution behavior and resultant properties of the final product. Because of this complexity, advanced characterization techniques are required to fully understand the chemistry of each fly ash and predict properties of the corresponding geopolymer [52].

However, such advanced characterization methods are expensive and require high expertise. As a result, mix design of FAGP often relies on a trial-and-error approach; several factors (type of fly ash, alkaline liquid-to-fly ash ratio, curing temperature, etc.) are arbitrarily selected and their effects on a property of interest (typically compressive strength or workability) are evaluated in a series of experiments varying the levels of the design factors. As discussed above, results and findings obtained from the extensive laboratory studies might be specific to each fly ash source. Moreover, most of the proposed design methods for FAGP have been developed based on those results, and might not be universally applicable. It is therefore possible that another round of experiments needs to be done whenever a different source of fly ash is used.

In general, experiment is important to either develop a new material design or verify the existing one. To overcome the poor repeatability of FAGP, more systematic (but practical) approaches, instead of inefficient trial-and-error methods, to the material design need to be developed.

2.2 Engineered Cementitious Composite

2.2.1 History of development

Like alkali-activated binders, modern development of fiber-reinforced concrete (FRC) also began in the early 1960s: Romualdi, Baston, and Mandel published milestone papers in 1963 [53] and 1964 [54], which demonstrated improved tensile strength of concrete through randomly-oriented steel-wire reinforcement. Their work gained significant attention in both academic and industrial communities, showing the great promise of FRC as a new innovative construction material [55]. Research and development of FRC has expanded since then, introducing a variety of other fibers (glass, carbon, synthetic, natural fibers, and their combinations) and processing methods [56].

Fibers were originally introduced to improve the low tensile strength of concrete [57]. Their potential in enhancing toughness – energy absorbed before rupturing – was later recognized in the research community. The ability to suppress the brittle behavior of concrete and improve the structural resiliency might have been attractive to engineers and asset owners. As a result, since the early work of Aveston *et al.* in the early 1970s [58], considerable research and development work has been directed toward achieving high tensile ductility in concrete. It is such high ductility, accompanied by strain-hardening behavior, that distinguishes High Performance Fiber Reinforced Cementitious Composite (HPFRCC) [59] from other FRC materials.

HPFRCC materials typically exhibit a strain-hardening response where sequential formation of multiple cracks takes place, resulting in significantly higher tensile ductility than normal concrete and other FRC (Fig. 2.7). Such high ductility and strain-hardening characteristics were first achieved by using continuous, aligned fibers and/or high fiber content (typically 10-20% of

the total volume of composite). Those types of materials mostly require cost- and time-consuming casting processes or special processing methods (Hatschek, spray up, lay up, extrusion, and pultrusion), which are not suitable for large-scale and cast-in-place applications [60]. Accordingly, initial HPFRCC materials were limited to laboratory studies or non-structural applications during the early stage of development.

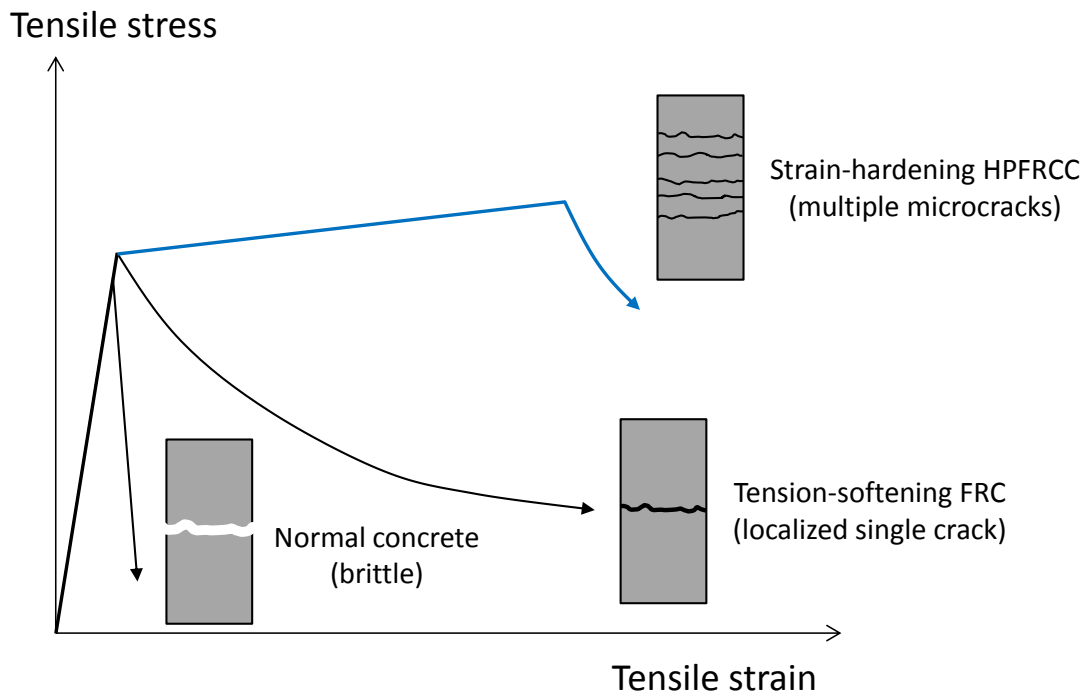


Fig. 2.7: Schematic illustration of brittle concrete, tension-softening FRC, and strain-hardening HPFRCC.

Later, the theoretical basis for discontinuous, randomly-oriented fiber-reinforced composites was established (e.g. [61–66]). As a result, a new class of economically viable, field-castable HPFRCC materials emerged in the 1990s; Li and co-workers proposed a multiscale modeling framework of short-fiber-reinforced composites [67–69], and developed a new strain-hardening ductile cement composite, named *Engineered Cementitious Composite* (ECC) [70]. Unlike most other FRC and HPFRCC materials, ECC meets the following technical requirements simultaneously [60]:

- *High performance* – strain-hardening behavior, high tensile strength and ductility, and self-controlled multiple microcracking, which offer structural resilience and durability.
- *Isotropic properties* – no weak planes under multiaxial loading conditions, which ensure robust performance.
- *Flexible processing* – can be used in conventional concrete mixing/placing equipment, without any special processing need.
- *Short fiber of lower volume fraction* – directly related to the cost and weight of the material, as well as the easy processing. ECC typically has 2% or less fiber content by volume.

The unique features of this material gained great interest in the research community, and ECC has been intensively studied from the 1990s onwards. The extensive investigations demonstrated various types of enhanced material durability and structural resilience of ECC (Table 2.1). During the course of investigations, it has been discovered that the self-controlled microcracks play an important role in the enhanced durability and resilience. In ECC materials, crack width is typically controlled to be less than 100 μm , which is tight enough to prevent accelerated penetration of aggressive agents through the cracks. In addition, even under a high imposed strain, damage of the composite is not localized but distributed as multiple microcracks, which maintains structural integrity. Consequently, degradation in mechanical properties of the composite is limited even after cracking. Through the improved resilience and durability confirmed in laboratory studies, ECC showed a great promise for large-scale structural applications.

Driven by the demonstrated excellent properties, ECC has already found a number of full-scale field applications worldwide [56] (Fig. 2.8). More importantly, enhanced durability of those buildings and infrastructure have been confirmed.

Table 2.1: Summary of previous studies on material durability and structural resilience of ECC.

Material durability	Structural resilience	
	Type of element	Type of loading
Water tightness [71, 72]	Flexural member	Monotonic [73, 74]
Chloride diffusivity [75]		Reversed cyclic [76–78]
Free-thaw-cycles [79, 80]	Shear beam	Monotonic [81–83]
Alkali-silicate reaction [84]		Reversed cyclic [85]
Temperature/fire resistance [86]	Wall element	cyclic shear [81, 87, 88]
Corrosion resistance [89, 90]	Beam-column connection	Reversed cyclic [91, 92]
Creep deformation [93–95]		
Drying shrinkage [96, 97]	Frame	Reversed cyclic [98]

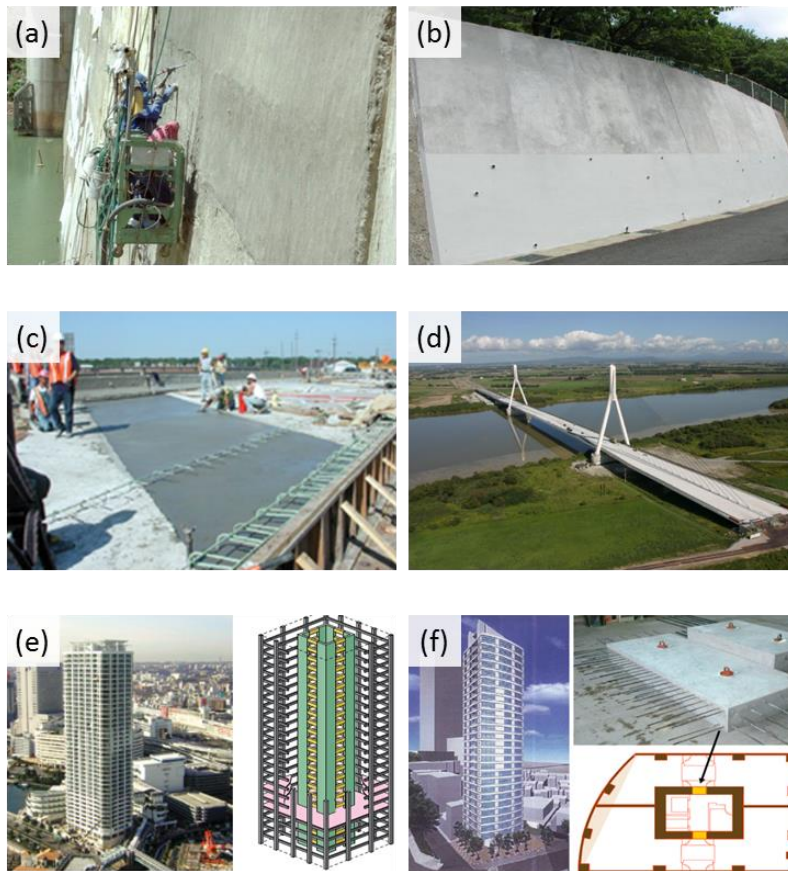


Fig. 2.8: Examples of various ECC applications: (a) structural repair of concrete dam [99], (b) surface repair of retaining wall [99], (c) bridge-deck link slab [100], (d) bridge-deck overlay [99], (e)(f) structural dampers for high-rise buildings [99, 100].

2.2.2 Previous studies for ECC design

Since the invention of the first version of ECC in the 1990s, various types of ECC materials have been developed to date. Added functionalities – besides the tensile strain-hardening behavior with high ductility and multiple microcracking – of those ECC materials include self-compacting [101], lightweight [102], sprayability [103], high early strength [104], and self-healing [105]. More recently, much effort has been placed in development of greener versions of ECC [106–111]. Surprisingly, a wide variety of those ECC materials were developed within a decade or so. Such rapid development was realized by a systematic micromechanics-based design method, which is briefly reviewed here. More detailed discussion of the micromechanical modeling is presented in Chapter 3.

It should be first mentioned that the high tensile ductility accompanied by distinct strain-hardening of ECC is a result of sequential initiation and steady-state propagation of multiple microcracks. When a crack initiates from a pre-existing flaw in ECC, the crack propagates in a steady-state manner, maintaining a constant crack opening. In contrast, crack opening in normal FRC increases with crack length as the crack propagates. As a consequence of the continuously increasing crack opening at the site, fibers away from the crack tip are mostly pulled-out or broken. The tension-softening behavior – i.e. decreasing load-carrying capacity – of FRC results from the loss of bridging fibers in this “Griffith-type” cracking [112]. It is therefore important to control the crack propagation type for achieving steady-state multiple cracking.

Marshall and Cox derived an energy-based criterion for steady-state crack propagation in fiber-reinforced brittle matrix composites [113]. Building on their derivation, Li and Leung presented two necessary conditions for achieving steady-state multiple cracking in randomly-distributed short fiber-reinforced composites [69], which can be expressed as follows:

$$\sigma_{ci}^i \leq \min_j \sigma_0^j \quad (2.1)$$

$$J_{tip}^i \leq \sigma_0^i \delta_0^i - \int_0^{\delta_0^i} \sigma^i(\delta^i) d\delta^i \equiv J_b^{i'} \quad (2.2)$$

Consider that a crack initiates from i -th plane of a composite, as shown in Fig. 2.9 (theoretically, an infinite number of planes can be defined). Because of material and processing-induced variability in the composite, different planes have different flaw-size distributions and numbers of bridging fibers with various orientation angles. Consequently, the crack-initiation stress (σ_{ci}), fiber-bridging capacity (σ_0), crack-tip toughness (J_{tip}), and fiber-bridging stress (σ) versus crack opening (δ) relation (σ - δ relation) are different among planes.

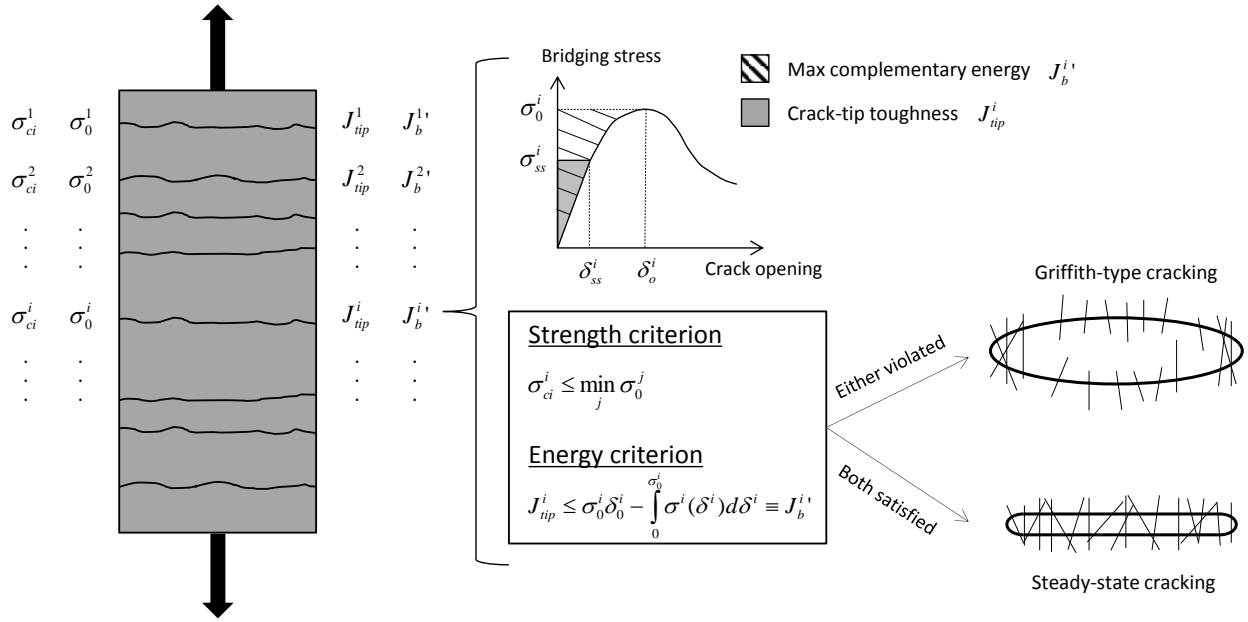


Fig. 2.9: Two required conditions for steady-state multiple cracking. Violation of either criterion results in oval-shaped Griffith-type crack propagation where fibers away from the crack tip are mostly pulled-out or broken. When both conditions are satisfied, the steady-state crack propagation takes place maintaining the constant crack opening and load-carrying capacity.

The first condition in Eq. 2.1 requires that stress to initiate the i -th crack be lower than the minimum fiber-bridging capacity (i.e. ultimate tensile strength) of the composite. In general, the lowest σ_0 is found in a plane where a crack has been already formed. The violation of this criterion triggers composite failure from the j -th plane, forming no more cracks.

If the i -th crack can be initiated, its propagation mode is determined by the second criterion in Eq. 2.2. As the crack opening increases from zero to that in a steady-state (δ_{ss}^i), applied energy from external load is partly consumed as strain energy in the bridging fibers. The rest of energy – complementary energy – is available for propagating the crack tip. The second condition requires that the crack-tip toughness of the i -th plane be lower than the maximum available complementary energy (J'_b). The violation of this criterion results in the Griffith-type crack propagation.

From the discussion above, it seems clear that understanding of the four variables in Eqs 2.1 and 2.2 (i.e. σ_{ci} , σ_0 , J_{tip} , and J'_b) are essential for achieving steady-state multiple cracking. Two of the four variables are easy to determine; σ_{ci} depends predominantly on the maximum flaw size (c) and matrix fracture toughness (K_m) of the plane; J_{tip} can be approximated as K_m^2/E_m at small fiber content where E_m is the Young's modulus of the matrix. These two variables and associated parameters can be easily measured by experiment and predicted from fracture-mechanics theories. The other two variables – σ_0 and J'_b – are more complex; they are determined from the σ - δ relation which depends on more than ten parameters of matrix, fiber, and interface properties and their interaction. Therefore, a comprehensive model to predict the σ - δ relation from given parameters is needed.

Li *et al.* derived a micromechanics-based constitutive model that relates the “micromechanical parameters” and macroscopic composite behavior [67]. The fundamental idea behind the micromechanical model is that the composite mechanical behavior is governed by pull-out behaviors of individual bridging fibers, while the pull-out behavior of a single fiber is determined from properties and phenomena at mm-to- μm scales [66]. Mathematically, the constitutive law of the σ - δ relation is expressed as follows:

$$\sigma(\delta) = \frac{V_f}{A_f} \int_{\phi_0}^{\phi_1} \int_{z=0}^{(L_f/2)\cos\phi} P(\delta, L_e) g(\phi) p_1(\phi) p_2(z) dz d\phi \quad (2.3)$$

V_f is the fiber volume fraction; A_f is the cross-sectional area of fiber; ϕ is the inclination angle of fiber with respect to the normal of the crack plane; L_f is the fiber length; z is the distance between the fiber centroid and the crack plane; L_e is the fiber embedment length. Figure 2.10 illustrates those parameters.

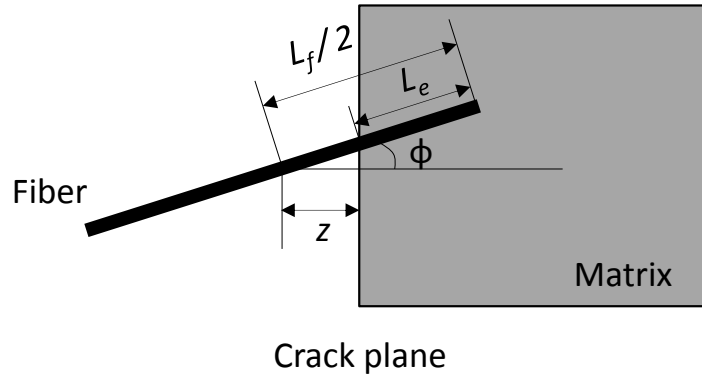


Fig. 2.10: Schematic illustration of a bridging fiber.

$P(\delta, L_e)$ represents the load carried by a single fiber aligned normal to the crack plane (i.e. $\phi=0$). The P - δ relation depends predominantly on the initial fiber embedment length (L_e), fiber properties (length, diameter, Young’s modulus), and chemical and frictional bonding properties

of fiber/matrix interface. Besides, when a fiber is inclined from the normal to the crack plane, additional frictional force occurs at the exit point of the fiber from the matrix [114]. This effect is taken into account by $g(\varphi)$, which is analogous to the belt friction equation. $P(\delta, L_e)$ together with $g(\varphi)$ represents the pull-out behavior of a single fiber with arbitrary embedment length L_e and inclination angle φ .

$p_1(\varphi)$ and $p_2(z)$ are probability density functions (PDFs) of the fiber inclination angle and location of fiber centroid, which account for the random distribution of fibers in the composite. The double integral in Eq 2.3 calculates the total load carried by all bridging fibers in the crack plane with various orientation angles and centroid locations. The bounds of φ integration might be limited between φ_0 and φ_1 depending on the casting condition. The upper bound of z integration is $(L_f/2)\cos(\varphi)$, since fibers with a larger centroid distance than that value have no embedded part in the matrix and therefore are not counted as bridging fibers.

V_f/A_f is equivalent to the number of fibers per unit area of the crack plane with $\varphi=0$. Eq. 2.3 then gives the fiber-bridging stress at a crack plane for given parameters of matrix, fiber, and interface properties. The complete mathematical expressions for $P(\delta, L_e)$, $g(\varphi)$, $p_1(\varphi)$, and $p_2(z)$, are presented in Chapter 3.

In essence, the micromechanics-based constitutive law enables systematic tailoring of design parameters for achieving desired composite tensile properties; the simulated σ - δ relation guides modification of parameters to satisfy the strength/energy criterion for steady-state multiple cracking, or to achieve higher tensile strength or smaller crack width of the composite. The micromechanical modeling has been modified and extended [115–118], providing further efficiency in materials design of ECC.

2.2.3 Unsolved problems

In development of ECC materials, the design process typically starts with the matrix design: matrix ingredients, their mix proportions, and curing method are first determined to achieve a desired function (e.g. high strength, lightweight, self-compactability, etc.). Then, an appropriate type of fiber and its volume fraction are selected, followed by experimental characterization of fiber/matrix interface properties. Finally, the σ - δ relation for the given matrix and fiber is simulated, which provides guidelines for required modification on matrix, fiber, and/or interface properties. Therefore, once the matrix with a desired property is developed, subsequent characterization, simulation, and modification can be systematically done.

Meanwhile, matrix design for various types of ECC has been drawing on accumulated scientific and empirical knowledge on cement materials; effects of design parameters (water-to-cement ratio, types of cement and aggregate, curing regime, etc.) on a variety of output properties (compressive strength, matrix toughness, workability, etc.) have been extensively studied for OPC-based materials for over a century. Ample data and literature are thus available for guiding the matrix design to achieve a desired property. Conversely, when the matrix is a relatively new material with short history of development (i.e. geopolymers), the matrix development tends to rely on exhaustive trial-and-error approaches.

Another problem is related to the requirement of multi-response optimization in ECC design. If the matrix with a desired property could be successfully developed, it is ideal to manipulate only fiber or interface properties in the subsequent composite design phase. In some cases, however, the simulated σ - δ relation indicates unrealistic modification of design parameters: very high fiber strength, too small fiber diameter, and large fiber content that needs special processing are good examples. Matrix modification would be also required in those cases, but such modification

could also affect the added function achieved in the preceding matrix design stage. Therefore, relevant parameters need to be optimized to simultaneously achieve the high tensile ductility and added function, which adds further difficulty in the ECC design.

2.3 Challenges for development of Engineered Geopolymer Composite

The preceding discussion on geopolymer and ECC design has implications on the difficulty in combining the two material technologies.

First and foremost, a geopolymer matrix that meets required mechanical performances, material durability, and rheology for good fiber dispersion needs to be developed. In this matrix development stage, there are more design variables in geopolymer than OPC-based matrix, including types of the solid aluminosilicate source and alkaline activator, concentration of the alkaline solution, curing temperature and duration, as well as mix proportions of ingredients. Effects of those design factors on matrix properties need to be determined. However, because of the relatively short history of geopolymers, accumulated knowledge on the matrix design is limited compared to OPC-based matrix. Advanced characterization techniques are helpful in understanding those factor effects, but the findings might be specific to each aluminosilicate source because of the material variability, especially in fly ash. It is time and cost intensive to explore the vast design space by trial-and-error approaches.

Development of EGC also requires design of fiber and fiber/matrix interface properties, which adds further degrees of freedom in the material design. As in ECC design, the micromechanical modeling is a promising tool to guide the composite design of EGC for achieving steady-state multiple cracking with high tensile ductility. However, due to technical and economical

limitations on possible modification of fiber and interface properties, matrix modification might be also required. As discussed above, such modification might diminish the matrix properties achieved in the matrix design stage. In addition, another limitation might be put on the selection of fiber and matrix constituents because of requirement of high material greenness. Therefore, optimization of multiple responses in EGC design is more complicated than geopolymer and ECC design.

The difficulty in the material design of EGC slows the overall progress in research, development, and applications of the technology. To overcome the challenges for rapid development of EGC, we need to develop a novel design methodology that systematically solves the multi-response optimization problem. This is explored in the next chapter.

References

- [1] O. B. H. Rowles M.R., Hanna J.V., Pike K.J., Smith W.E., “²⁹Si, ²⁷Al, ¹H and ²³Na MAS NMR Study of the Bonding Character in Aluminosilicate Inorganic Polymers,” *Appl.Magn.Reson*, vol. 32, no. 4, pp. 663–689, 2007.
- [2] H. Kühl, “Slag cement and process of making the same,” US Patent 900,939, 1908.
- [3] A. O. Purdon, “The action of alkalis on blast furnace slag,” *J. Soc. Chem. Ind.*, vol. 59, pp. 191–202, 1940.
- [4] D. M. Roy, “Alkali-activated cements: Opportunities and challenges,” *Cem. Concr. Res.*, vol. 29, no. 2, pp. 249–254, 1999.
- [5] J. L. Provis, P. Duxson, E. Kavalerova, P. V. Krivenko, Z. Pan, F. Puertas, and J. S. J. Van Deventer, “Historical aspects and overview,” in *Alkali Activated Materials - RILEM State-of-the-Art Reports*, vol. 13, 2014, pp. 11–57.
- [6] V. D. Glukhovskiy, “Ancient, modern and future concretes,” in *First International Conference on Alkaline Cements and Concretes*, 1994, pp. 1–8.
- [7] V. D. Glukhovskiy, *Soil silicates*. Kiev, Ukraine: Gosstroyizdat Ukrainy Publishing, 1959.
- [8] P. Duxson and J. S. J. Van Deventer, “17 – Commercialization of geopolymers for construction – opportunities and obstacles,” in *Geopolymers: Structure, processing, properties and industrial applications*, J. L. Provis and J. S. J. van Deventer, Eds. Cambridge (UK): Woodhead Publishing, 2009, pp. 379–400.
- [9] P. L. Pratt, S.-D. Wang, X.-C. Pu, and K. L. Scrivener, “Alkali-activated slag cement and concrete: a review of properties and problems,” *Adv. Cem. Res.*, vol. 7, no. 27, pp. 93–102, 1995.
- [10] X. Hua, J. L. Provis, J. S. J. Van Deventer, and P. V. Krivenko, “Characterization of Aged Slag Concretes,” *ACI Mater. J.*, vol. 105, no. 2, pp. 131–139, 2008.
- [11] J. Deja, “Carbonation aspects of alkali activated slag mortars and concretes,” *Silic. Ind.*, no. 3–4, pp. 37–42, 2002.
- [12] A. Palomo, P. Krivenko, I. Garcia-Lodeiro, E. Kavalerova, O. Maltseva, and A. Fernández-Jiménez, “A review on alkaline activation: new analytical perspectives,” *Mater. Construcción*, vol. 64, no. 315, p. e022, 2014.
- [13] J. Davidovits, *Geopolymer Chemistry and Applications*, Third ed. Saint-Quentin (France): Institut Geopolcle analysis of geopolymers,” in *Geopolymers - Structure, processing, properties and industrial applications*, J. L. Provis and J. S. J. van Deventer, Eds. Cambridge (UK): Woodhead Publishing, 2009, pp. 194–210.

- [18] B. C. McLellan, R. P. Williams, J. Lay, A. Van Riessen, and G. D. Corder, “Costs and carbon emissions for geopolymer pastes in comparison to ordinary portland cement,” *J. Clean. Prod.*, vol. 19, no. 9–10, pp. 1080–1090, 2011.
- [19] C. Ouellet-Plamondon and G. Habert, “Life cycle assessment (LCA) of alkali-activated cements and concretes,” in *Handbook of Alkali-Activated Cements, Mortars and Concretes*, F. Pacheco-Torgal, J. Labrincha, C. Leonelli, A. Palomo, and P. Chindaprasit, Eds. Woodhead Publishing Limited, 2015, pp. 663–686.
- [20] American Coal Ash Association, “American Coal Combustion Products Production & Use Statistics.” [Online]. Available: <https://www.acaa-usa.org/Publications/Production-Use-Reports>. [Accessed: 05-May-2017].
- [21] A. Fernández-Jiménez and A. Palomo, “Nanostructure/microstructure of fly ash geopolymers,” in *Geopolymers - Structure, processing, properties and industrial applications*, J. L. Provis and J. S. J. van Deventer, Eds. Cambridge (UK): Woodhead Publishing, 2009, pp. 89–117.
- [22] J. Davidovits, “Geopolymers - Inorganic polymeric new matymere, 2008.
- [14] P. G. Malone, C. J. Randall, and T. Kirkpatrick, *Potential Applications of Alkali-Activated alumino-silicate binders in military applications*, no. Report WES/MP/GL-85-15, U.S. Army Corps of Engineers. Vicksburg, MS, 1985.
- [15] J. Wastiels, X. Wu, S. Faignet, and G. Patfoort, “Mineral polymer based on fly ash,” *J. Resour. Manag. Technol.*, vol. 22, no. 3, pp. 135–141, 1994.
- [16] P. Duxson, J. L. Provis, G. C. Lukey, and J. S. J. van Deventer, “The role of inorganic polymer technology in the development of ‘green concrete,’” *Cem. Concr. Res.*, vol. 37, no. 12, pp. 1590–1597, Dec. 2007.
- [17] M. Weil, K. Dombrowski, and A. Buchwald, “Life-cyerials,” *J. Therm. Anal.*, vol. 37, no. 8, pp. 1633–1656, 1991.
- [23] H. Rahier, B. Van Mele, M. Biesemans, J. Wastiels, and X. Wu, “Low-temperature synthesized aluminosilicate glasses Part I low-temperature reaction stoichiometry and structure of a model compound,” *J. Mater. Sci.*, vol. 31, no. 1, pp. 71–79, 1996.
- [24] H. Rahier, B. Van Mele, and J. Wastiels, “Low-temperature synthesized aluminosilicate glasses Part II rheological transformations during low-temperature cure and high-temperature properties of a model compound,” *J. Mater. Sci.*, vol. 31, no. 1, pp. 80–85, 1996.
- [25] H. Rahier, W. Simons, B. Van Mele, and M. Biesemans, “Low-temperature synthesized aluminosilicate glasses Part III influence of the composition of the silicate solution on production, structure and properties,” *J. Mater. Sci.*, vol. 32, no. 9, pp. 2237–2247, 1997.
- [26] H. Xu and J. S. J. Van Deventer, “The geopolymerisation of alumino-silicate minerals,” *Int. J. Miner. Process.*, vol. 59, no. 3, pp. 247–266, 2000.

- [27] A. Palomo, S. Alonso, and A. Fernandez-Jiménez, “Alkaline Activation of Fly Ashes : NMR Study of the Reaction Products,” *J. Am. Ceram. Soc.*, vol. 87, no. 6, pp. 1141–1145, 2004.
- [28] A. Fernández-Jiménez, A. Palomo, and M. Criado, “Microstructure development of alkali-activated fly ash cement: A descriptive model,” *Cem. Concr. Res.*, vol. 35, no. 6, pp. 1204–1209, 2005.
- [29] J. L. Provis and J. S. J. van Deventer, “Geopolymerisation kinetics. 2. Reaction kinetic modelling,” *Chem. Eng. Sci.*, vol. 62, no. 9, pp. 2318–2329, 2007.
- [30] P. Duxson, A. Fernández-Jiménez, J. L. Provis, G. C. Lukey, A. Palomo, and J. S. J. Van Deventer, “Geopolymer technology: The current state of the art,” *J. Mater. Sci.*, vol. 42, no. 9, pp. 2917–2933, Dec. 2007.
- [31] A. Hajimohammadi, J. L. Provis, and J. S. J. Van Deventer, “Effect of alumina release rate on the mechanism of geopolymer gel formation,” *Chem. Mater.*, vol. 22, no. 18, pp. 5199–5208, 2010.
- [32] A. Hajimohammadi, J. L. Provis, and J. S. J. Van Deventer, “The effect of silica availability on the mechanism of geopolymerisation,” *Cem. Concr. Res.*, vol. 41, no. 3, pp. 210–216, 2011.
- [33] C. White and J. Provis, “Molecular mechanisms responsible for the structural changes occurring during geopolymerization: Multiscale simulation,” *AIChE J.*, vol. 58, no. 7, pp. 2241–2253, 2012.
- [34] C. E. White, J. L. Provis, B. Bloomer, N. J. Henson, and K. Page, “In situ X-ray pair distribution function analysis of geopolymer gel nanostructure formation kinetics.,” *Phys. Chem. Chem. Phys.*, vol. 15, no. 22, pp. 8573–82, 2013.
- [35] J. L. Provis and S. A. Bernal, “Milestones in the analysis of alkali-activated binders,” *J. Sustain. Cem. Mater.*, vol. 4, no. 2, pp. 74–84, 2015.
- [36] J. L. Provis and S. A. Bernal, “Geopolymers and Related Alkali-Activated Materials,” *Annu. Rev. Mater. Res.*, vol. 44, pp. 299–327, 2014.
- [37] K. Komnitsas and D. Zaharaki, “Geopolymerisation: A review and prospects for the minerals industry,” *Miner. Eng.*, vol. 20, no. 14, pp. 1261–1277, Nov. 2007.
- [38] J. L. Provis, “Geopolymers and other alkali activated materials: why, how, and what?,” *Mater. Struct.*, vol. 47, no. 1–2, pp. 11–25, 2014.
- [39] J. L. Provis and J. S. J. van Deventer, *Geopolymers-Structure, processing, properties and industrial applications*. Cambridge (UK): Woodhead Publishing, 2009.
- [40] C. Shi, P. V Krivenko, and D. Roy, *Alkali-Activated Cements and Concretes*. Abingdon, UK: Taylor & Francis, 2006.

- [41] M. Criado, M. Criado, A. Fernandez-Jimenez, A. Fernandez-Jimenez, a G. de la Torre, a G. de la Torre, M. a G. Aranda, M. a G. Aranda, A. Palomo, and A. Palomo, “An XRD study of the effect of the SiO₂/Na₂O ratio on the alkali activation of fly ash,” *Cem. Concr. Res.*, vol. 37, pp. 671–679, 2007.
- [42] A. Mishra, D. Choudhary, N. Jain, M. Kumar, N. Sharda, and D. Dutt, “Effect of concentration of alkaline liquid and curing time on strength and water absorption of geopolymer concrete,” *ARPJ. Eng. Appl. Sci.*, vol. 3, no. 1, pp. 14–18, 2008.
- [43] D. Hardjito and B. V. Rangan, *Development and properties of low-calcium fly ash-based geopolymer concrete*. Perth (Australia): Research report GC 1, Curtin University, 2005.
- [44] N. A. Lloyd and B. V. Rangan, “Geopolymer Concrete with Fly Ash,” in *Second International Conference on Sustainable Construction Materials and Technologies*, 2010.
- [45] M. T. Junaid, O. Kayali, A. Khennane, and J. Black, “A mix design procedure for low calcium alkali activated fly ash-based concretes,” *Constr. Build. Mater.*, vol. 79, pp. 301–310, 2015.
- [46] S. V. Patankar, Y. M. Ghugal, and S. S. Jamkar, “Mix Design of Fly Ash Based Geopolymer Concrete,” in *Advances in Structural Engineering*, 2015, pp. 1619–1634.
- [47] T. S. Ng and S. J. Foster, “Development of a mix design methodology for high-performance geopolymer mortars,” *Struct. Concr.*, vol. 14, no. 2, pp. 148–156, 2013.
- [48] İ. B. Topçu and M. Saridemir, “Prediction of compressive strength of concrete containing fly ash using artificial neural networks and fuzzy logic,” *Computational Materials Science*, vol. 41, no. 3, pp. 305–311, 2008.
- [49] D. Bondar, “The Use of Artificial Neural Network To Predict Compressive Strength of Geopolymers,” in *3rd International Conference on Sustainable Construction Materials and Technologies*, 2011.
- [50] A. Nazari and F. Pacheco Torgal, “Predicting compressive strength of different geopolymers by artificial neural networks,” *Ceram. Int.*, vol. 39, no. 3, pp. 2247–2257, 2013.
- [51] L. M. Keyte, “2 – Fly ash glass chemistry and inorganic polymer cements,” in *Geopolymers - Structure, processing, properties and industrial applications*, Cambridge (UK): Woodhead Publishing, 2009, pp. 15–36.
- [52] J. S. J. van Deventer, J. L. Provis, P. Duxson, G. C. Lukey, and J. S. J. Van Deventer, “Reaction mechanisms in the geopolymeric conversion of inorganic waste to useful products.,” *J. Hazard. Mater.*, vol. 139, no. 3, pp. 506–13, Jan. 2007.
- [53] J. P. Romualdi and G. B. Batson, “Mechanics of Crack Arrest in Concrete,” *J. Eng. Mech. Div.*, vol. 89, no. 3, pp. 147–168, 1963.

- [54] J. J. P. Romualdi and J. A. Mandel, "Tensile Strength of concrete Affected by Uniformly Distributed and Closely Spaced Short Lengths of wire Reinforcement," *ACI J. Proc.*, vol. 61, no. 6, pp. 657–672, 1964.
- [55] R. F. Zollo, "Fiber-reinforced concrete: an overview after 30 years of development," *Cem. Concr. Compos.*, vol. 19, no. 2, pp. 107–122, 1997.
- [56] V. C. Li, "Engineered Cementitious Composites (ECC) – Material , Structural , and Durability Performance," in *Concrete Construction Engineering Handbook*, E. G. Nawy, Ed. CRC Press, 2008, pp. 1–40.
- [57] V. Li, "Large volume, high - performance applications of fibers in civil engineering," *J. Appl. Polym. Sci.*, no. November 2000, pp. 660–686, 2002.
- [58] J. . Aveston, G. A. . Cooper, and A. Kelly, "Single and multiple fracture," in *Properties of Fiber Composites*, 1971, pp. 15–24.
- [59] A. E. Naaman, "High Performance Fiber Reinforced Cement Composites: Classification and Applications," *CBM-CI Int. Work. Karachi, Pakistan*, vol. 1, no. 1, pp. 389–401, 2009.
- [60] V. C. Li, "Engineered Cementitious Composites (ECC) – Tailored Composites through Micromechanical Modeling," in *Fiber reinforced concrete: present and future*, N. Banthia, A. Bentur, and A. A. Mufti, Eds. Montreal (Canada): Canadian Society for Civil Engineering, 1998, pp. 64–97.
- [61] J. Aveston and A. Kelly, "Theory of multiple fracture of fibrous composites," *J. Mater. Sci.*, vol. 8, no. 3, pp. 352–362, 1973.
- [62] A. E. Naaman, A. S. Argon, and F. Moavenzadeh, "A fracture model for fiber reinforced cementitious materials," *Cem. Concr. Res.*, vol. 3, no. 4, pp. 397–411, 1973.
- [63] A. E. Naaman and S. P. Shah, "Pull-out Mechanism in Steel Fiber-reinforced Concrete," *J. Struct. Div.*, vol. 102, no. 8, pp. 1537–1548, 1976.
- [64] V. S. Gopalaratnam and S. P. Shah, "Tensile Failure of Steel Fiber-Reinforced Mortar," *J. Eng. Mech.*, vol. 113, no. 5, pp. 635–652, 1987.
- [65] Y. Wang, V. C. Li, and S. Backer, "Modelling of fibre pull-out from a cement matrix," *Int. J. Cem. Compos. Light. Concr.*, vol. 10, no. 3, pp. 143–149, 1988.
- [66] Y. Wang, S. Backer, and V. Li, "A statistical tensile model of fibre reinforced cementitious composites," *Composites*, vol. 20, no. 3, pp. 265–274, 1989.
- [67] V. C. Li, Y. Wang, and S. Backer, "A micromechanical model of tension-softening and bridging toughening of short random fiber reinforced brittle matrix composites," *J. Mech. Phys. Solids*, vol. 39, no. 5, pp. 607–625, 1991.
- [68] H. Wu and V. Li, "Conditions for pseudo strain-hardening in fiber reinforced brittle matrix composites," *J. Appl. Mech. Rev.*, no. 195819, pp. 3487–3489, 1992.

- [69] V. C. Li and C. K. Y. Leung, "Steady-State and Multiple Cracking of Short Random Fiber Composites," *J. Eng. Mech.*, vol. 118, no. 11, pp. 2246–2264, 1992.
- [70] V. C. Li, "From Micromechanics to Structural Engineering - The Design of Cementitious Composites for Civil Engineering Applications," *Struct. Eng. /Earthquake Eng.*, vol. 10, no. 2, pp. 37–48, 1993.
- [71] M. Şahmaran and V. C. Li, "Influence of microcracking on water absorption and sorptivity of ECC," *Mater. Struct.*, vol. 42, no. 5, pp. 593–603, Jul. 2008.
- [72] M. D. Lepech and V. C. Li, "Water permeability of engineered cementitious composites," *Cem. Concr. Compos.*, vol. 31, no. 10, pp. 744–753, Nov. 2009.
- [73] M. Maalej and V. Li, "Introduction of strain-hardening engineered cementitious composites in design of reinforced concrete flexural members for improved durability," *ACI Struct. J.*, 1995.
- [74] V. Li and S. Wang, "Flexural behaviors of glass fiber-reinforced polymer (GFRP) reinforced engineered cementitious composite beams," *ACI Mater. J.*, 2002.
- [75] M. Sahmaran, M. Li, and V. C. Li, "Transport properties of engineered cementitious composites under chloride exposure," *ACI Mater. J.*, vol. 104, no. 6, pp. 604–611, 2007.
- [76] G. Fischer, H. Fukuyama, and V. Li, "Effect of matrix ductility on the performance of reinforced ECC column members under reversed cyclic loading conditions," *Proc. JCI Int. Work. DFRCC*, pp. 269–278, 2002.
- [77] G. Fischer and V. C. Li, "Deformation behavior of fiber-reinforced polymer reinforced engineered cementitious composite (ECC) flexural members under reversed cyclic loading conditions," *ACI Struct. J.*, vol. 100, no. 1, pp. 25–35, 2003.
- [78] G. Fischer and V. Li, "Effect of Matrix Ductility on Deformation Behavior of Steel-Reinforced ECC Flexural Members under Reversed Cyclic Loading Conditions," *ACI Struct. J.*, vol. 99, no. 6, pp. 781–790, 2002.
- [79] M. Şahmaran, E. Özbay, H. E. Yücel, M. Lachemi, and V. C. Li, "Frost resistance and microstructure of Engineered Cementitious Composites: Influence of fly ash and micro poly-vinyl-alcohol fiber," *Cem. Concr. Compos.*, vol. 34, no. 2, pp. 156–165, Feb. 2012.
- [80] M. Şahmaran and V. C. Li, "De-icing salt scaling resistance of mechanically loaded engineered cementitious composites," *Cem. Concr. Res.*, vol. 37, no. 7, pp. 1035–1046, Jul. 2007.
- [81] T. Kanda, S. Watanabe, and V. C. Li, "Application of Pseudo Strain Hardening Cementitious Composites to Shear Resistant Structural Elements," in *FRAMCOS-3*, 1998, pp. 1477–1490.
- [82] K. Shimizu, T. Kanakubo, T. Kanda, and S. Nagai, "Shear behavior of PVA-ECC Beams," in *Int'l RILEM Workshop HPRCC in Structural Applications*, 2006, pp. 443–451.

- [83] P. Kabele and M. Kanakubo, “Experimental and Numerical investigation of shear behavior of PVA-ECC in structural elements,” in *Proceedings of the Fifth International Workshop on HPFRCC (HPFRCC5)*, 2007, pp. 137–145.
- [84] M. Sahmaran, V. C. V. Li, and M. Şahmaran, “Durability of mechanically loaded engineered cementitious composites under highly alkaline environments,” *Cem. Concr. Compos.*, vol. 30, no. 2, pp. 72–81, Feb. 2008.
- [85] H. Fukuyama, Y. Matsuzaki, K. Nakano, and Y. Sato, “Structural Performance of Beam Elements with PVA-ECC,” in *High Performance Fiber Reinforced Cement Composites 3 (HPFRCC 3)*, 1999, pp. 531–542.
- [86] M. Sahmaran, M. Lachemi, and V. C. Li, “Assessing Mechanical Properties and Microstructure of Fire-Damaged Engineered Cementitious Composites,” *Aci Mater. J.*, vol. 107, no. 3, pp. 297–304, 2010.
- [87] K. Kesner and S. L. Billington, “Investigation of Infill Panels Made from Engineered Cementitious Composites for Seismic Strengthening and Retrofit,” *J. Struct. Eng.*, vol. 131, no. 11, pp. 1712–1720, 2005.
- [88] H. Fukuyama, H. Suwada, and T. Mukai, “Test on High-Performance Wall Elements With Hpfrc,” in *Int’l RILEM Workshop HPFRCC in Structural Applications*, 2006, pp. 365–374.
- [89] S. Miyazato and Y. Hiraishi, “Transport properties and steel corrosion in Ductile Fiber Reinforced Cement Composites,” *11th Int. Conf. Fract. 2005, ICF11*, vol. 2, pp. 1500–1505, 2005.
- [90] M. Sahmaran, V. C. V. Li, and C. Andrade, “Corrosion resistance performance of steel-reinforced engineered cementitious composite beams,” *ACI Mater. J.*, no. 105, pp. 243–250, 2008.
- [91] V. C. Li and D. K. Mishra, “Structural applications of engineered cementitious composites,” *Indian Concr. J.*, vol. October, pp. 561–567, 1996.
- [92] G. Parra-Montesinos and James K. Wight, “Seismic Response of Exterior Rc Column-To-Steel Beam Connections,” *J. Struct. Eng.*, vol. 126, no. October, pp. 1113–1121, 2000.
- [93] W. P. Boshoff and G. P. A. G. van Zijl, “Time-dependent response of ECC: Characterisation of creep and rate dependence,” *Cem. Concr. Res.*, vol. 37, no. 5, pp. 725–734, 2007.
- [94] J. M. Rouse and S. L. Billington, “Creep and shrinkage of high-performance fiber-reinforced cementitious composites,” *ACI Mater. J.*, vol. 104, no. 2, pp. 129–136, 2007.
- [95] B. Suryanto, K. Maekawa, and K. Nagai, “Predicting the Creep Strain of PVA-ECC at High Stress Levels based on the Evolution of Plasticity and Damage,” *J. Adv. Concr. Technol.*, vol. 11, no. 2, pp. 35–48, 2013.

- [96] M. Li and V. C. Li, "Behavior of ECC-concrete layered repair system under drying shrinkage conditions," *Restor. Build. Monum.*, vol. 12, no. 2, pp. 143–160, 2006.
- [97] J. Zhang, C. Gong, Z. Guo, and M. Zhang, "Engineered cementitious composite with characteristic of low drying shrinkage," *Cem. Concr. Res.*, vol. 39, no. 4, pp. 303–312, 2009.
- [98] G. Fischer and V. Li, "Intrinsic response control of moment-resisting frames utilizing advanced composite materials and structural elements," *ACI Struct. J.*, no. 100, 2003.
- [99] M. Kunieda and K. Rokugo, "Recent Progress on HPFRCC in Japan Required Performance and Applications," *J. Adv. Concr. Technol.*, vol. 4, no. 1, pp. 19–33, 2006.
- [100] V. C. Li, "Can Concrete Be Bendable?," *Am. Sci.*, vol. 100, no. 6, p. 484, 2012.
- [101] H.-J. Kong, S. G. Bike, and V. C. Li, "Development of a self-consolidating engineered cementitious composite employing electrosteric dispersion/stabilization," *Cem. Concr. Compos.*, vol. 25, no. 3, pp. 301–309, Apr. 2003.
- [102] S. Wang, V. Li, A. Naaman, and H. Reinhardt, "Lightweight engineered cementitious composites (ECC)," in *4th International RILEM Workshop on High Performance Fiber - Reinforced Cement Composites (HPFRCC4)*, 2003, pp. 379–390.
- [103] Y. Y. Kim, H. J. Kong, and V. C. Li, "Design of Engineered Cementitious Composite Suitable for Wet-Mixture Shotcreting," *ACI Mater. J.*, vol. 100, no. 6, pp. 511–518, 2003.
- [104] S. Wang and V. C. Li, "High-early-strength engineered cementitious composites," *ACI Mater. J.*, vol. 103, no. 2, pp. 97–105, 2006.
- [105] Y. Yang, M. D. Lepech, E. Yang, and V. C. Li, "Autogenous healing of engineered cementitious composites under wet–dry cycles," *Cem. Concr. Res.*, vol. 39, no. 5, pp. 382–390, May 2009.
- [106] V. C. Li, M. Lepech, S. Wang, M. Weimann, and G. A. Keoleian, "Development of Green ECC for Sustainable Infrastructure Systems," in *Int'l Workshop on Sustainable Development and Concrete Technology*, 2004, pp. 181–192.
- [107] E. H. Yang, Y. Yang, and V. C. Li, "Use of high volumes of fly ash to improve ECC mechanical properties and material greenness," *ACI Mater. J.*, vol. 104, no. 6, pp. 620–628, 2007.
- [108] M. Lepech, G. Keoleian, S. Qian, and V. C. Li, "Design of green engineered cementitious composites for pavement overlay applications," in *Int'l Association for Life Cycle Civil Engineering conference (IALCCE 08)*, 2008, pp. 837–842.
- [109] X. Huang, R. Ranade, Q. Zhang, W. Ni, and V. C. Li, "Mechanical and thermal properties of green lightweight engineered cementitious composites," *Constr. Build. Mater.*, vol. 48, pp. 954–960, Nov. 2013.

- [110] H. Siad, A. Alyousif, O. K. Keskin, S. B. Keskin, M. Lachemi, M. Sahmaran, and K. M. Anwar Hossain, "Influence of limestone powder on mechanical, physical and self-healing behavior of Engineered Cementitious Composites," *Constr. Build. Mater.*, vol. 99, pp. 1–10, 2015.
- [111] X. Huang, R. Ranade, W. Ni, and V. C. Li, "Development of green engineered cementitious composites using iron ore tailings as aggregates," *Constr. Build. Mater.*, vol. 44, no. null, pp. 757–764, Jul. 2013.
- [112] A. A. Griffith, "The Phenomena of Rupture and Flow in Solids," *Philos. Trans. R. Soc. A Math. Phys. Eng. Sci.*, vol. 221, no. 582–593, pp. 163–198, 1921.
- [113] D. Marshall and B. N. Cox, "A J-INTEGRAL METHOD FOR CALCULATING STEADY-STATE MATRIX CRACKING STRESSES IN COMPOSITES," *Mech. Mater.*, vol. 7, pp. 127–133, 1988.
- [114] J. Morton and G. W. Groves, "The effect of metal wires on the fracture of a brittle-matrix composite," *J. Mater. Sci.*, vol. 11, no. 4, pp. 617–622, 1976.
- [115] Z. Lin, T. Kanda, and V. Li, "On interface property characterization and performance of fiber-reinforced cementitious," *Concr. Sci. Eng.*, vol. 1, no. September, pp. 173–174, 1999.
- [116] T. Kanda and V. C. Li, "Practical Design Criteria for Saturated Pseudo Strain Hardening Behavior in ECC," *J. Adv. Concr. Technol.*, vol. 4, no. 1, pp. 59–72, 2006.
- [117] E.-H. Yang, S. Wang, Y. Yang, and V. C. Li, "Fiber-Bridging Constitutive Law of Engineered Cementitious Composites," *J. Adv. Concr. Technol.*, vol. 6, no. 1, pp. 181–193, 2008.
- [118] C. Lu, C. K. Y. Leung, and V. C. Li, "Numerical model on the stress field and multiple cracking behavior of Engineered Cementitious Composites (ECC)," *Constr. Build. Mater.*, vol. 133, pp. 118–127, 2017.

CHAPTER 3: Integrated Design Method

An integrated design method for Engineered Geopolymer Composite (EGC) is proposed in this chapter. The new methodology combines three material-design techniques: design of experiment, micromechanical modeling, and material sustainability indices, which synergistically work to solve the multi-response optimization problem in EGC design.

3.1 Framework of proposed design method

As has been discussed in Chapter 2, material design of EGC involves many design parameters and multiple responses to be optimized. Specifically, both high tensile ductility and enhanced material greenness need to be achieved, as well as fundamental engineering properties such as strength. While some existing design methods are useful to partly aid the multi-response optimization, a comprehensive framework to integrate those approaches has not been developed yet. In the present chapter, a new integrated design methodology is proposed to facilitate the research and development of EGC.

Figure 3.1 illustrates the design scheme of the proposed design method. It consists of three design phases: matrix, composite, and environmental designs, each of which utilizes a specific material-design technique. This section outlines each design phase and corresponding design technique. The detailed theories and procedures are later presented in the following sections.

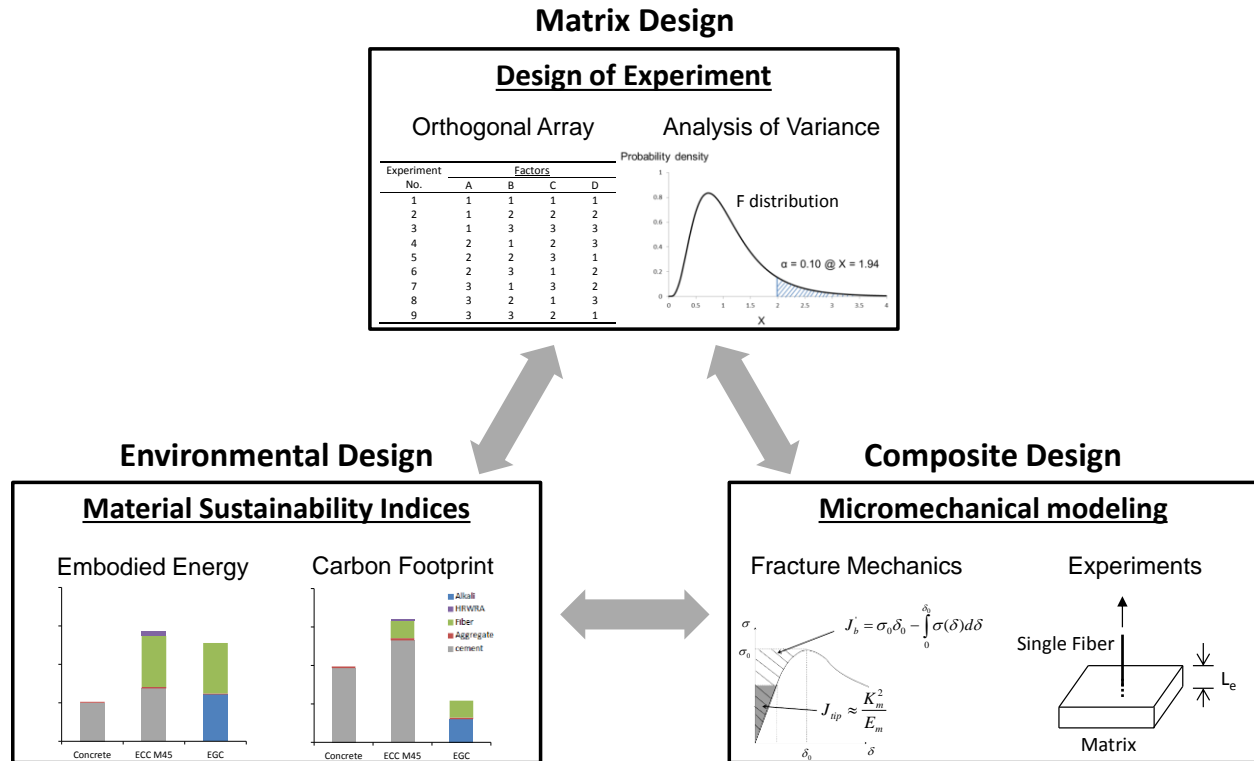


Fig. 3.1: Design scheme of the proposed integrated design method. Three design techniques for matrix, composite, and sustainability design phases are utilized, working synergistically to guide the optimization.

The design process of EGC starts with developing the matrix; this design phase is aimed at meeting requirements in fundamental engineering properties or at achieving desired added functions. First and foremost, the relationship between design variables (types of ingredients, mix proportions, curing regime, etc.) and a property of interest (compressive strength, workability, setting time, etc.) needs to be known, preferably in a quantitative manner. To achieve this, a statistics-based design method, called Design of Experiment (DOE), is used. Specifically, the method is that developed by Taguchi [1], which has been applied to numerous science and engineering fields.

In Taguchi’s approach, effects of design variables (or “input factors”) on performance (or “output”) are systematically quantified without explicitly testing every combination of input

factors. There are two key steps there. First, out of numerous possible combinations of input factors and factor levels, only a portion of them is selected to test, based on a fractional-factorial design using orthogonal arrays (OAs). Second, test results from the planned experiments are statistically analyzed by using the Analysis of Variance (ANOVA) method. This step offers quantitative evaluation on the significance of each factor and suggests optimum factor levels. With Taguchi's DOE technique, experimental costs can be substantially reduced, yet robust information about the relationship between input factors and an output is obtained. The optimum matrix design can be determined based on the information.

Once a desired EGC matrix is developed, fiber and fiber/matrix interface properties are tailored to impart high tensile ductility and multiple-cracking characteristic to the material. Micromechanical modeling is a design technique adopted in this composite-design phase [2], which has been outlined in Section 2.2.2. In this design stage, micromechanical parameters – fracture toughness and tensile strength of matrix, bonding properties between fiber and matrix, and so forth – are first measured for the developed matrix and selected fiber. Then, the composite tensile behavior is simulated by an analytical model that relates the measured micromechanical parameters and macroscopic composite properties. Based on the simulation result, required modification of micromechanical parameters are determined for achieving desired composite properties.

The last phase is the environmental design that evaluates material sustainability of the developed composite. Here, Material Sustainability Indices (MSI) are employed to measure the energy consumption and carbon footprints associated with the material production [3]. MSI values represent a partial life cycle analysis (LCA) of the material greenness that accounts for raw-material acquisition, processing, and manufacturing, while the use and disposal phases are

omitted. In general, reliable life-cycle inventory data are collected from literature or database, for all ingredients of the material. MSI values are then calculated by taking the sum of the energy/carbon footprints of the ingredients. MSI are useful for comparing the carbon and energy footprints of different materials on a mass or volume basis, and for quantifying the overall environmental performance of materials, regardless of the application.

Each of the three design techniques above has been individually applied to geopolymer and ECC development. The uniqueness of the proposed integrated design method is that those three design stages are linked with each other and work in a synergistic manner. For example, sustainability aspects are considered in both the matrix-design and composite-design stages by pre-screening out energy/carbon-intensive ingredients. In addition, information from the matrix-design stage can be utilized in the other stages; a DOE study in the matrix development may identify some design variables as “insignificant factors” on the property of interest. Then, without compromising the target matrix property, those design variables can be used to either modify micromechanical parameters for the composite design or lower the energy/carbon footprints for the environmental design. Thus, information from all three design techniques can be fed back into each design step, systematically confining the vast design space of multi-response optimization in EGC.

Detailed theories and procedures of the method are most easily understood through an example, which is presented in the following sections.

3.2 Matrix development

As a simple example, consider that a geopolymer matrix with higher compressive strength than that of the current design needs to be developed, and that four design factors are studied: A, B, C, and D, which may influence the compressive strength of the matrix. Preferably, design factors are those taking on numerical values; the amount of fly ash, mixing ratio of fly ash to alkaline activator, curing temperature, and curing duration are good examples. Then, to evaluate the effect of each factor on the compressive strength, levels for each factor are selected, e.g. 30, 60, and 90 °C for curing temperature. The number of factor levels is important; if two factor levels are selected, nonlinearity in the relationship between the input factor and output performance cannot be detected; if many factor levels are chosen, the number of experiments to be conducted is impractical. Here, three factor levels are set for the four design variables each. The objective is to identify factors that significantly affect the compressive strength, and to find the optimum factor levels.

3.2.1 Orthogonal array

The most reliable but least efficient way to investigate is to test all possible combinations of factor levels; it requires $3^4 = 81$ experimental runs, if only one sample is tested for each combination. As mentioned in Section 2.1.3, this full-factorial experiment is the trial-and-error approach which has often been taken in geopolymer development. However, strength of geopolymers is typically associated with many design variables, and the number of required experiments exponentially increases with the number of factors. It is here that Taguchi's orthogonal arrays are utilized.

Orthogonal arrays (OAs) are a tool to aid the design of efficient fractional-factorial experiments. Table 3.1 shows an orthogonal array, called an L9 array, which is used for the example here.

Underlined tabulated values in a row represent the combination of factor levels that is tested in the experimental run indicated in the first column. For example, in the third experiment (i.e. trial no. 3), the level of Factor A is set at the first level, while the levels of the other factors are set at the third one. In general, actual numerical values are assigned to each factor level (e.g. 30, 60, and 90 °C for the three levels of the curing-temperature factor). In the case of the present example, geopolymer specimens are prepared based on the nine different combinations of factor levels, and tested to measure the compressive strength of each series. Thus, only nine of 81 possible combinations are selected with the aid of the OA.

Table 3.1: L9 standard orthogonal array. Underlined tabulated values represent the coded factor levels.

Trial No.	Column ID			
	A	B	C	D
1	<u>1</u>	<u>1</u>	<u>1</u>	<u>1</u>
2	<u>1</u>	<u>2</u>	<u>2</u>	<u>2</u>
3	<u>1</u>	<u>3</u>	<u>3</u>	<u>3</u>
4	<u>2</u>	<u>1</u>	<u>2</u>	<u>3</u>
5	<u>2</u>	<u>2</u>	<u>3</u>	<u>1</u>
6	<u>2</u>	<u>3</u>	<u>1</u>	<u>2</u>
7	<u>3</u>	<u>1</u>	<u>3</u>	<u>2</u>
8	<u>3</u>	<u>2</u>	<u>1</u>	<u>3</u>
9	<u>3</u>	<u>3</u>	<u>2</u>	<u>1</u>

It should be noted that each column contains three tests under each level of the factor; for example, there are three experimental runs for the first level of Factor A (i.e. trials no. 1, 2, and 3), and the same is true for the second and third levels of the factor. This is one of the characteristics of OAs that provides “orthogonality” among the factors; here, the orthogonality means that the effect of a factor can be evaluated independently of effects of the other factors.

To understand orthogonality, consider that the effect of Factor A is to be assessed. For simplicity, it is suppose that an output performance can be expressed as the superposition of each factor effect:

$$y_{ijkl} = a_i + b_j + c_k + d_l \quad (3.1)$$

where y_{ijkl} is the output performance under i-, j-, k-, and l-th levels of Factors A, B, C, and D, respectively, and x_n represents the effect of Factor X at the n-th level. Then, one way to evaluate the factor effect is to compare the averaged output values between different factor levels. Namely, for Factor A in the above L9 array, the following quantities are compared:

$$\bar{T}_1 = \frac{y_{1111} + y_{1222} + y_{1333}}{3} = a_1 + \frac{(b_1 + b_2 + b_3) + (c_1 + c_2 + c_3) + (d_1 + d_2 + d_3)}{3} \quad (3.2)$$

$$\bar{T}_2 = \frac{y_{2123} + y_{2231} + y_{2312}}{3} = a_2 + \frac{(b_1 + b_2 + b_3) + (c_1 + c_2 + c_3) + (d_1 + d_2 + d_3)}{3} \quad (3.3)$$

$$\bar{T}_3 = \frac{y_{3132} + y_{3213} + y_{3321}}{3} = a_3 + \frac{(b_1 + b_2 + b_3) + (c_1 + c_2 + c_3) + (d_1 + d_2 + d_3)}{3} \quad (3.4)$$

It should be noted that subtracting one of the above three quantities from another gives the effect of Factor A only, by cancelling out the effects of the other factors. In other words, evaluation of a factor effect is not bothered by the other factors. OAs are designed such that this orthogonality holds true for every factor assigned to the columns.

It should be however mentioned that, more generally, there are two other terms to be considered in the above discussion: *interaction effects* and *errors*. First, the effect of a factor often differs depending on the level of another factor. Mathematically, additional terms need to be included in

Eq. 3.1. Those terms are typically not cancelled out in evaluating factor effects, and the interaction effect is therefore mixed with main effects of factors (called “confounding”, which is discussed in detail in Appendix A). Thus, if interaction effects are expected to be significant, an appropriate OA that can separate the interaction effects from main-factor effects needs to be chosen. Second, the output performance measured in experiment always contains errors to some extent. Aside from random experimental errors, those errors could be caused by “noise factors”, which cannot be controlled and “unknown factors”, which are not considered in the selected OA. In either case, it might be possible to misevaluate the significance of factors if the error effect is relatively large. To overcome this problem, it is required that the estimated factor effect be compared with the error effect. This is the essence of Analysis of Variance, which is discussed below.

3.2.2 Analysis of Variance

Once the fractional-factorial experiment is well planned and conducted, the obtained test data need to be analyzed and interpreted. Analysis of Variance (ANOVA) is the most objective method to examine the significance of factors through the test result.

As an example, Factor A is evaluated here; the following procedure is equally applicable to the other factors. Suppose that three samples are tested for each experimental run in the L9 array. Table 3.2 lists an example data set of the measured compressive strength. Also, Fig. 3.2 plots the mean compressive strength at each trial, the total mean of all the data (\bar{T}), and the group mean for each factor level (\bar{T}_i), which is the average of data in the same factor level. As can be seen in the L9 array (Table 3.1), the first level of Factor A (A_1) is included in the first to third trials, A_2 in the fourth to sixth, and A_3 in the seventh to ninth ones.

Table 3.2: Example data set of measured compressive strength.

Trial No.	Compressive strength (MPa)			Mean
	Sample 1	Sample 2	Sample 3	
1	43	45	44	44
2	38	39	43	40
3	32	35	41	36
4	40	36	29	35
5	33	31	38	34
6	31	32	45	36
7	40	44	48	44
8	52	52	52	52
9	48	52	50	50

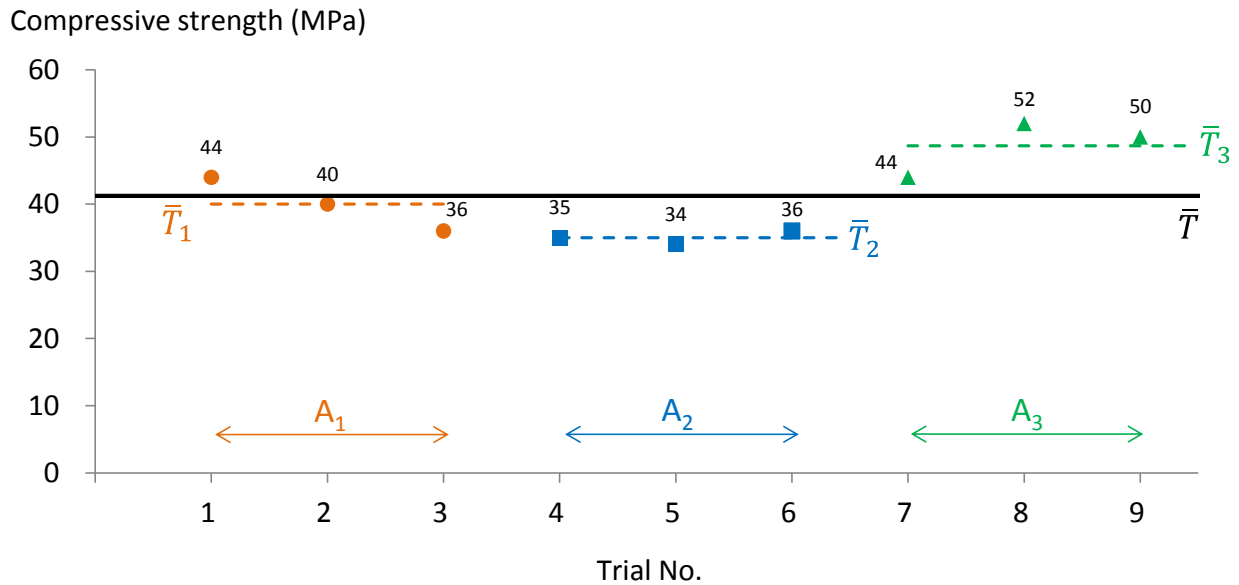


Fig. 3.2: Mean compressive strength at each trial, and the total and group means.

When Factor A has a statistically significant effect, some of the group means should be largely deviated from the total mean. One way to quantify this deviation is to use the *sum of squares* (SS):

$$SS_A = \sum_i n_i (\bar{T}_i - \bar{T})^2 \quad (3.5)$$

where n_i is the sample size in the i -th level of the factor, by which the squared deviation for the group is weighted. SS of other factors can be also calculated in the same manner. This quantity reflects the variation caused by the factor.

Similarly, the total sum of squares can be defined as the squared deviation of each data point from the total mean:

$$SS_T = \sum_i \sum_j (x_{ij} - \bar{T})^2 \quad (3.6)$$

where x_{ij} is the data for j -th sample in the i -th trial. This quantity reflects the total variation in the data set. In general, the total variation is larger than the sum of the variations caused by factors. Thus, the variation due to errors (SS_e) can be defined as the difference between the total variation and variation due to factors:

$$SS_e = SS_T - (SS_A + SS_B + SS_C + SS_D) \quad (3.7)$$

This quantity includes not only effects of random errors, but also interaction effects and unknown-factor effects.

Then, to determine the significance of Factor A, the variation due to the factor and the variation due to errors are compared; if the former is relatively large compared to the latter, then Factor A is a statistically significant factor. However, the magnitude of SS depends on the number of data points included in the calculation. Thus, direct comparison of SS might not reflect the significance of the factor. Here, *degree of freedom* (DOF) is introduced to normalize SS; in the

present example, the total DOF (v_T) is calculated as the number of all data points minus one (i.e. $27 - 1 = 26$). It should be noted that one DOF is consumed by the total mean (i.e. if the total mean is fixed, values of 26 points can be independently selected, while that of the remaining one point is not). Similarly, since three factor levels are considered in the example, the DOF for Factor A (v_A) is $3 - 1 = 2$. The same is true for the other factors. Finally, the DOF for errors (v_e) is calculated by subtracting the sum of DOF for factors from the total DOF (i.e. $26 - 2 \times 4 = 18$).

Now, each SS is normalized by the corresponding DOF, which gives the *mean square* (MS):

$$MS_A = \frac{SS_A}{v_A} \quad (3.8)$$

$$MS_e = \frac{SS_e}{v_e} \quad (3.9)$$

MS is also known as *variance* because the formula is similar to that for the sample variance in statistics. Also, this is the reason why the method is called *Analysis of Variance*. Next, a statistical F-test is conducted on the ratio of MS_A to MS_e :

$$F_A = \frac{MS_A}{MS_e} \quad (3.10)$$

The null hypothesis here is that two normally-distributed populations have the same variance. In other words, it hypothesizes that the variation due to Factor A is not statistically significant compared to the variation due to errors. Here, a confidence level of 5% is used for the hypothesis test. Then, the required F-ratio to achieve the confidence level is:

$$F_{\alpha, v_A, v_e} = F_{0.05, 2, 18} = 3.55 \quad (3.11)$$

This value can be found from the F-table in most textbooks on statistics. If the calculated F-value in the Eq 3.10 is larger than the required F-ratio in Eq. 3.11, then the null hypothesis is rejected and it is concluded that Factor A is a significant factor. Further, the larger F-value typically suggests the larger magnitude of the factor effect.

Table 3.3 summarizes the ANOVA result in this example. According to the F-ratios, it is suggested that Factors A and C have significant effects on the matrix compressive strength, while Factors B and D do not. In addition, Factor A is the most significant factor, and Factor B is the most insignificant one.

Table 3.3: ANOVA results on the example problem.

Factors	DOF	Sum of square	Mean square	F-ratio
A	2	860.67	430.33	25.15
B	2	8.67	4.33	0.25
C	2	164.67	82.33	4.81
D	2	32.67	16.33	0.95
Error	18	308	17.11	–
Total	26	1374.67	–	–

3.2.3 Main-effect plot and optimum conditions

The ANOVA study only determines whether each factor is a significant one or not. To understand trends of the factor effect on the output, main-effect plots are useful.

Figure 3.3 shows a main-effect plot for the present example; it plots mean compressive strength at each level of the factors. The most influential effect of Factor A is made clear by the graph, but more importantly, the third level gives the highest compressive strength on average. In contrast, the effect of Factor C has a decreasing trend, and the first level gives the maximum.

Thus, the predicted optimum design should include the third level of Factor A and the first level of Factor C.

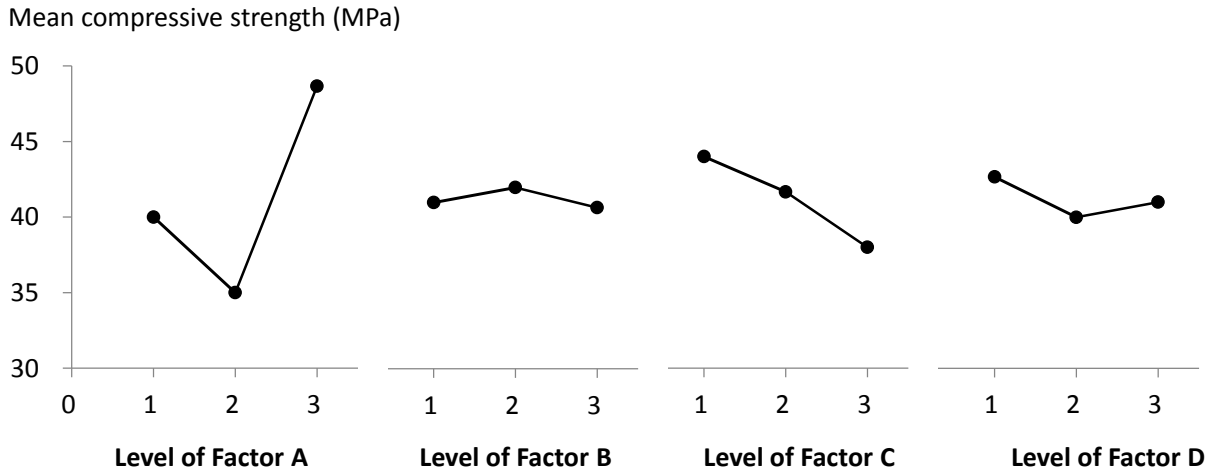


Fig. 3.3: Main-effect plots showing mean compressive strength at each level of factors.

Meanwhile, other factor levels can be arbitrarily set, without diminishing the compressive strength. It is here that the proposed design method links the material-development stage with the other design stages: these insignificant factors are utilized to complement optimization in the other design phases. For example, levels of those factors can be selected so that desired modification on micromechanical parameters are made in the composite design phase. Or, a higher material greenness can be achieved by choosing appropriate levels of the factors, for the environmental design stage. The decision is made based on what is most required in the material.

It should be noted that the determination of significant factors and their trends is based on the selected ranges of the factor levels. It might be possible that different trends are found outside the ranges, and that different conclusions on the significance of factors are made. This is why the selection of levels is critical, and why the subsequent confirmation experiment is essential.

3.2.4 Confirmation experiment

The primary objective of the confirmation experiment is to verify the predicted optimum design. The first step is to prepare samples based on the optimum design and test them for compressive strength. Then, based on statistics, the mean compressive strength and its confidence interval (CI) of the predicted optimum design are estimated. If the measured mean is inside the estimated CI, then it is concluded that the predicted optimum design is valid.

The following formula gives a statistical estimate of the mean for the present example:

$$\hat{\mu}_{A_3C_1} = \bar{A}_3 + \bar{C}_1 - \bar{T} \quad (3.12)$$

where $\hat{\mu}_{A_3C_1}$ is the estimated mean at the optimum condition, \bar{X}_i represents the mean at i-th level of Factor X (as plotted in the main-effects plots), and \bar{T} is the total mean of all data points. The estimated mean is calculated to be 51.44 MPa in this example. More generally, the formula takes the sum of mean values of significant factors at the predicted optimum levels, and subtracts the total mean multiplied by the number of significant factors minus one.

Next, to calculate the CI, the SS and DOF of insignificant factors are combined with those of errors, which is a procedure known as “pooling”. Table 3.4 lists the pooled ANOVA result for the present example.

Table 3.4: Pooled ANOVA results on the example problem.

Factors	DOF	Sum of square	Mean square	F-ratio
A	2	860.67	430.33	27.10
C	2	164.67	82.33	5.19
Error	22	349.33	15.88	–
Total	26	1374.67	–	–

Then, the corresponding CI is given by the following equation:

$$CI = \hat{\mu}_{A_3C_1} \pm \sqrt{F_{\alpha;1;v_e} V_{ep} \left[\frac{1}{\eta_{eff}} + \frac{1}{r} \right]} \quad (3.13)$$

$F_{\alpha;1;v_e}$ represents the F-ratio at a significance level of α with the DOF of pooled errors (v_e); V_{ep} is the variance (equivalent to MS) of the pooled errors; η_{eff} is the effective number of replications expressed as (Total number of samples) / (1 + Total DOF associated with significant factors); r is the sample size for the confirmation experiment. In the present case, α , v_e , V_{ep} , and η_{eff} are 0.05, 22, 15.88, and 5.4, respectively. If three samples are tested for the confirmation experiment, the CI ranges from 45.49 to 57.40 MPa in this example.

As mentioned above, it is checked if the measured mean compressive strength is inside the estimated CI. Then, if the predicted design is indeed an optimum one, further improvement may be explored; for example, because of the observed monotonically-decreasing trend of Factor C, using a smaller factor level than the optimum design (i.e. outside the selected range), with other factors set at the optimum-design levels, may result in a higher compressive strength. Conversely, if the measured compressive strength is outside the estimated CI, more rounds of experiments will be required; a new experimental plan needs to be prepared to detect any significant confounded interaction or unknown factor that was not considered in the first trial. The detailed strategies and procedures for this can be found in the literature [4].

In this section, the concept and procedures of the matrix development aided by the Taguchi's DOE have been presented through an example. More information on the DOE technique, such as different OAs and their characteristics, can be found in the literature (e.g. [5]). In the next section, the subsequent composite-design stage to impart desired tensile properties to the developed matrix is discussed.

3.3 Composite Design

3.3.1 Experimental characterization

The first step of the composite-design stage is to select the type of reinforcing fiber. Apart from the economical aspect, the selection may be confined by the environmental-design aspect: energy- or carbon-intensive fibers may be pre-screened out for achieving higher material greenness. This is another type of integration in the proposed design method that links different design stages.

Then, the next step is to characterize micromechanical parameters of the developed matrix, selected fiber and their interface, which govern composite tensile properties. As has been discussed in Section 2.2.2, there are two required conditions for the steady-state multiple cracking characteristic:

$$\sigma_{ci}^i \leq \min_j \sigma_0^j \quad (3.14)$$

$$J_{tip}^i \leq \sigma_0^i \delta_0^i - \int_0^{\sigma_0^i} \sigma^i(\delta^i) d\delta^i \equiv J_b^i \quad (3.15)$$

The variables in the left hand side of Eqs 3.14 and 3.15 represent the crack-initiation stress (σ_{ci}) and crack-tip toughness (J_{tip}) for a plane of the composite. These two can be determined by experiment, which is first discussed in this section.

(i) Crack-initiation stress

For the crack-initiation stress σ_{ci} , a typical measurement method is uniaxial tension testing on composite specimens. Specifically, a dog bone test recommended by the Japan Society of Civil

Engineers (JSCE) [6] is most commonly used. The specimen geometry and test setup are shown in Fig. 3.4.

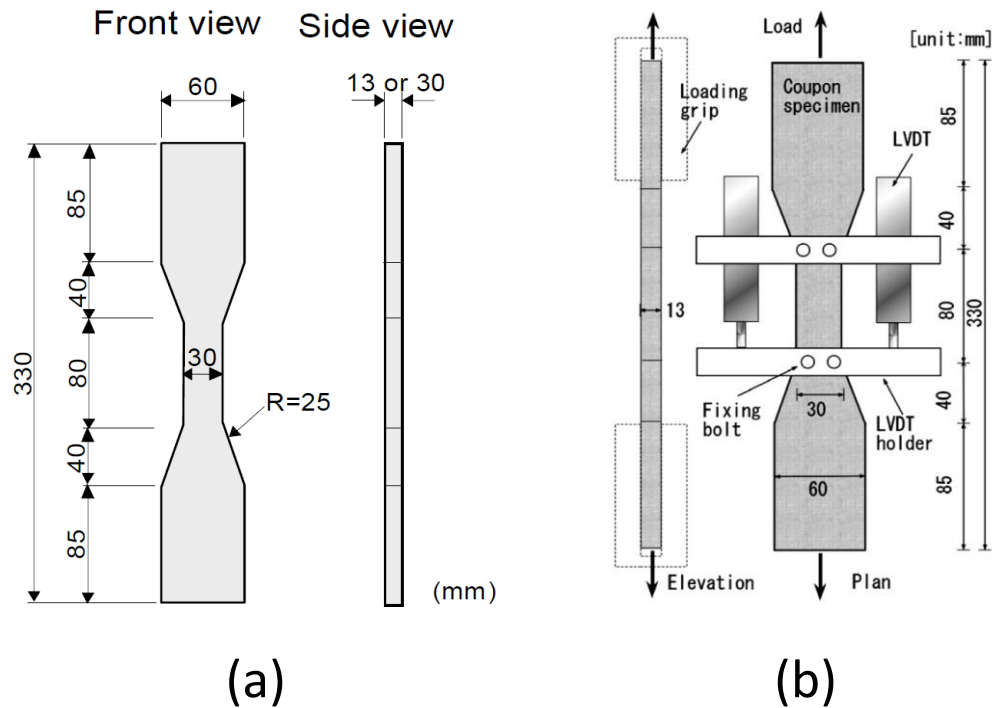


Fig. 3.4: (a) Specimen geometry and (b) test setup for JSCE dog bone testing [6].

In this testing, the load should be applied under displacement control, using a chucking mechanism with a fixed support on one end and a pin (hinge) support on the other end. The loading rate is approximately 0.5 mm/min. For strain measurement, two linear variable differential transformers (LVDTs) are typically attached on the specimen to measure extensions within gauge length. Tensile strain is computed from the average of the extensions divided by the gauge length. Then, for the obtained stress-strain curve, the first-cracking strength (equivalent to σ_{ci}) is determined by a data point above which linear-elasticity assumption does not hold. Because of material and processing-induced variability, testing more than four specimens is recommended to obtain the average first-cracking strength.

(ii) *Crack-tip toughness*

An approximation can be used for the crack-tip toughness J_{tip} ; at small fiber content, J_{tip} can be approximated as K_m^2/E_m where K_m and E_m are the fracture toughness and Young's modulus of the matrix. Both of the properties can be experimentally determined.

In the case of E_m , the composite Young's modulus (E_c), which can be obtained in the above dog bone test, may be used instead; there is no significant difference between the two quantities when the fiber volume is low. Or, it might be possible to directly measure E_m by using mortar dog bone specimens in the uniaxial tension test. In this case, the composite crack-initiation stress (σ_{ci}) could be approximated as the cracking strength of the mortar. This method has been adopted in the development of an optimized EGC, which is detailed in Chapter 4.

To measure K_m , a three-point bending test specified by ASTM E399 [7] can be used. Figure 3.5 shows an example of the specimen geometry. A single-edge notch is made on the beam specimen with the notch depth-to-height ratio of about 0.4. The loading rate of 0.5 mm/min can be used, and only the peak load needs to be recorded during the test. Then, the following formula is used to calculate K_m :

$$K_m = \frac{PS}{BW^{1.5}} \cdot f\left(\frac{a}{W}\right) \quad (3.16)$$

where

$$f\left(\frac{a}{W}\right) = 3\sqrt{\frac{a}{W}} \cdot \frac{1.99 - \left(\frac{a}{W}\right)\left(1 - \frac{a}{W}\right) \left[2.15 - 3.93\frac{a}{W} + 2.7\left(\frac{a}{W}\right)^2 \right]}{2\left(1 + 2\frac{a}{W}\right)\left(1 - \frac{a}{W}\right)^{1.5}} \quad (3.17)$$

P is the peak load; S is the span of the beam; B is the specimen thickness; W is the specimen height; a is the notch depth.

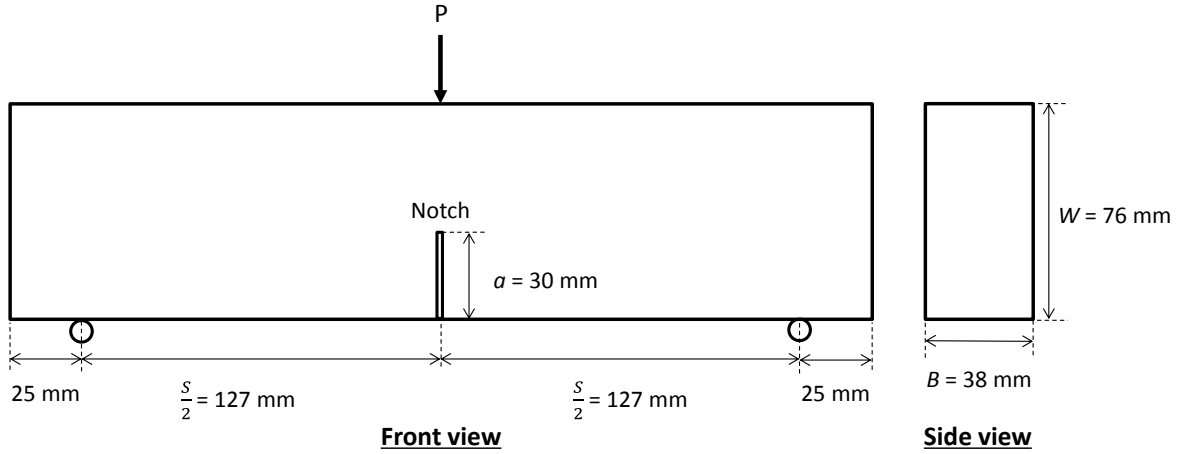


Fig. 3.5: Specimen geometry for matrix fracture-toughness test.

Next, fiber-bridging capacity (σ_0) and complementary energy (J'_b) in the right-hand sides of Eqs 3.14 and 3.15 are considered. As mentioned in Section 2.2.2, the σ - δ relation needs to be known for determining these two quantities. The micromechanical modeling offers an analytical scale-linking model that predicts the σ - δ relation (i.e. macroscopic composite property) from micromechanical parameters. For the σ - δ simulation, some of the micromechanical parameters need to be characterized by experiment.

(iii) Chemical bond, frictional bond, and slip-hardening coefficient

Fiber/matrix interface properties are major micromechanical parameters that need to be experimentally determined. A single-fiber pullout test is most commonly used to measure them. Figure 3.6 shows the specimen geometry and test setup. The specimen consists of a single fiber embedded in a small geopolymer-mortar prism, with a fiber inclination angle of φ . The fiber embedment length (L_e) is identical to the specimen thickness (d) when φ equals zero. Details on

the specimen preparation can be found in [8]. In the test setup, the bottom surface of the specimen is first glued to a specimen mount equipped with a load cell. The free end of the fiber is then firmly attached to an aluminum plate, which is gripped by the load frame, by using masking tape and super glue. This method prevents the slippage between the fiber and aluminum plate. After the glue sufficiently dries, the specimen position is carefully adjusted to align the fiber with the loading direction, by using the X-Y stage. The loading is applied under displacement control at the rate of 0.5 mm/min.

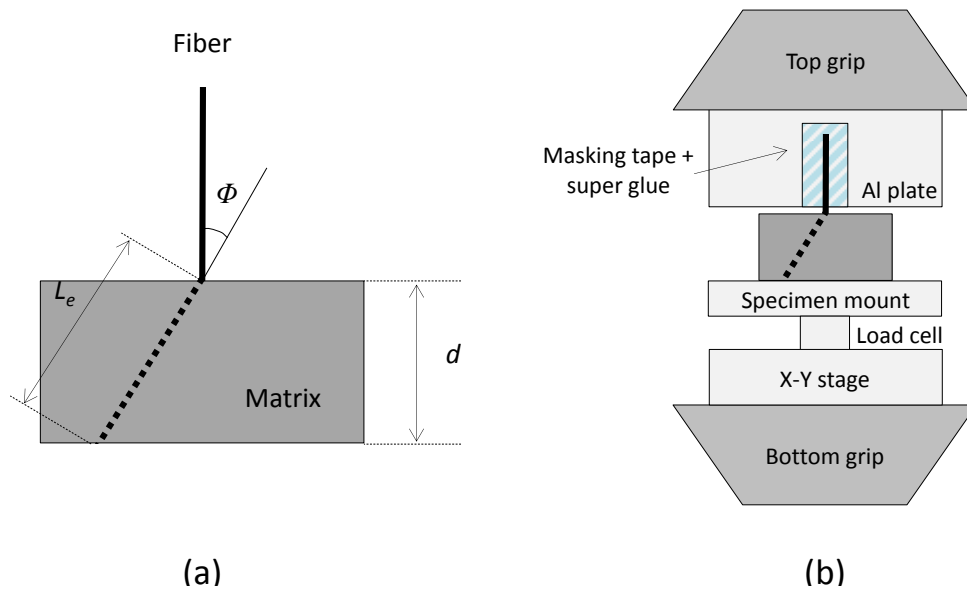


Fig. 3.6: (a) Specimen geometry and (b) test setup for single-fiber pullout test.

In general, there are three distinct stages in the fiber-pullout load versus pullout displacement curve ($P-u$ curve) [9]. The first stage is associated with the elastic stretch of the free end of the fiber. This stage is negligible if the fiber free length (the distance between the aluminum plate and the specimen) is sufficiently small. The second stage is called “debonding stage”; if the fiber is chemically bonded to the surrounding matrix, it must first debond the interface before being pulled out. This chemical bond is significant in hydrophilic fibers such as poly-vinyl alcohol

(PVA) fiber. Then, after complete debonding, the pullout process is controlled by frictional bond only, which is called “pullout stage”. Typically, the pullout load suddenly drops at the onset of the pullout stage. The load drop is an evidence of the significant chemical bond, and its magnitude reflects the bond strength. In addition, depending on the fiber type, a slip-hardening effect could be observed in the pullout stage: the frictional bond effectively increases with the pullout displacement, mainly due to jamming effect resulted from fiber-surface abrasion [10]. The general profile of the $P-u$ curve is illustrated in Fig. 3.7.

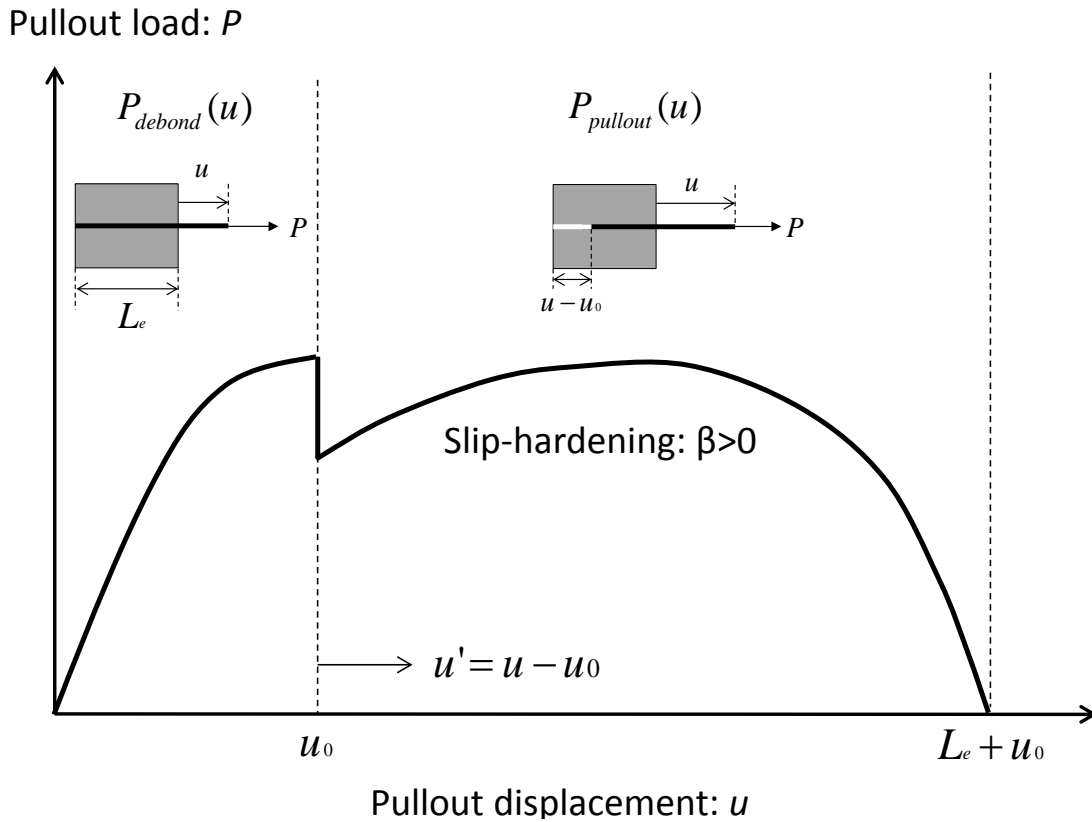


Fig. 3.7: Typical single-fiber pullout curve with slip-hardening.

From the obtained $P-u$ curve for a single aligned fiber (i.e. $\varphi = 0$), the chemical bond (G_d) and frictional bond (τ_0) can be determined as follows:

$$G_d = \frac{2}{\pi^2 E_f d_f^3} \{P_{debond}(u_0) - P_{pullout}(u_0)\}^2 \quad (3.18)$$

$$\tau_0 = \frac{P_{pullout}(u_0)}{\pi d_f L_e} \quad (3.19)$$

E_f and d_f are the Young's modulus and diameter of the fiber; $P_{debond}(u_0)$ and $P_{pullout}(u_0)$ are the pullout loads in the debonding and pullout stages, for the threshold pullout displacement (u_0) at which the full-debonding is completed and the load drop takes place. In addition, the least-square estimation (LSE) can be used for determining the slip-hardening coefficient β ; define $u' = u - u_0$ where $u > u_0$ (i.e. the post-peak pullout displacement) and $P_{ex}(u_i')$ as the measured pullout load at the i -th data of the post-peak pullout displacement. Then, the least square estimation of β is obtained by:

$$\hat{\beta} = \frac{\sum_i P_{ex}(u_i') \cdot \frac{u_i'(L_e - u_i')}{\pi \tau_0} - \sum_i d_f u_i'(L_e - u_i')^2}{\sum_i \{u_i'(L_e - u_i')\}^2} \quad (3.20)$$

Detailed derivations for G_d , τ_0 , and β can be found in Appendix B.

(iv) *Snubbing coefficient and fiber-strength reduction factor*

It should be noted that the formulae above are those for aligned fibers. When the inclination angle φ is nonzero, two more parameters need to be considered: *snubbing coefficient* (f) and *fiber-strength reduction factor* (f').

Morton and Glove [11] and Li *et al.* [12] studied the fiber-inclination effect on the pullout load. They suggested an empirical equation to express the increased fiber-bridging force P due to inclination angle φ :

$$P(u, \phi) = P(u, \phi = 0)g(\phi) = P(u, 0)e^{f\phi} \quad (3.21)$$

where $P(u, 0)$ is either $P_{debond}(u)$ or $P_{pullout}(u)$, depending on the pullout displacement u . To experimentally determine f , the peak pullout load in the single-fiber pullout test is typically compared between aligned and inclined fibers:

$$f = \frac{1}{\phi} \ln \left\{ \frac{P_{peak}(\phi)}{P_{peak}(0)} \right\} \quad (3.22)$$

In addition to the increased pullout load, Kanda and Li found the decreased *in-situ* strength for both aligned and inclined fibers [13]. First, when an aligned fiber is embedded in a mortar matrix, its strength is typically less than the nominal strength reported by the manufacturer. It is suggested that the reduction is attributed to fiber-surface abrasion that occurs in the debonded zone of the fiber. Further, another significant reduction is observed for inclined fibers. Based on experimental results for PVA fiber, Kanda and Li suggested an exponential function to express the strength-reduction effect of inclined fibers:

$$\sigma_f(\phi) = \sigma_f(0)e^{-f'\phi} \quad (3.23)$$

where $\sigma_f(0)$ and $\sigma_f(\phi)$ are the in-situ strength of aligned and inclined fibers. Then, the strength-reduction factor f' is determined by:

$$f' = \frac{1}{\phi} \ln \left\{ \frac{\sigma_f(\phi)}{\sigma_f(0)} \right\} \quad (3.24)$$

It is suggested that both f and f' depend mainly on the fiber type. The snubbing coefficient f ranges from 0.2 to 0.8 [14], and the strength-reduction factor f' is about 0.3, for PVA fiber [9].

3.3.2 Analytical model

After characterizing micromechanical parameters, the composite tensile behavior is predicted by using the analytical scale-linking model. Here, the fiber-bridging constitutive law presented by Yang *et al.* [15] is used, with a slight modification to the model.

As presented in Section 2.2.2, the constitutive law is expressed as:

$$\sigma(\delta) = \frac{V_f}{A_f} \int_{\phi_0}^{\phi_1} \int_{z=0}^{(L_f/2)\cos\phi} P(\delta, L_e) g(\phi) p_1(\phi) p_2(z) dz d\phi \quad (3.25)$$

There are four functions in the double integral: $P(\delta, L_e)$, $g(\phi)$, $p_1(\phi)$, and $p_2(z)$. The third function $g(\phi)$ is identical to that in Eq. 3.21. The other three functions are presented below. In addition, two additional mechanisms that modify the σ - δ relation – *matrix micro-spalling* and *Cook-Gordon effect* – are introduced.

(i) $P(\delta, L_e)$

$P(\delta, L_e)$ represents the bridging force of a single aligned fiber for a crack opening δ . The embedment length L_e may be that for the short-embedment side, and the other side has the embedment length of $L_f - L_e$. It should be noted that pullout displacements for both ends of the embedded fiber contribute to the crack opening:

$$\delta = u_L + u_S \quad (3.26)$$

where u_L and u_S are the pullout displacements for the long- and short-embedment sides. The solution of $P(\delta, L_e)$ can be obtained from Eq. 3.26 and the equilibrium of pullout loads for the long- and short-embedment segments, which are given by either $P_{debond}(u)$ or $P_{pullout}(u)$. Here, $P_{debond}(u)$ or $P_{pullout}(u)$ can be modeled by the following equations [9]:

$$P_{debond}(u) = \sqrt{\frac{\pi^2 E_f d_f^3 (1+\eta)}{2}} \{\tau_0 u + G_d\}, \quad 0 < u \leq u_0 \quad (3.27)$$

$$P_{pullout}(u) = \pi d_f \tau_0 \left\{ 1 + \frac{\beta(u - u_0)}{d_f} \right\} (L_e - u + u_0), \quad u_0 \leq u \leq L_e + u_0 \quad (3.28)$$

η is expressed as $V_f E_f / V_m E_m$ where V_f and V_m are the volume fractions of fiber and matrix, and E_m is the matrix Young's modulus. Also, the threshold displacement u_0 can be expressed as

$$u_0 = \frac{2\tau_0 L_e^2 (1+\eta)}{E_f d_f} + \sqrt{\frac{8G_d L_e^2 (1+\eta)}{E_f d_f}} \quad (3.29)$$

For the single-fiber pullout, V_f is so small that η is assumed to be negligible.

In determining the pullout load for each side, there are two scenarios, which are illustrated in Fig. 3.8. In either scenario, both sides of the fiber first undergo the debonding stage. This is the case when $\delta < 2u_{0S}$, where u_{0S} is the threshold displacement for the short-embedment side. Also, pullout displacements for the two sides are identical in this case (i.e. $u_L = u_S = \delta/2$). Thus, $P(\delta, L_e)$ is expressed as

$$P(\delta, L_e) = P_{debond} \left(\frac{\delta}{2} \right), \quad \delta < 2u_{0S} \quad (3.30)$$

Subsequently, in the first scenario, the short-embedment side enters the pullout stage, while the other side remains in the debonding stage. Mathematically, it is expressed as $\delta = u_L + u_S$ such that $u_S > u_{0S}$ and $u_L < u_{0L}$ where u_{0L} is the threshold displacement for the long-embedment side.

For this pullout-debonding case, $P(\delta, L_e)$ is given by

$$P(\delta, L_e) = P_{pullout}(u_S; L_e) = P_{debond}(u_L; L_f - L_e), \quad u_S > u_{0S} \quad \text{and} \quad u_L < u_{0L} \quad (3.31)$$

While the second scenario also has the pullout-debonding phase, the pullout load of the short-embedment side can exceed the peak debonding load of the long-embedment side, $P_{debond}(u_{0L})$.

Thus, for $\delta = u_L + u_S$ such that $u_S > u_{0S}$ and $u_L > u_{0L}$, both sides can undergo the pullout stage:

$$P(\delta, L_e) = P_{pullout}(u_S; L_e) = P_{pullout}(u_L; L_f - L_e), \quad u_S > u_{0S} \quad \text{and} \quad u_L > u_{0L} \quad (3.32)$$

This two-way fiber pullout occurs for fibers with a large slip-hardening coefficient β such as PVA fiber.

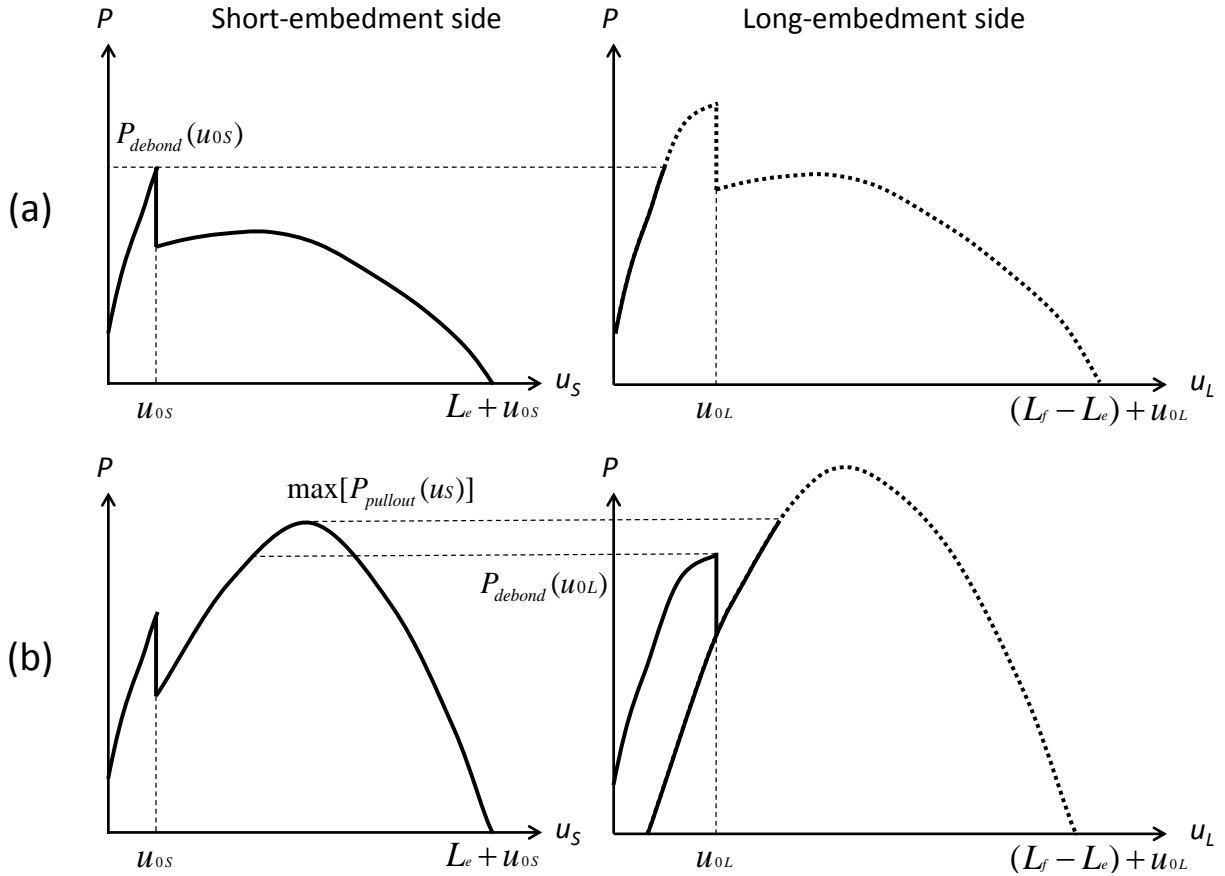


Fig. 3.8: (a) One-way pullout case; only the short-embedment side enters the pullout stage, while the other side remains in the debonding stage. (b) Two-way pullout case; the long-embedment side also undergo the pullout stage for $\delta = u_L + u_S$ such that $u_S > u_{0S}$ and $u_L > u_{0L}$.

Here, a slight refinement to the above model is introduced, regarding the pullout–debonding case (i.e. Eq. 3.31). As detailed in Appendix B, $P_{debond}(u)$ is derived by assuming the tunnel-crack propagation along the fiber/matrix interface, which initiates from the fiber free end. Based on this assumption, the long-embedment segment should have some debonded zone at the onset of the pullout-debonding phase. Then, unless further tunnel-crack propagation in the long-embedment side occurs in this phase, the P - u relationship should be modified for taking into account the debonded zone. However, the existing model assumes no hysteresis for the P - u relationship of the debonding side.

In this study, the following hysteresis curve is used for the debonding load in the pullout-debonding phase:

$$P_{debond}^h(u_L) = \frac{\pi E_f d_f^2}{4a'} u_L + \frac{\pi \tau_0 d_f (1 + \eta)}{2} a', \quad 0 < u_L < u'_L \quad (3.33)$$

a' is the length of the debonded zone and can be obtained by solving the following quadratic equation:

$$\frac{\pi \tau_0 d_f (1 + \eta)}{2E_f} a'^2 - \frac{P_{debond}(u'_L)}{E_f} a' + \frac{\pi d_f^2 u'_L}{4} = 0 \quad (3.34)$$

where u'_L is the maximum pullout displacement of the debonding side in the preceding loading history. It should be noted that, during further tunnel-crack propagation (i.e. $u_L > u'_L$), the debonding load is given by Eq. 3.27, as in the original model.

Figure 3.9 shows the proposed hysteresis in the P - u relationship. Parameters used for the plot are those for a standard ECC (M45) [15], and a' has been supposed to be the same as the short-embedment length L_s , which is 4 mm here. As can be seen, the difference between P_{debond} and

P_{debond}^h becomes more significant as the pullout displacement gets smaller. Nevertheless, the effect of this modification on the composite tensile property (i.e. σ - δ relation) is negligible; this might be attributed to the fact that the pullout-debonding phase is not predominant in M45. Conversely, the effect of the modification could be significant for composites with higher chemical bond. Detailed discussion on this is presented in Appendix C, as well as the derivation of this modification.

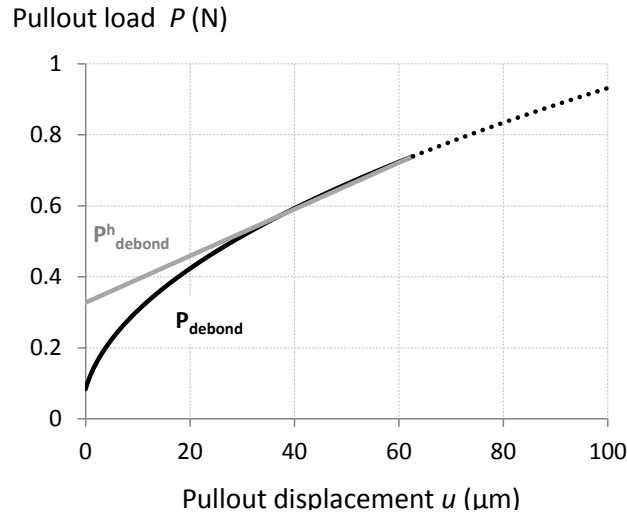


Fig. 3.9: Proposed hysteresis of the debonding curve for a standard ECC (M45).

(ii) $p_1(\phi)$ and $p_2(z)$

As mentioned in Section 2.2.2, $p_1(\phi)$ and $p_2(z)$ are probability density functions (PDFs) of fiber inclination angle and fiber-centroid location, respectively. These two PDFs account for the random distribution of discontinuous fibers in the composite. When fibers are randomly oriented with uniform distribution, $p_1(\phi)$ and $p_2(z)$ are expressed as

$$p_1(\phi) = \begin{cases} \frac{\sin(\phi)}{\cos(\phi_0) - \cos(\phi_1)} & \text{for 3D distribution} \\ \frac{1}{\phi_1 - \phi_0} & \text{for 2D distribution} \end{cases}, \quad 0 \leq \phi_0 \leq \phi \leq \phi_1 \leq \frac{\pi}{2} \quad (3.35)$$

$$p_2(z) = \frac{2}{L_f}, \quad 0 \leq z \leq \frac{L_f}{2} \quad (3.36)$$

It should be noted that, depending on the specimen geometry and processing method, the fiber inclination angle ϕ might be limited to the range of ϕ_0 to ϕ_1 , as indicated in the bounds of the double integral in Eq. 3.25. Derivations of these formulae can be found in [16].

(iii) Matrix micro-spalling

When an inclined fiber is pulled out from the mortar matrix, stress concentration can occur at the bearing point, leading to local failure of the matrix. This phenomenon is often observed in brittle matrices with low tensile strength. As a result of this matrix micro-spalling, the fiber inclination angle gets smaller, while the crack opening becomes larger, as illustrated in Fig. 3.10. Then, the modified inclination angle (ϕ') and corresponding effective crack opening (δ_{eff}) can be expressed as [17]

$$\phi' = \sin^{-1}\left(\frac{\delta \sin \phi}{\delta'}\right) \quad (3.37)$$

$$\delta_{eff} = \delta' - 2s \quad (3.38)$$

where

$$\delta' = \sqrt{4s^2 + 4s\delta \cos \phi + \delta^2} \quad (3.39)$$

and

$$s = \frac{P \sin\left(\frac{\phi}{2}\right)}{kd_f \sigma_m \cos^2\left(\frac{\phi}{2}\right)} \quad (3.40)$$

Here, s is the size of the spalled matrix piece, P is the pullout load of the fiber, k is the spalling coefficient, and σ_m is the matrix tensile strength. Derivations of these semi-empirical equations can be found in [17]. To experimentally determine k , the actual spalling size (s) may be measured in the single-fiber pullout test, from which k can be calculated based on Eq. 3.40. In the σ - δ simulation, δ_{eff} and φ' replace the original δ and φ , and the fiber pullout load is updated based on the modification.

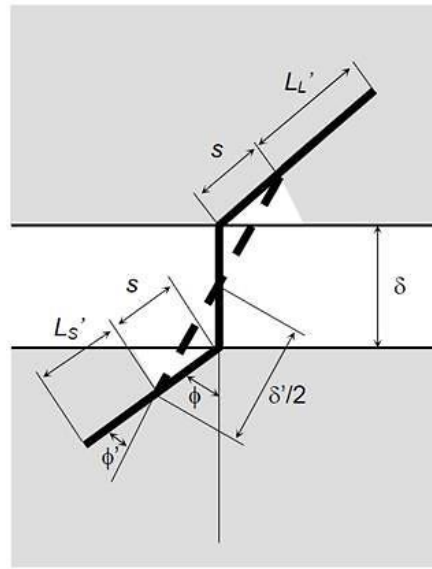


Fig. 3.10: Schematic illustration of matrix micro-spalling [17].

(iv) *Cook-Gordon effect*

When a steady-state matrix crack propagates toward an embedded fiber, debonding of premature fiber/matrix interface can occur even before the crack tip reaches the interface [18] (Fig. 3.11). Stretching of the debonded segment (α) causes additional crack opening δ_{cg} , which may be estimated as

$$\delta_{cg} = \frac{4\alpha P}{\pi d_f^2 E_f} \quad (3.41)$$

Here, α is typically expected to be multiples of the fiber diameter d_f . Details can be found in a study by Li *et al.* [19]. Based on experimental results, they suggested that Eq. 3.41 is applicable to all fibers regardless of the inclination angle φ . Thus, the total crack opening $\delta_{total} = \delta + \delta_{cg}$ simply replaces the δ (may have been updated by the matrix micro-spalling consideration) in the σ - δ simulation.

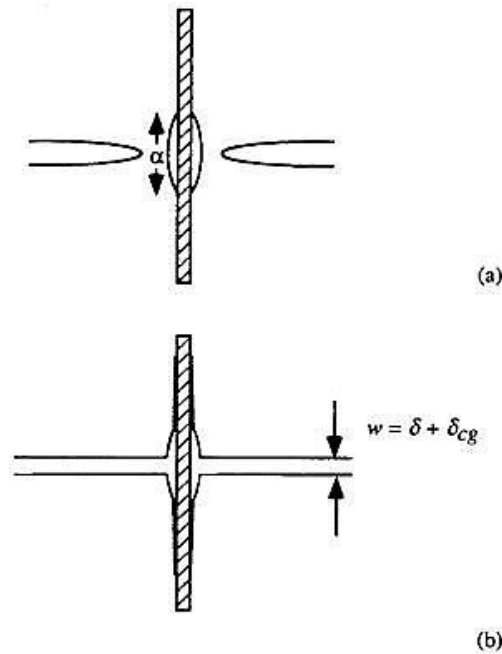


Fig. 3.11: Schematic illustration of Cook-Gordon effect [19]. (a) Matrix crack approaching an embedded fiber triggers debonding of the premature fiber/matrix interface, (b) which results in additional crack opening δ_{cg} .

3.3.3 Analytical simulation

Based on the analytical model detailed above, the σ - δ relation can be simulated by using micromechanical parameters as the inputs. Due to the complexity of the model, numerical analysis is typically used to compute the σ - δ curve. Figure 3.12 shows a flow chart of the computation, which was originally proposed by Yang *et al.* [15].

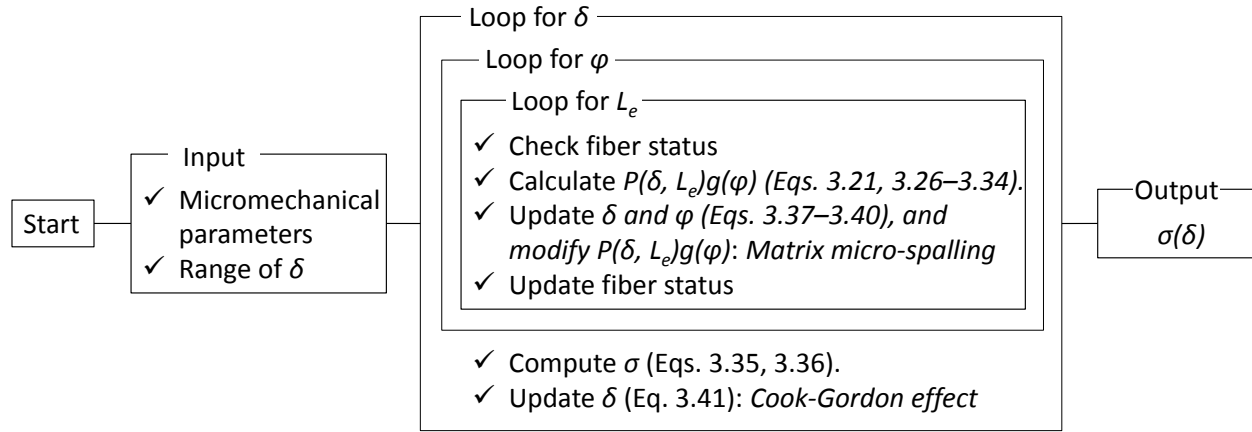


Fig. 3.12: Flow chart of numerical simulation of σ - δ curve.

The computation starts with inputting micromechanical parameters and the range of crack opening (δ), for which the composite fiber-bridging stress (σ) is computed. The maximum δ may be half of the fiber length (L_f).

The next step is to calculate σ for a given δ in loop calculation. The loop computes and averages pullout loads of individual fibers, varying the fiber embedment length (L_e) and fiber inclination angle (φ). Thus, there are two loops inside the loop for δ : one for L_e and the other for φ . For efficient computation, each step in the loop starts with checking the fiber status; if a single fiber with given L_e and φ has been already pulled out or broken in the preceding step, its pullout force is not calculated in the following steps. Otherwise, $P(\delta, L_e)g(\varphi)$ is computed based on Eqs. 3.21 and 3.26–3.34, and corresponding fiber status is determined: the computed pullout displacement (u_s) is compared with L_e to check the fiber pullout, and $P(\delta, L_e)g(\varphi)$ with the in-situ fiber strength (Eq. 3.23) to check the fiber rupture. Here, if the matrix micro-spalling is taken into account, then δ and φ are updated based on Eqs. 3.37–3.40, and $P(\delta, L_e)$ and the fiber status are modified accordingly.

After completing the loops for L_e and φ , the composite bridging stress σ is computed by averaging the computed pullout loads of effective bridging fibers, based on Eqs. 3.35 and 3.36. Also, if the Cook-Gordon effect is included, Eq. 3.41 is used to modify δ . Then, the final σ - δ curve is obtained by completing the loop for δ . As an example, Fig. 3.13 shows the simulated σ - δ curve of M45.

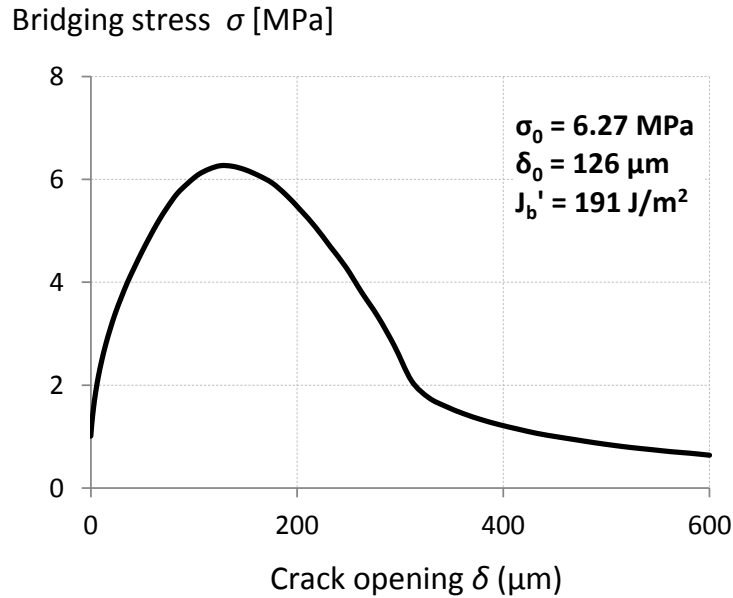


Fig. 3.13: Simulated σ - δ curve of ECC M45 (input data from [15]). Three-dimensional uniform fiber distribution was assumed, and both matrix micro-spalling and Cook-Gordon effect were included.

The σ - δ simulation provides lots of insights on the composite design; along with the experimentally determined σ_{ci} and J_{tip} , the strength- and energy-based criteria (Eqs. 3.14 and 3.15) can be checked for the developed matrix and selected fiber. Here, the ratios of σ_0/σ_{ci} and J_b'/J_{tip} – pseudo strain-hardening (PSH) index for strength and energy, respectively – are calculated to check if both are greater than unity. For achieving robust tensile strain-hardening of the composite, Kanda and Li suggested to use $\sigma_0/\sigma_{ci} \geq 1.3$ and $J_b'/J_{tip} \geq 2.7$, due to the material variability caused by the random matrix flaw size and fiber dispersion [20]. If either criterion is

violated, then the analytical simulation guides the required modification on micromechanical parameters by manipulating the inputs in the computation. In addition, optimization of the subsequent environmental design can be complemented; for example, the simulation can find the minimum fiber volume fraction to satisfy the criteria, which is beneficial for the enhanced environmental performance.

3.3.4 Confirmation experiment

To verify the optimum composite design predicted by the σ - δ simulation, confirmation experiment is conducted. The simplest way is to conduct the JSCE dog bone testing (detailed in Section 3.3.1) on composite specimens; the test checks if the desired composite tensile properties – strain-hardening behavior, high tensile ductility, and multiple tight cracking – have been achieved. Another way is to conduct the single-crack test proposed by Fischer and co-workers [21–23] (Fig. 3.14). In this test, a notched uniaxial-tension specimen is loaded to deliberately create a single crack in the notched section. The obtained stress-strain curve is a direct measurement of the σ - δ relation. This method is useful to validate the σ - δ simulation and identify required modification on the analysis or input data.

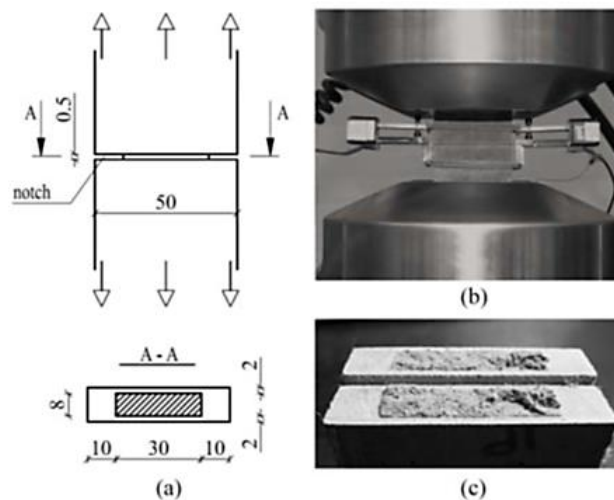


Fig. 3.14: Single-crack test: (a) specimen geometry, (b) test setup, and (c) fracture plane after testing [23].

In this section, experimental and analytical methods used in the composite-design stage have been detailed. With the aid of the micromechanics-based design technique, strain-hardening ductile EGC can be systematically developed. Then, in the subsequent environmental design stage, the material sustainability of the developed composite is evaluated.

3.4 Environmental assessment

The final stage of the proposed integrated design is the assessment of the material greenness. In this study, Material Sustainability Indices (MSI) are used to quantify environmental impacts associated with production of the developed composite. Here, as an example, the material greenness of a preliminary version of EGC developed in a previous study is evaluated, with respect to the energy and carbon intensity. The calculation of MSI values for ECC has been detailed in [24].

The environmental impact categories to investigate are first specified. Here, *embodied-energy consumption* and *global warming intensity* (GWI) are used. The embodied energy includes both the *process energy*, which is electricity and fuel directly used in material production, and the *feedstock energy*, which represents organic resource inputs that comprise the material, rather than being used as a fuel. The feedstock energy is significant especially in plastics (i.e. organic polymers) in which petroleum-based inputs are the primary constituent. For geopolymer materials, GWI (i.e. carbon dioxide (CO₂)-equivalent emission) is often used to show the advantage of the materials compared to cement-based counterparts. Other impact categories – acidification potential (AP), eutrophication potential (EP), water consumption, solid waste generated, and so forth – may be crucial, depending on the application of the material.

Next, life-cycle inventory (LCI) data are collected for all ingredients of the developed composite. The LCI data account for all inputs (energy and natural resources) and outputs (solid waste and air pollutants generated) associated with raw-material acquisition, processing and manufacturing of each ingredient. While there are a number of data sources available for various materials, reliable data must be selected; specifically, reasonable and consistent system boundaries (the range of processes and phases included in the calculation) are important. Among various databases, *ecoinvent*, originally developed by the Swiss Centre for Life Cycle Inventories, is one of the most-cited [25]. The database covers many areas, including energy supply, agriculture, transport, biomaterials, chemicals, construction materials, and waste treatment, with 12,800 LCI datasets. The data are typically calculated for the average conditions of European industries. Meanwhile, for the US industries, US National Renewable Energy Laboratory (NREL) offers a comprehensive database for various materials and processes [26]. Also, the Portland Cement Association (PCA) provides extensive LCI data for concrete ingredients, including portland cement, aggregate, supplementary cementitious materials (e.g. fly ash, slag, and silica fume) and admixtures [27].

For the GWI evaluation, the LCI emission data of various greenhouse gasses need to be converted into a single category indicator (i.e. CO₂-equivalent emission). For this purpose, the characterization model and corresponding characterization factor are specified. In this example, the ICPP 2013 model and the 100-year Global Warming Potential (GWP) values are used [28]. The weighting values of the characterization factor are shown in Table 3.5. Then, based on the LCI data and weighting factors, the total GWI value is determined for each ingredient. Table 3.6 lists an example dataset for ingredients of EGC.

Table 3.5: 100-year GWP values of greenhouse gasses [28].

Greenhouse gas	100-year GWP* (kg CO ₂ -eq/kg)
Carbon dioxide (CO ₂)	1
Methane (CH ₄)	28
Hydrofluorocarbon (HFC-134a)	1300
Chlorofluorocarbon (CFC-11)	4660
Nitrous oxide (N ₂ O)	265
Carbon tetrafluoride (CF ₄)	6630

* Climate-carbon feedbacks are not included. Details can be found in [28].

Table 3.6: Life-cycle inventory data of EGC ingredients.

Ingredients [data source]	Embodied energy (MJ/kg)	GWI (kg CO ₂ -eq/kg)
Fly ash [27]	0.11	0.0074
Fine silica sand [29]	0.17	0.025
Sodium silicate (3.3WR, 37% solids) [30]	4.6	0.43
Sodium hydroxide pellets [31]	18	0.86
Water *	0	0
PVA fiber [32]	101	3.4

* Assumed negligible.

From the converted inventory data and mix proportions of ingredients, the energy- and carbon-MSI values of the preliminary EGC can be calculated. Here, the embodied energy and GWI associated with a unit volume of the EGC are computed. Table 3.7 presents the mix design and computed embodied energy and GWI. Following the procedures presented above, MSI of the optimized EGC can be also calculated. Then, by comparing their MSI values, the degree of improvement in material greenness can be quantified. In addition, if further improvement is required, the matrix- and composite-design stages can be revisited to do the iterative design process.

Table 3.7: Mix design and computed energy- and carbon-MSI of preliminary EGC.

Ingredient	Mix design (kg/m ³)	Embodied energy (GJ/m ³)	GW (kg CO ₂ -eq/m ³)
Fly ash	1131	0.12	8.4
Fine silica sand	340	0.06	8.5
Sodium silicate	289	1.34	125.2
Sodium hydroxide	63.5	1.15	54.6
Water	179	0	0
PVA fiber	26	2.63	88.4
Total		5.29	285

3.5 Summary

This chapter has documented the detailed procedures of the proposed integrated design method for EGC. There are three stages in the EGC design: matrix development, composite design, and environmental assessment.

The EGC design starts with the matrix-design stage. Here, Taguchi's Design of Experiment (DOE) technique is used to develop an optimum EGC matrix that meets required engineering properties or has desired added functions. Specifically, orthogonal arrays (OA) aid the design of efficient fractional-factorial experiments, and the Analysis of Variance (ANOVA) statistically analyze the obtained experimental results to determine significance of design variables. Based on the ANOVA result and complementary main-effect plots, an optimum EGC-matrix design can be identified by choosing appropriate levels of the significant factors. Besides, factors that have been determined to be insignificant can be used to complement optimization in other design stages.

In the subsequent composite-design stage, the micromechanical modeling is used to systematically tailor the fiber and fiber/matrix interface properties. First, micromechanical

parameters for the developed matrix, selected fiber and their interface are measured by various experimental techniques. Then, the analytical model simulates the composite σ - δ relation by using the measured micromechanical parameters as the inputs. The simulation result guides required modification on the parameters to satisfy the two criteria for achieving the steady-state multiple cracking characteristic. Also, by determining the minimum fiber volume content to satisfy the criteria, the σ - δ simulation can complement optimization in the environmental design stage.

For the optimized EGC, the overall material greenness is evaluated in the environmental design stage. Here, Material Sustainability Indices (MSI) are used to quantify environmental impacts of the material production. Particularly, embodied-energy consumption and global warming potential are focused for EGC materials, but other impact categories may be of concern, depending on the application. By comparing the MSI values of the optimized EGC with those of other counterparts (preliminary EGC, normal concrete, ECC, etc.), the degree of improvement in material greenness can be quantified. If further improvement is required, another round of experiment/analysis can be conducted in the matrix- and composite-design stages to do the iterative design process.

With the aid of the proposed integrated design method, EGC materials can be systematically designed. Thus, this comprehensive design method can facilitate the research and development in both the academic and industrial communities. To demonstrate the applicability and effectiveness of the design method, an optimized EGC is developed in the following chapter.

References

- [1] G. Taguchi, *System of experimental design: engineering methods to optimise quality and minimize cost*. White Plains, New York: UNIPUB/Kraus International Publications, 1987.
- [2] V. C. Li, “Engineered Cementitious Composites (ECC) – Tailored Composites through Micromechanical Modeling,” in *Fiber reinforced concrete: present and future*, N. Banthia, A. Bentur, and A. A. Mufti, Eds. Montreal (Canada): Canadian Society for Civil Engineering, 1998, pp. 64–97.
- [3] G. A. Keoleian, A. M. Kendall, M. D. Lepech, and V. C. Li, “Guiding the design and application of new materials for enhancing sustainability performance: Framework and infrastructure application,” *Mater. Res. Soc. Symp. Proc.*, vol. 895, 2006.
- [4] “Confirmation Experiment,” in *Taguchi techniques for quality engineering*:, 2nd ed., New York, NY: McGraw Hill Professional, 1996, pp. 181–201.
- [5] P. J. Ross, *Taguchi techniques for quality engineering: loss function, orthogonal experiments, parameter and tolerance design*, Second. New York, NY: McGraw Hill Professional, 1996.
- [6] Japan Society of Civil Engineers, *Recommendations for Design and Construction of High Performance Fiber Reinforced Cement Composites with Multiple Fine Cracks (HPFRCC)* , vol. 82. Tokyo, Japan: JSCE, 2008.
- [7] ASTM E399-12e3, *Standard Test Method for Linear-Elastic Plane-Strain Fracture Toughness K_{IC} of Metallic Material*. West Conshohocken, PA: ASTM International, 2012.
- [8] A. Katz and V. Li, “A Special Technique for Determining the Bond Strength of Carbon Fibers in Cement Matrix by Pullout Test,” *J. Mater. Sci. Lett.*, vol. 15, no. 20, pp. 1821–1823, 1996.
- [9] Z. Lin, T. Kanda, and V. Li, “On interface property characterization and performance of fiber-reinforced cementitious,” *Concr. Sci. Eng.*, vol. 1, no. September, pp. 173–174, 1999.
- [10] Z. Lin and V. Li, “Crack bridging in fiber reinforced cementitious composites with slip-hardening interfaces,” *J. Mech. Phys. Solids*, vol. 45, no. 5, pp. 763–787, 1997.
- [11] J. Morton and G. W. Groves, “The effect of metal wires on the fracture of a brittle-matrix composite,” *J. Mater. Sci.*, vol. 11, no. 4, pp. 617–622, 1976.
- [12] V. C. Li, Y. Wang, and S. Backer, “Effect of inclining angle, bundling and surface treatment on synthetic fibre pull-out from a cement matrix,” *Composites*, vol. 21, no. 2, pp. 132–140, 1990.
- [13] T. Kanda and V. C. Li, “Interface Property and Apparent Strength of High-Strength Hydrophilic Fiber in Cement Matrix,” *Journal of Materials in Civil Engineering*, vol. 10, no. 1, pp. 5–13, 1998.

- [14] C. Wu, “Micromechanical Tailoring of PVA-ECC for Structural Applications,” University of Michigan, 2001.
- [15] E.-H. Yang, S. Wang, Y. Yang, and V. C. Li, “Fiber-Bridging Constitutive Law of Engineered Cementitious Composites,” *J. Adv. Concr. Technol.*, vol. 6, no. 1, pp. 181–193, 2008.
- [16] Y. Wang, S. Backer, and V. Li, “A statistical tensile model of fibre reinforced cementitious composites,” *Composites*, vol. 20, no. 3, pp. 265–274, 1989.
- [17] S. Wang, “Micromechanics based matrix design for engineered cementitious composites,” University of Michigan, Ann Arbor, 2005.
- [18] J. Cook, J. E. Gordon, C. C. Evans, and D. M. Marsh, “A mechanism for the control of crack propagation in all-brittle systems,” *Proc. R. Soc. London A Math. Phys. Eng. Sci.*, vol. 282, no. 1391, pp. 508–520, 1964.
- [19] V. Li, H. Stang, and H. Krenchel, “Micromechanics of crack bridging in fibre-reinforced concrete,” *Mater. Struct.*, vol. 26, pp. 486–494, 1993.
- [20] T. Kanda and V. C. Li, “Practical Design Criteria for Saturated Pseudo Strain Hardening Behavior in ECC,” *J. Adv. Concr. Technol.*, vol. 4, no. 1, pp. 59–72, 2006.
- [21] G. Fischer, H. Stang, and L. Dick-Nielsen, “Initiation and development of cracking in ECC materials: Experimental Observations and modeling,” in *6th International Conference on Fracture Mechanics of Concrete and Concrete Structures*, 2007, pp. 1517–1522.
- [22] E. Pereira, G. Fischer, J. A. O. Barros, and M. Lepech, “Crack formation and tensile stress-crack opening behavior of Fiber Reinforced Cementitious Composites (FRCC),” in *7th International Conference on Fracture Mechanics of Concrete and Concrete Structures (FramCoS 7)*, 2010, pp. 1638–1647.
- [23] I. Paegle and G. Fischer, “Evaluation of test methods used to characterize fiber reinforced cementitious composites,” *Proc. Int. Conf. „Innovative Mater. Struct. Technol.*, pp. 122–128, 2013.
- [24] M. D. Lepech, V. C. Li, R. E. Robertson, and G. A. Keoleian, “Design of green engineered cementitious composites for improved sustainability,” *ACI Mater. J.*, vol. 105, no. 6, pp. 567–575, 2008.
- [25] The Swiss Centre for Life Cycle Inventories, “Ecoinvent.” [Online]. Available: <http://www.ecoinvent.org/home.html>. [Accessed: 28-Jul-2017].
- [26] NREL, “U.S. Life Cycle Inventory Database,” 2012. [Online]. Available: <https://www.lcacommons.gov/nrel/search>. [Accessed: 28-Jul-2017].
- [27] M. A. Nisbet, M. L. Marceau, and M. G. Vangeem, *Environmental Life Cycle Inventory of Portland Cement Concrete*. Stokie, IL: Portland Cement Association, 2002.

- [28] G. Myhre, D. Shindell, F. Bréon, W. Collins, J. Fuglestvedt, J. Huang, D. Koch, J. Lamarque, D. Lee, B. Mendoza, T. Nakajima, A. Robock, G. Stephens, T. Takemura, and H. Zhang, “Anthropogenic and natural radiative forcing,” in *Climate Change 2013: The Physical Science Basis, Working Group I Contribution to the Fifth Assessment Report of the Intergovernmental Panel on Climate Change*, T. F. Stocker, D. Qin, G.-K. Plattner, M. Tignor, S. K. Allen, J. Boschung, A. Nauels, Y. Xia, V. Bex, and P. M. Midgley, Eds. Cambridge (UK): Cambridge University Press, 2013, p. 714.
- [29] R. Ranade, “Advanced Cementitious Composite Development for Resilient and Sustainable Infrastructure,” University of Michigan, Ann Arbor, 2014.
- [30] M. Fawer, M. Concannon, and W. Rieber, “Life cycle inventories for the production of sodium silicates,” *Int. J. Life Cycle Assess.*, vol. 4, no. 4, pp. 207–212, 1999.
- [31] Euro Chlor, “An Eco-profile and Environmental Product Declaration of the European Chlor-Alkali Industry,” 2013. [Online]. Available: https://www1.ethz.ch/ifu/ESD/education/master/AESEEA/Euro_Chlor_Eco-profile_Chlorine_2014-03.pdf. [Accessed: 10-Mar-2017].
- [32] R. Frazão and R. Fernandes, *Comparative Analysis of the Life Cycle of AT Fibre-cement and NT Fibre-cement*. International Chrysotile Association, 2004.

CHAPTER 4: Application of Integrated Design Method

This chapter reports analytical and experimental investigations to demonstrate the applicability and effectiveness of the proposed integrated design method. Optimized EGC with enhanced compressive strength, high tensile ductility, and lower energy and carbon footprints is developed.

4.1 Preliminary study

Before the development of the integrated design method, a preliminary study was conducted to confirm the feasibility of ductile fiber-reinforced geopolymer composites. The matrix design was determined from the literature of fly ash-based geopolymers (FAGP) and several trial mixings, such that good workability and setting time of the fresh paste were achieved. Polyvinyl alcohol (PVA) fiber at a volume fraction of 2% was used, which is the most common reinforcement in current ECC materials. To measure mechanical properties of the composite, uniaxial compressive and tensile tests were conducted. In addition, crack patterns were measured and visualized by using the Digital Image Correlation (DIC) technique [1]. Detailed information on the materials and methods can be found in [2].

Table 4.1 lists the compressive and tensile strengths, and tensile ductility of the composite. The tensile stress-strain curves of four specimens in the same series are shown in Fig. 4.1. As can be seen, the distinct strain-hardening behavior was observed in all specimens. The achieved tensile ductility of 4.3% on average is as high as ECC materials, and several hundred times that of

normal concrete. In addition, saturated multiple microcracks were confirmed by the DIC analysis; the computed average crack width was less than 50 μm , even at a high imposed tensile strain of over 4%. The summary of crack patterns is presented in Table 4.2, and visualized strain maps of a uniaxial-tension specimen are shown in Fig. 4.2.

Table 4.1: Mechanical properties of preliminary EGC.

Compressive strength (MPa)	Tensile strength (MPa)	Tensile ductility (%)
27.6 ± 1.7	3.4 ± 0.5	4.3 ± 0.3

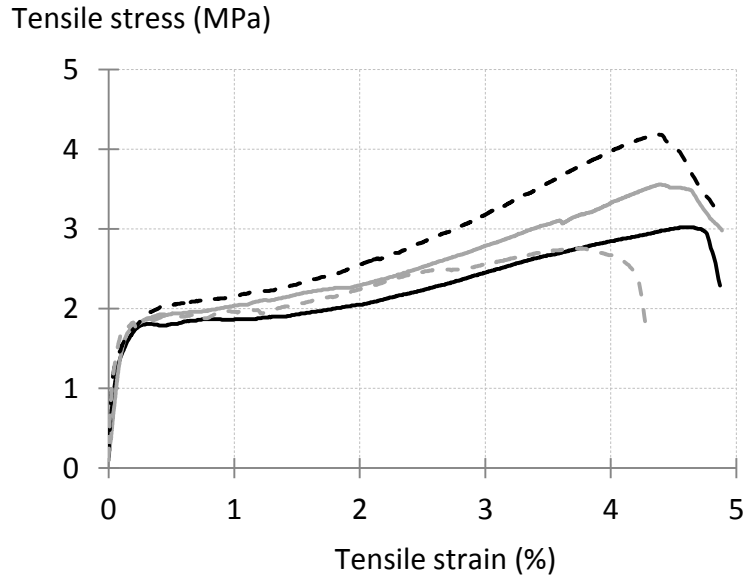


Fig. 4.1: Stress-strain curves of preliminary EGC specimens under uniaxial tension.

Table 4.2: Number of cracks and crack width of preliminary EGC at various strain levels.

Strain level (%)	Number of cracks	Maximum crack width (μm)	Average crack width (μm)
1.0	12	79	47 ± 17
2.0	27	83	43 ± 17
3.0	36	92	47 ± 19
4.0	43	100	45 ± 22
4.5	45	117	45 ± 23

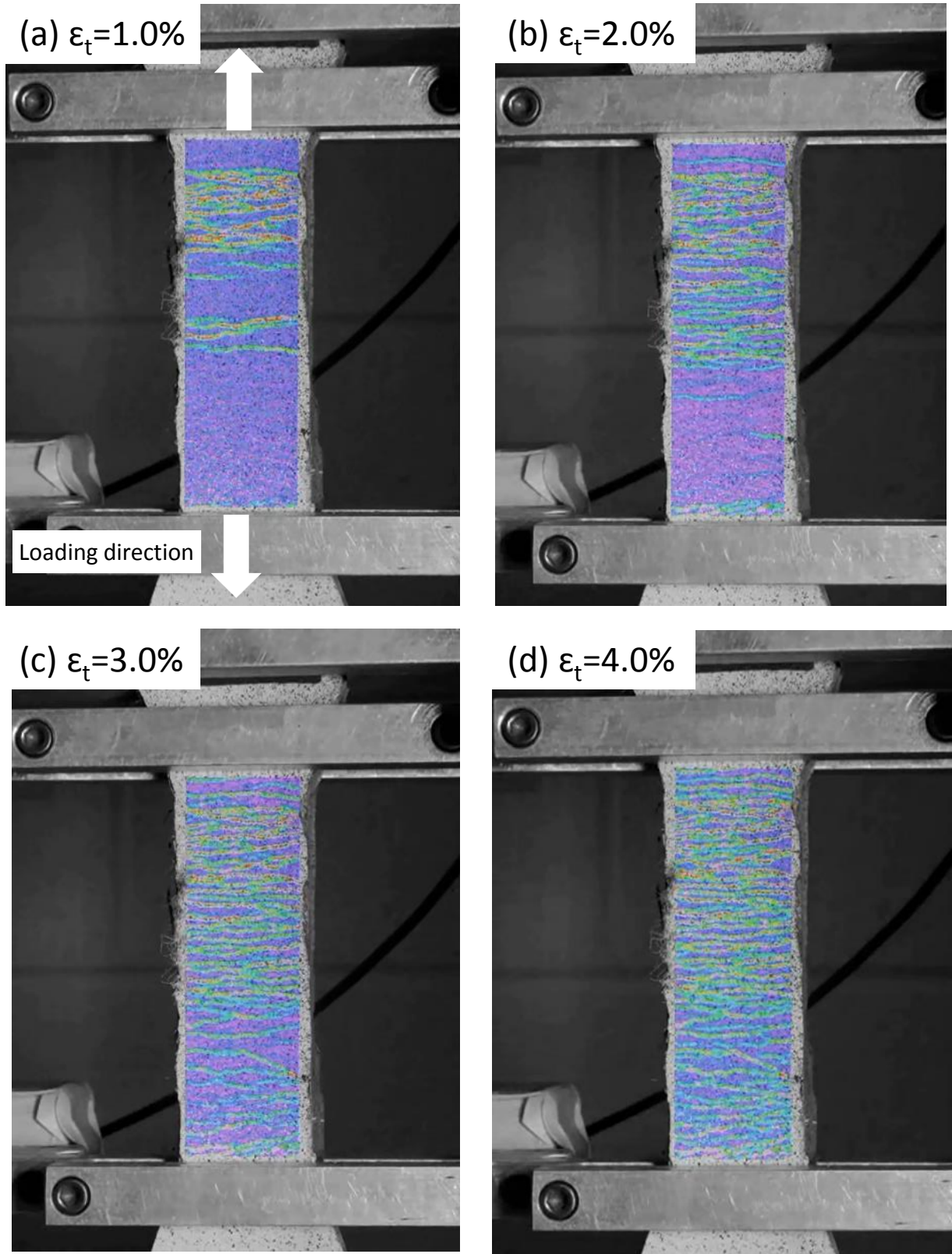


Fig. 4.2: Strain maps obtained from the DIC analysis. Multiple-crack formation at progressively increased imposed strain was visualized.

While the desired tensile properties could be achieved in the preliminary version of EGC, its compressive strength was relatively low compared to ECC. The lower strength might limit the range of possible applications of the material, especially in large-scale structural applications. Moreover, the material was not optimized with respect to the material greenness.

In the following sections, the proposed integrated design method is applied to the preliminary version of EGC so as to simultaneously achieve three objectives: to (i) improve the compressive strength, (ii) maintain the high tensile ductility and tight-cracking characteristics, and (iii) lower the energy and carbon footprints of the EGC.

4.2 Matrix development

A DOE study was first conducted to develop an optimized EGC matrix with higher compressive strength. Types of ingredients, mixing and casting methods, and curing conditions of the preliminary EGC are used as a basis. In this study, the mix proportion of ingredients is mainly optimized.

4.2.1 Materials and testing methods

Table 4.3 presents the mix proportion of the preliminary EGC matrix. Two types of fly ash were blended in the mixture: one from the W.H. Sammis power plant in Stratton, Ohio (labeled “Fly ash A”), and the other from a power plant in Monroe, Michigan (labeled “Fly ash B”). Both of them are classified as class F fly ash as designated by ASTM C 618 [3]. Table 4.4 lists their chemical compositions and physical properties reported by the manufacturer. F-75 Ottawa silica sand (US Silica) was used as aggregate. As in ECC, coarse aggregate was not used since it tends to increase the matrix fracture toughness, which is a disadvantage in achieving steady-state

multiple cracking (See Section 3.3.1). The alkaline activator was prepared by dissolving laboratory-grade sodium hydroxide (NaOH) pellets (Fischer Chemical) in mixture of sodium silicate solution (PQ Corporation, Type N – Na₂SiO₃ with 8.9 wt% Na₂O, 28.7 wt% SiO₂, and 62.5 wt% H₂O) and tap water (labeled “Pre-mix water” in Table 4.3). The solution preparation was done at least 24 hours before its use as the activator so that chemical equilibrium is attained, as suggested by Davidovits [4]. Additional water (labeled “Mix water”) was used when mixed with solid materials (i.e. fly ash and silica sand) so that the rheology of the fresh mortar becomes similar to that of a standard ECC.

Table 4.3: Mix proportion of preliminary EGC matrix (by mass).

Fly ash A (Sammis)	Fly ash B (Monroe)	Sand	Na ₂ SiO ₃	NaOH (pellet)	Pre-mix water	Mix water
0.8	0.2	0.3	0.256	0.056	0.039	0.12

Table 4.4: Chemical compositions (mass %) and physical properties of fly ash.

	Fly ash A (Sammis)	Fly ash B (Monroe)
SiO ₂	46.09	42.20
Al ₂ O ₃	23.15	22.51
Fe ₂ O ₃	19.48	9.20
CaO	5.08	15.66
SO ₃	0.77	1.85
MgO	1.12	3.20
Na ₂ O	0.58	0.98
K ₂ O	1.73	1.53
Moisture	0.16	0.12
Loss on ignition	1.99	1.34
density (g/cm ³)	2.58	2.53
Fineness (% retained on 45 μm sieve)	22.24	16.58

Fly ash and silica sand were first dry-mixed for 2 minutes. The activator solution and mix water were then added to the mixture. After the fresh mortar reached the desired rheological state, the mixture was cast into molds on a vibration table, and cured at room temperature (23 ± 3 °C) for

24 hours. Subsequently, the hardened specimens were cured in an oven at 60 °C for another 24 hours, followed by air curing at room temperature until testing.

To measure the compressive strength, three 2-inch (51-mm) cube specimens were prepared for each mix proportion and subjected to uniaxial compression with the loading rate of 50 ± 10 psi/s (0.34 ± 0.07 MPa/s). The test was conducted at the specimen age of 28 days.

4.2.2 Design of Experiment

In this study, six ratios of the ingredients by mass were investigated as the design variables:

- (1) $FA_{(B)} / FA$ – ratio of fly ash B to the total amount of fly ash (i.e. fly ash A plus B)
- (2) S / FA – ratio of silica sand to FA
- (3) Alk / FA – alkaline activator-to-FA ratio where Alk is the total amount of Na_2SiO_3 solution, NaOH pellets, and pre-mix water
- (4) $Na_2SiO_3 / NaOH_{(sol)}$ – ratio of Na_2SiO_3 to NaOH solution where $NaOH_{(sol)}$ is the total amount of NaOH pellets and pre-mix water
- (5) $Pre-W / NaOH_{(sol)}$ – reflecting the concentration of NaOH solution where Pre-W is the amount of pre-mix water, and
- (6) $Mix-W / FA$ – ratio of mix water to FA, which affects the rheology of the mixture.

In the preliminary EGC matrix, those six ratios were (1) 0.2, (2) 0.3, (3) 0.35, (4) 2.7, (5) 0.41, and (6) 0.12, respectively. To quantify individual effects of the six factors, three different factor levels were considered for each mixing ratio, meaning that there were $3^6 = 729$ possible combinations.

The L18 orthogonal array was used in this study to assign the six factors with three levels each. The factor levels and corresponding absolute values of each mixing ratio are shown in Table 4.5.

Table 4.5: L18 orthogonal array for EGC-matrix development.

Mix no.	Assigned factors, their absolute values and codes (levels)							
	–	–	FA _(B) / FA	S / FA	Alk / FA	Na ₂ SiO ₃ / NaOH _(sol)	Pre-W / NaOH _(sol)	Mix-W / FA
1	(1)	(1)	0.2 (1)	0.2 (1)	0.30 (1)	2.4 (1)	0.31 (1)	0.10 (1)
2	(1)	(1)	0.3 (2)	0.3 (2)	0.35 (2)	2.7 (2)	0.41 (2)	0.12 (2)
3	(1)	(1)	0.4 (3)	0.4 (3)	0.40 (3)	3.0 (3)	0.51 (3)	0.14 (3)
4	(1)	(2)	0.2 (1)	0.2 (1)	0.35 (2)	2.7 (2)	0.51 (3)	0.14 (3)
5	(1)	(2)	0.3 (2)	0.3 (2)	0.40 (3)	3.0 (3)	0.31 (1)	0.10 (1)
6	(1)	(2)	0.4 (3)	0.4 (3)	0.30 (1)	2.4 (1)	0.41 (2)	0.12 (2)
7	(1)	(3)	0.2 (1)	0.3 (2)	0.30 (1)	3.0 (3)	0.41 (2)	0.14 (3)
8	(1)	(3)	0.3 (2)	0.4 (3)	0.35 (2)	2.4 (1)	0.51 (3)	0.10 (1)
9	(1)	(3)	0.4 (3)	0.2 (1)	0.40 (3)	2.7 (2)	0.31 (1)	0.12 (2)
10	(2)	(1)	0.2 (1)	0.4 (3)	0.40 (3)	2.7 (2)	0.41 (2)	0.10 (1)
11	(2)	(1)	0.3 (2)	0.2 (1)	0.30 (1)	3.0 (3)	0.51 (3)	0.12 (2)
12	(2)	(1)	0.4 (3)	0.3 (2)	0.35 (2)	2.4 (1)	0.31 (1)	0.14 (3)
13	(2)	(2)	0.2 (1)	0.3 (2)	0.40 (3)	2.4 (1)	0.51 (3)	0.12 (2)
14	(2)	(2)	0.3 (2)	0.4 (3)	0.30 (1)	2.7 (2)	0.31 (1)	0.14 (3)
15	(2)	(2)	0.4 (3)	0.2 (1)	0.35 (2)	3.0 (3)	0.41 (2)	0.10 (1)
16	(2)	(3)	0.2 (1)	0.4 (3)	0.35 (2)	3.0 (3)	0.31 (1)	0.12 (2)
17	(2)	(3)	0.3 (2)	0.2 (1)	0.40 (3)	2.4 (1)	0.41 (2)	0.14 (3)
18	(2)	(3)	0.4 (3)	0.3 (2)	0.30 (1)	2.7 (2)	0.51 (3)	0.10 (1)

The L18 orthogonal array can accommodate 1 two-level factor and 7 three-level factors, testing only 18 combinations. The advantage in use of the L18 orthogonal array is the more reliable evaluation on main effects of factors; in some types of orthogonal arrays and their arrangements, interaction effects between factors are confounded with a specific factor effect, which might result in misevaluation on the main effect. In contrast, in the L18 orthogonal array, all interaction effects are almost evenly spread across main-factor effects, allowing more accurate evaluation on the main effects. When only 6 three-level factors are considered, they should be assigned to the third through eighth columns so that the degree of uniform distribution of confounding is

maximized. The first and second columns are thus set as empty columns which have no assigned factors. Based on the prepared L18 orthogonal array, specimens were prepared for each of the 18 different mix proportions.

Using experimental data obtained from the L18 series, an ANOVA study was conducted to analyze the relationship between each design variable and the output (i.e. compressive strength). The sum of squares (SS) for each factor, which reflects deviation from the mean caused by the factor, was first calculated, and then normalized by the degree of freedom (DOF) to find the mean square (MS). SS and MS for error were also computed to measure the variation attributed to inherent experimental errors. Subsequently, the F-ratio was calculated for each factor by taking the ratio of MS-for-factor to MS-for-error, the magnitude of which reflects the significance of the factor on the output. Finally, factors were classified as either significant or insignificant factors based on a statistical F-test with 5% significance level. Detailed procedures and formulae have been presented in Section 3.2.2.

As has been discussed in Section 3.2.3, trends of factor effects in the above approach are derived from the selected ranges of the factor levels. It is possible that a different trend is found outside the ranges, resulting in a different conclusion on the significance of the factors. Therefore, the selection of factors and factor levels should be carefully done based on the knowledge and experience on the subject; otherwise more rounds of experiments would be required. Nevertheless, a lot of insights on the main factor effects can be obtained from the smaller number of experiments, predicting the most promising direction for optimization of the design variables. In addition, confirmation experiments are typically conducted to verify the prediction from the analysis results. Based on those findings, optimum levels of significant factors are determined to achieve the best performance.

4.2.3 Results and discussion

Table 4.6 lists the compressive strength of the 18 mixtures with three specimens each. The SS, MS, and F-ratio of each factor are summarized in Table 4.7. According to the ANOVA results, the most influential factor is Pre-W / NaOH_(sol), which reflects the concentration of NaOH solution. The second highest F-ratio is found in Mix-W / FA; this factor affects the rheology of the mixture and is therefore assumed to affect the pore size distribution of the hardened matrix. The third most significant factor is FA_(B) / FA, followed by S / FA. The other factors – Alk / FA and Na₂SiO₃ / NaOH_(sol) – are suggested to be insignificant within the selected ranges of the factor levels; those F-ratios are less than the theoretical F-score at 5% significance level (i.e. $F_{0.05,2,41} = 3.23$), meaning that there is less than a 5% chance that they are significant factors.

Table 4.6: Compressive strength of 18 EGC mixtures with 3 samples each (in MPa).

Mix no.	Measured compressive strength (3 samples)			Mean ± standard deviation
1	45.5	33.9	31.5	37.0 ± 7.5
2	33.5	33.1	33.0	33.2 ± 0.3
3	24.9	27.4	26.2	26.2 ± 1.3
4	24.3	21.8	22.1	22.7 ± 1.3
5	50.1	49.7	53.1	51.0 ± 1.8
6	49.2	48.6	49.0	48.9 ± 0.3
7	26.9	26.7	28.3	27.3 ± 0.9
8	39.3	37.6	37.0	38.0 ± 1.2
9	40.5	38.7	43.4	40.8 ± 2.4
10	38.0	34.5	39.5	37.4 ± 2.6
11	27.6	31.1	32.1	30.3 ± 2.3
12	52.7	39.9	35.6	42.7 ± 8.9
13	32.6	38.5	36.5	35.9 ± 3.0
14	46.8	46.8	47.9	47.2 ± 0.6
15	44.6	45.4	45.5	45.2 ± 0.5
16	47.0	43.0	43.7	44.6 ± 2.1
17	34.1	33.8	37.4	35.1 ± 2.0
18	38.9	36.0	37.1	37.3 ± 1.5

Table 4.7: ANOVA results on six design variables of EGC matrix (unpooled).

Factors	DOF	Sum of square	Mean square	F-ratio
FA _(B) / FA	2	377	189	7.47
S / FA	2	242	121	4.80
Alk / FA	2	0.903	0.452	0.0179
Na ₂ SiO ₃ / NaOH _(sol)	2	92.9	46.4	1.84
Pre-W / NaOH _(sol)	2	1,330	665	26.3
Mix-W / FA	2	530	265	10.5
Error	41	1,035	25.2	–
Total	53	3,608	–	–

Note: $F_{0.01,2,41} = 5.16$, $F_{0.05,2,41} = 3.23$, $F_{0.10,2,41} = 2.44$

It should be noted that, in contrast to the above finding here, the alkaline activator-to-FA ratio is often considered an influential factor on strength of geopolymer materials; indeed, this parameter has been intensively studied in the research community. For example, Hardjito and Rangan conducted an extensive experimental investigation on effects of various design parameters on compressive strength and workability of fly ash-based geopolymer concrete [4]. Based on the observed complex relationship between the parameters and the compressive strength, they proposed a single parameter called “water-to-geopolymer solids ratio” to assist mix design of geopolymer concrete. The water-to-geopolymer solids ratio represents the ratio of the total mass of water (including water contained in Na₂SiO₃ and NaOH solution) to the total mass of fly ash and solids in Na₂SiO₃ and NaOH solution. This parameter is, by its definition, linked to the alkaline activator-to-fly ash ratio. However, the Alk / FA ratio is concluded – in the selected range – to be the most insignificant factor in the present study. This fact indicates the complex chemistry in geopolymer formation, which has not been fully understood yet, as discussed in Chapter 2. That would be a primary reason that there is currently no comprehensive design procedure for geopolymer concrete, and that trial-and-error approaches are still often used in the research field.

To study the detailed trends of the factor effects, main-effects plots, which plot mean compressive strength at each level of parameters, are prepared for the test results (Fig. 4.3). As can be seen, an increase of Pre-W / NaOH_(sol) and Mix-W / FA monotonically lowers the compressive strength in the selected ranges. Conversely, an increase of FA_(B) / FA and S / FA raises the compressive strength. Besides, statistically insignificant effects of Alk / FA and Na₂SiO₃ / NaOH_(sol) can be seen in the plots.

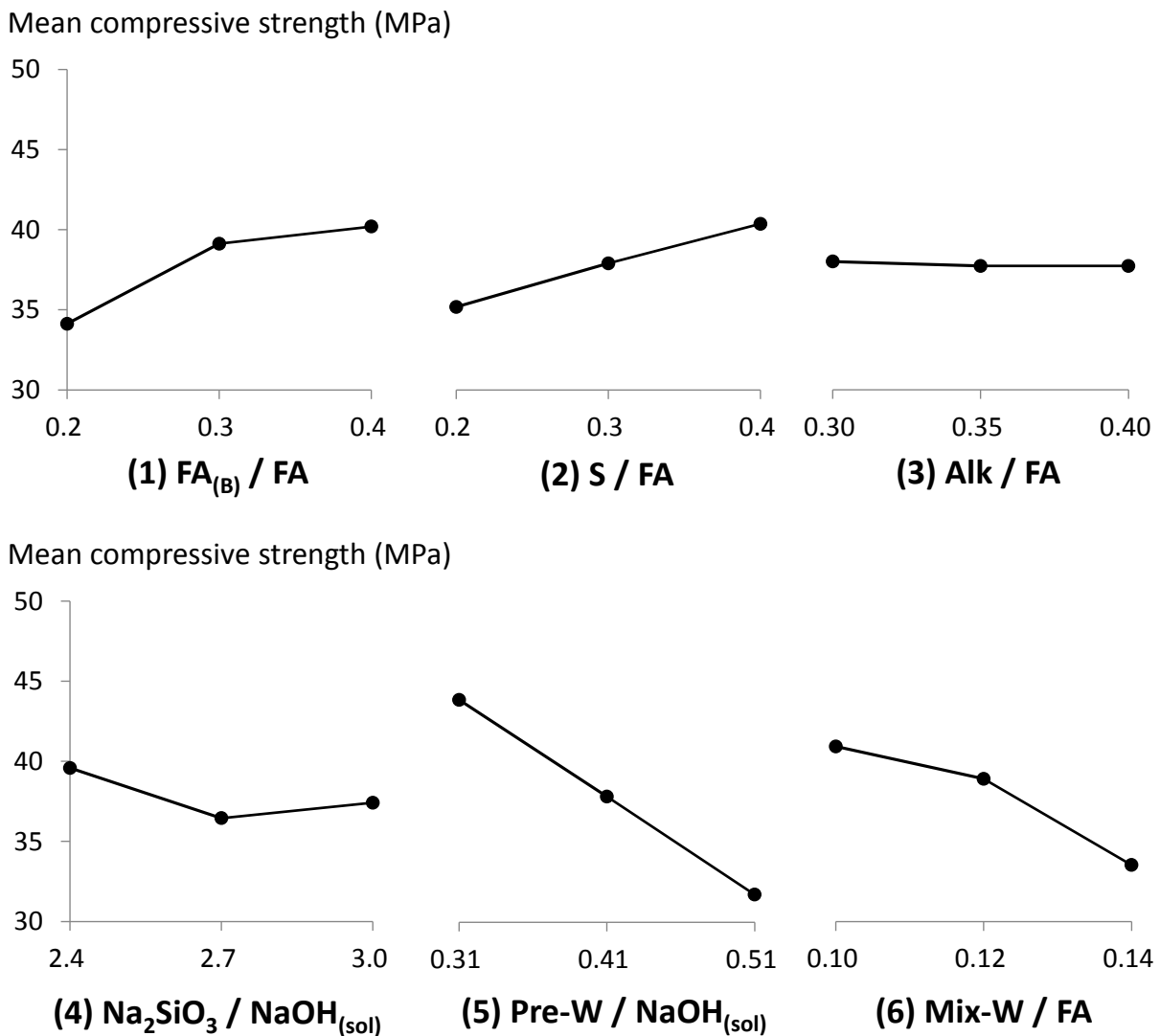


Fig. 4.3: Plots of mean responses at each level of factors to visualize the main factor effects.

Some of the observed trends agree with previous studies while others do not. Regarding either Pre-W / NaOH_(sol) or Mix-W / FA ratio, it is consistent with research findings by Hardjito and Rangan [4] that a higher amount of water in the mixture reduces the compressive strength by increasing the porosity. Also, the observed trend of FA_(B) / FA is in agreement with positive effects of calcium compounds on compressive strength of geopolymers, reported in [5]; since fly ash B contains a larger amount of calcium oxide (CaO) than fly ash A, it is suggested that a higher FA_(B) / FA ratio would cause more formation of C-S-H gel in the geopolymer matrix, contributing to higher compressive strength development, as suggested by Yip *et al.* [6]. On the other hand, the increasing trend of S/ FA ratio does not agree with the decreasing trend observed by Thakur and Ghosh [7]. As mentioned above, insignificant effects of Alk / FA and Na₂SiO₃ / NaOH_(sol) are also inconsistent with the study by Hardjito and Rangan [4] and many other studies. A further study is required to fully understand the mechanisms behind the relationships between the design variables and compressive strength of EGC mortar. Nevertheless, an optimum EGC-mixture design can be systematically predicted by means of the statistical approach without a complete understanding of such mechanisms.

4.2.4 Optimum conditions

The ANOVA results and main-effects plots suggest that optimum conditions for the significant factors are (1) FA_(B) / FA = 0.4, (2) S / FA = 0.4, (5) Pre-W / NaOH_(sol) = 0.31, and (6) Mix-W / FA = 0.10. Due to their monotonic increasing/decreasing trends, it is suggested that a higher/lower ratio than the selected ranges could offer further improvement on the compressive strength. However, it was found in a subsequent verification experiment that any of those directions resulted in too fast setting or too high viscosity of the fresh mixture to cast.

Meanwhile, due to their insignificant effects, factor levels of (3) Alk / FA and (4) Na_2SiO_3 / $\text{NaOH}_{(\text{sol})}$ can be set to any value in the selected ranges, without compromising the compressive strength. In the present study, priority is put in the sustainability aspect: appropriate factor levels are determined such that material greenness of the matrix is maximized. For Alk / FA, a lower ratio provides a higher material greenness, since fly ash is an industrial byproduct while the alkaline activator consists of primary products. On the other hand, a higher ratio is preferred for Na_2SiO_3 / $\text{NaOH}_{(\text{sol})}$ since Na_2SiO_3 production is less energy and carbon intensive than NaOH (detailed in Section 4.4). Therefore, (3) Alk / FA = 0.3 and (4) Na_2SiO_3 / $\text{NaOH}_{(\text{sol})}$ = 3.0 are chosen for their optimum EGC-matrix mixture.

The resultant mixture design is presented in Table 4.8. It should be noted that all mixing ratios have been modified from the preliminary design, through the minimal effort of experiment. If conventional trial-and-error approaches were taken, it could take considerable amounts of time and cost to arrive at the optimized condition with many possible mixture combinations.

Table 4.8: Mix proportion of optimum EGC matrix (by mass).

Fly ash A (Sammis)	Fly ash B (Monroe)	Sand	Na_2SiO_3	NaOH (pellet)	Pre-mix water	Mix water
0.6	0.4	0.4	0.225	0.052	0.023	0.10

4.2.5 Verification experiment for compressive strength

To confirm that the mix proportion predicted by the DOE study is actually an optimum, verification experiments were conducted. Three 2-inch (51-mm) cube specimens were prepared for the predicted optimum design, and their compressive strength was measured as in the L18 experiments. The measured compressive strength was then compared with a statistically-predicted mean and its confidence interval (CI). As detailed in Section 3.2.4, the predicted

optimum design is valid if the measured mean compressive strength is inside the predicted CI. Otherwise, more rounds of experiments would be required to detect any significant confounded interaction or unknown factor that was not considered in the first trial.

To calculate the predicted mean compressive strength and its CI, SS and DOF of the insignificant factors were combined with those of errors (i.e. pooling). The pooled ANOVA results are summarized in Table 4.9. An example calculation of the pooled ANOVA has been presented in Section 3.2.4.

Table 4.9: Pooled ANOVA results on six design variables of EGC matrix.

Factors	DOF	Sum of square	Mean square	F-ratio
FA _(B) / FA	2	377	189	7.52
S / FA	2	242	121	4.83
Pre-W / NaOH _(sol)	2	1,330	665	26.5
Mix-W / FA	2	530	265	10.6
Error	45	1,129	25.1	–
Total	53	3,608	–	–

Table 4.10 presents the measured and predicted compressive strengths of the optimum EGC matrix. As can be seen, the measured compressive strength of 50.5 MPa (with a standard deviation of 0.2 MPa) is inside the CI ranging from 44.8 to 59.1 MPa, and close to the predicted mean of 52.0 MPa. Therefore, the test result verifies the predicted optimum condition for EGC-matrix mixture.

Further, the compressive strength of the optimized EGC is relatively high compared to those reported in the literature; the design compressive strength of geopolymers concrete – with the same “water-to-geopolymer solids ratio” and curing temperature and duration as the optimized EGC – is about 32.5 MPa, according to a design method which was developed by Rangan and co-workers [8] based on their extensive laboratory experiments [4, 9, 10].

Since the achieved compressive strength in the optimized EGC matrix is sufficiently high for various kinds of infrastructure applications, the primary objective of this matrix-development stage has been successfully achieved.

Table 4.10: Measured and predicted compressive strengths of optimum EGC matrix (in MPa).

Measured compressive strength (3 samples)			Measured mean	Predicted mean	Predicted CI
50.2	50.9	50.5	50.5	52.0	[44.8, 59.1]

4.3 Composite design

In this design stage, the micromechanical modeling technique is used to develop strain-hardening ductile EGC based on the optimized EGC matrix.

4.3.1 Experimental and analytical methods

Fiber/matrix interface properties were first determined by experiment. For the optimized EGC matrix, small prismatic specimens with an embedded single fiber were prepared for conducting the single-fiber pullout test. The specimen thickness – equivalent to the fiber embedment length – varied from 0.9 mm to 2.7 mm. Polyvinyl alcohol (PVA) fiber with 1.2% oil coating by weight [11] was employed, considering its preceding successful applications in ECC materials. The embedded fiber in each specimen was uniaxially pulled out with the loading rate of 0.5 mm/min. From the obtained single-fiber pullout curves, τ_o , G_d , and β were computed based on Eqs. 3.18–3.20 presented in Section 3.3.1.

Matrix properties were also experimentally evaluated. To determine the matrix fracture toughness (K_m), notched beam specimens with 305 mm in length, 76 mm in height and 38 mm in thickness were prepared for conducting a three-point bending test. Four specimens with the notch depth-to-height ratio of 0.4 were tested in accordance with ASTM E399 [12]. The loading rate

was 0.5mm/min. In addition, four dog bone-shaped mortar specimens were prepared to measure the matrix Young's modulus (E_m) and the matrix tensile strength, which was approximated as the composite first-cracking strength (σ_{fc} ; equivalent to crack initiation stress σ_{ci}). The rectangular gauge section of specimens measured 100 mm in length, 30 mm in width, and 13 mm in thickness. Specimens were subjected to quasi-static uniaxial tension loading under displacement control at the rate of 0.5 mm/min. For precise measurement of tensile strain, two LVDTs were attached on each specimen to measure extensions within the gauge length. Tensile strain was computed from the average of extensions divided by the gauge length.

For all the above tests, specimens were subjected to the same curing condition as that in the DOE study and tested at the age of 28 days. The detailed testing configurations can be found in Section 3.3.1 or the literature (e.g. [13] and [14]).

Following the experimental characterization, the σ - δ relation was computed by using a modified fiber-bridging constitutive law developed by Yang *et al.* [15], as presented in Section 3.3.2. In their study, the contribution of the matrix micro-spalling and Cook-Gordon effect to the σ - δ curve of a PVA-ECC was small. Thus, for the sake of brevity, both the matrix spalling and the Cook-Gordon effect were not taken into account in this study. Also, two-dimensional fiber distribution was assumed based on the specimen geometry, and the apparent strength [16], snubbing coefficient [16], and strength reduction factor [17, 18] of PVA fiber were assumed to be the same as those found or estimated for cement matrix. To determine the effect of fiber volume fractions (V_f), three different input values of 1.0, 1.5, and 2.0% were used. The micromechanical parameters used in the simulation are listed in Table 4.11. From the predicted σ - δ relation, σ_0 and J_b' were determined to compare with experimentally measured σ_{fc} and J_{tip} .

Table 4.11: Micromechanical parameters used as model input.

Fiber properties					Interface properties	
Diameter (μm)	Length (mm)	Young's modulus (GPa)	Apparent strength (MPa)	Volume (%)	Snubbing coefficient	Strength reduction coefficient
39	12	42.8	1092 ^a	1.0, 1.5, 2.0	0.2 ^b	0.33 ^b

^a Reduced fiber strength when the fiber is embedded in cementitious matrix [11].

^b Assumed values based on experiment [15].

4.3.2 Results and discussion

Table 4.12 summarizes the test results of the single-fiber pullout test, matrix fracture toughness test, and mortar dog bone uniaxial tension test. According to the test results, EGC is characterized by the strong chemical bond and weak frictional bond and slip-hardening, compared to ECC: the chemical bond (G_d) between the optimized EGC matrix and PVA fiber is 6.1 J/m^2 , which is 4-5 times higher than those found in ECC materials [11, 15]; on the other hand, the frictional bond (τ_0) of 0.7 MPa and the slip-hardening coefficient (β) of 0.33 for EGC are both lower than τ_0 of 1.11MPa and β of 1.15 reported by Li and Wu [11], or 1.31-1.91 MPa and 0.58-0.63 found by Yang *et al.* [15]. The strong chemical bond typically results in smaller crack width by limiting the crack opening during the strain-hardening stage. While the weaker frictional bond and smaller slip-hardening coefficient might cause lower bridging capacity (σ_0), a high tensile ductility can be achieved by suppressing fiber rupture and facilitating fiber pullout. These properties have been indeed demonstrated in the preliminary version of EGC; it exhibited smaller average crack width than ECC materials, with high tensile ductility of over 4.5% [2].

Table 4.12: Measured micromechanical parameters of optimum EGC matrix.

Interface properties *			Matrix properties		
Chemical bond (J/m ²)	Frictional bond (MPa)	Slip-hardening coefficient	Fracture toughness (MPa*m ^{1/2})	Young's modulus (GPa)	Tensile strength (MPa)
6.1	0.70	0.33	0.37	7.9	1.4

* Averaged values of 42 specimens for single-fiber pullout test

Regarding the matrix properties, EGC matrix shows relatively weaker and more brittle characteristics than ECC matrix: the fracture toughness (K_m) of 0.37 MPa*m^{1/2}, Young's modulus (E_m) of 7.9 GPa, and tensile strength (approximated as σ_{fc}) of 1.4 MPa are about half of those for ECC materials [19, 20]. It should be, however, mentioned that this is beneficial for satisfying the strength- and energy-based criteria, by reducing σ_{fc} and J_{tip} in Eqs. 2.1 and 2.2 in Chapter 2. From the obtained results, $J_{tip} \approx K_m^2/E_m$ is determined to be 17.3 J/m².

Figure 4.4 shows the computed fiber-bridging capacity (σ_0) and complementary energy (J_b') versus fiber volume fractions (V_f). As can be seen, an increase of V_f elevates both σ_0 and J_b' almost linearly. It is obvious that the fiber content has a significant impact on tensile properties of the composite. In addition, the ratios of σ_0/σ_{fc} and J_b'/J_{tip} – pseudo strain-hardening (PSH) index for strength and energy, respectively – are shown as the secondary y-axis in the graphs of Fig. 4.4. Both of them are greater than unity for all the series, meaning that both the strength- and energy-based criteria are satisfied. As mentioned in Section 3.3.3, $\sigma_0/\sigma_{fc} \geq 1.3$ and $J_b'/J_{tip} \geq 2.7$ are recommended to achieve robust tensile strain-hardening in ECC, due to the material variability caused by the random matrix flaw size and fiber dispersion [21]. The computed energy-PSH values are considerably higher than the recommended value, while there is a smaller margin between the computed strength-PSH index of the $V_f=1.0\%$ case and the recommended value.

If either of the computed PSH values violates the corresponding necessary condition, appropriate modifications will be done on the micromechanical parameters; using a different length, diameter, volume fraction, or oiling quantity [11] of PVA fiber are good examples. The use of a different type of fiber, such as polyethylene (PE) or polypropylene (PP) fiber, is another possibility. In this study, such modification is, in fact, not required; the predicted σ - δ relation and resultant PSH indices suggest that the optimized EGC matrix reinforced with PVA fiber can exhibit tensile strain-hardening and multiple microcracking, even for a fiber volume fraction of 1.0%.

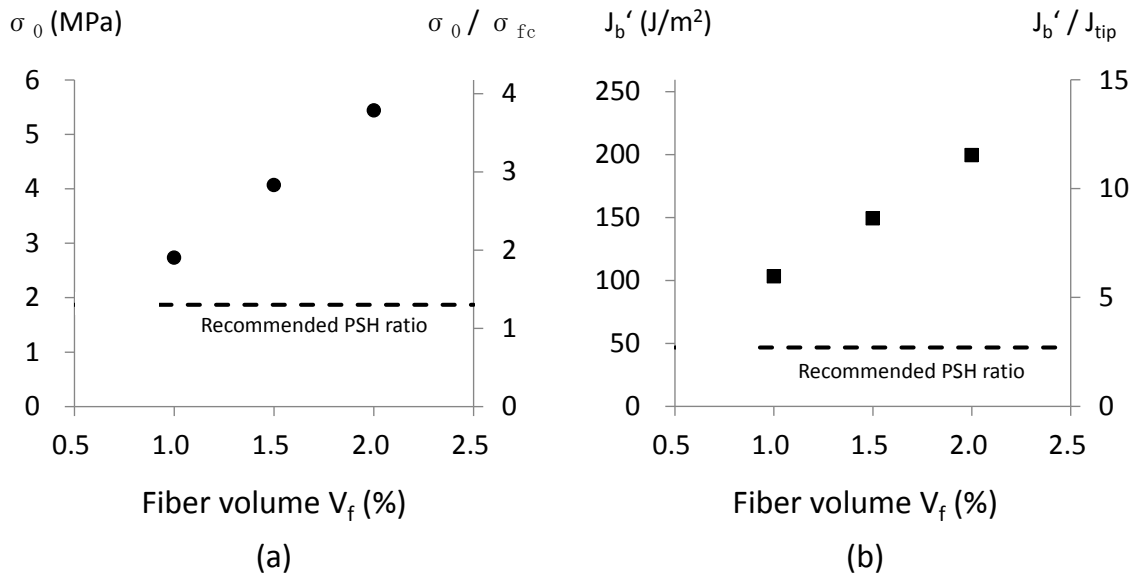


Fig. 4.4: Computed (a) fiber-bridging capacity and (b) complementary energy with their PSH indices. Dashed lines indicate recommended PSH values for practical design [21].

4.3.3 Verification experiment for tensile ductility

To verify the prediction from the micromechanical-modeling study, a confirmation experiment was conducted. Three batches of the optimized fresh EGC mortar were first prepared and the PVA fiber was then slowly added so that each of the batches had the fiber content of 1.0, 1.5,

and 2.0%. Four dog bone-shaped specimens were prepared from each mixture and subjected to the same curing condition as that in the DOE study. The uniaxial tension test was conducted on the composite specimens, with the same test configuration as that for the mortar dog bones, detailed in Section 4.3.1.

Figure 4.5 shows tensile stress-strain curves of the EGC specimens with three different fiber volume fractions. As predicted, all the series exhibit strain-hardening behavior with high tensile ductility. There is, however, significant difference in performance among the series. First, EGC with 1% fiber volume shows relatively large load drops during the strain-hardening stage, which is associated with larger crack width, compared to the other series. Moreover, variability among specimens is large in the $V_f=1.0\%$ case, while both the first-cracking strength (σ_{fc}) and ultimate tensile strength (i.e. fiber-bridging capacity σ_0) are limited.

It is suggested that the degree of performance variability is related to the predicted PSH indices. While both the strength- and energy-PSH indices of all series are greater than the recommended values, the margin gets smaller as the fiber volume is decreased (Fig. 4.4). Meanwhile, variability among specimens, especially in tensile ductility, gets larger with the reduced fiber content. It is therefore suggested that PSH indices determine the degree of robustness in tensile ductility, as well as the satisfaction of the strength and energy criteria. In addition, from the magnitude of load drops during the strain-hardening stage, it may be concluded that the larger the PSH indices, the smaller the crack width will be. To confirm this hypothesis, extensive crack-width measurement will be conducted on EGC materials in the following chapter.

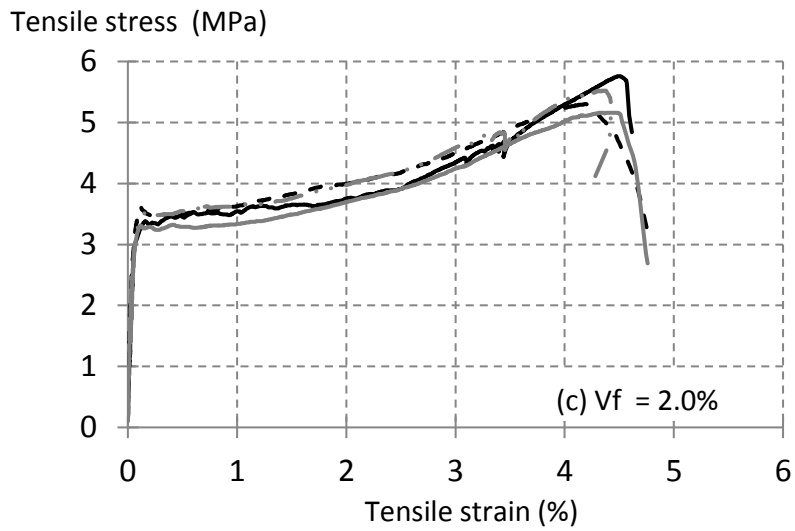
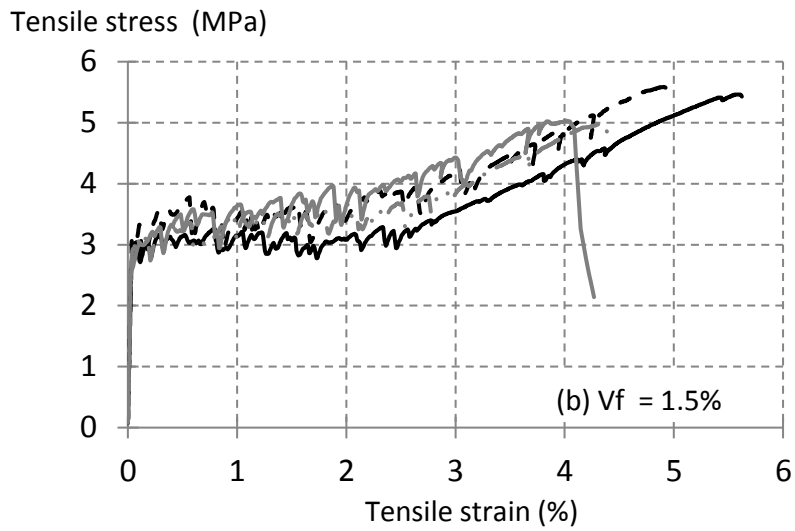
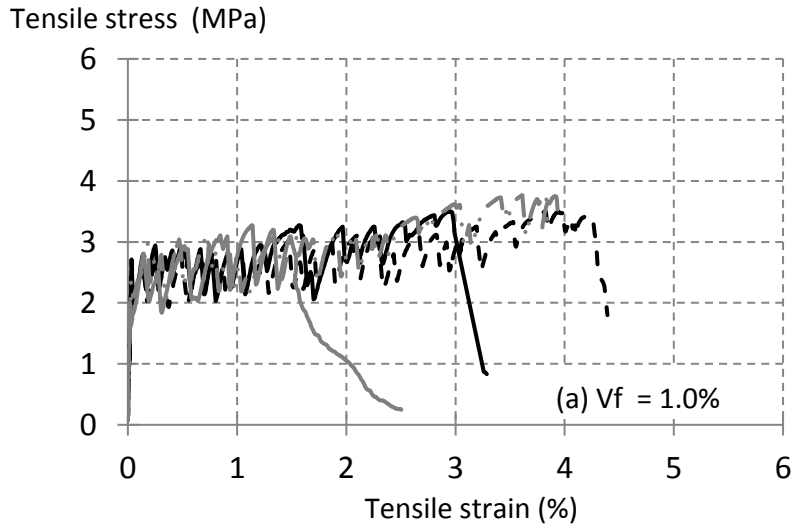


Fig. 4.5: Tensile stress-strain curves of all EGC series show strain hardening with high ductility.

Table 4.13 summarizes the measured mechanical properties of the three EGC series. As the fiber volume increases, the compressive strength, first-cracking strength and ultimate tensile strength are all increased. However, it should be noted that the composite compressive strength is significantly lower than that of the EGC mortar (50.5 MPa as measured in Section 4.2.5). It should be noted that fiber reinforcement does not always increase compressive strength of concrete; some positive effect can be provided by the matrix-confining effect, while some negative effect is also possible when fiber addition causes more voids and larger flaw size in the matrix due to the lowered workability. In the case of V_f -1.0% series, that negative effect seems dominant, and the confinement effect might be limited due to the low fiber volume. The higher compressive strength in V_f -1.5% and 2.0% cases would be a result of combined effects of improved confinement effect and increased voids and flaw size, because of the larger fiber content than the V_f -1.0% series.

Nevertheless, EGC with 1.5% and 2.0% fiber volume fractions have strength of over 40 MPa, which is favorable for various applications. In the case of ductility, EGC with 1.5% V_f has slightly larger tensile-strain capacity than V_f -2.0% series, but the variability among specimens is much smaller in the V_f -2.0% case, as discussed above.

Table 4.13: Mechanical properties of EGC with three different fiber volume fractions.

Series	Compressive strength (MPa)	Tensile-strain capacity (%)	First-cracking strength (MPa)	Ultimate tensile strength (MPa)	Strength PSH
V_f -1.0%	38.5 ± 5.4	3.0 ± 1.3	2.5 ± 0.3	3.5 ± 0.2	1.40
V_f -1.5%	43.1 ± 3.0	4.7 ± 0.7	2.9 ± 0.2	5.3 ± 0.3	1.83
V_f -2.0%	43.3 ± 1.0	4.4 ± 0.1	3.5 ± 0.1	5.4 ± 0.3	1.54

Interestingly, the observed strength-PSH indices in Table 4.13 (i.e. ratio of the ultimate composite tensile strength to the first-cracking strength) are significantly lower than the model-predicted values. This discrepancy results from the difference between the composite first-cracking strength and the mortar tensile strength that was used as the model input; as presented in Table 4.13, the composite first-cracking strength for any of the three series is significantly higher than the mortar strength of 1.4 MPa. Also, the measured first-cracking strength increases with an increment of the fiber volume, while the same value was used for all the three cases in the model. Therefore, it seems inappropriate to approximate mortar tensile strength as composite first-cracking strength.

The increased first-cracking strength might be attributed to the way of measurement; in this study, the composite first-cracking strength was determined by a point of the stress-strain curve after which a significant non-linearity was observed. However, Yang and Li showed in their numerical simulation study [22] that composite stress at the peak, after which a significant non-linearity occurs (and the steady-state-cracking stage begins), can be larger than the matrix strength because of fiber bridging. This is especially the case when the matrix tensile strength is significantly low compared with cohesive traction associated with the fiber bridging. Due to the higher first-cracking strength of the composite, the observed strength-PSH values reported in Table 4.13 can be apparently lower than the model predicted values. Therefore, the definition of composite first-cracking strength should be carefully considered for calculating the strength-PSH index.

From this verification experiment, it has been found that smaller fiber content lowers compressive and tensile strengths, and also causes larger variability in the ductility. Nevertheless, all the EGC series have strain-hardening and multiple cracking characteristics with high tensile

ductility. In addition, due to the adequate compressive strength and excellent tensile properties, EGC with 1.5 or 2.0% V_f seems promising for large-scale infrastructure applications. In the following section, material greenness of these two series is assessed in the final design stage.

4.4 Environmental performance comparison

4.4.1 Materials and methods

Environmental performances of the developed EGC-1.5% and EGC-2.0% were compared with that of the preliminary version of EGC, in terms of the Material Sustainability Indices (MSI) [23]. As references, MSI of OPC concrete and ECC materials were also investigated. Specifically, embodied-energy consumption and global warming intensity (GWI) associated with unit volume of the materials were calculated by accounting for all required energy and generated emissions in the cradle-to-gate phases: raw-material acquisition, processing and manufacturing. Energy and emissions associated with temperature curing of EGC were not included; similar heat/steam-induced accelerated curing is often employed in precast-concrete production, and the comparison study of the materials is therefore not affected by the exclusion. For the carbon-footprint calculations, 100-year GWP values of the IPCC 2013 report [24] were used to calculate the carbon dioxide (CO₂) equivalent emissions.

For the MSI calculation, the quality and reliability of life-cycle inventory data for ingredients are crucial. The inventory data used in this study are listed in Table 4.14. The data were collected from literature that uses consistent system boundaries and assumptions, report both the energy consumption and greenhouse gas emissions, and have significance in the research field. It should be noted, however, that some of the data are a little too old; current production of those

ingredients might have lower energy and emissions than those in the data. Unfortunately, such data have been not available so far, and the collected data seem the latest and most reliable.

Table 4.14: Life-cycle inventories of raw ingredients of concrete, ECC and EGC materials.

Ingredients	Embodied energy (MJ/kg)	GWI (kg CO ₂ -eq/kg)
Portland cement [25]	4.8	0.93
Coarse/fine aggregate [26]	0.12	0.0062
Fine silica sand [27]	0.17	0.025
Fly ash [26]	0.11	0.0074
PVA fiber [28]	101	3.4
Super plasticizer [27, 29]	35	1.5
Water *	0	0
Sodium hydroxide pellets [30]	18	0.86
Sodium silicate (3.3WR, 37% solids) [31]	4.6	0.43

* Assumed negligible based on [29].

For the reference studies, two types of cement concrete were considered: non-air-entrained (Non-AE) and air-entrained (AE) concrete. Both of them were designed to have 6,000 psi (41 MPa) compressive strength (i.e. similar strength to the developed EGC materials), based on the ACI 211 mix-design method [32]. For ECC materials, the most studied version (called M45 [33]) and a greener version that contains high volumes of fly ash (HVFA ECC with FA/C = 2.8 [34]) were examined. The mixture designs of these materials are shown in Table 4.15.

Table 4.15: Mixture proportions of EGC, concrete, and ECC materials (in kg/m³).

	Prelim EGC	EGC- 2.0%	EGC- 1.5%	Non-AE concrete *	AE concrete *	ECC M45	HVFA ECC
Type I cement				470	547	571	324
Coarse aggregate				1079	1079		
Fine aggregate				647	492		
Fine silica sand	340	460	463			456	456
Fly ash	1131	1151	1157			685	906
PVA fiber	26	26	19.5			26	26
SP						6.8	5.3
Water	179	142	142	193	175	332	320
NaOH (pellet)	63.5	59.8	60.1				
Na ₂ SiO ₃	289	259	260				

* Designed for compressive strength of 6000 psi (41 MPa), slump of 3 in (76 mm), maximum aggregate size of 1 in (25 mm), fine aggregate modulus of 2.80, and absorption capacity of 0.5% and 0.7% for coarse and fine aggregate, respectively. The air contents of Non-AE and AE concrete are 1% and 4.5%, respectively.

4.4.2 Results and discussion

Figure 4.6 shows the computed energy- and carbon-MSI of EGC, concrete, and ECC materials. For EGC materials, the effect of optimizations during the matrix- and composite-design phases can be quantified; the embodied energy of the preliminary EGC is reduced from 5.29 to 4.46 GJ/m³ in EGC-1.5%, while the GWI decreases from 285 to 251 kg CO₂-eq/m³. These are 16 and 12% reduction in the embodied energy and CO₂ equivalent emissions, respectively.

The large contributors to the embodied energy of EGC series are the alkaline activator and PVA fiber, which account for 45 and 51%, respectively, of the total energy for EGC-2.0%, and 51 and 44% for EGC-1.5%. While the total energy consumption of EGC is greater than that of concrete, the geopolymer binder (i.e. fly ash plus alkaline activator) consumes comparable or even less

energy than the cement binder in normal concrete. Thus, use of the energy-intensive PVA fiber is the primary cause of the higher energy consumption of EGC.

The large embodied energy of the synthetic fiber is associated with the feedstock energy (i.e. heat content of the petroleum-based ingredients), as well as the process energy consumed in the manufacturing process. Due to the high energy intensity of the PVA fiber, ECC materials also have larger embodied energy than normal concrete. Therefore, regardless of the type of matrix, the amount of PVA fiber dominates the material greenness of the composite. In other words, significant improvement can be made if the fiber volume is lowered. Indeed, EGC-1.5% has 13% less embodied energy than EGC-2.0%, which is slightly less than the greener version of ECC (HVFA ECC).

In the case of CO₂ equivalent emissions, EGC materials show higher performance than the OPC-based counterparts: GWI of EGC-1.5% is about half of those of concrete materials, and 40% less than the green HVFA ECC. The substantially low GWI of EGC materials can be explained by two aspects. First, the carbon footprints of PVA fiber are moderate, unlike its high embodied energy; use of PVA fiber is not a significant disadvantage in the comparison with cement concrete. In addition, use of no cement materials in EGC has a huge impact on the GWI reduction. Indeed, cement contributes to a large portion of high GWI values in both concrete and ECC materials (Fig. 4.6). It should be mentioned that, while this study used the value of 0.93 kg CO₂-eq per kilogram of portland cement, the carbon intensity of cement is highly dependent on the efficiency of the combustion kiln. For instance, Damftoft *et al.* estimated that the total CO₂ emissions in cement production range from 0.84 – 1.15 kg per kilogram of clinker [35]. Therefore, the GWI values of concrete and ECC could be higher in developing countries that

have relatively old and inefficient kilns. EGC will be particularly promising in such countries to replace cement concrete.

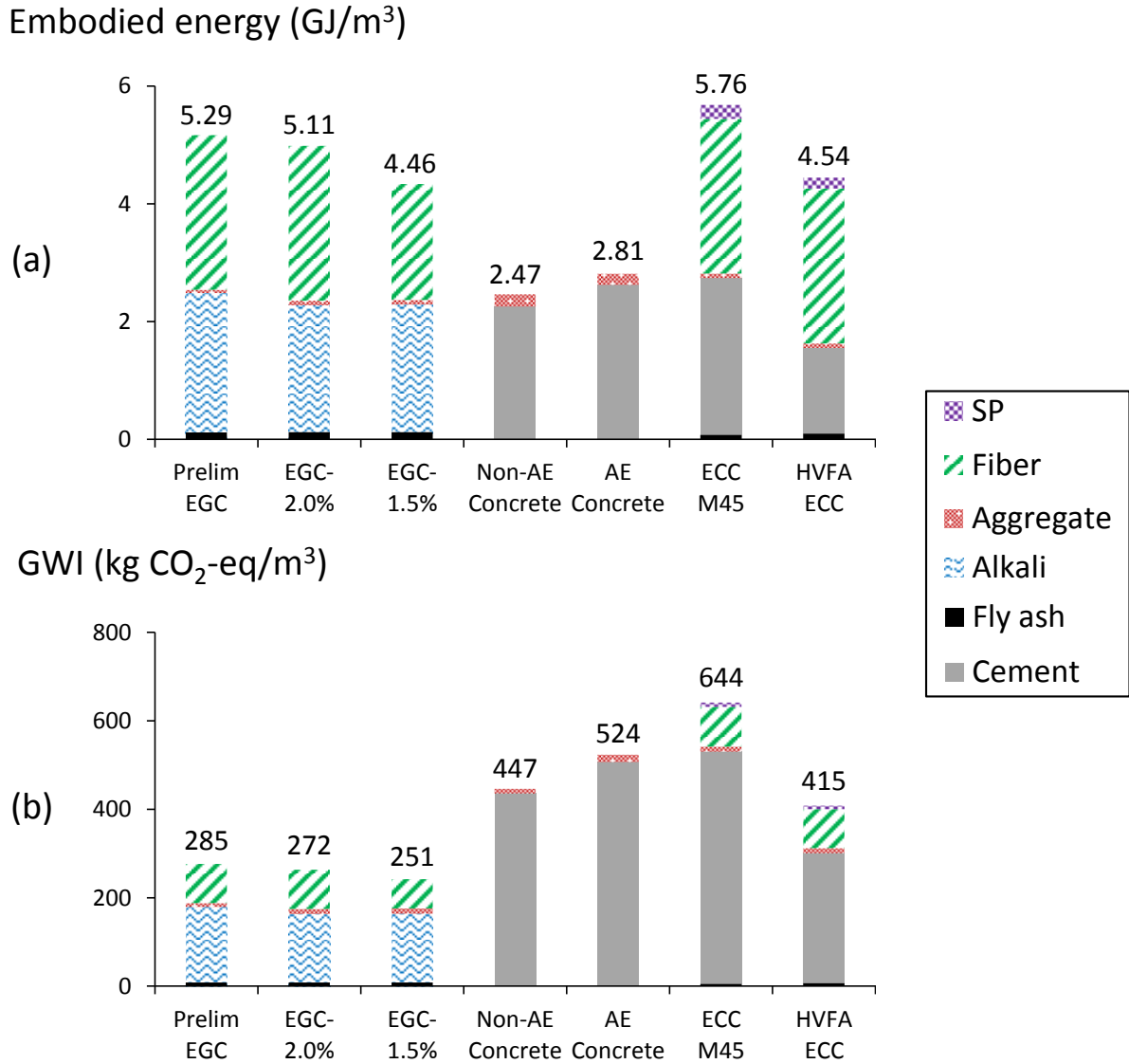


Fig. 4.6: (a) Embodied energy and (b) global warming potential for EGC, concrete, and ECC materials. CO₂ equivalent emissions of EGC-1.5% are about half of regular concrete.

4.5 Summary and conclusions

In this chapter, an optimized EGC with compressive strength of 43.1 ± 3.0 MPa and tensile ductility of $5.3 \pm 0.3\%$ has been successfully developed, while reducing 16% embodied energy

and 12% CO₂ equivalent emissions compared to the preliminary EGC. The embodied energy and GWI of the optimized EGC are 23 and 61% lower, respectively, than those of a standard version of ECC (M45). Therefore, the applicability and effectiveness of the proposed design method have been demonstrated through the systematic design process and the achieved results.

The proposed design method is applicable to not only fly ash-based fiber-reinforced geopolymers but most other types of fiber-reinforced brittle matrix composites. The efficient and systematic design process facilitates the research and development of high-performance sustainable composite materials.

In addition, the following new findings can be derived from this study:

- The alkaline activator-to-fly ash ratio is the most insignificant factor for compressive strength of the EGC matrix, in the selected range of this study. This contrasts with previous studies that reported the alkaline activator-to-fly ash ratio as the most significant factor.
- Compressive strength of EGC matrix increases when a larger amount of fly ash with higher calcium content is incorporated, even if the fly ash is classified as class F (i.e. low-calcium).
- EGC matrix has relatively low tensile strength and more brittle behavior compared to ECC matrix materials. This is, however, beneficial in achieving robust tensile strain-hardening and multiple microcracking.
- Interface between EGC matrix and PVA fiber has strong chemical bond, weak frictional bond and small slip-hardening coefficient. The strong chemical bond is beneficial for achieving smaller crack width, while increasing the chance of fiber rupture and lowering the complementary energy (J_b'). On the other hand, weak frictional bond and small slip-

hardening coefficient might reduce the bridging capacity (σ_0), but could contribute to a high tensile ductility by suppressing fiber rupture and facilitating fiber pullout. In the case of the developed EGCs, both smaller crack width and higher tensile ductility could be achieved because of the synergistic effects of bonding properties.

- The optimized EGC shows high tensile ductility of 3.0% even with the small fiber volume fraction of 1.0%. However, due to a small margin between the first-cracking strength and fiber-bridging capacity, variability among specimens is larger than EGC with higher fiber contents.
- EGC materials have a huge advantage in terms of the global warming intensity (GWI) associated with the material production. Although the embodied energy of EGC is higher than that of normal concrete, improvement is possible by reducing the volume fractions of energy-intensive PVA fiber, or by replacing the PVA fiber with one with lower embodied energy.
- EGC with 1.5% PVA fiber shows balanced properties in tension and compression, and in MSI. This composite has suitable mechanical properties for civil infrastructure applications and support infrastructure sustainability through a low GWI.

As mentioned in the last finding, EGC-1.5% seems to be the most promising material because of the high mechanical performances and material greenness. Despite the superiority of EGC-1.5%, it might be too early to draw the conclusion; indeed, crack width of EGC-1.5% is suggested to be larger than that of EGC-2.0%, based on their stress-strain curves. The larger crack width might result in lower durability properties, which is detrimental to sustainability of the structure.

Therefore, it is necessary to evaluate durability properties of the developed EGC, which is addressed in the next three chapters.

References

- [1] M. Sutton, J. Orteu, and H. Schreier, *Image Correlation for Shape, Motion and Deformation Measurements: basic concepts, theory and applications*. Boston, MA: Springer US, 2009.
- [2] M. Ohno and V. C. Li, “A feasibility study of strain hardening fiber reinforced fly ash-based geopolymer composites,” *Constr. Build. Mater.*, vol. 57, pp. 163–168, Apr. 2014.
- [3] ASTM C618, *Standard specification for coal fly ash and raw or calcined natural pozzolona for use in concrete*. West Conshohocken, PA: ASTM International, 2015.
- [4] D. Hardjito and B. V. Rangan, *Development and properties of low-calcium fly ash-based geopolymer concrete*. Perth (Australia): Research report GC 1, Curtin University, 2005.
- [5] J. Temuujin, A. van Riessen, and R. Williams, “Influence of calcium compounds on the mechanical properties of fly ash geopolymer pastes,” *J. Hazard. Mater.*, vol. 167, no. 1–3, pp. 82–88, 2009.
- [6] C. K. Yip, G. C. Lukey, and J. S. J. Van Deventer, “The coexistence of geopolymeric gel and calcium silicate hydrate at the early stage of alkaline activation,” *Cem. Concr. Res.*, vol. 35, no. 9, pp. 1688–1697, 2005.
- [7] R. N. Thakur and S. Ghosh, “Effect of mix composition on compressive strength and microstructure of fly ash based geopolymer composites,” *J. Eng. Appl. Sci.*, vol. 4, no. 4, pp. 68–74, 2009.
- [8] N. A. Lloyd and B. V. Rangan, “Geopolymer Concrete with Fly Ash,” in *Second International Conference on Sustainable Construction Materials and Technologies*, 2010.
- [9] D. Hardjito, S. E. Wallah, D. M. J. Sumajouw, and B. V. Rangan, “On the Development of Fly Ash-Based Geopolymer Concrete,” *ACI Mater. J.*, vol. 101, no. 6, pp. 467–472, 2004.
- [10] B. V. Rangan, “Mix design and production of fly ash based geopolymer concrete,” *Indian Concr. J.*, vol. 82, no. 5, pp. 7–15, 2008.
- [11] V. C. Li, C. Wu, S. Wang, A. Ogawa, and T. Saito, “Interface tailoring for strain-hardening polyvinyl alcohol-engineered cementitious composite (PVA-ECC),” *ACI Mater. J.*, vol. 99, no. 5, pp. 463–472, 2002.
- [12] ASTM E399-12e3, *Standard Test Method for Linear-Elastic Plane-Strain Fracture Toughness K_{1C} of Metallic Material*. West Conshohocken, PA: ASTM International, 2012.
- [13] M. Li and V. C. Li, “Cracking and healing of engineered cementitious composites under chloride environment,” *ACI Mater. J.*, vol. 108, no. 3, pp. 333–340, 2011.

- [14] B. Felekoglu, K. Tosun-Felekoglu, R. Ranade, Q. Zhang, and V. C. Li, "Influence of matrix flowability, fiber mixing procedure, and curing conditions on the mechanical performance of HTPP-ECC," *Compos. Part B Eng.*, vol. 60, pp. 359–370, Apr. 2014.
- [15] E.-H. Yang, S. Wang, Y. Yang, and V. C. Li, "Fiber-Bridging Constitutive Law of Engineered Cementitious Composites," *J. Adv. Concr. Technol.*, vol. 6, no. 1, pp. 181–193, 2008.
- [16] T. Kanda and V. C. Li, "Interface Property and Apparent Strength of High-Strength Hydrophilic Fiber in Cement Matrix," *Journal of Materials in Civil Engineering*, vol. 10, no. 1, pp. 5–13, 1998.
- [17] J. Morton and G. W. Groves, "The effect of metal wires on the fracture of a brittle-matrix composite," *J. Mater. Sci.*, vol. 11, no. 4, pp. 617–622, 1976.
- [18] V. C. Li, "Postcrack scaling relations for fiber reinforced cementitious composites," *J. Mater. Civ. Eng.*, vol. 4, no. 1, pp. 41–57, 1992.
- [19] S. Wang and V. C. Li, "High-early-strength engineered cementitious composites," *ACI Mater. J.*, vol. 103, no. 2, pp. 97–105, 2006.
- [20] E. Yang, "Designing Added Functions in Engineered Cementitious Composites," University of Michigan, Ann Arbor, 2008.
- [21] T. Kanda and V. C. Li, "Practical Design Criteria for Saturated Pseudo Strain Hardening Behavior in ECC," *J. Adv. Concr. Technol.*, vol. 4, no. 1, pp. 59–72, 2006.
- [22] E. Yang and V. Li, "Numerical study on steady-state cracking of composites," *Compos. Sci. Technol.*, vol. 67, no. 2, pp. 151–156, Feb. 2007.
- [23] G. A. Keoleian, A. M. Kendall, M. D. Lepech, and V. C. Li, "Guiding the design and application of new materials for enhancing sustainability performance: Framework and infrastructure application," *Mater. Res. Soc. Symp. Proc.*, vol. 895, 2006.
- [24] G. Myhre, D. Shindell, F. Bréon, W. Collins, J. Fuglestedt, J. Huang, D. Koch, J. Lamarque, D. Lee, B. Mendoza, T. Nakajima, A. Robock, G. Stephens, T. Takemura, and H. Zhang, "Anthropogenic and natural radiative forcing," in *Climate Change 2013: The Physical Science Basis, Working Group I Contribution to the Fifth Assessment Report of the Intergovernmental Panel on Climate Change*, T. F. Stocker, D. Qin, G.-K. Plattner, M. Tignor, S. K. Allen, J. Boschung, A. Nauels, Y. Xia, V. Bex, and P. M. Midgley, Eds. Cambridge (UK): Cambridge University Press, 2013, p. 714.
- [25] M. L. Marceau, M. A. Nisbet, and M. G. Vangeem, *Life Cycle Inventory of Portland Cement Manufacture*. Stokie, IL: Portland Cement Association, 2006.
- [26] M. A. Nisbet, M. L. Marceau, and M. G. Vangeem, *Environmental Life Cycle Inventory of Portland Cement Concrete*. Stokie, IL: Portland Cement Association, 2002.
- [27] R. Ranade, "Advanced Cementitious Composite Development for Resilient and Sustainable Infrastructure," University of Michigan, Ann Arbor, 2014.

- [28] R. Frazão and R. Fernandes, *Comparative Analysis of the Life Cycle of AT Fibre-cement and NT Fibre-cement*. International Chrysotile Association, 2004.
- [29] G. A. Keoleian, A. Kendall, J. E. Dettling, V. M. Smith, R. F. Chandler, M. D. Lepech, and V. C. Li, “Life Cycle Modeling of Concrete Bridge Design: Comparison of Engineered Cementitious Composite Link Slabs and Conventional Steel Expansion Joints,” *J. Infrastruct. Syst.*, vol. 11, no. 1, pp. 51–60, 2005.
- [30] Euro Chlor, “An Eco-profile and Environmental Product Declaration of the European Chlor-Alkali Industry,” 2013. [Online]. Available: https://www1.ethz.ch/ifu/ESD/education/master/AESEA/Euro_Chlor_Eco-profile_Chlorine_2014-03.pdf. [Accessed: 10-Mar-2017].
- [31] M. Fawer, M. Concannon, and W. Rieber, “Life cycle inventories for the production of sodium silicates,” *Int. J. Life Cycle Assess.*, vol. 4, no. 4, pp. 207–212, 1999.
- [32] ACI Committee 211, *Standard Practice for Selecting Proportions for Normal Heavyweight, and Mass Concrete (Reapproved 2009)*, no. Reapproved. Farmington Hills, MI: American Concrete Institute, 2009.
- [33] S. Wang, “Micromechanics based matrix design for engineered cementitious composites,” University of Michigan, Ann Arbor, 2005.
- [34] E. H. Yang, Y. Yang, and V. C. Li, “Use of high volumes of fly ash to improve ECC mechanical properties and material greenness,” *ACI Mater. J.*, vol. 104, no. 6, pp. 620–628, 2007.
- [35] J. S. Damtoft, J. Lukasik, D. Herfort, D. Sorrentino, and E. M. Gartner, “Sustainable development and climate change initiatives,” *Cem. Concr. Res.*, vol. 38, no. 2, pp. 115–127, 2008.

PART III: CHARACTERIZATION OF EGC DURABILITY

CHAPTER 5: Cracking Characteristics and Water Permeability of EGC

This chapter describes experimental characterization of crack patterns and water tightness of the developed EGC. Crack patterns of EGC materials with different fiber volumes are first determined, and permeability coefficients of intact and cracked EGC are then measured. Based on the experimental result, the relationship between the cracking characteristics and water permeability is investigated.

5.1 Introduction

Durability of concrete materials is highly dependent on their transport properties. Buenfeld pointed out that major deterioration mechanisms of concrete – reinforcement corrosion, sulfate attack, frost attack, and alkali-silica reaction (ASR) – are controlled by the transport of aggressive agents [1]. There are many transport processes within concrete, but most of them are governed by three mechanisms: permeation, diffusion, and absorption. Their driving forces are hydrostatic head, chemical concentration gradient, and capillary suction, respectively. Detailed discussion on the three mechanisms can be found in the literature (e.g. [2]). In general, the dominant mechanism is determined by the surrounding environment of the concrete structure.

Transport properties of concrete drastically change if cracking occurs; particularly, increase in permeability is significant. Wang *et al.* reported that water permeability of cracked concrete was five orders of magnitude higher than that of intact concrete, when the crack opening was 350 μm [3]. Tsukamoto also found that the water flow rate in concrete scales to the third power of crack width [4]. The severe degradation in water tightness is detrimental to concrete durability, as well as functionality when used as hydraulic infrastructure. It should be noted that some design codes use a maximum permissible crack width of 300 μm (e.g. [5–7]), meaning that such a degree of damage can occur in actual concrete structures. In reality, due to the difficulty in crack-width control, crack width in structures may far exceed the permissible value [8].

Despite the marked effect of cracking on concrete permeability, the degree of degradation is limited when the crack opening is sufficiently small; Shah and coworkers suggested from extensive experimental studies that approximately 100 μm is a threshold value of crack opening under loading, below which the water permeability of concrete materials does not increase significantly [3, 9–12]. In addition, Lepech and Li demonstrated that water permeability of cracked ECC, which has tightly-controlled crack width of less than 80 μm , is comparable to that of uncracked ECC and cement mortar [13]. Therefore, cracking characteristics of concrete play a key role in determining the water tightness and associated durability properties.

In this chapter, crack patterns of the developed EGC with 1.5% and 2.0% fiber volume fractions are first investigated. The number of cracks and residual crack-width distribution are determined, by using an optical microscope, for EGC specimens that are uniaxially strained to either 1 or 2%. Subsequently, the preloaded EGC specimens, as well as intact specimens, are tested for their water permeability by means of a newly-developed test setup. To calculate the permeability

coefficient for the new test configuration, a formula is derived based on Darcy’s law. Based on the test results, the relationship between crack width and water permeability is discussed.

5.2 Materials and methods

5.2.1 Materials and mix design

Table 5.1 lists the ingredients and mix proportions of two types of EGC used in this study. The mix designs are those developed in Chapter 4 – optimized EGC with fiber content of either 1.5 or 2.0%. Detailed information on the ingredients can be found in Section 4.2.1.

Table 5.1: Mix designs of EGC used in this study (by mass).

Series	Fly ash A (Sammis)	Fly ash B (Monroe)	Sand	Na ₂ SiO ₃	NaOH (pellet)	Pre-mix water	Mix water	PVA fiber
Vf-1.5%	0.6	0.4	0.4	0.225	0.052	0.023	0.10	0.017
Vf-2.0%								0.023

5.2.2 Specimen preparation

The fresh EGC mortar was first prepared as detailed in Section 4.2.1. Then, PVA fiber was slowly added to the mixture, and mixing continued until good fiber dispersion was achieved. The mixture of each series was cast into 12 × 3 × 0.5 inch (305 × 76 × 12.7 mm) prism molds. The molds were designed so that specimens had smooth molded surfaces on both the 305 × 76 mm faces, with the 305 × 12.7 mm face sitting on the bottom of the mold (Fig. 5.1). This casting method could reduce variability in crack patterns between one surface and the opposite side of the surface. Consistent crack patterns were beneficial for relating permeability coefficients to crack width, as well as obtaining more uniform water flow in the permeability test. However, it was difficult to achieve good compaction due to the narrow opening of the molds (12.7 mm). To

improve the compaction, molds were placed on a vibration table during casting, and additional manual compaction was applied to the fresh EGC with a mallet.

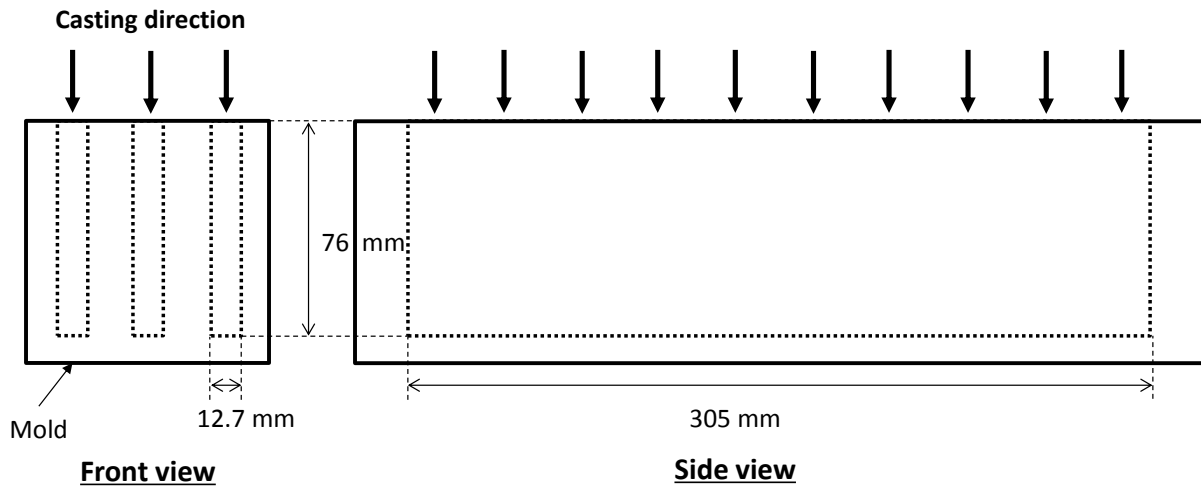


Fig. 5.1: Design of prism mold.

Seven prisms were prepared for each series and divided into three groups. The first group had one prism that was cut into three specimens with 90 mm in length. The specimens were tested for their water permeability without preloading. On the other hand, another three prisms in the second group were preloaded to a uniaxial tensile strain of 1.0% before the permeability test. Prior to the preloading, the specimens were cut to 180 mm in length so as to minimize edge effects and bending stress that could occur in the tensile test. The third group also had three prisms, but they were preloaded to 2.0% strain prior to the permeability test. Respectively, specimens in the three groups were referred to as $V_{f1.5-\epsilon0}$, $V_{f1.5-\epsilon1}$, $V_{f1.5-\epsilon2}$ for the series of fiber volume fraction of 1.5%, and $V_{f2.0-\epsilon0}$, $V_{f2.0-\epsilon1}$, $V_{f2.0-\epsilon2}$ for the series of 2.0% fiber content.

The curing procedure is illustrated in Fig. 5.2. All specimens were demolded 24 hours after casting, and then oven-cured at 60 °C for additional 24 hours. Subsequently, the $V_{f1.5-\epsilon0}$ and

$V_f2.0-\epsilon_0$ specimens were cured at room temperature ($23 \pm 3 \text{ }^\circ\text{C}$) for 12 days, followed by water curing at room temperature for at least 14 days (i.e. age of 28 days or older). In this curing method, the specimens are water-saturated and at least 28 days old prior to permeability testing. The water saturation ensures steady-state water flow through the specimens during the permeability testing, which is a required condition for using Darcy's law to compute the permeability coefficient. In the case of preloaded specimens, the same oven-curing method was applied but the subsequent room-temperature curing continued for 26 days. The specimens were then loaded at the age of 28 days. After the preloading, the cracked specimens were sectioned into 90 mm in length to fit the permeability test apparatus, and cured in a water bath for at least 14 days prior to the permeability test, as in the uncracked specimens.

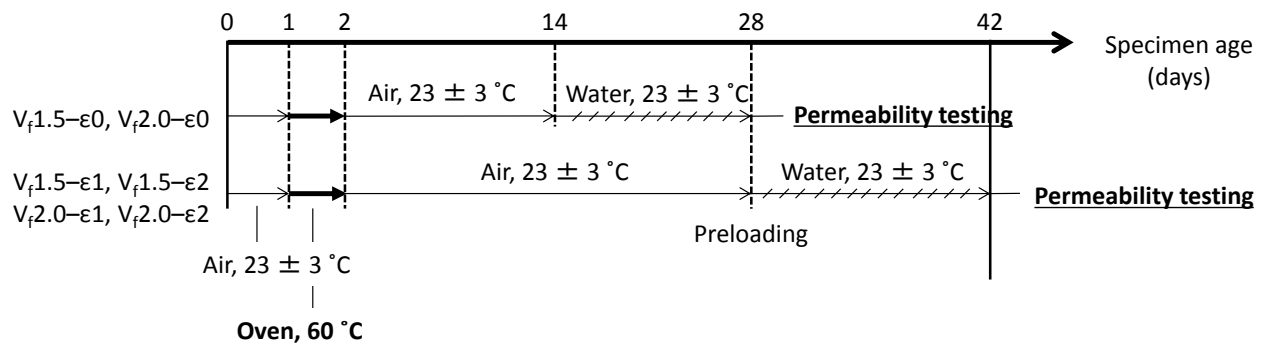


Fig. 5.2: Curing conditions for intact and cracked EGC specimens prior to permeability testing.

5.2.3 Preloading and crack width measurement

The 1%- and 2%-strain specimens were loaded in uniaxial tension under displacement control at the rate of 0.5 mm/min. Prior to the preloading, aluminum plates were glued to both ends of the specimens so as to facilitate the gripping of the specimens by the load frame. Two LVDTs were attached to each specimen for measuring extensions within gauge length of about 80 mm. Tensile strain was computed from the average of extensions divided by the gauge length.

Once the desired strain level was reached, the load was incrementally removed from the specimens to obtain their unloading stress-strain curves. The unloaded specimens were then observed by a digital optical microscope to record the number of microcracks and their crack width. To accurately characterize the crack patterns, crack-width measurement was performed across three lines parallel to the loaded direction, which were drawn on the center and both near-edge sides of the specimen surface. Variability in crack width between one surface and the other side was assumed to be small, because of the employed casting method mentioned above.

5.2.4 Permeability testing

The permeability-test setup in this study followed the falling-head test method proposed by Wang *et al.* [3]. Figure 5.3 schematically illustrates the apparatus developed by Lepech and Li [13]. The specimen was mounted and clamped between the top and bottom open-head containers, both of which were filled with water. Water permeated from the top to bottom because of the pressure head. The test started with filling both the inflow and outflow pipes with water, and the water-level decrease in the inflow pipe was measured at regular time intervals. The outflow-pipe water level was kept constant since extra water overflowed from the end of the pipe. The water-pressure head was thus measured between the falling water level and the constant outflow-pipe water level.

For this test configuration, Wang *et al.* derived the following formula to calculate the permeability coefficient (k , in cm/sec), based on the Darcy's law [3]:

$$k = \frac{a_{in}L}{At} \ln \frac{h_0}{h_f} \quad (5.1)$$

where a_{in} and A are the cross-sectional areas of the inflow pipe and specimen, L is the specimen thickness, t is the test duration, and h_0 and h_f are the initial and final water heads.

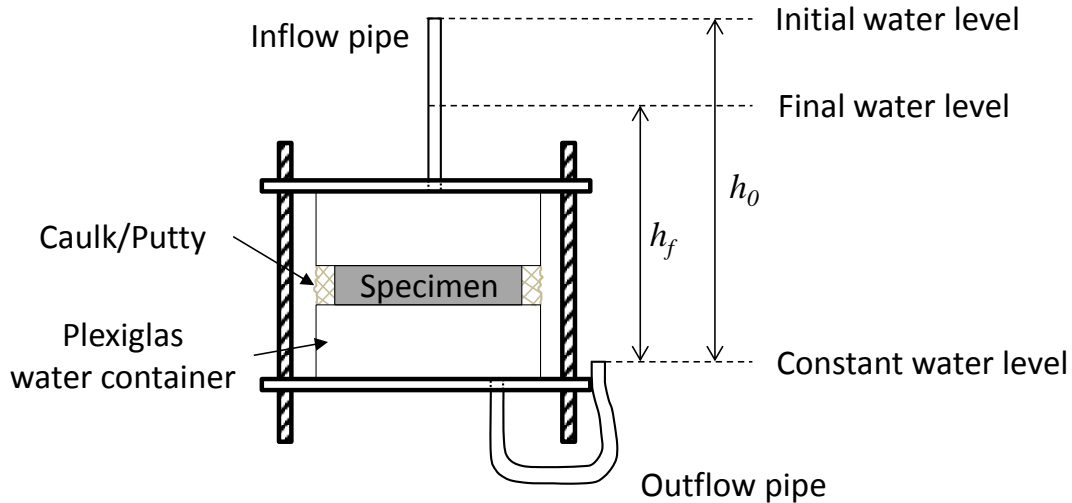


Fig. 5.3: Permeability-testing apparatus developed by Lepech and Li [13].

It should be mentioned that Li and Lepech used a constant-head method for cracked ECC specimens, while the falling-head setup was used for intact ECC. They reported that cracked ECC specimens had too high permeability to practically use the falling-head method. In this study, however, emphasis is placed on that the identical test setup and conditions are used for both intact and cracked specimens, so that the measured values can be fairly compared.

There were two major problems in the above test setup: unintended multi-directional flows and leakage of water. To ensure unidirectional flow, specimen edges were sealed with epoxy before being subjected to water curing. To prevent leakage, silicon caulk and plumber's putty were filled into gaps between the apparatus and the specimen. Despite such a careful setup, small, but non-negligible, leakage occasionally happened. The effect of leakage was significant especially in intact specimens with low permeability, even when the amount of leakage was small and difficult to measure or detect.

To solve the leakage-derived problem, the test condition was slightly modified, and a corresponding formula to compute the permeability coefficient was derived. The modified test condition is shown in Fig. 5.4. In the setup, the outflow-pipe water level is not constant but rises with time, without overflowing. Then, the permeability coefficient can be determined using the following equation:

$$k = \frac{a_{in} a_{out} L}{(a_{in} + a_{out}) At} \ln \frac{h_0}{h_f} \quad (5.2)$$

where a_{out} is the cross-sectional area of the outflow pipe. The detailed derivation can be found in Appendix D. In this study, the values of a_{in} , a_{out} , A , and L were 0.71 cm^2 , 1.23 cm^2 , 42.71 cm^2 , and 1.27 cm , respectively.

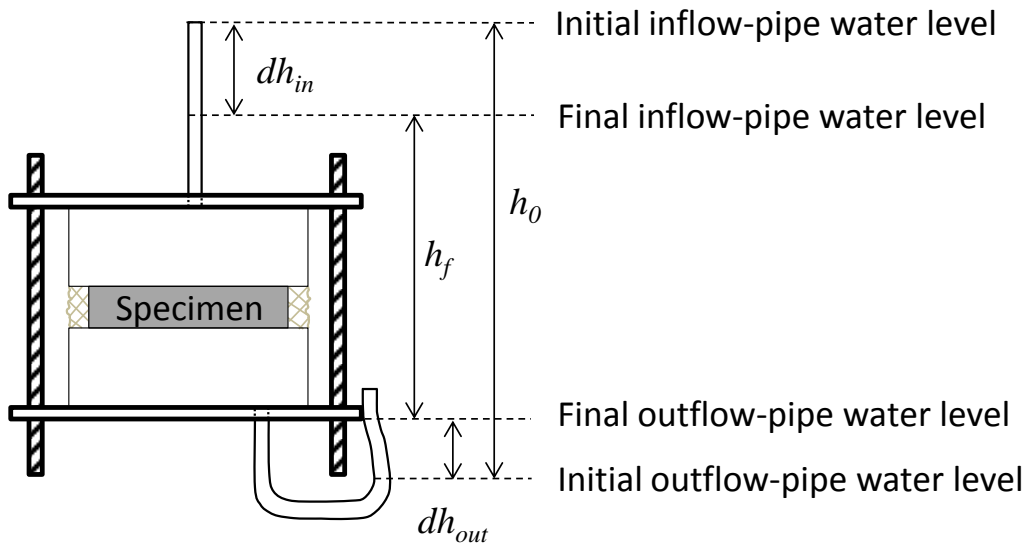


Fig. 5.4: Modified permeability-testing setup used in this study.

In addition, validity of measured values was examined as follows. From the mass conservation law, the volume of water associated with the change in the inflow-pipe water level should be equal to that associated with the outflow-pipe water-level change (i.e. $dh_{in} \times a_{in} = dh_{out} \times a_{out}$).

The total absence of leakage was assumed when this condition was met, and the permeability coefficient was then calculated by using Eq. 5.2.

5.3 Results and discussion

5.3.1 Crack patterns of EGC

Figure 5.5 shows tensile stress-strain curves of preloaded specimens. The strain-hardening behavior can be seen in all series. However, a few specimens showed a localized crack during the loading. The unintended large cracking might be attributed to poor compaction and resultant large flaws in those specimens, caused by the difficult casting method mentioned above. Despite the localized damage, significant difference is not observed in their stress-strain curves. Regarding the comparison between $V_f1.5$ and $V_f2.0$ series, the former shows larger load drops during the strain-hardening stage and has larger residual strain, especially in the 2% strain case. Both of these characteristics imply the larger crack width of $V_f1.5$ than that of $V_f2.0$.

Table 5.2 presents measured crack patterns of preloaded specimens. Overall, tightly-controlled multiple cracks are observed in most of the specimens. However, there are significantly large cracks in a few specimens (i.e. $V_f1.5-\epsilon2$ Specimen 1 with 779.9 μm , $V_f2.0-\epsilon1$ Specimen 3 with 351 μm , and $V_f2.0-\epsilon2$ Specimen 1 with 770.4 μm), as mentioned above. Such cracking characteristic is not an inherent material property of EGC, and it is therefore reasonable to regard those specimens as outliers. With the outliers excluded, the overall average crack width ends up with 26.8, 38.2, 17.7, and 24.5 μm for $V_f1.5-\epsilon1$, $V_f1.5-\epsilon2$, $V_f2.0-\epsilon1$, and $V_f2.0-\epsilon2$, respectively. The average crack width of $V_f1.5$ series is 1.5 times that of $V_f2.0$, at both 1% and 2% strains.

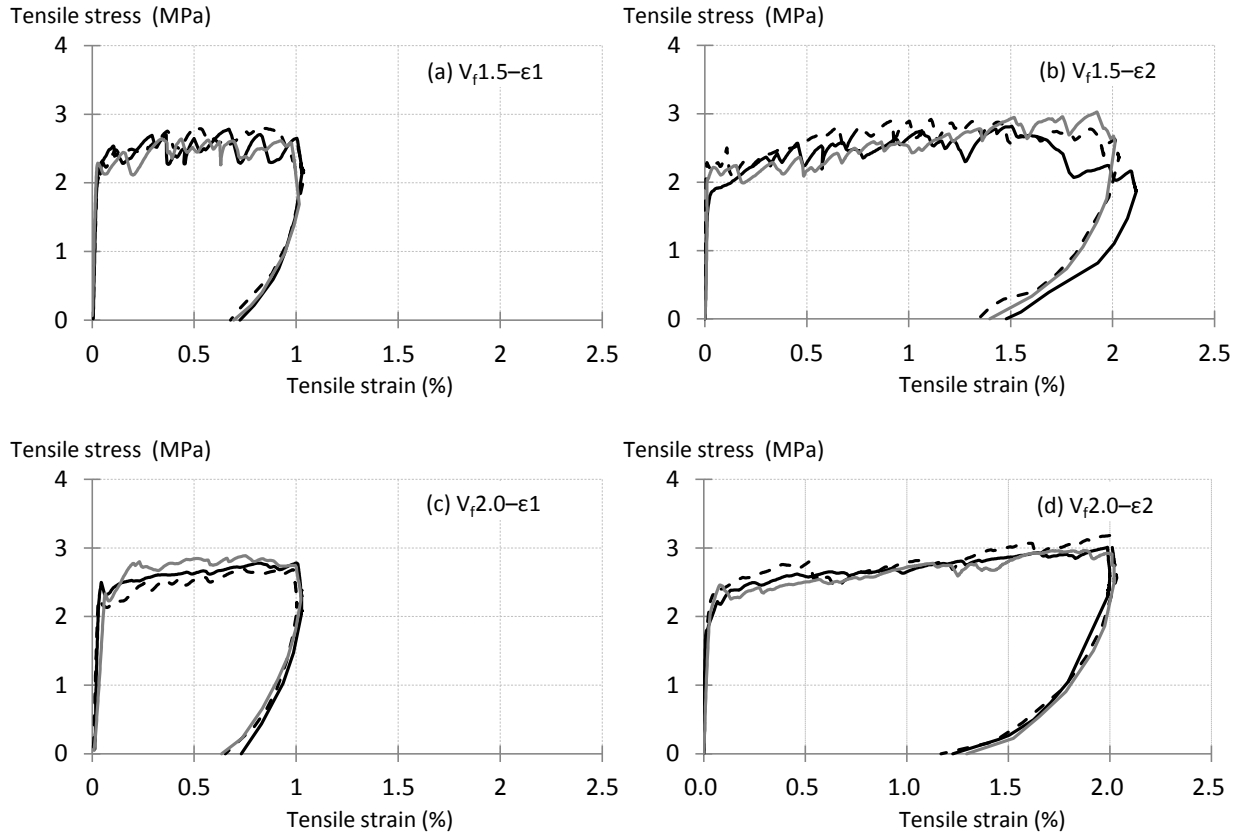


Fig. 5.5: Tensile stress-strain curves of EGC specimens under preloading.

Table 5.2: Residual-crack patterns of EGC.

Series	Specimen	Number of cracks			Maximum crack width (μm)	Average crack width (μm)
		Left edge	Center	Right edge		
$V_{f1.5-\epsilon 1}$	1	13	12	9	73.4	30.3
	2	8	14	10	66.8	24.6
	3	15	8	12	57.3	25.4
$V_{f1.5-\epsilon 2}$	1	16	15	12	779.9*	61.8
	2	15	16	19	156.0	38.6
	3	23	23	17	110.1	37.9
$V_{f2.0-\epsilon 1}$	1	13	12	22	78.8	16.5
	2	17	14	11	54.8	19.1
	3	17	19	15	351.0*	28.4
$V_{f2.0-\epsilon 2}$	1	25	36	17	770.4*	33.8
	2	24	22	28	61.4	22.8
	3	24	27	42	102.8	25.8

* A large localized crack was observed, probably due to insufficient compaction. These specimens might be regarded as outliers.

It should be noted that the number of cracks varies among the center and near-edge areas of the specimen surface. This variation results from cracks that bifurcated during propagation, and cracks that did not fully propagate through the matrix. In addition, crack width at the near-edge area was mostly larger than that at the central area. Typically, crack width measurement for ECC materials is performed on only the central longitudinal area [14], assuming that the crack opening is constant along each crack. However, the result here shows that the assumption of a constant crack width is not always true in ECC-type materials. Thus, multiple-point measurement for each crack is important, especially for the permeability test on cracked specimens where any part of the surface, not only the central area, can serve as a dominant pathway of water.

To better illustrate EGC cracking characteristics, density histograms of crack width and their fitted probability distributions are plotted in Fig. 5.6. The sample size N represents the total number of measurements on each series (i.e. measurements on the center and near-edge areas of each specimen), excluding the outliers. The bin width of $10\mu\text{m}$ is used as in previous studies on ECC [15, 16]. As can be seen, lognormal distributions are well fitted to all series of EGC. When compared with $V_f2.0$ series, $V_f1.5$ specimens have larger standard deviations for both 1% and 2% strain levels, as well as the larger estimated means. As a result, the $V_f1.5$ series has wider distributions with a higher probability of forming larger cracks (Fig. 5.7).

Lognormal distributions of crack width have been also reported for ECC materials [15–17], and are therefore regarded as general cracking characteristics of multiple-cracking fiber-reinforced cementitious composites. Besides, Ranade *et al.* demonstrated for ECC materials that the mean and standard deviation – two required parameters to fully characterize the lognormal distribution – of crack width can be expressed as cubic functions of the applied tensile strain. Based on the

estimated parameters, evolution of the crack-width distribution with strain can be predicted. However, the estimated mean and standard deviation might depend on the number of measurement points for each crack, as discussed above. To avoid inaccurate prediction of crack width distributions, multiple-point measurement is recommended in future studies.

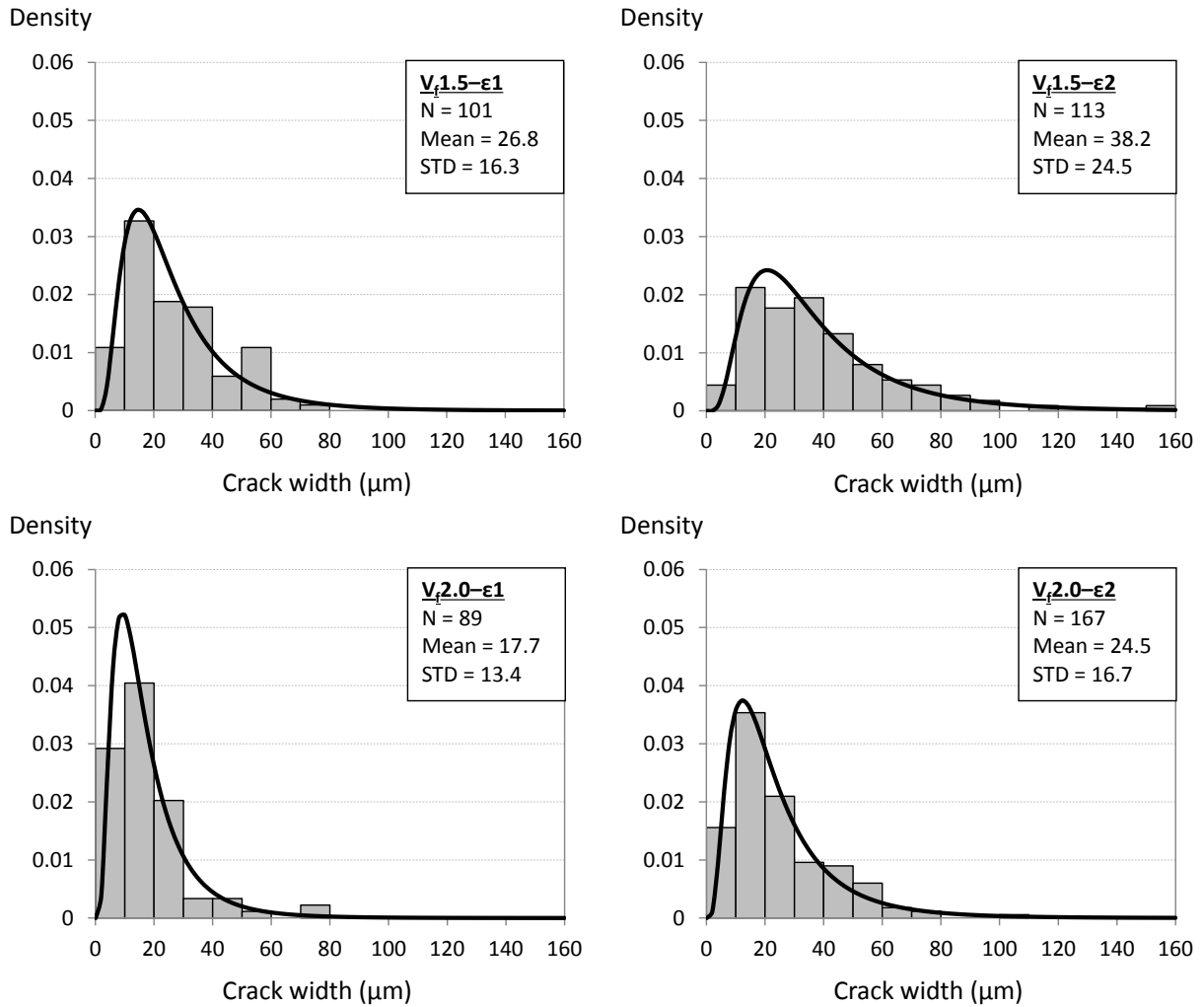


Fig. 5.6: Density histograms of EGC crack width and their fitted lognormal distributions.

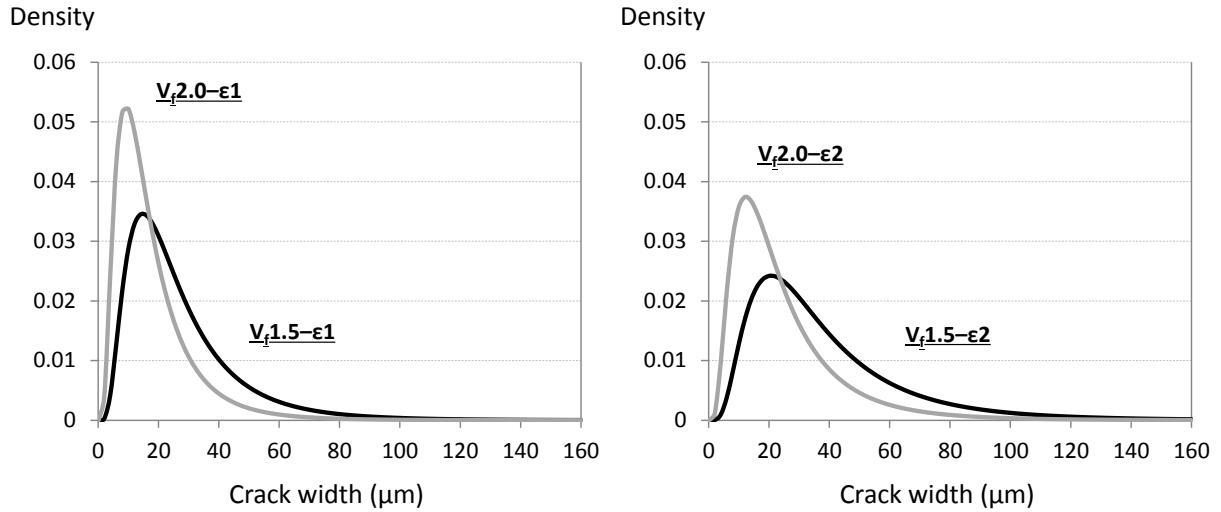


Fig. 5.7: Comparison between fitted probability distributions of $V_{f1.5}$ and $V_{f2.0}$ series.

5.3.2 Water permeability

Figure 5.8 shows coefficients of permeability for intact and cracked EGC, excluding the outliers. The average permeability coefficients of intact $V_{f1.5}$ and $V_{f2.0}$ specimens are 3.82×10^{-9} , and 2.28×10^{-9} cm/sec, respectively. This compares well with the permeability coefficients of uncracked normal concrete, FRC, and ECC reported in previous studies [3, 10, 11, 13, 16]. When strained up to 1%, both EGC series show considerable increase of 3 to 4 orders of magnitude in their permeability coefficients. On the other hand, the difference in permeability coefficients between 1% and 2% strains is only one order of magnitude or less.

Despite the larger crack width of $V_{f1.5}$ series, their water tightness is comparable to that of $V_{f2.0}$. When compared with $V_{f2.0}$ series, $V_{f1.5}$ specimens have larger permeability coefficients, but the difference is less than one order of magnitude in all strain levels. Therefore, while $V_{f1.5}$ series has 1.5 times larger average crack width than $V_{f2.0}$, the present result implies their similar durability performance related to permeation of aggressive agents.

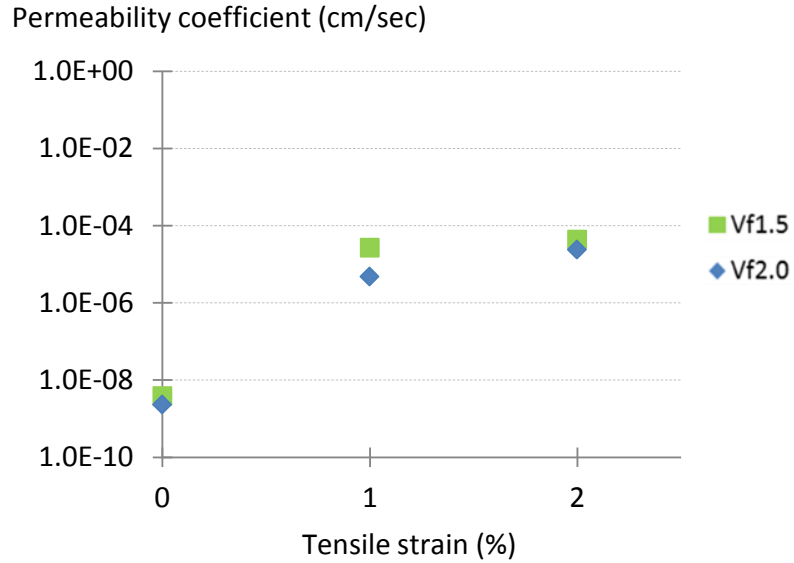


Fig. 5.8: Permeability coefficient of EGC versus applied tensile strain.

To further evaluate the water permeability of EGC, it is necessary to compare their permeability coefficients with those of normal concrete materials. However, when subjected to a similar tensile strain applied to the above EGC series, normal concrete definitely develops a very large crack and even fails. Thus, most previous studies on concrete permeability carefully controlled the applied deformation to specimens, and investigated the relationship between permeability and maximum crack width. Meanwhile, Lepech and Li prepared a series of reinforced-mortar specimens with various amounts of steel reinforcing mesh (ranging from 1.9% to 2.9%) to prevent the brittle failure and achieve desired crack widths [13]. The specimens were deformed to uniaxial tensile strain of 1.5%, and their water permeability coefficients were compared with those of ECC specimens subjected to similar strain levels. Detailed information on the reinforced mortar and ECC can be found in [13]. Those data from the study by Lepech and Li are useful to compare with EGC permeability data obtained in this study.

Figure 5.9 shows the comparison of permeability coefficients for EGC, ECC and reinforced cement mortar. Permeability coefficients of cracked reinforced mortars range from 3.02×10^{-6} to 4.46×10^{-2} cm/sec. Only one of the series shows a comparable permeability to cracked EGC, but the specimen has a high amount of steel reinforcement of 2.9%, which is not economical in practice. Therefore, when subjected to the same strain level, degradation in water permeability is significantly limited in EGC compared to typical reinforced mortar/concrete. On the other hand, cracked ECC shows better water tightness than cracked EGC: their permeability coefficients range from 1.95×10^{-8} to 7.74×10^{-8} cm/sec, which are 2 to 3 orders of magnitude smaller than those of cracked EGC, even at a tensile strain of 3%.

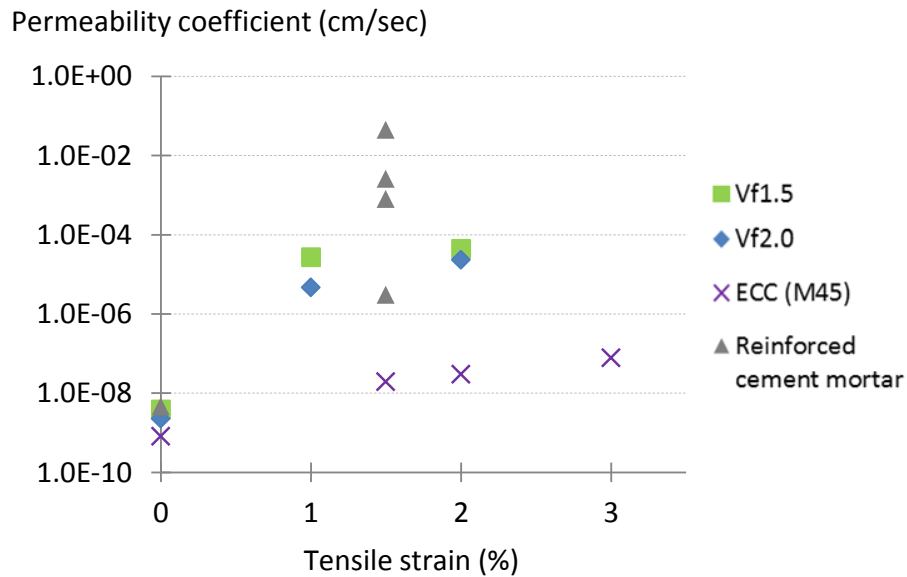


Fig. 5.9: Comparison of permeability coefficients for EGC, ECC and reinforced cement mortar.

The test results also show that permeability coefficients are highly dependent on crack width, regardless of the material type. The reinforced-mortar specimen that shows comparable permeability to EGC has similar maximum crack width and number of cracks to those of EGC. Other reinforced mortars have fewer cracks with a large localized crack of 240 to 500 μm , and

show 2 to 3 orders of magnitude higher permeability coefficients than EGC. In the case of ECC, the maximum crack width is only 63 μm even at 3% strain. While the average crack width is not reported in the paper, those ECC specimens have more microcracks and smaller crack spacing than EGC, implying a tighter average crack width.

The critical role of crack width in concrete permeability has been also pointed out by many researchers. In those studies, permeability coefficients are typically plotted against maximum crack width. Since the water flow rate in concrete materials scales to the third power of crack width [4], the largest crack is supposed to dominantly govern the water permeation. The permeability coefficient versus maximum crack width is thus analyzed for EGC, as well as cement concrete studied by Wang *et al.* [3], and reinforced cement mortar and ECC by Lepech and Li [13] (Fig. 5.10). The outliers of EGC are also plotted in the graph for reference.

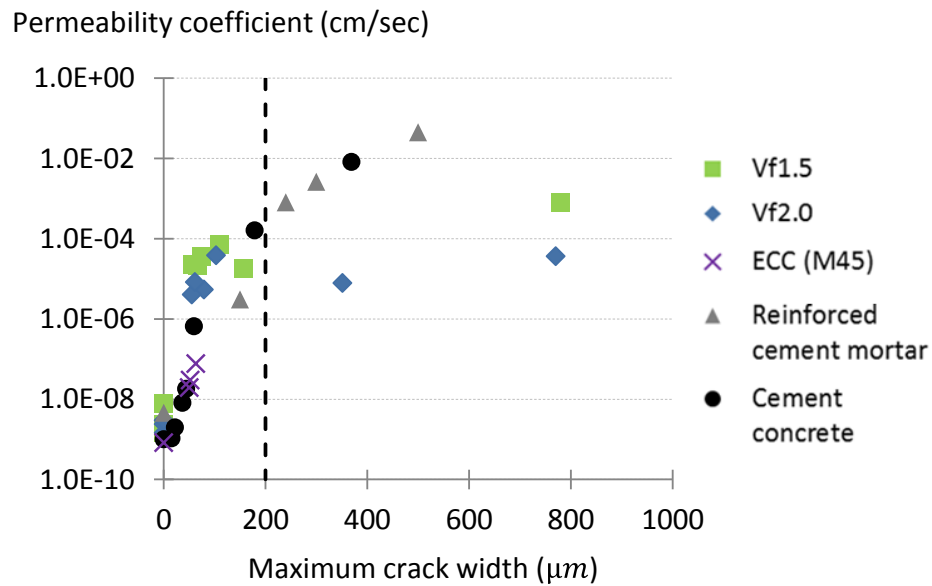


Fig. 5.10: Permeability coefficient versus maximum crack width (after unloading) for cement concrete [3], reinforced cement mortar, ECC [13], and EGC (outliers included).

For crack width of less than 200 μm , similar increasing trends in the permeability coefficient can be seen in all the materials. Data on EGC do not include the outliers in this range and therefore represent the inherent property of EGC permeability. It should be noted, however, that EGC specimens have many microcracks in the tested area, with a small variance in crack width. In such cases, many cracks – not only the largest one – can serve as a significant pathway of water. In contrast, concrete and reinforced mortar have fewer cracks, with damage localized in a single crack. The largest crack has a dominant effect on the permeability in such materials. Therefore, when related to maximum crack width, EGC permeability coefficients tend to be overestimated compared to normal concrete materials. The same is true for ECC materials. To make a fair comparison, Lepech and Li suggested normalizing the permeability coefficients of cracked ECC by the number of cracks [13]. By applying this normalization, permeability coefficients of EGC compare well to those of concrete and reinforced mortar.

A different trend can be seen in data for crack width of over 200 μm : permeability coefficients of EGC are limited compared to those of concrete and reinforced mortar in this range. As discussed in the preceding section, those EGC specimens have localized large cracking and do not reflect the inherent cracking characteristics of EGC. However, if the quality of workmanship were poor in actual applications, it might be possible for such a large crack to form in the EGC structure. The test result implies that EGC can significantly limit the permeability increase even in the unfavorable case. On the other hand, a large crack is not uncommon in RC structures even when the concrete is well compacted and finished. Then, water permeability of the structure considerably increases with crack opening, as suggested by the data of concrete and reinforced mortar in Fig. 5.10.

The limited EGC permeability for crack width of over 200 μm might be attributed to the unique distribution of damage. As mentioned in the preceding section, crack width in EGC is not constant along each crack. The unintended large cracking mostly started from the edge of the specimen, but the localized damage did not propagate fast and was confined to the near-edge area. Indeed, the measured maximum crack width only represents the crack opening at a small area. As a result, the rate of water flow in that small area might not be dominant in the total flow rate of the tested area. This could explain the little correlation between permeability coefficient and maximum crack width of EGC, especially for $V_f2.0$ series. It should be noted that ECC materials with unintended poor compaction or fiber dispersion typically exhibit strain-softening behavior with a localized crack that propagates through the matrix much faster. Further research is required to understand mechanisms behind the suppressed propagation of unintended localized cracking in EGC.

From the discussion above, the maximum crack width is not an appropriate factor to relate the water permeability of EGC. However, when plotted against average crack width, EGC permeability shows a distinct positive correlation even when the outliers are included (Fig. 5.11). Particularly, a linear relationship can be seen between the average crack width and the log of permeability coefficient of cracked EGC. While few previous studies focused on the average crack width of the tested specimens, it might be possible to predict water permeability from average crack width for ECC-type materials. Further research is also needed to verify this hypothesis.

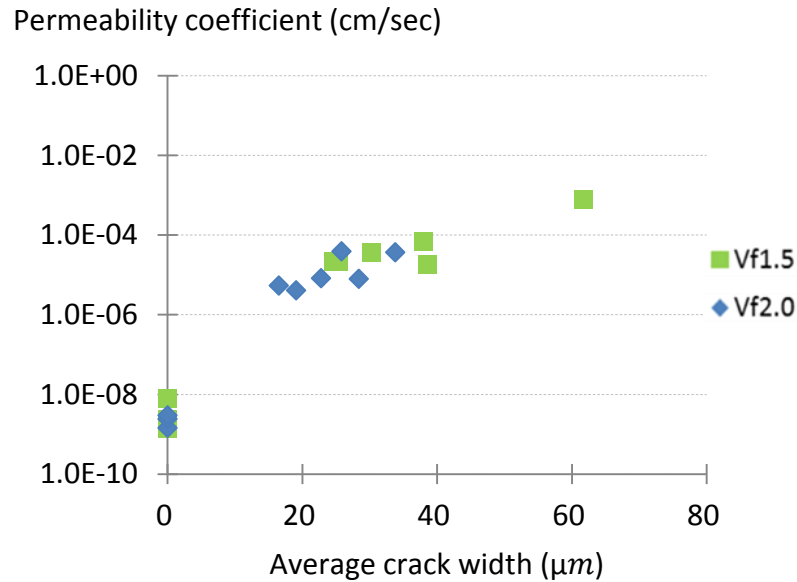


Fig. 5.11: Permeability coefficient versus average crack width of EGC.

5.3.3 Sealed cracks and reduction in permeability

During the course of this study, a possibility of self-healing in EGC was discovered. There was an extra specimen that was preloaded to create microcracks and then stored in water for months. Interestingly, white substance was formed on the specimen surface, especially within the cracks. The same phenomenon was also reported for ECC in previous studies [13, 18]. As a result of the sealed cracks, cracked ECC specimens showed significant decrease in permeability coefficients (i.e. recovery in water tightness) with time. This could be another reason that permeability coefficients of cracked ECC are significantly lower than those of EGC, apart from the difference in crack width (discussed in the preceding section). The white substance in EGC implied that a similar decrease in the permeability was possible. Therefore, the preloaded specimens used in the permeability test were moved back to a water bath after the test, and cured for about 90 days prior to the second round of the permeability measurement.

The test result indicates that consistent decrease in permeability coefficients is only observed in $V_f1.5-\epsilon1$ and $V_f2.0-\epsilon1$. Table 5.3 lists the initial permeability coefficients (labeled “Pre-permeability coefficient”) and permeability coefficients measured in the second round (labeled “Post-permeability coefficient”). Positive values in Percent change represent permeability coefficients that decreased after the 90-day water curing. Thus, all specimens show recovery in water tightness to some extent.

Table 5.3: Change in permeability coefficients of EGC with time.

Series	Specimen	Pre-permeability coefficients (cm/sec)	Post-permeability coefficients (cm/sec)	Percent change (%)
$V_f1.5-\epsilon1$	1	3.65E-05	1.27E-05	65.1
	2	2.16E-05	3.28E-06	84.8
	3	2.21E-05	5.50E-06	75.1
$V_f2.0-\epsilon1$	1	5.37E-06	2.56E-06	52.4
	2	4.04E-06	6.03E-07	85.1
	3	7.90E-06	6.37E-06	19.4

Despite the observed decrease in permeability coefficients, there was a limited amount of white substance visible on the specimen surface, compared to the extra specimen mentioned above. In addition, the degree of reduction in EGC permeability coefficients was significantly smaller than that found in ECC by Lepech and Li [13]. Therefore, robust self-healing in EGC materials could not be completely evidenced by this result.

Precipitation of the white residue might be even detrimental. Some studies reported that white precipitates on geopolymer surface were a result of *efflorescence* – formation of salt deposits caused by the reaction of cations leached from the pore solution with CO_2 in air [19]. In portland cement concrete, efflorescence also occurs from the reaction of leached calcium ions with water and CO_2 , but is generally considered harmless; the amount of calcium ions in the pore solution is

typically limited, and the effect of efflorescence on binder degradation is thus negligible. Conversely, efflorescence in geopolymers might be a significant issue because of the higher concentrations of soluble alkali metal cations available [20]. Indeed, Zhang *et al.* found that efflorescence had negative effects on compressive strength and stiffness of fly ash-based geopolymers [21]. Therefore, it is important to know whether the white substance formed in EGC results from beneficial self-healing or detrimental efflorescence. Further research to address this question has been conducted, which is reported in the following chapter.

5.4 Summary and conclusions

Cracking characteristics and water tightness have been experimentally determined for the developed EGC with fiber contents of 1.5% and 2.0%. The test result indicates that $V_f1.5$ series has 1.5 times larger crack width on average than $V_f2.0$ series. Nevertheless, their water permeability is comparable at both 1% and 2% strain levels. It is therefore suggested that the $V_f1.5$ series has comparable transport properties and related durability to the $V_f2.0$, even with the smaller fiber content. Combined with the results on their mechanical properties and environmental performances obtained in Chapter 4, it can be concluded that the $V_f1.5$ series is preferable to $V_f2.0$. In addition, it has been found that degradation in water tightness of EGC is significantly limited compared to that of normal reinforced mortar/concrete. This result suggests better transport properties and related durability of EGC.

The other findings obtained in this study are listed below;

- Residual crack width of EGC is lognormally distributed for both 1% and 2% strain levels.

- A few specimens showed a localized large crack during the uniaxial tension test, but the crack did not propagate through the matrix and the damage was confined to the near-edge area. Mechanisms behind this suppressed propagation of localized cracking would be a subject of further studies.
- Crack width of EGC is not constant along each crack, and the numbers of cracks are different between the central area and near-edge sides of the specimen surface. Measuring multiple points for each crack is recommended to accurately evaluate the crack patterns.
- Due to the nonuniform opening along each crack, maximum crack width only represents the crack opening in a small area. As a result, there is little correlation between the maximum crack width and permeability coefficients of EGC.
- Instead, a distinct linear relationship is observed between average crack width and permeability coefficient. It might be possible to predict EGC water permeability from the average crack width, but further research is required to verify the hypothesis.
- During the course of this study, a white substance formed on the specimen surface and blocking the microcracks was observed. Time-dependent decrease in permeability coefficients has been also confirmed in specimens subjected to 1% strain.

The last finding suggests a possibility of self-healing phenomenon in EGC materials. However, it is also possible that precipitation of the white substance resulted from efflorescence, which could be detrimental to mechanical properties of geopolymers. Thus, a further investigation on the white precipitate is required to confirm the feasibility of self-healing EGC. The following chapter is concerned with this.

References

- [1] N. R. Buenfeld, “Measuring and modeling transport phenomena in concrete for life prediction of structures,” in *Prediction of concrete durability: proceedings of STATS 21st anniversary conference*, J. Glanville and A. Neville, Eds. London, UK: E & FN Spon, 1995, pp. 77–90.
- [2] H. W. Reinhardt, “Transport Properties of Concrete,” in *Penetration and Permeability of Concrete: Barriers to organic and contaminating liquids*, H. W. Reinhardt, Ed. London, UK: E & FN Spon, 1997, pp. 213–264.
- [3] K. Wang, D. C. Jansen, S. P. Shah, and A. F. Karr, “Permeability study of cracked concrete,” *Cem. Concr. Res.*, vol. 27, no. 3, pp. 381–393, 1997.
- [4] M. Tsukamoto, “Tightness of fiber concrete,” *Darmstadt Concr.*, vol. 5, no. 3, pp. 215–225, 1990.
- [5] ACI 318S, *Building Code Requirements for Structural Concrete and Commentary*. Farmington Hills, MI: American Concrete Institute, 2011.
- [6] AASHTO, “AASHTO LRFD Bridge Design Specifications, 7th Edition,” 2014.
- [7] ASTM C76-16, *Standard Specification for Reinforced Concrete Culvert, Storm Drain, and Sewer Pipe*. West Conshohocken, PA: ASTM International, 2016.
- [8] V. Li and H. Stang, “Elevating FRC material ductility to infrastructure durability,” in *6th RILEM Symposium on Fiber-Reinforced Concretes (FRC) - BEFIB 2004*, 2004, pp. 1–16.
- [9] C.-M. Aldea, S. P. Shah, and K. Alan, “Effect of cracking on water and chloride permeability of concrete,” *J. Mater. Civ. Eng.*, vol. 11, no. 3, pp. 181–187, 1999.
- [10] C.-M. Aldea, S. P. Shah, and A. Karr, “Permeability of cracked concrete,” *Mater. Struct.*, vol. 32, no. 5, pp. 370–376, 1999.
- [11] J. Rapoport, C.-M. Aldea, S. P. Shah, B. Ankenman, and A. Karr, “Permeability of Cracked Steel Fiber-Reinforced Concrete,” *J. Mater. Civ. Eng.*, vol. 14, no. 4, pp. 355–358, Aug. 2002.
- [12] J. S. Lawler, D. Zampini, and S. P. Shah, “Permeability of cracked hybrid fiber-reinforced mortar under load,” *ACI Mater. J.*, vol. 99, no. 4, pp. 379–385, 2002.
- [13] M. D. Lepech and V. C. Li, “Water permeability of engineered cementitious composites,” *Cem. Concr. Compos.*, vol. 31, no. 10, pp. 744–753, Nov. 2009.
- [14] Japan Society of Civil Engineers, *Recommendations for Design and Construction of High Performance Fiber Reinforced Cement Composites with Multiple Fine Cracks (HPFRCC)*, vol. 82. Tokyo, Japan: JSCE, 2008.

- [15] R. Ranade, J. Zhang, J. P. Lynch, and V. C. Li, "Influence of micro-cracking on the composite resistivity of Engineered Cementitious Composites," *Cem. Concr. Res.*, vol. 58, pp. 1–12, Apr. 2014.
- [16] H. Liu, Q. Zhang, C. Gu, H. Su, and V. C. Li, "Influence of micro-cracking on the permeability of Engineered Cementitious Composites," *Cem. Concr. Res.*, vol. 72, pp. 104–113, 2016.
- [17] P. Wang, F. H. Wittmann, T. Zhao, and W. Huang, "EVOLUTION OF CRACK PATTERNS ON SHCC AS FUNCTION OF IMPOSED STRAIN," in *2nd int. RILEM conf. on strain hardening cementitious composites*, 2011, pp. 217–224.
- [18] H. Liu, Q. Zhang, C. Gu, H. Su, and V. Li, "Influence of microcrack self-healing behavior on the permeability of Engineered Cementitious Composites," *Cem. Concr. Compos.*, vol. 82, pp. 14–22, 2017.
- [19] J. L. Provis and S. A. Bernal, "Geopolymers and Related Alkali-Activated Materials," *Annu. Rev. Mater. Res.*, vol. 44, pp. 299–327, 2014.
- [20] Z. Zhang, H. Wang, J. L. Provis, and A. Reid, "Efflorescence : A Critical Challenge for Geopolymer Applications?," in *Concrete Institute of Australia's Biennial National Conference*, 2013.
- [21] Z. H. Zhang, T. Yang, and H. Wang, "The Effect of Efflorescence on the Mechanical Properties of Geopolymers," in *23rd Australasian Conference on the Mechanics of Structures and Materials*, 2014, vol. I, pp. 107–112.

CHAPTER 6: Feasibility Study of Self-healing EGC

In this chapter, a feasibility study on self-healing functionality of EGC is documented. An experimental investigation is conducted to measure the mechanical-performance recovery of pre-cracked EGC due to self-healing. In addition, self-healing products are observed by scanning electron microscopy (SEM) and examined using energy dispersive spectroscopy (EDS).

6.1 Introduction

Cement materials have inherent self-healing functionality. Indeed, autogenous healing of cracks in cement concrete has been reported for many years, even since the 19th century [1]. Early academic research on the phenomenon dates back to the end of 19th century [2], and active research activities have been done in the past few decades. Based on the intensive studies, three major mechanisms have been proposed for the self-healing phenomenon in cement-based materials:

- Hydration of unreacted cement – unhydrated cement in the hardened matrix reacts with water in cracks, creating calcium silicate hydrates (CSH) and other hydration products.
- Calcite ($CaCO_3$) formation – binding of calcium ions on crack surfaces with carbonate ions dissolved from atmospheric carbon dioxide (CO_2).
- Pozzolanic reaction – aluminate or silicate species and calcium hydroxide ($CaOH$) in the matrix react with water, producing CSH and other phases.

Theoretically, self-healing can occur in the presence of only water and CO₂ (i.e. under a normal condition of most structures).

Recently, the concept of self-healing concrete has been gaining increasing attention. Particularly, the technology is attractive to many developed countries facing a huge financial burden for repair and rehabilitation of their aging infrastructure. Moreover, smart concrete structures that can autogenously recover from damage are also promising for enhancing the resiliency for public safety. Such societal needs are driving the active research and development of new technologies to maximize the self-healing functionality of cement concrete. Today, various types of self-healing concrete and relevant techniques have been developed, including encapsulation of healing chemicals [3] or calcite-producing bacteria [4], inclusion of mineral admixtures [5], and healing agents activated by a heating device embedded in the cement matrix [6].

ECC is another promising candidate for self-healing concrete. Yang *et al.* experimentally demonstrated that ECC exhibits significant stiffness recovery (more than 80% of the initial stiffness) even when strained up to 3% [7]. Herbert and Li also found that self-healing of ECC is repeatable under multiple loading cycles [8]. Moreover, ECC has been demonstrated to self-heal even under chloride or highly alkaline environments [9, 10]. More importantly, self-healing ECC simply utilizes the intrinsic healing functionality of cement materials to achieve the high performance recovery, repeatability, and versatility; in contrast, other technologies often require cost-intensive additives, components, or devices to impart the self-healing capability to the concrete material.

It is the self-controlled microcracking that realizes the enhanced self-healing in ECC. The tight crack width is beneficial for self-healing products to precipitate and fully seal the crack.

Conversely, even if a material has a self-healing functionality, it cannot autogenously heal large cracks, just as human bodies cannot cure serious wounds by themselves. Therefore, damage control plays a key role in bringing out the healing potential of cement materials. The same may be true for geopolymers; today, only a handful of papers have been published to report the self-healing of geopolymers [5, 11, 12], which does not necessarily imply low/no self-healing functionality of the material. If the crack width can be tightly controlled, robust self-healing might also be possible in geopolymers.

The objective of this study is to demonstrate the feasibility of self-healing EGC. EGC specimens are first uniaxially loaded to create cracks and subjected to three different conditioning regimes prior to reloading: air-curing or water-curing for 120 days, or no curing (i.e. reloading right after preloading). Stiffness recovery due to self-healing is evaluated by comparing the initial stiffness of intact specimens and the residual stiffness in reloading. During the course of curing, cracks are photographically recorded regularly, to capture the formation of healing products. In addition, the microstructure of healing products is observed by using a scanning electron microscope (SEM). An elemental analysis is also conducted by using an energy dispersive spectroscopy (EDS) system.

6.2 Materials and methods

6.2.1 Mix design and specimen preparation

The mix design of EGC in this study is similar to the $V_f2.0$ series developed in Chapter 4. Table 6.1 presents the mix proportion of ingredients. A lower amount of sand was incorporated to facilitate the self-healing by relatively increasing the paste volume. Also, the fiber volume

fraction of 2% was used since it has been reported that self-healing products in cement materials are preferably precipitated around PVA fibers due to the high polarity of the hydroxyl group [13].

Table 6.1: Mix design of EGC used in this study (by mass).

Fly ash A (Sammis)	Fly ash B (Monroe)	Sand	Na ₂ SiO ₃	NaOH (pellet)	Pre-mix water	Mix water	PVA fiber
0.6	0.4	0.2	0.225	0.044	0.031	0.10	0.021

The mixing procedure and the method of temperature curing were the same as those detailed in Section 4.2.1 and 5.2.2. A total of 11 dog bone specimens were prepared, two of which included no sand and were investigated by SEM and EDS. Those two specimens consisted of only components involved in self-healing (i.e. paste, fiber, and self-healing products), which were easier to be differentiated in the microscopic observation and elemental analysis.

6.2.2 Mechanical testing

Specimens were divided into four groups, referred to as “W-1%”, ”A-1%”, ”R-1%”, and “SEM-1%”, respectively. Test procedures for each group are schematically illustrated in Fig. 6.1.

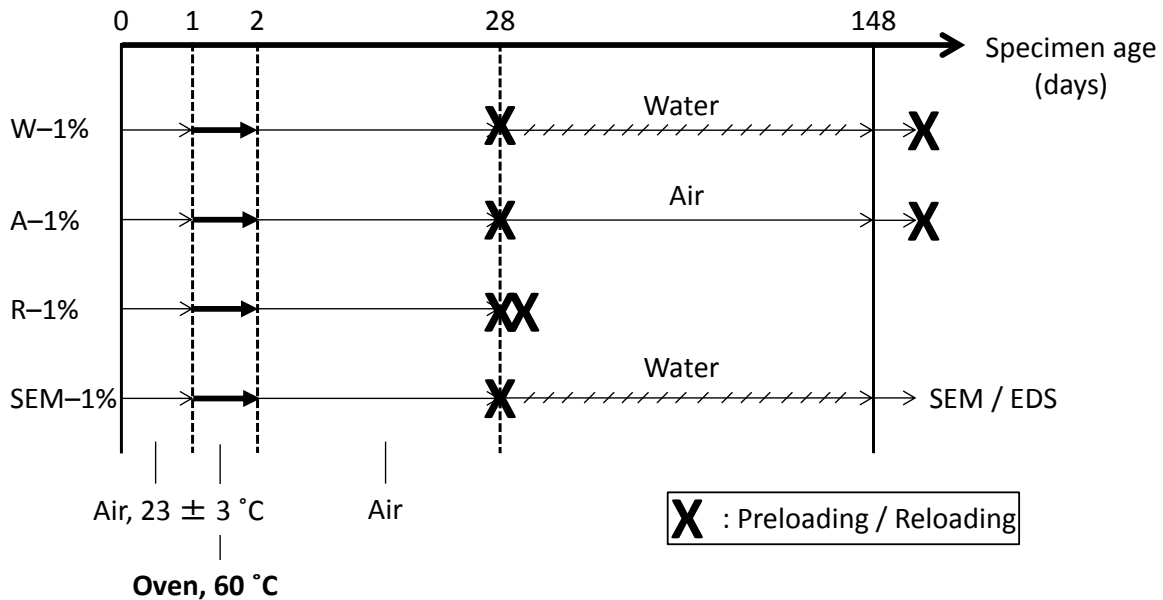


Fig. 6.1: Test schedule and curing condition for each series of EGC.

The first group, W-1%, had specimens that were uniaxially loaded to a tensile strain of 1% at the age of 28 days. The test setup was the same as the dog bone testing detailed in Section 4.3.1. After unloading, the preloaded specimens were cured in water for 120 days, during which the microcracks were regularly photographed under an optical microscope. The specimens were then air-dried for at least 24 hours, followed by reloading of the specimens in the identical test setup. Specimens in the second group were also preloaded to 1% strain, but cured in air for 120 days prior to reloading. For the third group, specimens were also preloaded to 1% and unloaded. Reloading was then conducted right after the preloading, without any conditioning. Specimens in the fourth group underwent the same preloading and conditioning as those of W-1%. The preloaded specimens were then investigated by using the SEM and EDS analysis. Each group had three specimens, except the fourth group (SEM-1%) which had only two specimens.

If self-healing of geopolymers requires the presence of water as in self-healing cement concrete, W-1% series should have the largest amount of healing products and the highest stiffness recovery. Conversely, the degree of self-healing might be limited in A-1%. Therefore, effects of water curing on geopolymer self-healing can be evaluated by comparing the stiffness recovery of W-1% and A-1%. On the other hand, the third group, R-1%, is a control series without any conditioning, and can be used to determine the stiffness reduction due to the applied 1% strain.

For stiffness measurement, chord modulus was used in this study; chord modulus is the slope of the line drawn between two specified points on the stress-strain curve [14], and calculated by using the following equation:

$$E_{\sigma_b - \sigma_a} = \frac{\sigma_b - \sigma_a}{\varepsilon_b - \varepsilon_a} \quad (6.1)$$

where $E_{\sigma_b-\sigma_a}$ is the chord modulus between two stresses σ_b and σ_a (at point b and a , respectively); ε_b and ε_a are the corresponding strain values. As in a previous study on self-healing ECC [8], chord modulus between 0.5 and 2 MPa was measured for each specimen. Then, stiffness ratio was defined as the ratio of residual stiffness at reloading to initial stiffness at preloading:

$$R_{\sigma_b-\sigma_a} = \frac{E'_{\sigma_b-\sigma_a}(\text{reload})}{E_{\sigma_b-\sigma_a}(\text{preload})} \quad (6.2)$$

When the full recovery is achieved, the value of R becomes unity.

6.2.3 SEM observation and EDS analysis

After the 120-day water curing, a small prism that contained a microcrack and white precipitates within the crack was cut from a specimen of SEM-1% series. Grinding and polishing were not applied so as to prevent damage on the white deposits. For SEM observation, a large-field detector that captures secondary electrons was used in a low-vacuum environment.

For the elemental analysis of white precipitates, an EDS analyzer equipped with the SEM was used. The accelerating voltage and spot size were 10 kV and 0.23 nA, respectively. Elemental compositions were analyzed along a line segment that crossed a microcrack (and healing products within the crack), starting from the uncracked region of the composite. This line-scan function was useful to detect the relative difference in chemical compositions between the EGC matrix and healing products. In addition, a map-scan was conducted to complement the line-scan elemental analysis. The mapping function enabled information on the element concentration to be overlaid on top of the SEM image. Thus, the relative difference in the atomic percent could be visualized at any point in the mapped region.

6.3 Results and discussion

6.3.1 Visual appearance of sealed crack

During the course of water curing, white precipitates were observed within microcracks of W-1% and SEM-1% specimens. The degree of precipitation was, however, variable; some cracks were completely sealed with the white residue, while some cracks were only partially sealed. Figure 6.2 shows images of completely- and partially-sealed cracks in the water-cured series. In addition, different rates of healing were also found; white precipitates in the completely- and partially-sealed cracks can be seen in photographs taken at 7 and 30 days after preloading, respectively. Despite the different degrees and rates of healing, both cracks are tightly controlled, and there is no significant difference in their crack width. Although factors causing the variability are not clear, self-healing in EGC is clearly limited compared to that in ECC where most of microcracks are completely sealed. This limited formation of healing products implies lower performance recovery in EGC.

In the case of A-1% series, no white substance was observed in all specimens during the 120-day air curing. The number of cracks and crack width distribution is similar to those of W-1%, and SEM-1% series. Yang *et al.* reported that air-cured ECC specimens also showed no significant healing product [15]. Therefore, the presence of water is essential in self-healing of geopolymers, as in cement-based self-healing. The total absence of white precipitates in A-1% specimens suggests no performance recovery in this series, and their stiffness ratio R should be close to the reference values of R-1% series.

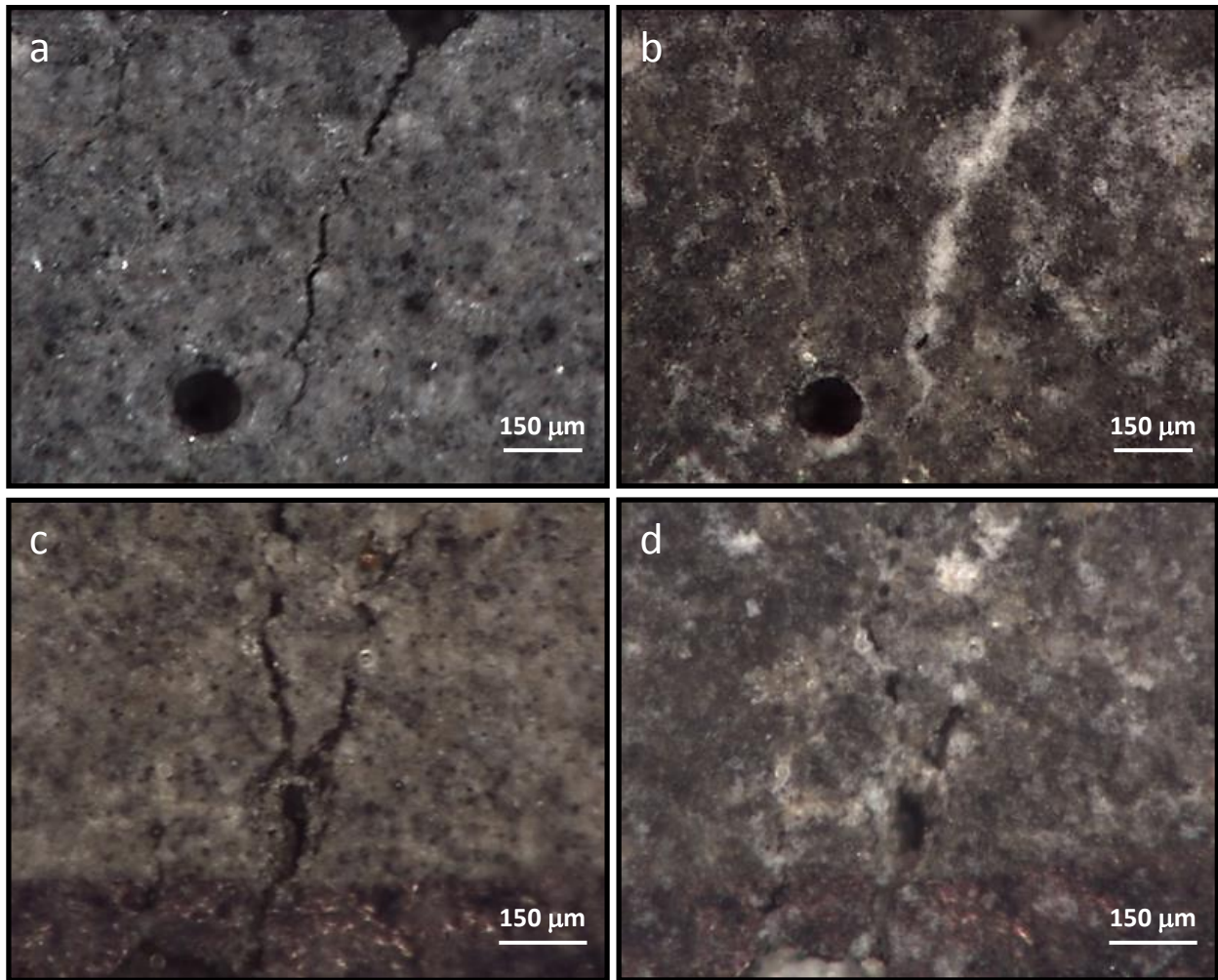


Fig. 6.2: Images of EGC microcracks right after preloading and after water curing: (a)(b) a completely-sealed microcrack; and (c)(d) a partially-sealed microcrack.

6.3.2 Stiffness recovery

Table 6.2 summarizes the averaged initial and residual stiffnesses, and stiffness ratio for each series. First and foremost, no significant recovery can be found in all series. The stiffness ratios of W-1% and A-1% are 9.0 ± 3.8 and $7.8 \pm 3.1\%$. The difference between the two series is statistically insignificant based on a t-test assuming that the data are normally distributed with the equal variance. Therefore, completely or partially sealed cracks in W-1% specimens provide no significant recovery in the chord modulus between 0.5 and 2 MPa. It should be also noted that

the stiffness ratio of R-1% (i.e. no conditioning and aging) is larger than that of W-1%. This might be attributed to the relatively lower initial stiffness of R-1%, probably caused by material variability. Due to the lower initial stiffness, the stiffness ratio of R-1% is calculated to be higher by its definition. Indeed, the residual stiffness of R-1% is close to those of W-1% and A-1%. This implies that the applied 1% strain reduces the stiffness to a similar level in all series, and that no significant recovery has been achieved in both W-1% and A-1% series.

Table 6.2: Initial and residual stiffness and stiffness ratio for the range of 0.5 – 2.0 MPa.

Series	Initial stiffness $E_{0.5-2.0}$ (GPa)	Residual stiffness $E'_{0.5-2.0}$ (GPa)	Stiffness ratio $R_{0.5-2.0}$ (%)
W-1%	8.4 ± 2.2	0.70 ± 0.17	9.0 ± 3.8
A-1%	8.7 ± 3.0	0.62 ± 0.07	7.8 ± 3.1
R-1%	5.6 ± 0.8	0.68 ± 0.06	12.5 ± 2.6

Despite the no recovery observed for the chord modulus between 0.5 and 2.0 MPa, detailed examination of the stress-strain curves has revealed a possibility of stiffness recovery in W-1% series. Figure 6.3 shows portions of typical stress-strain curves of each series during preloading and reloading, and corresponding chord modulus between 0.5 and 2 MPa for reloading. As can be seen, there is a high nonlinearity in the reloading curve of W-1% compared to the drawn chord. In contrast, deviation of the stress-strain curve from the chord is limited in both A-1% and R-1%. It is clear that W-1% series has significantly higher stiffness in the range of lower stress than those of the other series. Thus, the chord modulus between 0.5 and 2 MPa does not fully reflect the stiffness profile of EGC in reloading.

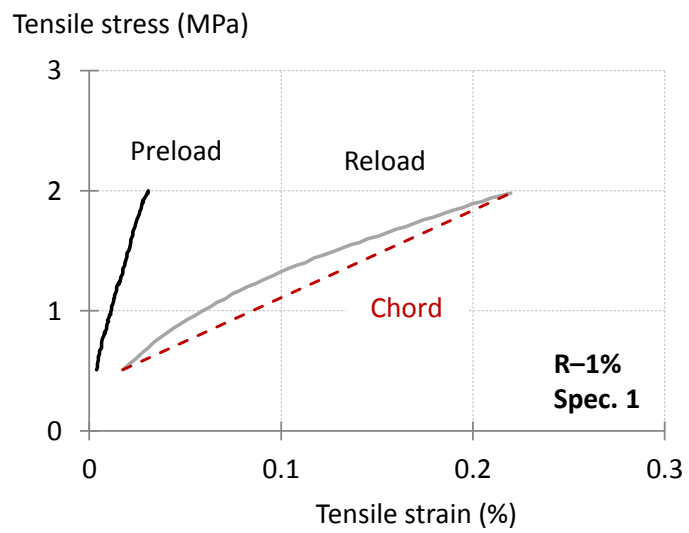
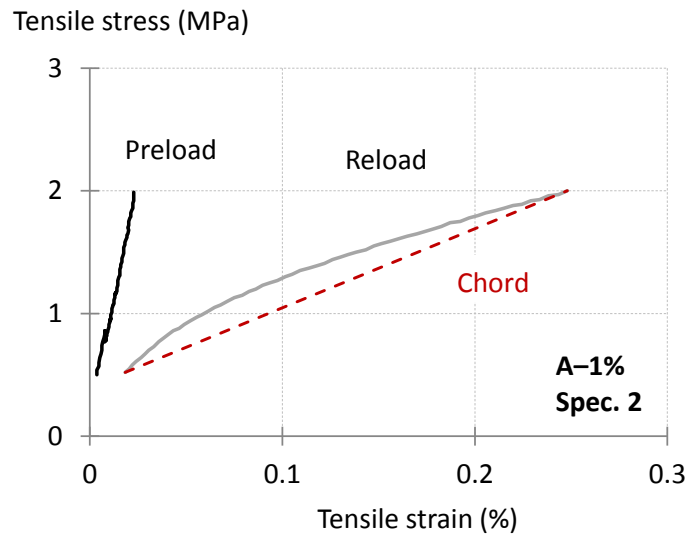
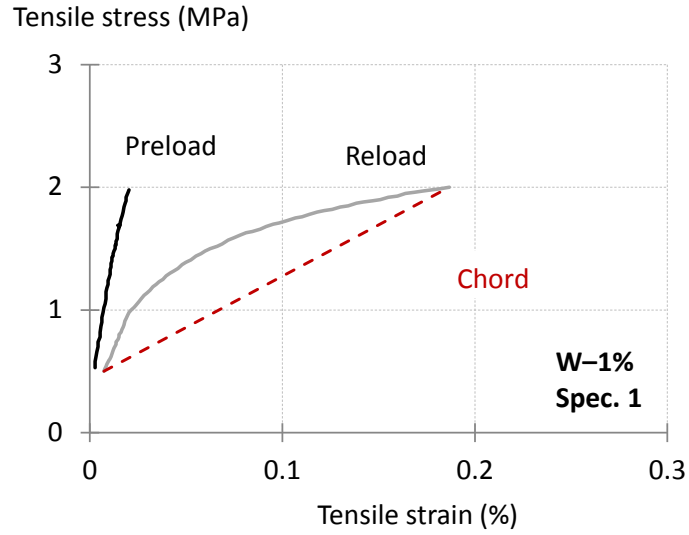


Fig. 6.3: Portions of stress-strain curves at preloading and reloading and chord modulus for reloading.

To accurately evaluate the stiffness recovery, the chord modulus between 0.5 and 1.0 MPa is measured for all series, which is presented in Table 6.3. Now, the averaged residual stiffness of W-1% is more than twice that of A-1% or R-1%. The W-1% stiffness ratio is 24.6% on average, which is significantly higher than the other series. Also, the stiffness ratio of A-1% is similar to that of R-1% for this chord modulus. This agrees with the initial expectation that the stiffness ratio of A-1% should be close to that of R-1%, as a result of no self-healing. Therefore, the chord modulus for the lower stress levels seems appropriate for evaluating the stiffness recovery in EGC.

Table 6.3: Initial and residual stiffness and stiffness ratio for the range of 0.5 – 1.0 MPa.

Series	Initial stiffness $E_{0.5-1.0}$ (GPa)	Residual stiffness $E'_{0.5-1.0}$ (GPa)	Stiffness ratio $R_{0.5-1.0}$ (%)
W-1%	10.4 ± 1.1	2.60 ± 0.91	24.6 ± 8.6
A-1%	8.1 ± 2.1	1.18 ± 0.17	15.5 ± 5.2
R-1%	7.0 ± 1.5	1.11 ± 0.09	16.2 ± 2.6

From the above discussion, stiffness recovery in the present version of EGC is limited and only significant for lower stress levels. Nevertheless, the present test result has confirmed the possibility of self-healing EGC with mechanical-performance recovery. If most of the microcracks could be completely healed, enhanced recovery should be possible. To improve the self-healing functionality, mechanisms behind self-healing in EGC should be investigated. The following SEM observation and EDS analysis provide some information to understand the mechanisms.

6.3.3 Observation and elemental analysis on self-healing products

Figure 6.4 shows SEM micrographs of a sealed crack in an SEM-1% specimen. Most of the white precipitates sealing the microcrack seem to have angular, stone-like shape (Fig. 6.4(a)). As

mentioned in Section 6.2.1, no silica sand is incorporated in this specimen. Kan *et al.* reported that stone-like particles were formed within microcracks of self-healing ECC, and found to be mainly composed of calcite ($CaCO_3$). While they also found fiber-like healing products (identified as CSH gel), such substance has not been observed in EGC. Instead, the magnified view of the healing products in Fig. 6.4 (b) reveals the presence of spherical particles, which are unreacted fly ash. The presence of unreacted fly ash suggests a possibility of further geopolymerization (reaction between the unreacted fly ash and alkaline solution that may be supplied from some source) and/or pozzolanic reaction, which forms hardened matrix and can seal the crack.

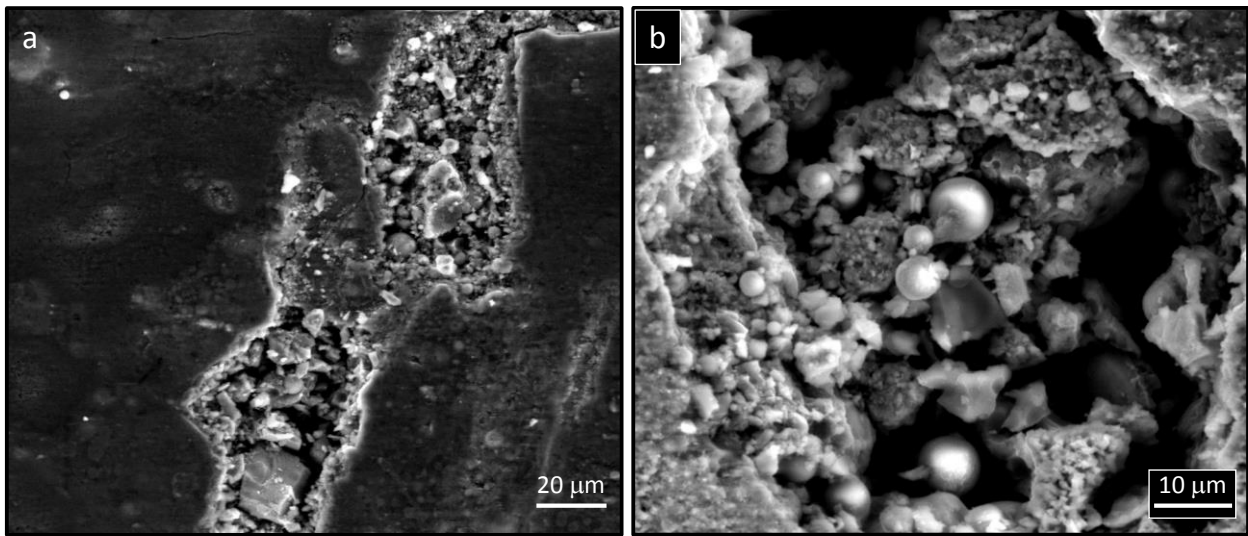


Fig. 6.4: (a) SEM image of a microcrack and self-healing products sealing the crack; and (b) magnified view of the healing products.

Then, to characterize chemical compositions of the white precipitates, EDS analysis was conducted along the line shown in Fig. 6.5. In general, the surface analyzed by EDS should be flat for accurate characterization. Thus, the region where a microcrack and white deposits formed such flat and continuous surface was selected for the line-scan analysis. In addition, PVA fibers

were not visible along the line, and therefore the detected elements should be those of geopolymer matrix or white precipitates. The line was 78 μm long with the scanning interval of 0.08 μm . Detected elements were carbon (*C*), oxygen (*O*), iron (*Fe*), sodium (*Na*), magnesium (*Mg*), aluminum (*Al*), silicon (*Si*), phosphorous (*P*), sulfur (*S*), and potassium (*K*). The atomic percent of each element was calculated as x-ray counts for the element divided by the total counts for all elements.

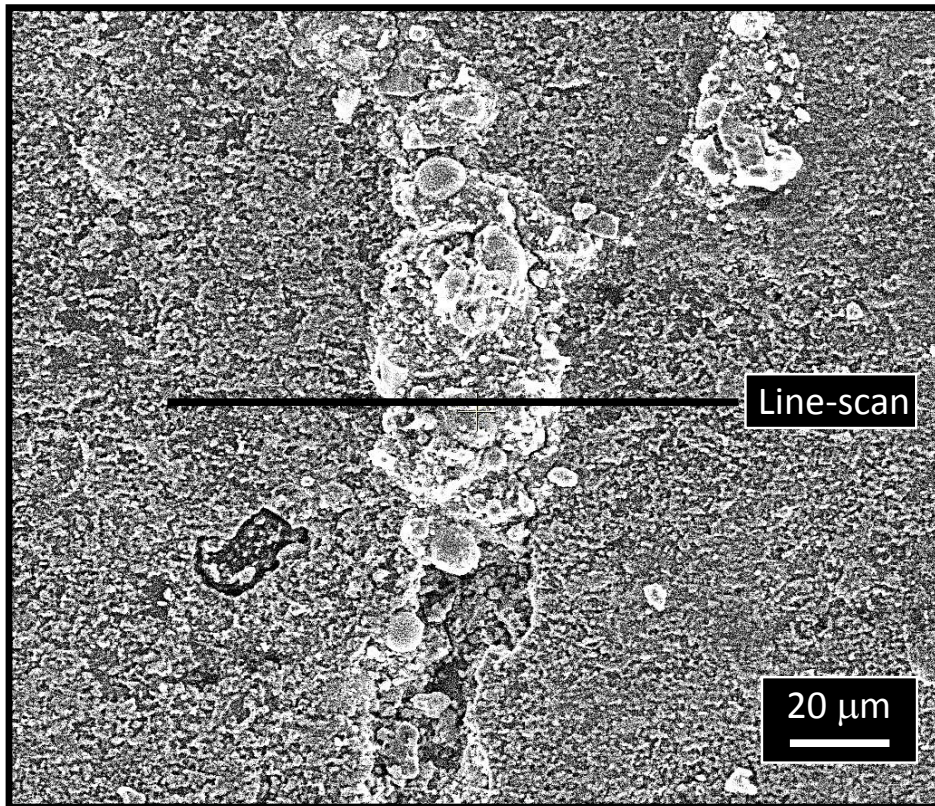


Fig. 6.5: EDS line-scan analysis was performed on the line that crosses a microcrack sealed with white precipitates, including the uncracked region of the geopolymer matrix.

As discussed in Section 5.3.2, white precipitates in EGC might be a result of efflorescence as reported in previous research. In a study by Zhang *et al.*, the efflorescence product in a fly ash-based geopolymer has been identified to be $\text{Na}_2\text{CO}_3 \cdot 7\text{H}_2\text{O}$ [16]. It should be noted that geopolymer binders are mainly composed of aluminosilicate phases (i.e. *Al*, *Si*, and *O*) with some

amount of charge-balancing Na^+ ions. Thus, if the white deposits results from efflorescence, the relative amount of Na or C should be higher in the region. On the other hand, if the EGC self-healing forms calcite ($CaCO_3$) as in cement-based materials, the region of the sealed crack should indicate a high concentration of Ca in the EDS analysis.

Figure 6.6 shows the atomic percent of Na , O , C , Ca , Si , and Al along the scanned line. The sum of x-ray counts for these elements is almost 90% of the total detected counts, over the entire scanned region. As can be seen in the upper graph, the amount of Na does not significantly vary along the line, keeping the low level. A similar trend is found for C , except in a small region that has a short peak. The peak might be associated with the presence of unreacted fly ash or PVA fiber which may be embedded near the surface, affecting the analysis through the interaction volume of the electron beam. Such peaks do not represent typical chemical characteristics of the white precipitates, which is indeed evidenced by the EDS mapping in Fig. 6.7 discussed below. Therefore, the EDS result suggests that efflorescence is unlikely to be the mechanism of sealing microcracks in EGC. In addition, the lower graph in Fig. 6.6 shows that Ca concentration is relatively low within the sealed crack, compared to the intact binder phase. Instead, the relative increase of Si and Al can be observed in the cracked region. Thus, calcite is not the main product of the white deposits, either.

From the above discussion, it seems clear that self-healing in EGC is distinct from efflorescence and cement-type self-healing, but produces Si- and Al-rich precipitates. This can be supported by the EDS mapping shown in Fig. 6.7; higher concentrations of Si and Al , and lower concentration of Ca can be clearly seen over the entire region of the microcrack. To completely understand the chemical nature of the healing products, a further research using more advanced techniques such as X-ray diffraction (XRD) is required.

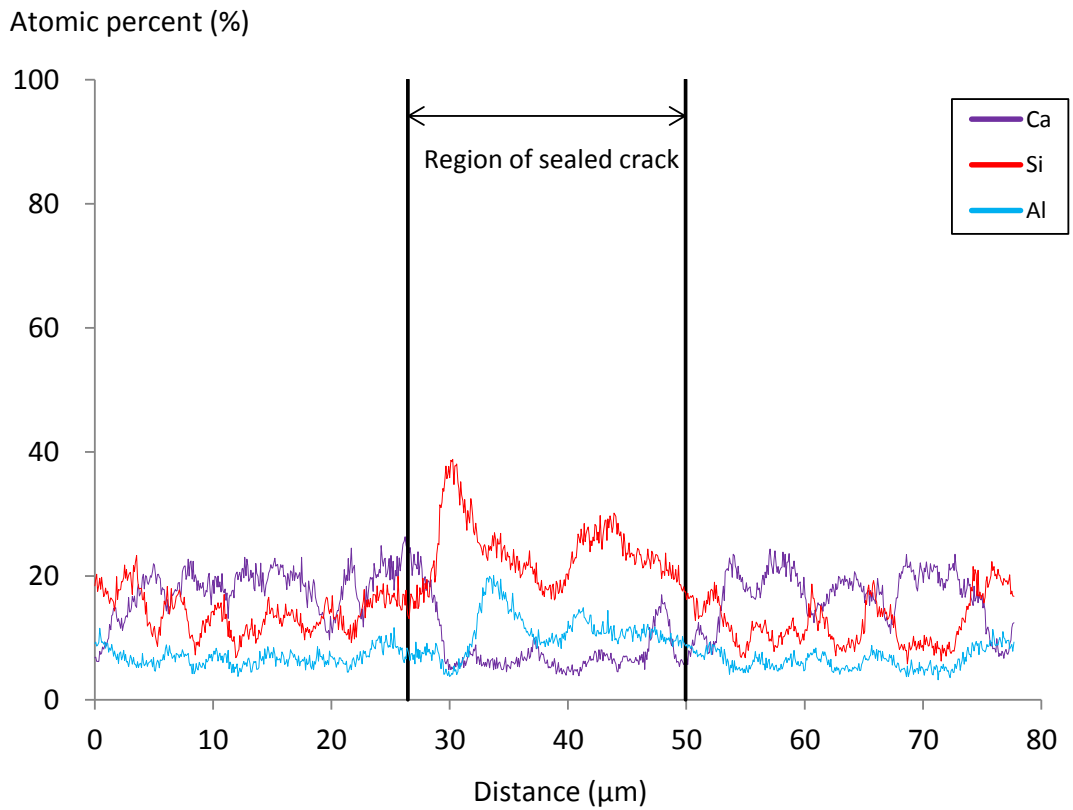
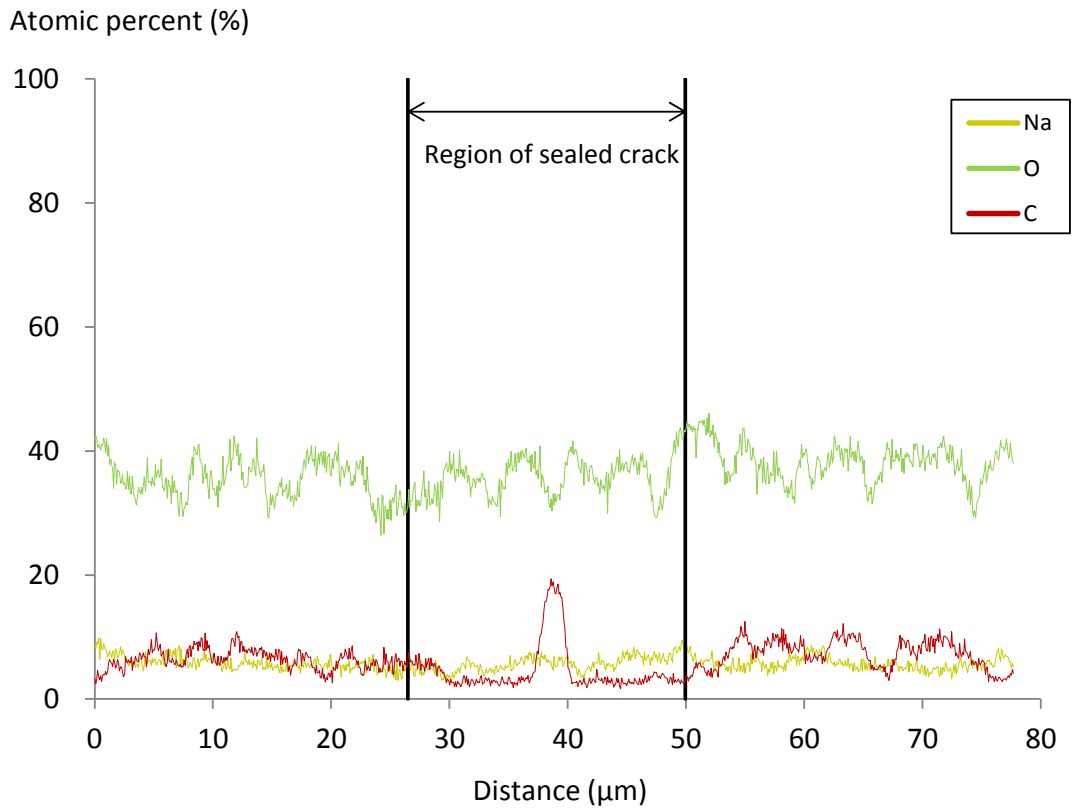


Fig. 6.6: Elemental compositions along the scanned line. The presence of efflorescence products (Na_2CO_3) and calcite (CaCO_3) is not confirmed. The healing products are Si- and Al-rich substance.

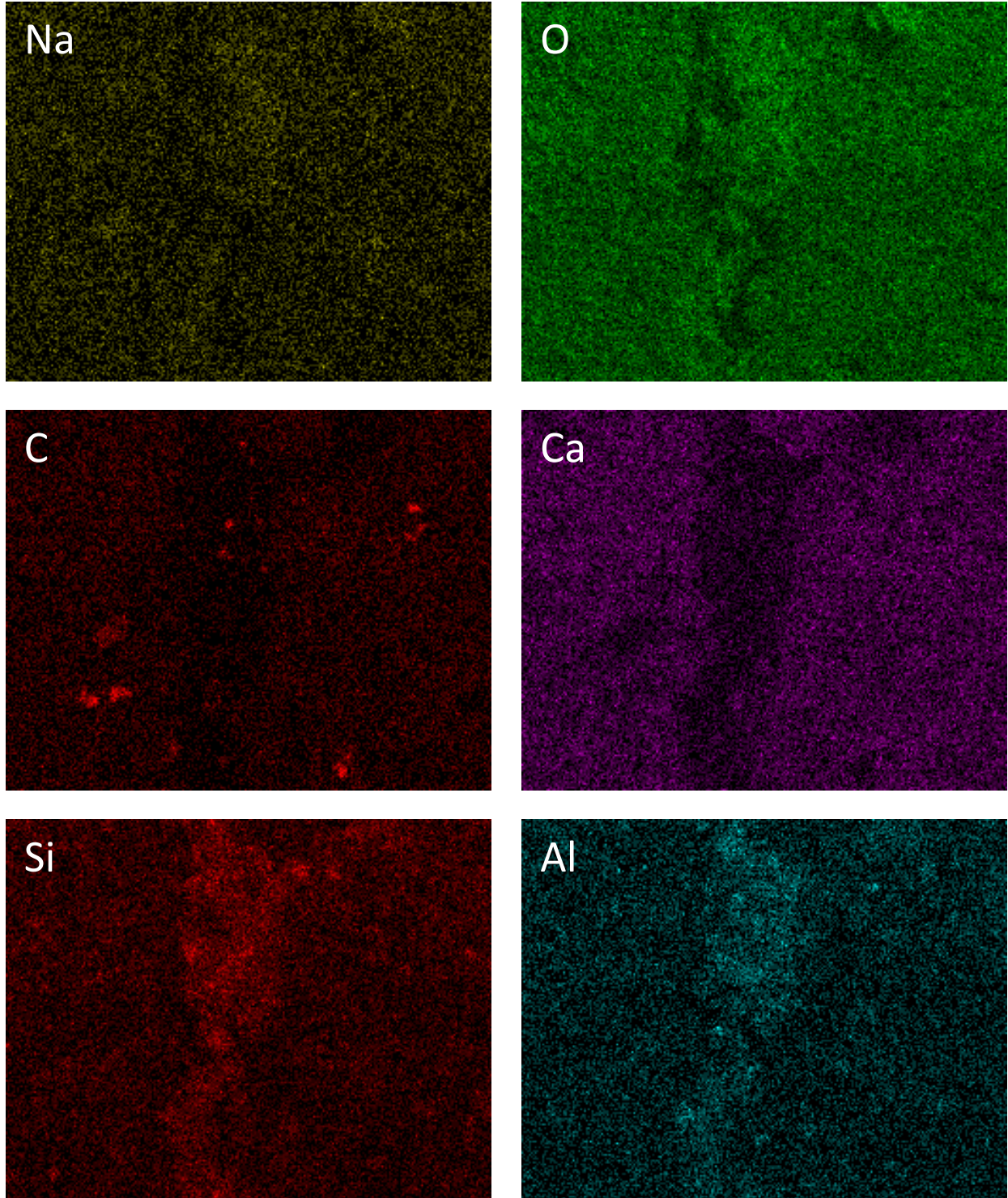


Fig. 6.7: EDS mapping. Regions of higher concentration are shown in higher brightness. Higher concentration of *Si* and *Al*, and lower concentration of *Ca* in the sealed crack can be clearly seen.

6.4 Summary and conclusions

The feasibility of self-healing EGC has been confirmed in the present study. In cracked EGC specimens subjected to water curing, white precipitates are formed on the surface, sealing the microcracks. Also, while the degree of performance recovery is relatively low compared to ECC, significant stiffness recovery can be observed for lower stress levels. In addition, the elemental analysis by EDS has revealed that the healing products are not likely to be a result of detrimental efflorescence.

The SEM observation has discovered the presence of unreacted fly ash within EGC microcracks. Therefore, it might be possible to enhance the self-healing functionality by promoting further geopolymerization and/or pozzolanic reaction from the unreacted fly ash (e.g. cured in alkaline solution, or at higher temperature).

The other findings obtained in this study are summarized below;

- The degree and rate of self-healing in EGC are variable; some microcracks are completely sealed within 7 days of water curing, while others are partially sealed after 30 days. The limited formation of healing products explains the relatively low performance recovery in stiffness, as well as water tightness studied in Section 5.3.2.
- Because of the limited performance recovery, chord modulus between 0.5 and 2.0 MPa is not appropriate to evaluate the stiffness recovery in EGC. A parameter that can reflect lower stress levels should be used.
- No healing product is formed in air-cured cracked EGC. Consequently, no stiffness recovery is observed in the series. This indicates that EGC self-healing requires the presence of water, as in cement-type self-healing.

- Healing products in EGC are mostly angular, stone-like substance, and relatively rich in *Si* and *Al* but low in *Ca*, compared to the geopolymer matrix. Thus, calcite ($CaCO_3$) is unlikely to be a main healing product of EGC self-healing.

Chemical compositions of the healing products have not been completely identified in this study. A further study is required to fully understand the chemical nature of the healing products and corresponding reaction mechanisms. With that information, it would be possible to develop an effective method to improve the self-healing functionality of EGC.

References

- [1] K. Van Breugel, “Is there a market for self-healing cement-based materials,” *Proc. First Int. Conf. Self Heal. Mater.*, no. April, pp. 1–9, 2007.
- [2] N. Hearn, “Self-sealing, autogenous healing and continued hydration: What is the difference?,” *Mater. Struct.*, vol. 31, no. 8, pp. 563–567, 1998.
- [3] H. Huang and G. Ye, “Application of sodium silicate solution as self-healing agent in cementitious materials,” *Int. RILEM Conf. Adv. Constr. Mater. Through Sci. Eng.*, no. 1993, pp. 530–536, 2011.
- [4] H. M. Jonkers, A. Thijssen, G. Muyzer, O. Copuroglu, and E. Schlangen, “Application of bacteria as self-healing agent for the development of sustainable concrete,” *Ecol. Eng.*, vol. 36, no. 2, pp. 230–235, 2010.
- [5] T.-H. Ahn and T. Kishi, “Crack Self-healing Behavior of Cementitious Composites Incorporating Various Mineral Admixtures,” *J. Adv. Concr. Technol.*, vol. 8, no. 2, pp. 171–186, 2010.
- [6] T. Nishiwaki, H. Mihashi, B.-K. Jang, and K. Miura, “Development of Self-Healing System for Concrete with Selective Heating around Crack,” *J. Adv. Concr. Technol.*, vol. 4, no. 2, pp. 267–275, 2006.
- [7] Y. Yang, M. D. Lepech, E. Yang, and V. C. Li, “Autogenous healing of engineered cementitious composites under wet–dry cycles,” *Cem. Concr. Res.*, vol. 39, no. 5, pp. 382–390, May 2009.
- [8] E. Herbert and V. Li, “Self-Healing of Microcracks in Engineered Cementitious Composites (ECC) Under a Natural Environment,” *Materials (Basel)*, vol. 6, no. 7, pp. 2831–2845, Jul. 2013.
- [9] M. Li and V. C. Li, “Cracking and healing of engineered cementitious composites under chloride environment,” *ACI Mater. J.*, vol. 108, no. 3, pp. 333–340, 2011.
- [10] M. Sahmaran, V. C. V. Li, and M. Şahmaran, “Durability of mechanically loaded engineered cementitious composites under highly alkaline environments,” *Cem. Concr. Compos.*, vol. 30, no. 2, pp. 72–81, Feb. 2008.
- [11] M. K. Ali, A. I. Abu-tair, J. M. Kinuthia, and R. Babecki, “Self-healing and strength development of geopolymer concrete made with Waste by products,” in *International Conference on Biological, Civil and Environmental Engineering*, 2015, pp. 32–42.
- [12] X. Liu, M. J. Ramos, S. D. Nair, H. Lee, D. N. Espinoza, and E. van Oort, “True Self-Healing Geopolymer Cements for Improved Zonal Isolation and Well Abandonment,” in *SPE/IADC Drilling Conference and Exhibition*, 2017.

- [13] T. Nishiwaki, M. Koda, M. Yamada, H. Mihashi, and T. Kikuta, “Experimental Study on Self-Healing Capability of FRCC Using Different Types of Synthetic Fibers,” *J. Adv. Concr. Technol.*, vol. 10, no. 6, pp. 195–206, 2012.
- [14] ASTM E1111-04, *Standard Test Method for Young’s Modulus, Tangent Modulus, and Chord Modulus*. West Conshohocken, PA: ASTM International, 2010.
- [15] Y. Yang, E. Yang, and V. C. Li, “Autogenous healing of engineered cementitious composites at early age,” *Cem. Concr. Res.*, vol. 41, no. 2, pp. 176–183, Feb. 2011.
- [16] Z. Zhang, H. Wang, J. L. Provis, and A. Reid, “Efflorescence : A Critical Challenge for Geopolymer Applications?,” in *Concrete Institute of Australia’s Biennial National Conference*, 2013.

CHAPTER 7: Sulfuric Acid Resistance of EGC

This chapter presents an experimental study on sulfuric acid resistance of EGC. Weight loss and residual mechanical performances of acid-exposed EGC specimens are measured, in comparison with OPC concrete and ECC.

7.1 Introduction

Sulfuric acid resistance is an important durability property for wastewater infrastructure. Under sewer environments, sulfate compounds present in the wastewater are typically converted into sulfuric acid, through metabolisms of sulfate-reducing and sulfur-oxidizing bacteria. This sulfuric acid reacts with calcium hydroxide, calcium silicate hydrates and calcium monosulfate in the cement matrix, forming loose and expansive gypsum and ettringite. As a result, the structural integrity and load-bearing capacity of the sewer concrete are reduced. Detailed information about the mechanisms of sulfuric acid formation in the wastewater can be found in literature [1, 2].

Because of the biogenic sulfuric acid attack, unexpected early deterioration of concrete wastewater facilities has been often reported [2, 3]. Further, much of sewer infrastructure is outdated, reaching the end of their service life in many countries. The aging and deterioration of wastewater infrastructure systems create an urgent need for repair and replacement; for example, according to the US Environmental Protection Agency (EPA), \$271 billion would be

required to maintain and upgrade the deteriorating wastewater infrastructure in the US [4]. Since sewage treatment is essential for maintaining the quality of life of citizens and ecosystems, their failure can result in social and environmental impacts (including drinking water contamination), as well as economic burden. For overcoming the challenge of crumbling wastewater infrastructure, much effort has been made to improve the vulnerability of concrete pipes under wastewater environments [5–8].

Of those newly developed technologies, geopolymer is a promising alternative to cement materials for sewer-infrastructure applications. Previous studies reported high sulfuric acid resistance of geopolymer concrete, especially in terms of weight loss caused by acid exposure [9–13]. While strength reduction due to the acid attack is observed in geopolymer concrete, the degree and rate of degradation are considerably lower than those of portland cement concrete. It is suggested that the better performance of geopolymers in acidic environments is attributed to the lower calcium content involved in the matrix formation [12]. Driven by the promising acid-resistant property, many field-demonstration projects have been conducted in the US to use spray-applied geopolymer for repair/rehabilitation of concrete sewer pipes and culverts [14]. Further, precast geopolymer-concrete pipes have been commercially available in Australia [15]. Hence, more and more geopolymer applications for wastewater infrastructure will be expected in the near future.

However, as has been discussed throughout this dissertation, durability performance of geopolymers might be limited if extensive cracking takes place in field applications. Particularly, large-diameter concrete pipes, which typically require steel reinforcement, can be seriously damaged by corrosion that is induced by acidic media penetrating through the wide cracks. One promising solution to this challenge is to use EGC; EGC has tightly-controlled crack width even

under a high imposed strain (as demonstrated in Chapter 5), and it might be even possible to eliminate steel reinforcement in the pipe, fully relying on the ductile EGC for crack control. Therefore, applications of EGC for large-diameter concrete pipes are worth considering; the first step is to verify the durability of EGC under sulfuric acid attack.

This chapter reports an experimental investigation on sulfuric acid resistance of EGC in comparison with OPC concrete and ECC; the latter two materials serve as controls. Weight loss and residual compressive strength of cylinder specimens subjected to sulfuric acid exposure are presented. In addition, to study the combined effects of cracking and acid attack on mechanical-property degradation, residual flexural strength and deflection capacity are measured for beam specimens that are preloaded to create cracks before acid exposure.

7.2 Material and methods

7.2.1 Materials and mix designs

Table 7.1 lists the ingredients and their mix proportions of portland cement concrete, ECC and EGC used in this study. The EGC design is that of 1.5% fiber volume fraction, developed in Chapter 4. Properties of the ingredients can be found in Section 4.2.1. For cement concrete and ECC, Type I portland cement and ASTM class F fly ash from the Monroe power plant (Section 4.2.1), were used as their binder materials. Crushed limestone with a maximum size of 25 mm and silica sand with a fineness modulus of 2.43 were used as coarse and fine aggregate of cement concrete, respectively. F-75 Ottawa fine silica sand and short polyvinyl alcohol (PVA) fiber with 1.2% oil coating were used for ECC, as in EGC mixture. To obtain adequate workability, polycarboxylate-based superplasticizer (ADVA 190, GCP Applied Technologies Inc.) was added

to the concrete and ECC mixture. The mix proportion of cement concrete followed the mixture design by Payvandi *et al.*[16] , which is commonly used in dry-mixed concrete pipe production. ECC used in this research was the most-studied standard version, M45 [17], with a fiber volume fraction of 2%. It should be mentioned that the source of fly ash used for ECC in this study is different from that used when M45 was developed (the supplier was changed).

Table 7.1: Mixture proportions of cement concrete, ECC, and EGC (in kg/m³).

	Cement concrete	ECC M45	EGC ($V_f=1.5\%$)
Type I cement	292	581	
Fly ash (Sammis)			694
Fly ash (Monroe)	103	697	463
Coarse aggregate	873		
Fine aggregate	956		
Fine silica sand		464	463
PVA fiber		26	19.5
Super plasticizer	2.1	4.4	
Water	174	337	116
NaOH (pellet)			60.1
Na ₂ SiO ₃			260
Pre-mix water ^a			26.6

^a Pre-mix water is mixed with NaOH pellets and Na₂SiO₃ solution to prepare the alkaline activator.

7.2.2 Specimen preparation

The mixing procedure of EGC has been presented in Section 4.2.1 and 5.2.2. For concrete mixing, type I cement, fly ash, and silica sand were first dry-mixed for 2 min. Water along with the superplasticizer was then added to the mixture to prepare fresh cement mortar, which was followed by the addition of coarse aggregate. In the case of ECC, PVA fiber was added to the fresh ECC mortar, instead of coarse aggregate, and mixing continued until a desired fresh state

was obtained. The mixture of each material was cast into 3×6 inch (76×152 mm) cylinder and $4 \times 4 \times 14$ inch ($102 \times 102 \times 356$ mm) beam molds.

Steel wire reinforcement was placed for concrete beam specimens, as shown in Fig. 7.1. The steel wire mesh of W 1.4 (gauge 10) that meets ASTM 1064 [18] was used for both the longitudinal and transverse reinforcement. The reinforcement ratio satisfied requirements of Class IV, Wall C reinforced concrete pipe, specified in ASTM C76 [19], which has a wall thickness of 4 inches (102 mm) – the same as the thickness of the beam specimens – and an internal diameter of 27 inches (686 mm). The reinforced-concrete (RC) beam specimens were supposed to represent mechanical performances of the ASTM-specified RC pipes.

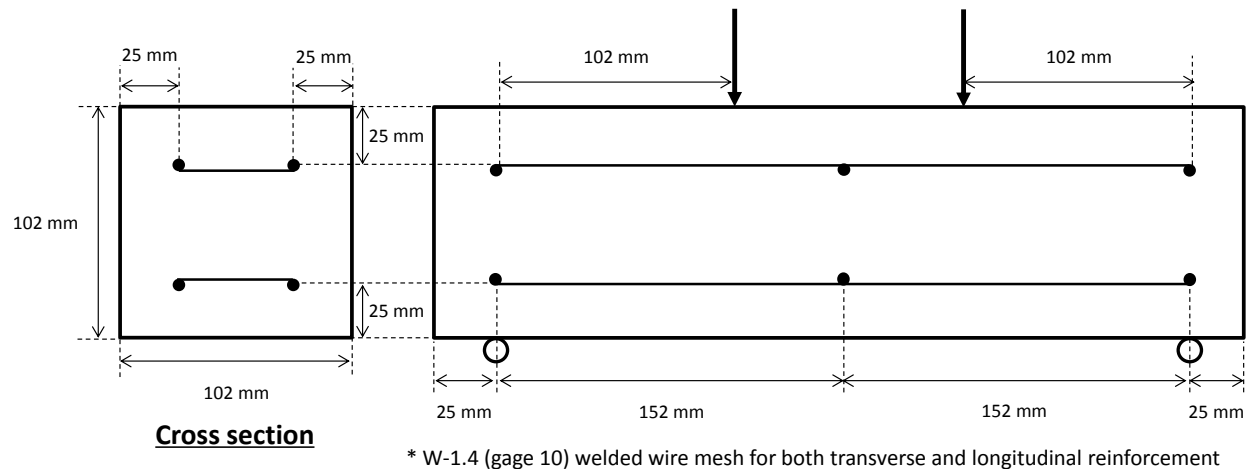


Fig. 7.1: RC beam design and testing setup of four-point bending.

All the specimens were demolded 24 hours after casting. Concrete specimens were then moist-cured with a relative humidity of over 95% at room temperature (23 ± 3 °C) until the age of 28 days. ECC specimens were moist-cured for only 6 days and then air-cured at room temperature until the age of 28 days, as recommended in previous studies. As presented in Section 4.2.1,

EGC specimens were dry-cured at 60 °C for 24 hours right after demolding, followed by air curing at room temperature until the age of 28 days.

7.2.3 Sulfuric acid exposure

A sulfuric acid resistance test developed by Kaempfer and Berndt [20] was adopted in this study. Figure 7.2 illustrates the exposure conditions. At the age of 28 days, specimens were immersed in tap water. They were removed from water after two days and wiped with paper towels. The water-saturated cylinder specimens were weighed with a precision of 0.01 g. Subsequently, specimens were immersed in diluted sulfuric acid solution with a pH value of 2. The pH value of the acid bath was checked daily and kept constant by adding extra sulfuric acid solution. After six days of acid exposure, specimens were gently brushed under running water to remove loose particles on their surface, followed by curing in a water bath for 24 hours. The weight measurement, 6-day acid exposure, and 1-day water bath, which constituted one cycle of the acid-resistance test, were then repeated. The sulfuric acid bath was replaced every cycle.

Based on a comparison study, Kaempfer and Berndt suggested that five cycles of the testing (i.e. 35-day acid and water exposure) represent the 20-year corrosion stress of ordinary concrete sewer pipes in the field [20]. It should be noted, however, that they used automated mixer and pump to continuously circulate the solution and adjust the pH, while the pH check and stirring in this study were manually done once a day. In addition, it has been argued that the accelerated sulfuric acid resistance test does not fully represent the microbial effects on sewer concrete in the field, where hydrogen sulfide gas and sulfates, as well as microbially produced sulfuric acid, in the wastewater attack the concrete [2]. Thus, the acid-induced damage observed in the present experiment might be less severe than that in actual field applications.

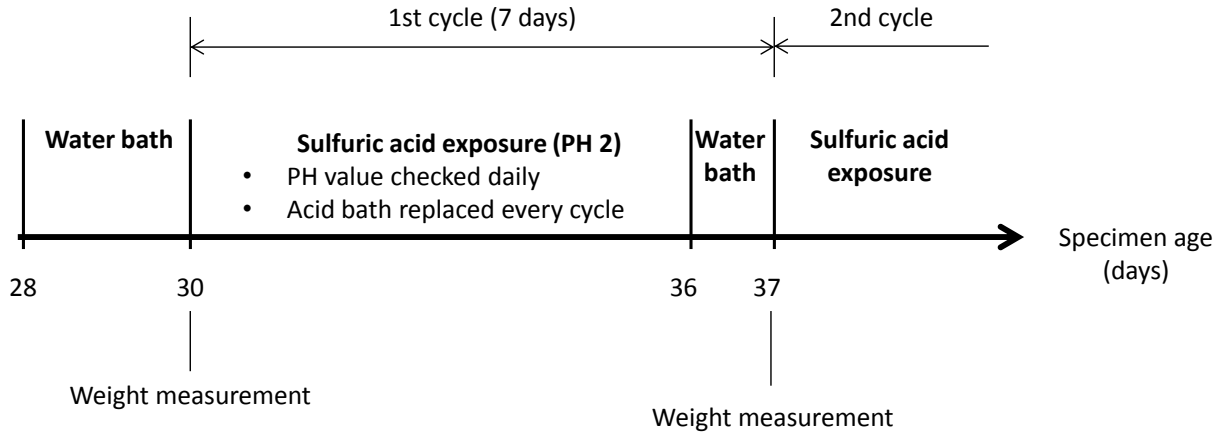


Fig. 7.2: Test conditions of sulfuric acid exposure. Five cycles (35-day exposure) correspond to average corrosion damage observed in 20-year-old ordinary concrete sewer pipes [20].

7.2.4 Test procedures

Cylinder specimens

Uniaxial compression testing was first conducted on three cylinder specimens of each material for their 28-day compressive strength. Specimens were capped with sulfur capping compounds at least one day prior to testing. The loading rate was 35 ± 7 psi/s (0.25 ± 0.05 MPa/s).

Nine intact cylinders for each material were subjected to the acid exposure. Out of these, three randomly-selected ones were tested for residual compressive strength after each five cycles (i.e. 35 days of exposure). Namely, the average weight change was determined for nine specimens for 1-5 cycles, six specimens for 6-10 cycles, and three specimens for 11-15 cycles. To evaluate the effects of continuous hydration of cementitious materials, another set of nine cylinders for concrete and ECC were prepared as control specimens and subjected to water bath for the same exposure periods as those of acid-exposed specimens. The control specimens were then tested for reference compressive strength. For EGC cylinders, no significant strength increase after 28 days was observed in preliminary studies. Thus, control specimens for EGC were not prepared here.

Beam specimens

A four-point bending test was first performed on three beam specimens of each material for their 28-day flexural strength – known as modulus of rupture (MOR) – and their deflection capacity (i.e. deflection at MOR). The span length was 12 inches (305 mm) and a constant loading rate of 0.003 in/min (0.076 mm/min) was applied under displacement control of the loading head. To measure the mid-point net deflection, two potentiometers were mounted on both sides of a rectangular jig that surrounded the beam specimen and was clamped at mid-depth directly above the loading supports.

Another set of three beams for each material was preloaded at the age of 28 days. The testing configurations were identical to the above flexural strength test, except that the test was stopped at the net mid-point deflection of 0.02 inches (0.51 mm), which was equivalent to 1/600 of the span length. After unloading the specimens, cracks were observed by an optical digital microscope to measure their crack width. For each crack, crack width was measured on the center and both edges of the specimen surface (i.e. measured at three points) and averaged. Subsequently, the preloaded specimens were immersed in tap water for two days, and subjected to the acid exposure of 15 cycles (105 days). The acid-exposed beams were then reloaded for their residual MOR and deflection capacity.

7.3 Results and discussion

7.3.1 Visual appearance and weight change

Figure 7.3 shows visual appearances of specimen surfaces before and after acid exposure. As can be seen, concrete and ECC specimens have remarkable erosion of the surface due to sulfuric acid

attack. Fine aggregate of concrete and PVA fiber of ECC on their surface are loose and easily brushed off after the acid exposure. However, from specimens crushed in the compressive strength test, it has been found that the marked color difference is only observed in a thin layer of the surface. In the case of EGC cylinders, fine surface cracking has been found while storing specimens in air after the acid immersion. This might be attributed to its relatively low tensile strength of the matrix and resultant damage by drying shrinkage. Nevertheless, the degree of surface erosion in EGC is not as severe as cement concrete and ECC; only a small number of PVA fibers have been brushed off from the EGC surface.

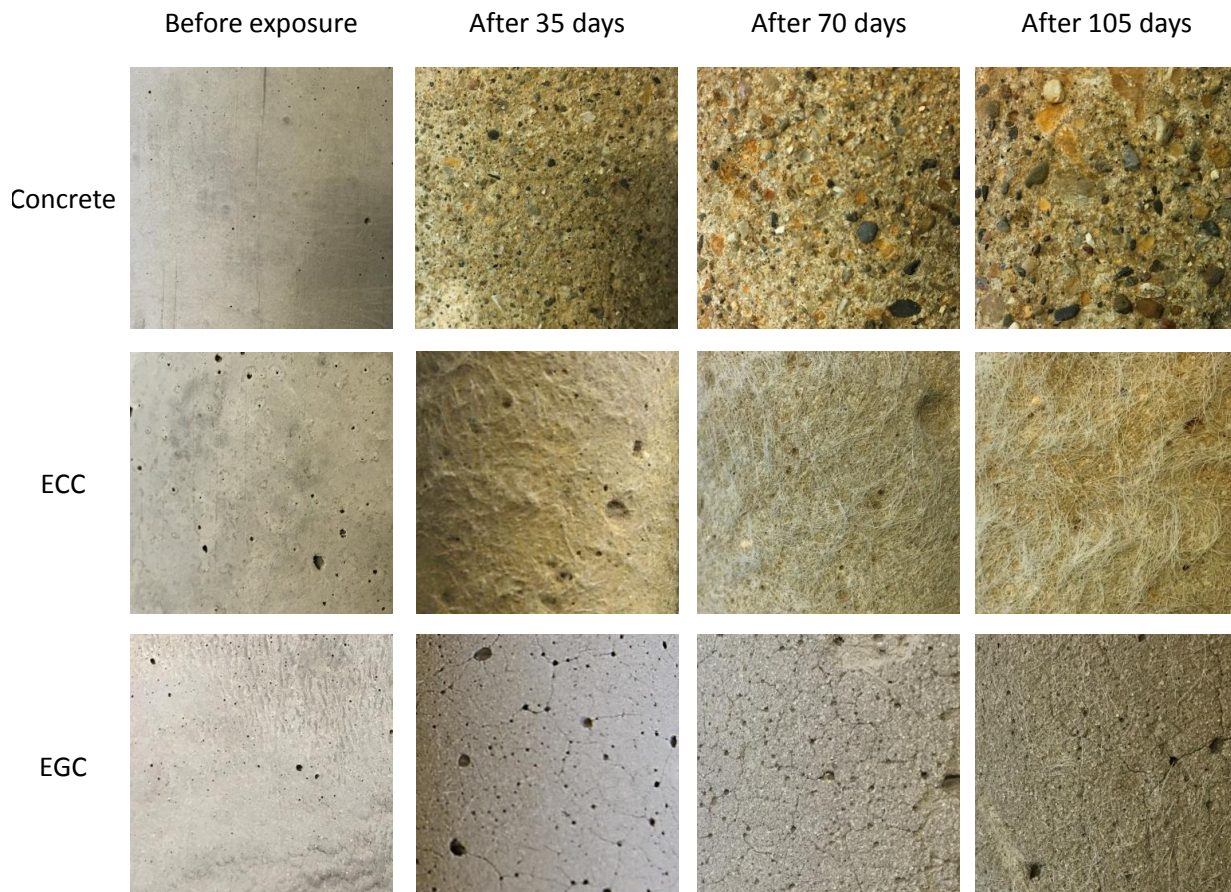


Fig. 7.3: Typical appearances of specimen surface with various acid exposure periods.

The limited erosion of EGC is also evidenced by the weight-change measurement (Fig. 7.4). Both concrete and ECC specimens show slight weight gain in the first two cycles, which has been also reported in many other studies. Chang *et al.* suggested that weight gain during the early exposure period could be attributed to many factors, including continuous cement hydration, formation of gypsum due to acid attack, and increase in absorbed water of specimens [5]. Despite the initial weight gain, the rate of subsequent weight loss of concrete and ECC is about three times that of EGC. Consequently, after 15 cycles (105 days), the weight loss of concrete and ECC is more than double that of EGC. Therefore, long-term sulfuric acid resistance of EGC is significantly higher than cement concrete and ECC, in terms of weight loss.

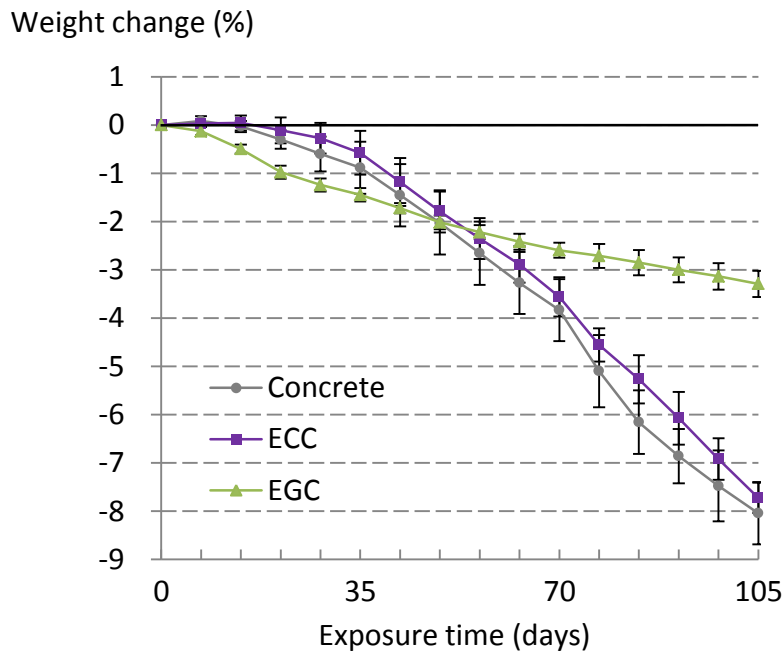


Fig. 7.4: Slight weight gain is observed for both concrete and ECC in the first two cycles (i.e. 14 days), but the rate of subsequent weight loss is three times that of EGC.

7.3.2 Compressive strength degradation

Results of the initial and residual compressive strength of each material are shown in Fig. 7.5.

Despite the observed surface erosion due to acid attack, all series show strength increase after

acid exposure, compared to their 28-day compressive strength (“0d” in the graph). These data imply that there is little correlation between the weight loss and compressive strength degradation, within the extent of erosion damage observed in this study. It should be noted, however, that continuous cement hydration and pozzolanic reaction of fly ash are supposed to continuously elevate the compressive strength of concrete and ECC, even under the acidic environment. Moreover, for concrete or ECC pipes in the field, much of continuous hydration would be completed within months, while significant acid-induced deterioration occurs after years. Therefore, to extract effects of continuous hydration of cementitious materials, the raw strength data should be normalized by those of water-cured control specimens with the same specimen age. The resultant net effects of sulfuric acid exposure represent the real-time strength degradation of concrete/ECC pipes in the field.

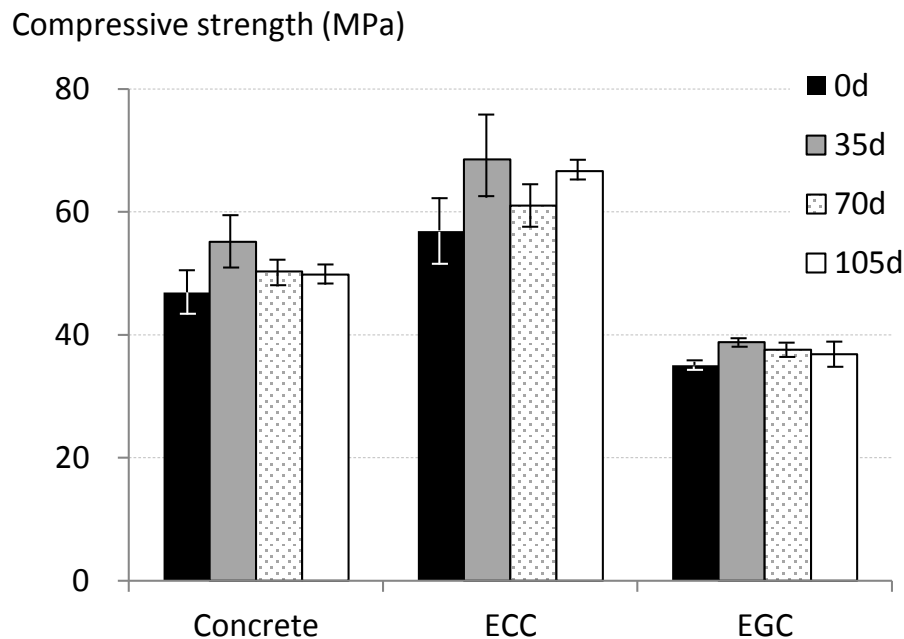


Fig. 7.5: Compressive strength of concrete, ECC, and EGC before and after sulfuric acid exposure. All the series show strength increase even after the acid attack, compared to their 28-day compressive strength (i.e. “0d”).

Figure 7.6 plots the normalized residual compressive strength. For EGC, the raw residual-strength data have been normalized by its 28-day compressive strength. No significant degradation is observed for ECC, suggesting negligible effects of the observed weight loss on strength degradation. Conversely, continuous degradation can be clearly seen for concrete. The average residual strength of concrete after 15 cycles (105 days) is 79% of that of the water-cured control specimens.

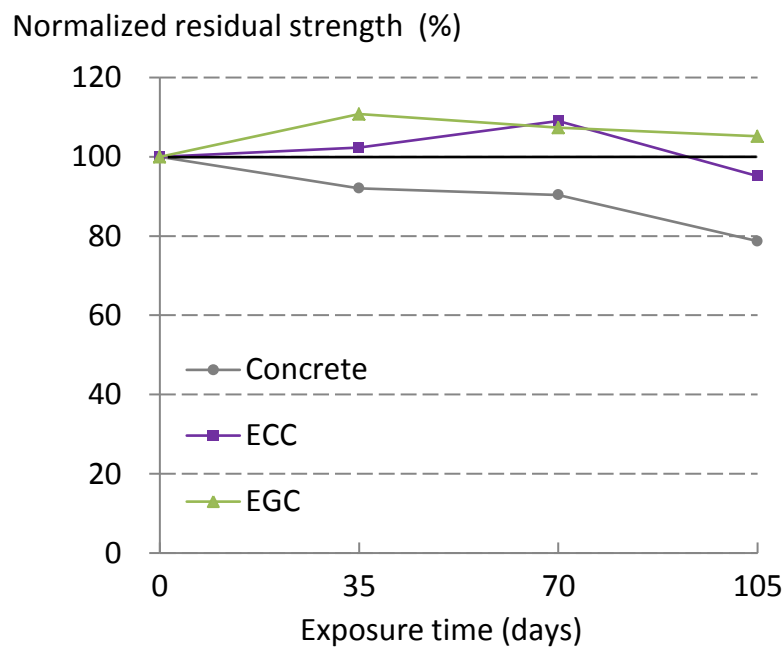


Fig. 7.6: Strength increase due to continuous hydration is extracted by normalizing the raw compressive strength data by those of control specimens cured in water. Continuous strength degradation due to the acid attack is observed in concrete, while there is no significant effect on ECC and EGC.

Although concrete and ECC show a similar trend in weight loss (Fig. 7.4), effects of the weight loss on compressive strength are limited in ECC. This could be attributed to a smaller amount of loss of cement matrix in ECC than cement concrete. The measured weight loss of ECC includes brushed-off PVA fibers from the surface. On the other hand, the weight loss of concrete is associated with lost hardened cement paste and aggregate. In addition, the larger amount of fly

ash incorporated in ECC than cement concrete could enhance the sulfuric acid resistance of the cement matrix, as reported by Torii and Kawamura [6]. As a result, relatively large loss of cement matrix in concrete could cause significant strength degradation, while effects of the lost fibers from ECC surface are limited. Nevertheless, if the ECC specimens were to undergo further acid exposure and lose more weight, the compressive strength degradation could be significant, compared to EGC that has a slower rate of weight loss.

7.3.3 Flexural strength and deflection capacity at 28 days

Of three specimens tested for each material, typical flexural stress-mid deflection curves in the flexural strength test are shown in Fig. 7.7. While ECC beams show considerably higher MOR than RC and EGC, only a few multiple cracks have been observed, with unexpectedly low deflection capacity. In contrast, EGC beams show more than ten microcracks in the deflection-hardening stage and have high deflection capacities. The average MOR and deflection capacity of EGC are 17 and 331% higher than those of RC, respectively. Results of the average flexural properties are later shown in Table 7.3, together with the residual flexural properties after acid exposure.

It should be noted that the flexural behavior of ECC beams is similar to that of ordinary fiber-reinforced concrete (FRC), rather than high performance fiber-reinforced cementitious composites (HPFRCCs). It is suggested that the Monroe fly ash, which has relatively high calcium content and reactivity, causes formation of a too strong cement matrix. The high tensile matrix strength could result in violation of a fracture mechanics-based criterion [21] that is essential for steady-state crack propagation and resultant multiple cracking with high tensile ductility. Therefore, it might be appropriate to consider that the ECC specimens prepared in this

study represent the behavior of ordinary FRC with limited strain-hardening under uniaxial tension.

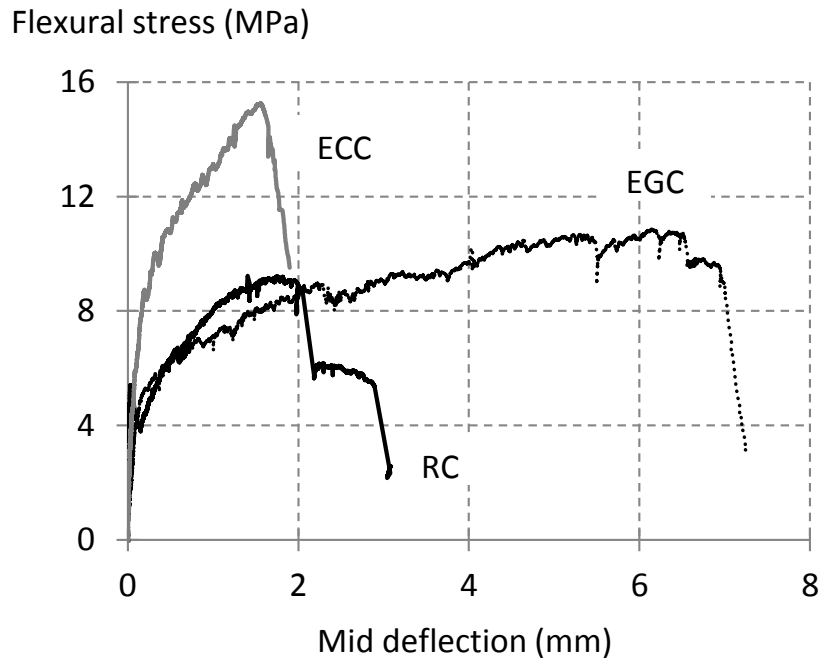


Fig. 7.7: Typical flexural stress–mid deflection curves of RC, ECC, and EGC beams. Due to relatively high reactive fly ash, ECC beams show lower deflection capacities than expected, with a few multiple cracks.

7.3.4 Crack patterns in preloading

Table 7.2 presents crack patterns of preloaded beam specimens. RC beams have a smaller number of cracks with larger crack width than ECC and EGC. The maximum crack width of RC beams is less than 300 μm , which is the permissible crack width in the ASTM specification of RC sewer pipe design [19]. It is suggested in the specification that cracks of less than 300 μm have limited effects on structural properties and water tightness of RC pipes. Therefore, the degree of damage introduced by the preloading is reasonable; the specification implies that such damage can occur in actual RC pipes in the field.

In the case of ECC and EGC beams, crack width is tightly controlled to be less than 100 μm . However, their crack width distributions are different; a lognormal distribution is well fitted to the EGC crack data, as in coupon specimens discussed in Section 5.3.1, while the crack data of ECC beams appear a more scattered, random distribution. This supports the above discussion that ECC beams prepared in this study behave like ordinary FRC. As a result, both the maximum and average crack widths of EGC are the smallest among the three materials.

Table 7.2: Crack patterns of preloaded beam specimens.

Material	Specimen	Number of cracks	Maximum crack width (μm)	Average crack width (μm)
RC	1	1	272	261
	2	1	274	220
	3	2	184	140
ECC	1	3	94	54
	2	3	84	42
	3	4	94	57
EGC	1	4	60	33
	2	4	34	21
	3	4	37	31

Note: Crack width was measured at three points for each crack, i.e. center and both edges of the surface, and averaged. Maximum crack width is the largest crack width observed at a single point.

It should be mentioned that cracks in both RC and ECC beams were completely sealed during the acid exposure. In contrast, crack sealing was not observed in EGC beams, and fine surface cracking was found instead, as in the cylinder specimens.

7.3.5 Residual flexural strength and deflection capacity

Average MOR and deflection capacities of beam specimens at 28 days and after acid exposure are summarized in Table 7.3. Unfortunately, data of one acid-exposed RC beam was lost due to an unexpected power outage during its reloading, and the average flexural properties are therefore computed for only two specimens. For RC and EGC series, slight increases/decreases

can be found in their residual MOR and deflection capacities, in comparison with their 28-day performances. However, with the assumption that the data are normally distributed with the equal variance, a statistical t-test reveals that those differences before and after acid exposure are insignificant, compared to the observed variations among specimens. Therefore, the acid-induced surface erosion observed in this study does not cause any remarkable degradation in the MOR and deflection capacity of RC and EGC.

Table 7.3: Flexural properties of RC, ECC, and EGC at 28 days and after acid exposure.

	28-day performance		After acid exposure		f_1 / f_0	δ_1 / δ_0
	MOR, f_0 (MPa)	Deflection at MOR, δ_0 (mm)	MOR, f_1 (MPa)	Deflection at MOR, δ_1 (mm)		
RC	9.2 ± 1.4	1.25 ± 0.27	8.3 ± 0.7	1.39 ± 0.14	0.90	1.11
ECC	15.0 ± 0.4	1.23 ± 0.49	13.8 ± 0.3	2.30 ± 0.16	0.92	1.87
EGC	10.8 ± 1.0	5.39 ± 1.09	11.6 ± 1.5	5.26 ± 0.95	1.08	0.98

In contrast, effects of acid exposure on both the MOR and deflection capacity of ECC are statistically significant. While the residual MOR has only 8% reduction from the 28-day value, the decrease is significant when the observed small sample variance is taken into account. The degradation could be mainly attributed to brushed-off PVA fibers due to the surface erosion; unlike compressive strength, flexural strength of ECC beams highly depends on the number of fibers that can bridge cracks. Thus, loss of a considerable number of PVA fibers has a direct impact on the load-carrying capacity. Conversely, 87% increase in the deflection capacity could be associated with the degraded cement matrix; due to the acid-induced surface erosion, first-cracking strength of ECC could be lowered, which is beneficial for achieving a higher ductility, as discussed in Section 2.2.2. Indeed, more multiple cracks have been observed during reloading

on ECC beams than the 28-day flexural strength test. Therefore, although ECC matrix is eroded by sulfuric acid attack, the damage can offer a higher deflection capacity of the composite.

7.3.6 Residual bending stiffness

Aside from the MOR and deflection capacity, significant reduction in bending stiffness has been observed for all the acid-exposed beams. Figure 7.8 shows typical bending curves of each material for preloading and reloading on the same specimen. For easy comparison of linear bending stiffness, bending curves are plotted up to a mid-deflection of 1 mm. As can be seen, the RC beam shows the largest stiffness reduction, despite the completely sealed cracking. The residual bending stiffness of ECC, on the other hand, is comparable to its initial performance. The stiffness reduction of EGC is moderate.

For conducting a quantitative evaluation, linear bending stiffnesses were computed for data with stresses from 0.5 to 4 MPa by linear regressions, which showed high r-squared values of over 0.9 in all the series. Then, the stiffness ratio was calculated as the ratio of residual stiffness at reloading to initial stiffness at preloading.

The average stiffness ratios of RC, ECC, and EGC are 5, 43, and 33%, respectively. This result indicates the mechanical-property recovery due to self-healing in ECC. On the contrary, cracking is completely sealed in RC beams, but not healed along with stiffness recovery. Remember that the observed crack width in preloaded RC beams is permissible based on ASTM C76 (discussed in Section 7.3.4). Nevertheless, their stiffness reduction due to combined effects of preloading and acid attack is remarkable. In the case of EGC, the stiffness ratio is significantly higher than that of RC, although no crack sealing has been observed.

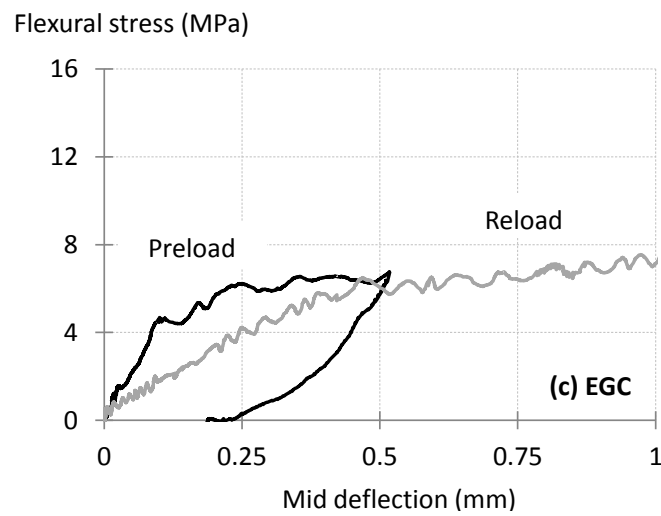
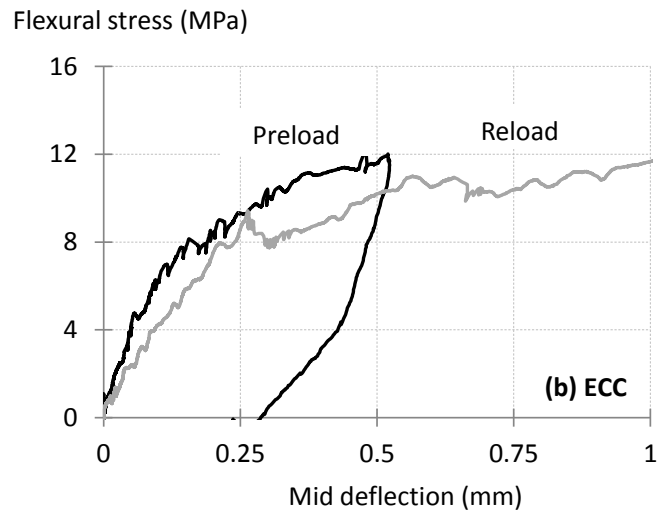
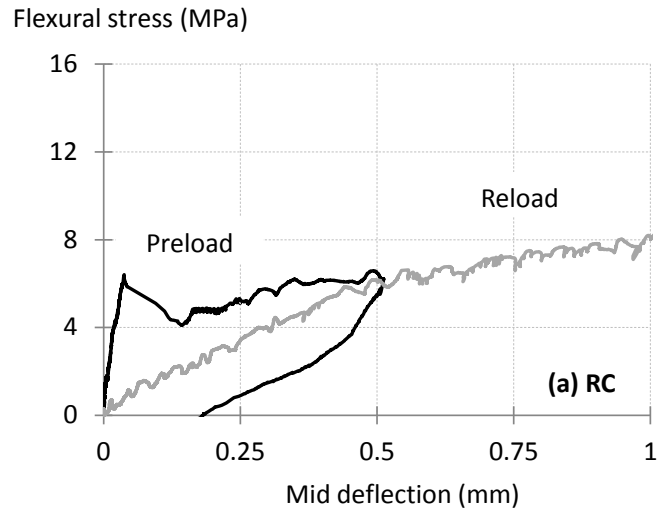


Fig. 7.8: (a) RC beam shows significant reduction in bending stiffness due to the preloading and subsequent acid attack. The smallest stiffness reduction of (b) ECC beam is suggested to be a result of recovery due to self-healing.

7.4 Summary and conclusions

This chapter has experimentally demonstrated the high sulfuric acid resistance of EGC. Acid-induced surface erosion of EGC specimens is limited compared to cement concrete and ECC, especially in terms of weight loss. No significant degradation has been observed for its compressive strength, MOR and deflection capacity after acid exposure. While combined effects of preloading and acid attack cause remarkable degradation in its linear bending stiffness, the degree of reduction is significantly less than RC. Due to the considerably slower rate of weight loss in EGC than concrete and ECC, differences in mechanical-property degradation among the materials would be more remarkable when subjected to longer acid exposure or more severe acidic environments.

The following findings have been also obtained during this study;

- A limited number of PVA fibers are brushed-off in EGC due to the acid-induced surface erosion, while acid-exposed ECC loses a significant amount of fibers. The loss of fiber does not reduce compressive strength of both materials, but causes statistically significant degradation in MOR of ECC.
- While the deflection capacity of EGC shows insignificant reduction after acid exposure, that of ECC can be rather increased. The increase could be attributed to the degraded cement matrix with lower matrix tensile strength, which is beneficial for achieving a higher ductility.
- Self-healing of EGC is not observed under acidic environments. Conversely, cement materials show significant healing; cracks of preloaded RC and ECC beams have been completely sealed during the acid exposure.

- Significant mechanical-performance recovery due to the self-healing has been observed in linear bending stiffness of ECC beams only. Despite the sealed cracking in preloaded RC beams, their stiffness reduction is the largest among the materials.

As mentioned in Section 7.2.3, the chemical test method used in this study might not fully represent the microbial effects on sewer concrete in the field. Therefore, further research would be required to verify the durability of EGC under sewer environments. Nevertheless, the high sulfuric acid resistance of EGC has been experimentally demonstrated, which shows the promise of EGC for sewer-pipe applications. Then, based on the experimental result obtained here, the next chapter conducts a life-cycle assessment on environmental performances of EGC sewer pipes.

References

- [1] D. J. Roberts, D. Nica, G. Zuo, and J. L. Davis, "Quantifying microbially induced deterioration of concrete: Initial studies," in *International Biodeterioration and Biodegradation*, 2002, vol. 49, no. 4, pp. 227–234.
- [2] M. O'Connell, C. McNally, and M. G. Richardson, "Biochemical attack on concrete in wastewater applications: A state of the art review," *Cem. Concr. Compos.*, vol. 32, no. 7, pp. 479–485, 2010.
- [3] W. Sand and E. Bock, "Concrete corrosion in the Hamburg Sewer system," *Environ. Technol.*, vol. 5, no. 12, pp. 517–528, 1984.
- [4] United States Environmental Protection Agency, "Clean Watersheds Needs Survey 2012 - Report to Congress," 2016.
- [5] Z. T. Chang, X. J. Song, R. Munn, and M. Marosszky, "Using limestone aggregates and different cements for enhancing resistance of concrete to sulphuric acid attack," *Cem. Concr. Res.*, vol. 35, no. 8, pp. 1486–1494, 2005.
- [6] K. Torii and M. Kawamura, "Effects of fly ash and silica fume on the resistance of mortar to sulfuric acid and sulfate attack," *Cem. Concr. Res.*, vol. 24, no. 2, pp. 361–370, 1994.
- [7] W. De Muynck, N. De Belie, and W. Verstraete, "Effectiveness of admixtures, surface treatments and antimicrobial compounds against biogenic sulfuric acid corrosion of concrete," *Cem. Concr. Compos.*, vol. 31, no. 3, pp. 163–170, 2009.
- [8] E. Vincke, E. Van Wanseele, J. Monteny, A. Beeldens, N. D. Belie, L. Taerwe, D. Van Gemert, and W. Verstraete, "Influence of polymer addition on biogenic sulfuric acid attack of concrete," *Int. Biodeterior. Biodegrad.*, vol. 49, no. 4, pp. 283–292, 2002.
- [9] J. Davidovits, D. C. Comrie, J. H. Paterson, and D. J. Ritcey, "Geopolymeric concrete for environmental protection," *Concr. Int.*, vol. 12, no. 7, pp. 30–40, 1990.
- [10] T. Bakharev, "Resistance of geopolymer materials to acid attack," *Cem. Concr. Res.*, vol. 35, no. 4, pp. 658–670, 2005.
- [11] X. J. Song, M. Marosszky, M. Brungs, and R. Munn, "Durability of fly ash based Geopolymer concrete against sulphuric acid attack," *Durab. Build. Mater.*, no. April, pp. 17–20, 2005.
- [12] S. E. Wallah and B. V. Rangan, "Low-Calcium Fly Ash-Based Geopolymer Concrete: Long-Term Properties," *Concrete*, 2006.
- [13] S. Thokchom, P. Ghosh, and S. Ghosh, "Resistance of Fly Ash Based Geopolymer Mortars in Sulfuric Acid," *ARPJ. Eng. Appl. Sci.*, vol. 4, no. 1, pp. 65–70, 2009.

- [14] D. Keaffaber, “GeoSpray: GeoPolymer Mortar System and Concrete Cloth for Structural Rehabilitation/Repair of Sewer and Storm Infrastructure,” *Milliken Infrastructure*, 2015. [Online]. Available:
<http://ctt.mtu.edu/sites/ctt/files/resources/bridge2016/conference/08keaffaber.pdf>. [Accessed: 04-Jul-2017].
- [15] J. T. Gourley and G. B. Johnson, “Developments in geopolymer precast concrete,” in *The worlded Congress Geopolymer*, 2005, pp. 139–143.
- [16] A. Peyvandi, P. Soroushian, and S. Jahangirnejad, “Enhancement of the structural efficiency and performance of concrete pipes through fiber reinforcement,” *Constr. Build. Mater.*, vol. 45, pp. 36–44, 2013.
- [17] S. Wang, “Micromechanics based matrix design for engineered cementitious composites,” University of Michigan, Ann Arbor, 2005.
- [18] ASTM A1064/A1064M-16b, *Standard Specification for Steel Wire and Welded Wire Reinforcement, Plain and Deformed, for Concrete*. West Conshohocken, PA: ASTM International, 2016.
- [19] ASTM C76-16, *Standard Specification for Reinforced Concrete Culvert, Storm Drain, and Sewer Pipe*. West Conshohocken, PA: ASTM International, 2016.
- [20] Kaempfer W and M. Berndt, “Estimation of Service Life of Concrete Pipes in Sewer,” *8th Conf. Durab. Build. Mater. Components*, p. Vol. 1, p. 36–45., 1999.
- [21] V. C. Li and C. K. Y. Leung, “Steady-State and Multiple Cracking of Short Random Fiber Composites,” *J. Eng. Mech.*, vol. 118, no. 11, pp. 2246–2264, 1992.

PART IV: APPLICATION OF EGC

CHAPTER 8: Application and Environmental Life Cycle Assessment

This chapter is concerned with a promising infrastructure application of EGC: large-diameter sewer pipes. The market demand, existing technologies, and technical challenges are first outlined. Then, an environmental life cycle analysis (LCA) is conducted to evaluate the sustainability of the EGC pipe, in comparison with RC and ECC pipes.

8.1 Introduction

Wastewater infrastructure is facing an increasing crisis worldwide. For example, there are over 800,000 miles of public sewer mains in the US, many of which were installed in the early 20th century [1]. Since then, repair and retrofit have been patchwork, and many of the outdated sewer systems are susceptible to blockages and leakages; according to the US Environmental Protection Agency (EPA), at least 23,000 to 75,000 sanitary-sewer overflows occur every year [2], mainly caused by blockages and line breaks. It is clear that such wastewater leakages affect the natural environment and human health. Therefore, there is an urgent need for replacement of old sanitary pipes reaching the end of their service life. Considering the expected long lifespan of public sewer systems, a durable piping material for new installation needs to be carefully selected.

Traditionally, concrete and steel were predominantly used for underground pipes; in recent years, plastic has emerged as a competitive alternative [3]. Plastic pipes offer a variety of advantages; for example, polyvinyl chloride (PVC) and high-density polyethylene (HDPE) pipes are lightweight and corrosive-resistant technologies. Lightweight is beneficial for reducing time and cost for installation, and high corrosion resistance prevents early deterioration/failure of the pipe, extending the service life. These technical advantages lower the life-cycle cost of plastic-pipe applications, which is attractive to asset owners. Indeed, demand for plastic pipes in the US is predicted to rise at the most rapid pace of all piping materials [4].

However, there are also limitations in plastic pipes. PVC pipes, for example, have relatively low crush resistance and are prone to cracking. Unlike reinforced-concrete (RC) pipes, plastic pipes can easily lose structural integrity if cracking is extensive. Further, the material becomes more brittle if the temperature is below 3 °C (37 °F), and therefore is not suitable for installation during cold temperatures [3]. Aside from the technical aspect, plastic pipes have large embodied energy due to petroleum-based raw ingredients. Indeed, embodied energy per unit mass of PVC or HDPE is more than 20 times that of RC [5] (it should be noted that the density of PVC or HDPE is roughly half that of RC). Meanwhile, the high carbon intensity of cement is a disadvantage of RC pipes. Hence, to select the best piping material, each technology should be comprehensively evaluated depending on the application.

The objective of this chapter is to investigate the feasibility of using EGC for sewer-pipe applications. The market size and trends are first outlined to determine the target market. Then, technical advantages of EGC pipes are presented in comparison with existing technologies in the market. Finally, an environmental life cycle analysis (LCA) is conducted to assess the sustainability of EGC pipes in terms of the energy use and carbon dioxide (CO₂) emissions.

8.2 Target Market

According to a comprehensive market report by the Freedonia Group [6], water- and wastewater-pipe demand in the US amounted to \$12.5 billion in 2013 and is expected to reach \$18.1 billion in 2018, with annual growth of 7.7%. The increasing trend mainly results from continuous need for repair and replacement of the aging water- and wastewater-pipe network.

Out of the total demand of \$12.5 billion, demand for plastic pipes accounts for 52.7%, while that for concrete pipes is only 14.4%. PVC and HDPE are the dominant materials for plastic-pipe applications, contributing to over 90% of the demand. One of the advantages of plastic pipes is the ease of partial replacement; plastic pipes can be customized to replace a specific part of a line, while concrete pipes must be replaced in whole sections. Also, plastic pipes are popular with installers because of the low cost and quick installation. Because of the technical and economical benefits, demand for plastic pipes is expected to increase by 8.9% annually through 2018, which is the largest growth rate of any major piping materials.

Although plastic is capturing market share from competing materials, continuous need still exists for concrete, especially in large-diameter underground pipes. Figure 8.1 shows demand for large-diameter pipes (diameter of 381 mm or more) in the US in 2011. For this market, concrete and steel pipes account for more than half of the market share. This results from the high crush resistance and pressure capabilities of the materials, which are essential for large-diameter pipe applications. While steel is the leading material in the market, it is typically used in oil and gas applications. For sanitary sewers, cast iron and ductile iron (in recent years) are commonly used, but they are generally more expensive than concrete [7]. As a result, concrete has a solid market share for large-diameter sewer pipes. It should be noted that sewer pipes are the dominant application in the market (Fig. 8.1 (b)).

Total demand: 145.6 million liner feet

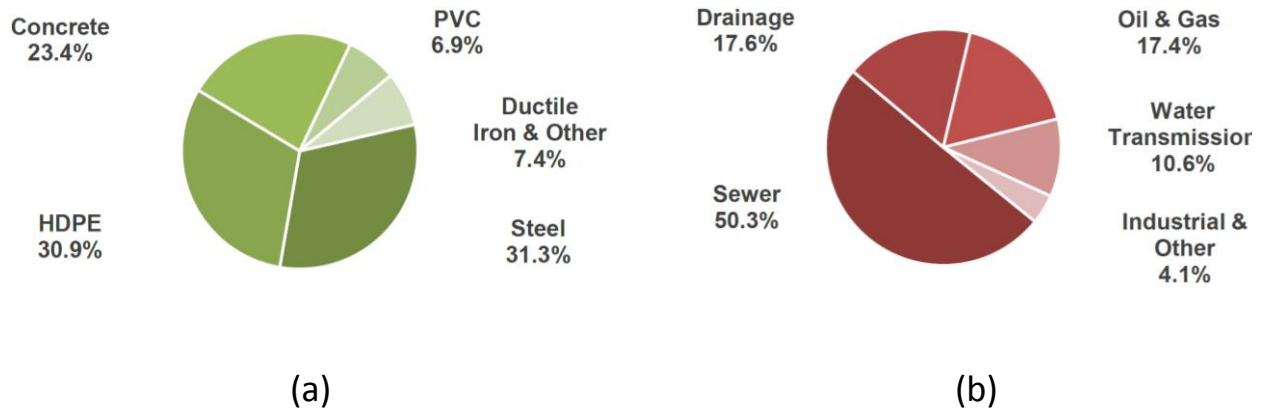


Fig. 8.1: Large-diameter pipe demand in the US (a) by material and (b) by application, 2011 [8].

As presented in Chapter 7, EGC possesses good compressive strength and comparable flexural strength to RC, which implies good crush resistance when used in pipe applications. Further, high tensile ductility and controlled multiple microcracking in EGC should be also beneficial; indeed, higher water tightness of cracked EGC than that of cracked reinforced mortar has been demonstrated in Chapter 5. Therefore, the market of large-diameter sewer concrete pipes seems promising for EGC to be introduced.

8.3 Technical advantage analysis

Major advantages of concrete pipes are the good crush resistance, reliability based on the long use history, and low cost compared to other nonplastic materials. In addition, long service life is often claimed for concrete pipes; in a design manual for conduits, culverts, and pipes, US Army Corps of Engineers (USACE) provides a list of expected lifespans for pipe materials as follows [9]:

- (i) Concrete – between 70 and 100 years.
- (ii) Steel – at least 50 years provided that coatings are properly applied.
- (iii) Plastic – less than 50 years.

It should be noted that the design manual was published in 1997, and the recommended service life for plastic pipes is relatively short because of the limited performance history of the material at that time; a longer service life might be able to be claimed today.

Despite the long life expectancy for concrete pipes, the actual longevity highly depends on the site conditions. Particularly, acidic environments significantly shorten the lifespan of concrete pipes (Fig. 8.2). Indeed, unexpected early deterioration of concrete sewer facilities has been reported worldwide [10, 11]. The severe deterioration is typically associated with formation of biogenic sulfuric acid in wastewater; cement-based materials are severely eroded due to their low sulfuric acid resistance, as discussed throughout Chapter 7. To improve the low acid resistance, various technologies including surface coatings or plastic liners have been introduced, which however require additional initial costs.

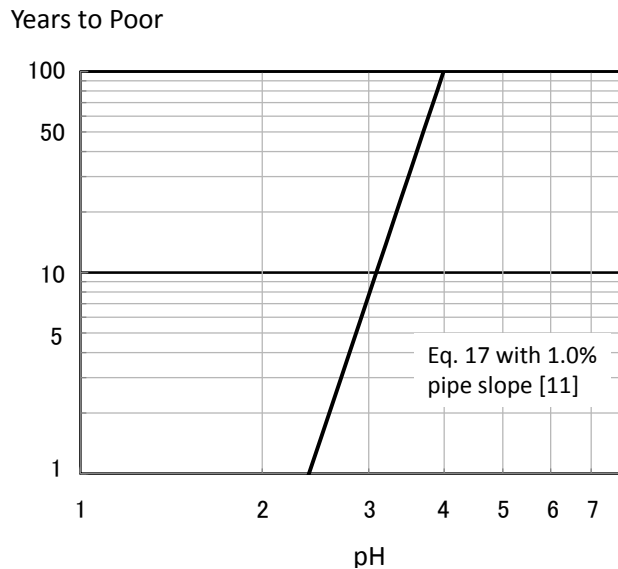


Fig. 8.2: Predicted concrete-pipe lifespan by Ohio Department of Transportation (ODOT) [12]. Years for the pipe to reach a poor condition (based on ODOT classification) highly depend on pH of the stream.

Another emerging technology is reinforced-geopolymer pipes, as mentioned in Section 7.1. The geopolymer matrix has excellent sulfuric acid resistance, as well as similar or even better mechanical properties compared to cement-based materials. Further, fly ash-based geopolymers offer enhanced material greenness, especially in carbon footprints. Driven by the acid-resistant property and low carbon intensity, geopolymer technologies are being accepted in the US and Australia (Fig. 8.3).



(a)



(b)

Fig. 8.3: (a) Precast geopolymer sewer pipes of 1.8 m diameter, commercially available in Australia [13]; (b) repair of deteriorated concrete sewer pipes in the US by spray-applied geopolymer [14].

However, even with the improved sulfuric acid resistance by either protective coatings or geopolymers, long service life might not be fully guaranteed. Cracking is practically inevitable in those technologies, and as long as the pipe relies on steel reinforcement, significant performance degradation could result from the steel corrosion. The resultant shorter lifespan of the pipe is unsustainable because of more frequent replacement required. In contrast, EGC can tightly control crack width and achieve high tensile ductility without steel reinforcement (Fig. 8.4). In addition, its high sulfuric acid resistance has been verified in Chapter 7. Therefore, the enhanced durability of EGC is expected to offer a longer lifespan and lower life-cycle environmental impacts for sewer-pipe applications, compared to conventional concrete pipes.

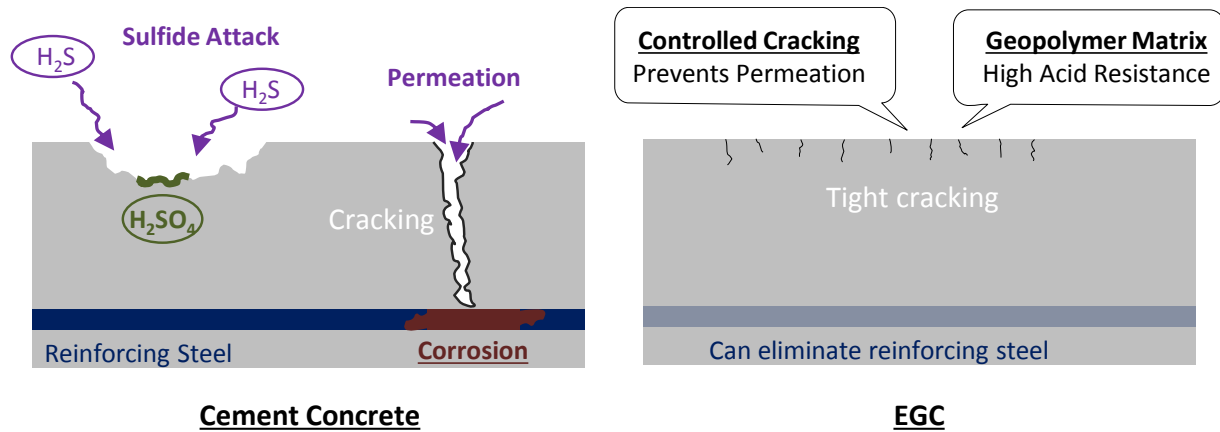


Fig. 8.4: Schematic illustrations of comparison between RC and EGC sewer pipes.

8.4 Life cycle environmental assessment

To verify and quantify the enhanced sustainability of EGC pipes, an environmental life-cycle analysis (LCA) is conducted in this section. Specifically, energy consumption and carbon emissions are inventoried here. For reference, life-cycle environmental performances of the EGC pipe are compared with those of RC and ECC pipes.

8.4.1 LCA methodology

In general, LCA considers the entire life cycle of a product: from raw-material acquisition, through production/manufacturing, to use and end-of-life treatment. The ISO 14040 provides general requirements of an LCA study, defining the following four phases [15];

- (i) *Goal and scope definition* – to state the objective(s) of the study and define the product system(s) to be studied. The functional unit, system boundary, assumptions, and impact categories are determined in this phase.
- (ii) *Inventory analysis* – to collect data of relevant inputs and outputs of the product system(s) and relate them to the functional unit.
- (iii) *Impact assessment* – to associate the inventory data with specific environmental-impact

categories and category indicators based on selected characterization models.

(iv) *Interpretation* – to draw conclusions about the product system(s) based on findings from the inventory analysis and impact assessment.

This standard LCA procedure is adopted in this study. The above four phases are detailed in the following sections.

8.4.2 Goal and scope definition

The objectives of this study are to quantify life-cycle environmental performances of a large-diameter EGC sewer pipe and compare them with those of RC and ECC counterparts.

The functional unit used in this study is a sanitary sewer pipe with length of 1 m, internal diameter of 686 mm (27 inches), and wall thickness of 102 mm (4 inches). The pipe diameter and thickness are determined based on the Class IV reinforced-concrete pipe specified in ASTM C76 [16]. As presented in Section 7.3.5, laboratory-scale experimentation has demonstrated that ECC and EGC have significantly higher flexural strength and deflection capacity than RC. Thus, it might be possible for ECC or EGC to meet mechanical-performance requirements with a smaller thickness. One way to verify the performance difference is to conduct a typical crushing test on laboratory-scale pipe specimens; from the peak line load and inner and outer pipe diameters, the crushing stress (i.e. property independent of pipe dimensions) can be determined for each pipe material based on a linear elastic analysis [17]. However, the ASTM C76 requires that the three-edge-bearing test (specified in ASTM C497 [18]) be conducted on a full-scale pipe to verify the crush resistance. Due to the lack of full-scale testing data, identical dimensions are assumed for all pipes in this study. As a result, environmental-impact estimations for ECC and EGC pipes might be conservative.

Figure 8.5 shows the system boundary in this study. In general, assumptions and simplifications are necessary to model the product system. First and foremost, the present LCA study omits the use and end-of-life phases. In most products, the use phase significantly contributes to the life-cycle environmental impacts. However, unlike pipes for drinking water, typical sewer lines are not pressurized to transport the wastewater, but run at a slope. Consequently, the energy consumption in the use phase is limited for a sewer pipe, compared to that for a pump-driven water pipe [19]. In addition, Vahidi *et al.* concluded in their LCA study on wastewater piping systems that maintenance and repair of a concrete pipe (15-year interval for a period of 50 years) had almost negligible impacts in the life-cycle energy/material use and greenhouse gas emissions [7]. Regarding the end-of-life stage, used concrete pipes are usually not recycled; the old pipes are often abandoned in the site after their service life, and the disposal phase is therefore omitted in many comparative LCA studies on underground pipe systems [5, 7, 19, 20]. Other assumptions and simplifications are summarized in Table 8.1.

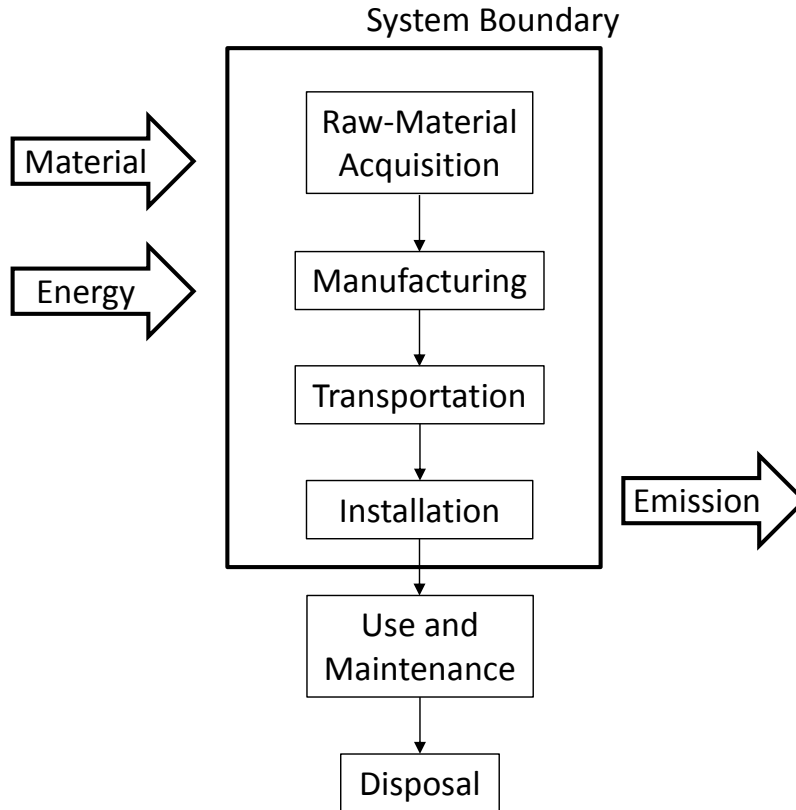


Fig. 8.5: System boundary of the sewer pipe system. Use and disposal phases are omitted because of the low contribution to the life-cycle environmental impacts.

Table 8.1: Summary of assumptions and simplifications for LCA.

LCA phase	Assumption/simplification
All	<ul style="list-style-type: none"> - All accessories such as gaskets and sealants are excluded from the analysis. - Production and maintenance of machinery, equipment, and transportation vehicles are excluded from the analysis.
Raw-material acquisition	<ul style="list-style-type: none"> - Transportation of manufactured ingredients (cement, fiber, steel, etc.) to the pipe plant is excluded from the analysis.
Manufacturing	<ul style="list-style-type: none"> - The same manufacturing method is assumed to be applicable to all pipe materials (See Section 8.4.3).
Transportation	<ul style="list-style-type: none"> - The distance from the pipe plant to the installation site is assumed to be 100 km.
Installation	<ul style="list-style-type: none"> - The same trench volume for pipe installation is assumed for all pipe materials.

Last but not least, two scenarios are considered about the lifespan of each pipe system.

(i) Scenario I: equal service life for all materials

The first scenario assumes a service life of 50 years for all pipe materials, for a project period of 100 years (i.e. all pipes are replaced once during the project period). There might be a couple of arguments for this assumption. First, the lifespan of 50 years might be short for RC pipes, considering the expected service life of 70 – 100 years by USACE (Section 8.3). However, as presented in Fig. 8.2, the deterioration rate of RC pipes is highly dependent on the pipe slope and pH of the wastewater; the 50-year lifespan is a reasonable estimate for a relatively acidic environment. Second, considering the enhanced sulfuric acid resistance of EGC, it might be argued that EGC pipes have a longer lifespan than RC and ECC pipes. However, longevity of sewer pipes depends on multiple factors; the ODOT classification system [21] determines the deterioration level of a pipe based on the crack width and depth, scaling/delamination area and depth, presence of corrosion and section loss of exposed reinforcing steel, etc. Because of limited knowledge on performance of ECC/EGC sewer pipes in the field, there is a great uncertainty in estimating their service life. Therefore, this scenario serves as a reference case that estimates the EGC-pipe lifespan conservatively.

(ii) Scenario II: service life estimated based on acid-resistance test data

Considering the uncertainty, the service life of each pipe material is estimated in this scenario, based on the result of the acid-resistance test in Chapter 7.

In the ODOT classification system, one of the criteria to determine the pipe condition is the surface scaling on the pipe invert caused by freeze-thaw cycles; if the scaling depth is greater than 0.5 inches (1.27 mm), then the pipe is ranked as “poor”. This suggests that the surface loss

of 0.5-inch depth can significantly affect the pipe performance (and possibly lose a large part of cover depth in RC pipes). This criterion is adopted here to determine the service life of each pipe material, combined with the relationship between weight loss and acid-exposure time for each material, shown in Fig. 7.4 in Chapter 7.

Figure 8.6 illustrates the method for the service life estimation. Two assumptions are made here. First, it is assumed that specimens in the acid-resistance test were uniformly eroded over the entire surface area; namely the diameter and height of the cylinder specimen are equally reduced. Then, the weight loss can be related to the reduced diameter and height as follows;

$$(1 - y)\rho\pi\frac{d^2h}{4} = \rho\pi\left(\frac{d - 2x}{2}\right)^2(h - 2x) \quad (8.1)$$

where y , ρ , d , and h are the weight loss (in percent), density, diameter, and height of the cylinder, respectively, and x represents the depth of lost surface due to erosion. It should be noted that the diameter and height are reduced by $2x$. Then, by substituting $x = 0.5$ (plus, $d = 3$ and $h = 6$ for the 3×6 inch cylinder specimen) into Eq. 8.1, a critical value of y for which the pipe is assumed to reach the end of the service life can be determined.

The second assumption is that the rate of weight loss does not accelerate but keeps constant after the test duration (105 days). Figure 8.7 shows the weight-loss data presented in Chapter 7 and their linear regressions. For concrete and ECC, data from 35 days were used for the regression analysis. As mentioned in Section 7.3.1, a slower rate of weight loss (and even weight gain) is typically observed for cement-based materials, mainly due to continuous cement hydration and formation of gypsum caused by acid attack. As a result, the weight loss-exposure time

relationship seems to have a bilinear relation for both concrete and ECC. Thus, a constant rate was assumed for data after 35 days, which gives the highest R^2 value.

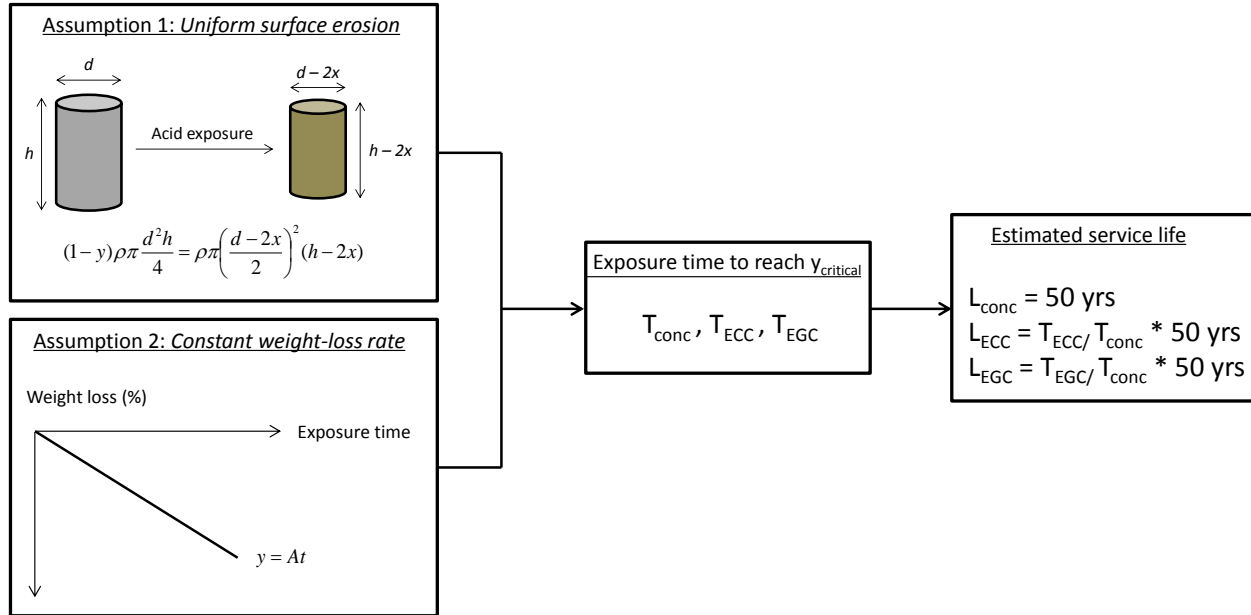


Fig. 8.6: Service-life estimation procedure.

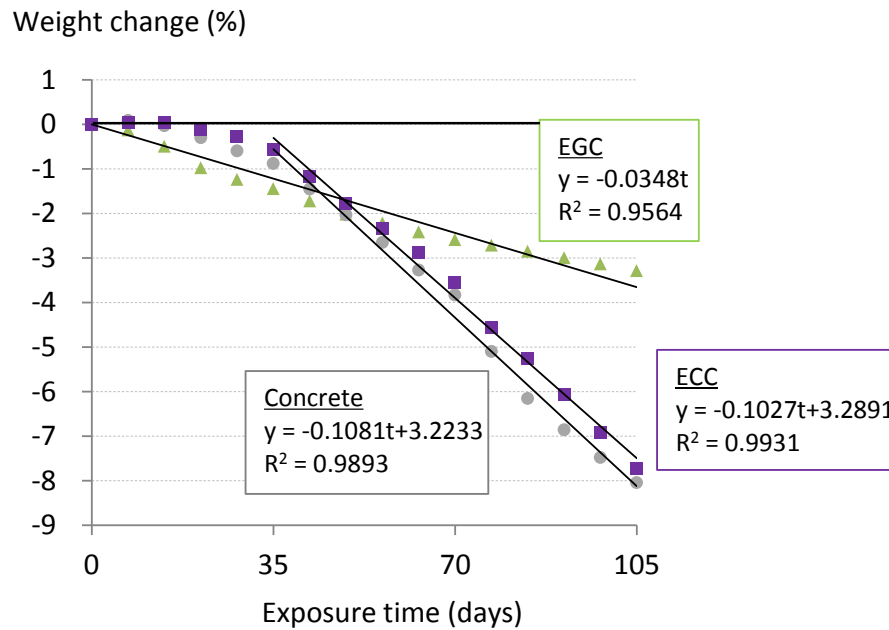


Fig. 8.7: Linear regressions for weight loss-exposure time relationship for acid-exposed concrete, ECC and EGC. For concrete and ECC, the constant rate was assumed for data after 35 days.

Based on the above two assumptions, the exposure time to reach the critical value of y (equivalent to critical surface-erosion depth) can be determined for each material. Then, by assuming that the calculated exposure time for concrete is equivalent to a service life of 50 years, lifespans of ECC and EGC can be determined by taking the ratio of their exposure times.

The calculated lifespans are 52.6 and 156.1 years for ECC and EGC pipes, respectively. It should be mentioned again that service life of sewer pipes is affected by many factors, and the above estimation method is therefore much simplified. A further study is required to develop a more comprehensive method for the service-life estimation. Considering the uncertainty in the current method, it is assumed for a project period of 100 years that RC and ECC pipes are replaced once, while no replacement is scheduled for the EGC pipe.

Regarding the impact categories, life-cycle energy use and carbon dioxide (CO₂) equivalent emissions are selected in this study. As in the MSI calculation in Chapter 4, 100-year GWP values of the ICPP 2013 report [22] are used to calculate the CO₂ equivalent emissions.

8.4.3 Inventory analysis

Data for the inventory analysis are collected from various sources, mainly from scientific literatures and environmental reports from industrial bodies. The data sources are selected based on the validity of system boundaries and assumptions, reliability, and significance in the research field. Information on the inventory data for each LCA phase is presented below.

(i) Raw-material acquisition

For ingredients of concrete, ECC, and EGC, associated embodied energy and GWI per unit mass of the materials have been presented in Table 4.14 in Chapter 4. For production of reinforcing steel, the dataset developed by the International Iron and Steel Institute is adopted [23].

The mix design for the RC pipe is that studied in Chapter 7, which is commonly used in dry-mixed concrete pipe production. It incorporates fly ash and is different from the OPC concrete studied in Chapter 4. Due to the use of fly ash, the RC is suggested to have a higher sulfuric acid resistance than normal design. Therefore, any surface coatings are not considered here. For ECC and EGC pipes, ECC M45 and EGC V_f-1.5% are used as in Chapter 7.

(ii) Pipe manufacturing

Inventory data for production energy of RC pipes are obtained from a comprehensive LCA study on water and wastewater pipe systems conducted by Recio *et al.* [19]. The study estimated that the production energy is 0.45 kWh per kilogram of RC pipe, assuming that the energy used in the production process is only electricity. Thus, carbon footprints of the pipe production can be estimated from the energy intensity multiplied by a CO₂-emission factor for electricity generation. In this study, a factor of 0.611 kg CO₂-eq/kWh is adopted, which is estimated from life-cycle greenhouse gas emissions from electricity generation in the US [24]. In addition, the same temperature-curing method (at 60 °C for 24 hours) is assumed to be used for all pipes. The associated carbon intensity is obtained from a study on CO₂ equivalent emissions from geopolymer and cement-concrete production by Turner and Collins [25]. They assumed that liquid petroleum gas (LPG) is used for the temperature curing, and used a CO₂-emission factor of 1.54 kg CO₂-eq/L for LPG. To calculate the energy associated with the LPG use, the higher heating value (HHV) of 25.4 MJ/L is used for LPG.

It is assumed that the same energy and carbon intensities are applied to production of both ECC and EGC pipes. Difference in pipe-manufacturing energy/emissions results from the different weight per unit volume of each pipe.

(iii) Transportation to the installation site

LCI data for production of cement, fly ash, and aggregate – obtained from LCA studies on portland cement concrete conducted by Portland Cement Association (PCA) [26, 27] – include energy and emissions for transportation from the extraction site to the manufacturing plant (note that transportation from the manufactured ingredients to the pipe manufacturing plant is excluded in the present LCA study). The study by PCA used energy consumption of 1,060 kJ/metric ton-km, assuming that the transportation energy efficiency was 0.024 L of diesel fuel per metric ton-km. This was based on the heat content of 44.2 MJ/L for diesel. Also, the carbon intensity was calculated based on a CO₂-emission factor of 2.77 kg-CO₂/L for diesel. In this study, the same energy and carbon intensities were used for transportation of the pipe to the installation site, assuming that the same transportation vehicle and fuel were used.

(iv) Installation

Energy and emissions in this phase are mainly associated with trench excavation for pipe installation. First, the required trench volume is determined based on an installation manual for concrete pipe and box culvert, published from the American Concrete Pipe Association [28]. According to the trench-design recommendation, the minimum trench width for an RC pipe with 686-mm diameter is 1300 mm, which is adopted in this study. Also, the class D bedding for circular pipes is selected as shown in Fig. 8.8; the minimum depth over the top of the pipe is 150 mm, and the trench depth of 937 mm (i.e. 150 mm plus 787 mm of the outside diameter) is used for the analysis. This class of bedding requires no special care to shape the foundation surface and to fill all spaces under and around the pipe with granular materials. Energy and emissions associated with the granular materials are excluded from the analysis, by assuming that the

excavated soil is used to backfill the pit. Based on this assumption, diesel used by the hydraulic excavator is only accounted in this phase. Data on diesel use and greenhouse gas emissions associated with excavation of 1-m³ trench is obtained from the ecoinvent database [29]. To calculate the energy intensity from the diesel use, the heat content of 44.2 MJ/L is used as in the transportation phase [26, 27]. It should be noted that, since the pipe dimensions are the same in all cases, the total energy and carbon footprints are also the same.

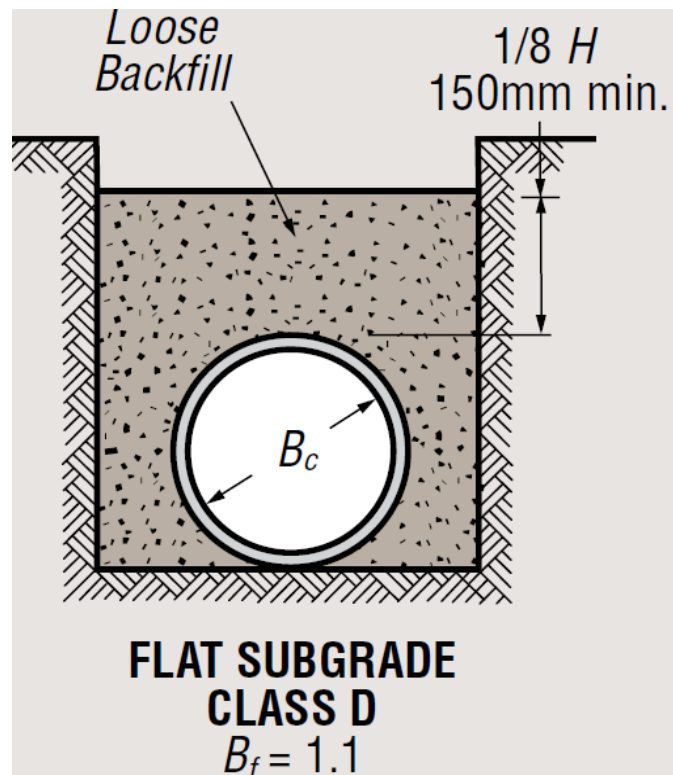


Fig. 8.8: Trench design for circular RC pipe [28]. The total trench volume for this study is 1.22 m³.

The LCA inputs for this study are summarized in Table 8.2. It should be noted that emissions data for all inputs have been converted into GWI values.

Table 8.2: Summary of inputs for life-cycle inventory analysis.

LCA phase	Material/process [data source]	Unit	Energy intensity (MJ/unit)	Carbon intensity (kg CO ₂ - eq/unit)	Inputs for 1-m pipe		
					RC	ECC	EGC
Raw material acquisition	Cement [27]	kg	4.8	0.93	34.4	67.1	
	Fly ash [26]	kg	0.11	0.0074	12.1	80.5	136
	Aggregate [26]	kg	0.12	0.0062	215		
	Fine silica sand [30]	kg	0.17	0.025		53.6	54.4
	PVA fiber [31]	kg	101	3.4		3.06	2.29
	Super plasticizer [30, 32]	kg	35	1.5	0.25	0.80	
	Water *	kg	0	0	20.4	39	16.7
	Sodium hydroxide [33]	kg	18	0.86			7.07
	Sodium silicate [34]	kg	4.6	0.43			30.6
	Reinforcing steel [23]	kg	8.4	0.44	8.23		
Manufacturing	Electricity [19]	kWh	3.6	0.611	131	110	111
	LPG [25]	L	25.4	1.54	26	26	26
Transportation	Diesel [26, 27]	L	44.2	2.77	0.70	0.59	0.59
Installation	Excavation [29]	m ³	6.95	0.409	1.22	1.22	1.22

* Assumed negligible.

8.4.4 Impact assessment and interpretation

To conduct the impact assessment, the sum of impacts from all LCA phases considered is calculated. The impact-assessment results based on the Scenario I and II are shown below.

(i) Scenario I: equal service life for all pipes

As mentioned in Section 8.4.2, all pipes have a service life of 50 years and are to be replaced once during a project period of 100 years. Thus, the summed energy and GWI values are simply

doubled to account for the replacement.

Figure 8.9 shows the assessment results. As can be seen, the RC pipe performs best with regard to life-cycle energy consumption. The biggest advantage of the material is its low impact from the material-acquisition phase; energy associated with production of RC-pipe ingredients is only 30 and 39% of those for ECC and EGC, respectively. The large difference results from two factors: the larger amount of fly ash incorporated in the RC mix design than normal concrete, and the use of energy-intensive PVA fibers in both ECC and EGC pipes. In the case of pipe-manufacturing energy use, the RC pipe has a slightly larger impact than ECC and EGC pipes due to the heavier weight. However, the difference is less than 15% and relatively small compared to that for the material-acquisition phase. The same is true for the transportation phase. In the case of installation energy (and emissions), the impacts are almost negligible in all pipes, which is consistent with previous LCA studies on water- and wastewater-pipe materials [5, 7, 19, 20].

On the other hand, the EGC pipe has the lowest impact for carbon emissions; the GWI for EGC is 86 and 70% of those for RC and ECC, respectively. The difference mainly results from the amount of cement used; EGC uses no cement and has the lower GWI for the material-acquisition phase; conversely, ECC has the largest amount of cement and highest GWI. Due to the high carbon intensity of cement, the material-acquisition phase has the largest contribution to the life-cycle GWI of the ECC pipe, while the manufacturing phase is dominant in the EGC pipe. In the case of RC, the material-acquisition phase is limited compared to ECC; the RC incorporates fly ash substituting for a portion of cement and uses a smaller amount of cement than ECC. It should be also noted that PVA fibers have relatively small impacts for GWI, as mentioned in Section 4.4 in Chapter 4.

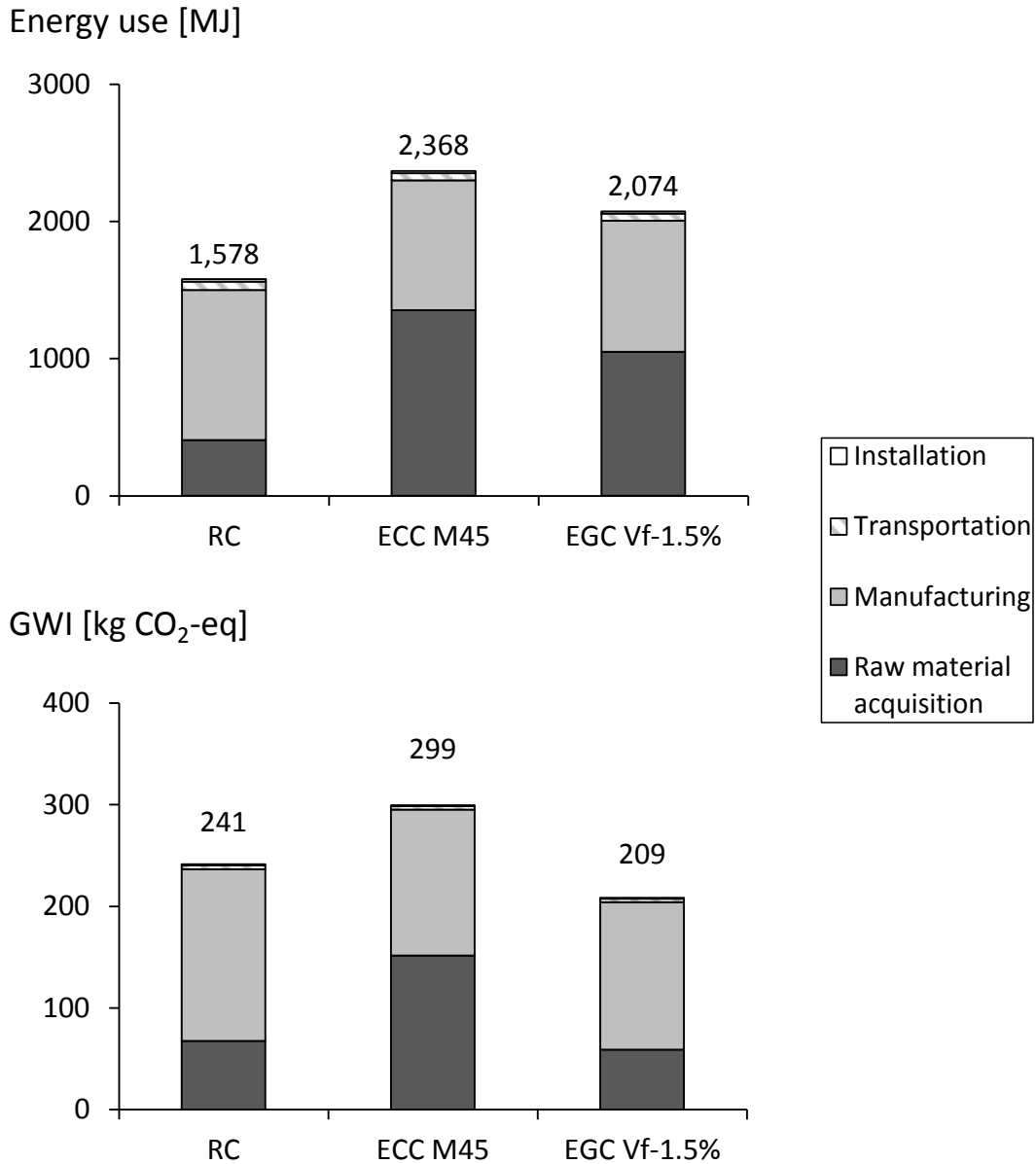


Fig. 8.9: Life-cycle energy use and GWI values of RC, ECC, and EGC pipes in Scenario I.

(ii) *Scenario II: service life estimated based on acid-resistance test data*

In this scenario, RC and ECC pipes are to be replaced once during the project period, while no replacement is scheduled for the EGC pipe. Thus, the energy use and GWI values for EGC are simply half those in Scenario I. As a result, the EGC pipe performs best with regard to both energy consumption and carbon emissions. The impact-assessment result for each phase is

presented in Tables 8.3 and 8.4. The total energy use and GWI for the EGC pipe is 66 and 43% of those for RC, and 44 and 35% for ECC.

Table 8.3: Energy use of RC, ECC, and EGC pipes for each LCA phase in Scenario II (in MJ).

Material	LCA phase				Total
	Raw-material acquisition	Manufacturing	Transportation	Installation	
RC	404	1,096	62	17	1,578
ECC	1,353	946	52	17	2,368
EGC	525	478	26	8.5	1,037

Table 8.4: GWI of RC, ECC, and EGC pipes for each LCA phase in Scenario II (in kg CO₂-eq).

Material	LCA phase				Total
	Raw-material acquisition	Manufacturing	Transportation	Installation	
RC	67	169	3.9	1.0	241
ECC	152	144	3.2	1.0	299
EGC	29	73	1.6	0.5	104

From the above LCA results, it seems promising to use EGC for replacing the current technology (i.e. RC pipes). However, as mentioned in Section 8.4.2, there is a great uncertainty in the service-life estimation of each pipe. To understand the sensitivity, the threshold service life of the EGC pipe, which results in the same energy use or GWI as that for the RC pipe, is calculated. First, it is assumed that the lifespan of the RC pipe is 50 years. Then, the ratio of the sum of energy use or GWI for EGC to that of RC (i.e. no replacement for both pipes) is calculated and multiplied by 50 years. The calculated threshold lifespans for energy use and GWI are 66 and 43 years. In other words, if the service life of EGC pipes is more than 1.3 times that of RC pipes, EGC has more environmental benefits than RC, with regard to both life-cycle energy consumption and carbon emissions.

8.5 Summary and conclusions

This chapter explored the feasibility of using EGC for sanitary sewer pipes. Based on the brief reviews of the market demand and current challenges of existing technologies, it seems promising to introduce EGC in the market of large-diameter sewer concrete pipes. In addition, to verify and quantify the enhanced sustainability of EGC pipes, a comparative LCA study has been conducted on three pipe materials: RC, ECC, and EGC. When equal service life is assumed for all pipes, the LCA result indicates that the EGC pipe performs best with regard to GWI. On the other hand, the RC pipe has the lowest life-cycle energy use. The sensitivity analysis shows that, if service life of EGC pipes is more than 1.3 times that of RC pipes, EGC performs best in both energy consumption and carbon emissions.

The other findings obtained in the LCA study are listed below;

- Life-cycle energy use for all pipes highly depends on the material-acquisition phase. Because of the high energy intensity of PVA fibers, the EGC pipe has 2.6 times larger energy use than the RC pipe for this phase.
- Life-cycle GWI is significantly affected by the amount of cement used. Since no cement is used in EGC, contributions from the material-acquisition phase are limited, while the pipe-manufacturing phase becomes dominant.
- For both life-cycle energy use and GWI, transportation and installation phases have negligible impacts.

It should be noted that, in the present LCA study, the high tensile ductility and multiple microcracking characteristic of EGC are not taken into account for the service life estimation. As a result, steel-reinforced geopolymer pipes would have better environmental performances than

EGC pipes. A further study is required to develop a more comprehensive method to estimate the pipe lifespan based on mechanical properties, as well as sulfuric acid resistance.

In addition, life-cycle cost analysis is also important to select the best pipe material, especially for asset owners. Considering the time and cost for manufacturing of steel cages, EGC pipes would have significant advantages against reinforced concrete and geopolymer pipes. This will also be a subject of future studies.

Another important aspect excluded from the present LCA study is the externalities associated with loss of use, repair, and replacement of sewer pipes. For example, when replacement of buried pipes under high-traffic roads requires the trench excavation, the construction activities could cause traffic congestion or delay. This leads to time loss of drivers on the route and more emissions from the vehicles. Such externalities are critical when frequent/extensive replacement is required, and are thus related to the pipe lifespan. The social cost and environmental impacts associated with those externalities should be quantified in a future study.

References

- [1] ASCE, “Wastewater: Infrastructure Report Card 2017,” 2017. [Online]. Available: <https://www.infrastructurereportcard.org/wp-content/uploads/2017/01/Wastewater-Final.pdf>. [Accessed: 15-Aug-2017].
- [2] US Environmental Protection Agency, “Sanitary Sewer Overflows: National Pollutant Discharge Elimination System.” [Online]. Available: <https://www.epa.gov/npdes/sanitary-sewer-overflows-ssos>. [Accessed: 10-Aug-2017].
- [3] C. A. Taylor and J. Marr, “A Research Plan and Report on Factors Affecting Culvert Pipe Service Life in Minnesota,” 2012.
- [4] The Freedonia Group, “Plastic & Competitive Pipe,” Cleveland (OH), 2014.
- [5] F. Du, G. Woods, and D. Kang, “Life Cycle Analysis for Water and Wastewater Pipe Materials,” *J. Environ. Eng.*, vol. 139, no. May, pp. 703–711, 2012.
- [6] The Freedonia Group, “Water & Wastewater Pipe: United States,” Cleveland (OH), 2014.
- [7] E. Vahidi, E. Jin, M. Das, M. Singh, and F. Zhao, “Comparative Life Cycle Analysis of Materials in Wastewater Piping Systems,” in *Procedia Engineering*, 2015, vol. 118, no. 813, pp. 1177–1188.
- [8] The Freedonia Group, “Large Diameter Pipe: United States,” Cleveland (OH), 2012.
- [9] U.S. Army Corps of Engineers, “Engineering and Design: Coduits, Culverts, and Pipes,” Washington, EC, 1997.
- [10] M. O’Connell, C. McNally, and M. G. Richardson, “Biochemical attack on concrete in wastewater applications: A state of the art review,” *Cem. Concr. Compos.*, vol. 32, no. 7, pp. 479–485, 2010.
- [11] W. Sand and E. Bock, “Concrete corrosion in the Hamburg Sewer system,” *Environ. Technol.*, vol. 5, no. 12, pp. 517–528, 1984.
- [12] D. G. Meacham, J. O. Hurd, and W. W. Shisler, “Ohio Culvert Durability Study,” Columbus, OH, 1982.
- [13] G. Johnson, “Encouraging the use of sustainable materials: Geopolymer Concrete,” *Rocla*, 2014. [Online]. Available: http://www.roads.org.au/News/Publications?EntryId=54&Command=Core_Download&method=attachment. [Accessed: 17-Aug-2017].
- [14] D. Keaffaber, “GeoSpray: GeoPolymer Mortar System and Concrete Cloth for Structural Rehabilitation/Repair of Sewer and Storm Infrastructure,” *Milliken Infrastructure*, 2015. [Online]. Available:

- <http://ctt.mtu.edu/sites/ctt/files/resources/bridge2016/conference/08keaffaber.pdf>.
[Accessed: 04-Jul-2017].
- [15] The International Standards Organisation, “Environmental management — Life cycle assessment — Principles and framework,” *Iso 14040*, vol. 2006, pp. 1–28, 2006.
- [16] ASTM C76-16, *Standard Specification for Reinforced Concrete Culvert, Storm Drain, and Sewer Pipe*. West Conshohocken, PA: ASTM International, 2016.
- [17] H. Stang and V. Li, “Extrusion of ECC-Material,” in *High Performance Fiber Reinforced Cement Composites 3 (HPFRCC 3)*, 1999, pp. 203–212.
- [18] ASTM C497-17, *Standard Test Methods for Concrete Pipe, Manhole Sections, or Tile*. West Conshohocken, PA: ASTM International, 2017.
- [19] J. M. B. Recio, P. J. Guerrero, M. G. Ageitos, and R. P. Narváez, “Estimate of energy consumption and CO₂ emission associated with the production, use and final disposal of PVC, HDPE, PP, ductile iron and concrete pipes,” Barcelona (Spain), 2005.
- [20] K. R. Piratla, S. M. Asce, S. T. Ariaratnam, M. Asce, and A. Cohen, “Estimation of CO₂ Emissions from the Life Cycle of a Potable Water Pipeline Project,” *J. Manag. Eng.*, vol. 28, no. January, pp. 22–30, 2012.
- [21] Ohio Department of Transportation, *Ohio Culvert Design Manual*. Columbus, OH, 2003.
- [22] G. Myhre, D. Shindell, F. Bréon, W. Collins, J. Fuglestvedt, J. Huang, D. Koch, J. Lamarque, D. Lee, B. Mendoza, T. Nakajima, A. Robock, G. Stephens, T. Takemura, and H. Zhang, “Anthropogenic and natural radiative forcing,” in *Climate Change 2013: The Physical Science Basis, Working Group I Contribution to the Fifth Assessment Report of the Intergovernmental Panel on Climate Change*, T. F. Stocker, D. Qin, G.-K. Plattner, M. Tignor, S. K. Allen, J. Boschung, A. Nauels, Y. Xia, V. Bex, and P. M. Midgley, Eds. Cambridge (UK): Cambridge University Press, 2013, p. 714.
- [23] International Iron and Steel Institute, “Rebar, EAF route,” in *Worldwide LCI Database for Steel Industry Products*, Brussels (Belgium), 2002.
- [24] T. J. Skone, “Life Cycle Greenhouse Gas Emissions: Natural Gas and Power Production.” [Online]. Available: <https://www.eia.gov/conference/2015/pdf/presentations/skone.pdf>. [Accessed: 15-Sep-2017].
- [25] L. K. Turner and F. G. Collins, “Carbon dioxide equivalent (CO₂-e) emissions: A comparison between geopolymer and OPC cement concrete,” *Constr. Build. Mater.*, vol. 43, pp. 125–130, Jun. 2013.
- [26] M. A. Nisbet, M. L. Marceau, and M. G. Vangeem, *Environmental Life Cycle Inventory of Portland Cement Concrete*. Stokie, IL: Portland Cement Association, 2002.
- [27] M. L. Marceau, M. A. Nisbet, and M. G. Vangeem, *Life Cycle Inventory of Portland Cement Manufacture*. Stokie, IL: Portland Cement Association, 2006.

- [28] American Concrete Pipe Association, *Concrete Pipe & Box Culvert Installation*. Irving, Texas.
- [29] The Swiss Centre for Life Cycle Inventories, “Ecoinvent.” [Online]. Available: <http://www.ecoinvent.org/home.html>. [Accessed: 28-Jul-2017].
- [30] R. Ranade, “Advanced Cementitious Composite Development for Resilient and Sustainable Infrastructure,” University of Michigan, Ann Arbor, 2014.
- [31] R. Frazão and R. Fernandes, *Comparative Analysis of the Life Cycle of AT Fibre-cement and NT Fibre-cement*. International Chrysotile Association, 2004.
- [32] G. A. Keoleian, A. Kendall, J. E. Dettling, V. M. Smith, R. F. Chandler, M. D. Lepech, and V. C. Li, “Life Cycle Modeling of Concrete Bridge Design: Comparison of Engineered Cementitious Composite Link Slabs and Conventional Steel Expansion Joints,” *J. Infrastruct. Syst.*, vol. 11, no. 1, pp. 51–60, 2005.
- [33] E. Chlor, “An Eco-profile and Environmental Product Declaration of the European Chlor-Alkali Industry,” 2013. [Online]. Available: https://www1.ethz.ch/ifu/ESD/education/master/AESEA/Euro_Chlor_Eco-profile_Chlorine_2014-03.pdf. [Accessed: 10-Mar-2017].
- [34] M. Fawer, M. Concannon, and W. Rieber, “Life cycle inventories for the production of sodium silicates,” *Int. J. Life Cycle Assess.*, vol. 4, no. 4, pp. 207–212, 1999.

PART V: CONCLUSION

CHAPTER 9: Concluding Remarks

This doctoral research focused on development and characterization of green and durable – therefore, truly sustainable – fiber-reinforced geopolymer composites for civil infrastructure applications. In this chapter, research impacts and scientific contributions achieved in this study are first highlighted. Major research findings are then summarized, and recommended subjects for future studies are presented in the end.

9.1 Research impacts and contributions

(i) Development of a comprehensive design method for EGC

A new design method for ductile fiber-reinforced geopolymer composites has been proposed in this dissertation. The method integrates three design techniques – Design of Experiment (DOE), micromechanical modeling, and Material Sustainability Indices (MSI) – to systematically optimize the matrix, fiber, and interface properties. Fundamental engineering properties, high tensile ductility, multiple microcracking characteristics, and enhanced material greenness can be simultaneously achieved with the aid of the multidisciplinary integrated scheme. This design method facilitates development of various types of EGC and promotes the overall progress in the research community. Further, the design concept is applicable to not only fiber-reinforced

geopolymer composites but also many other composite materials in a variety of engineering fields.

(ii) Development of green and durable geopolymer composites

By using the proposed integrated method, green and durable EGC materials have been developed in Chapter 4. The optimized EGC shows tensile strain-hardening behavior with high ductility of over 4%, and self-controls its microcracks as tight as 40 μm on average (in residual crack width). Such excellent tensile properties have not been achieved in any other geopolymer composites. The high tensile ductility and tight crack width can suppress the inherent brittleness of geopolymers, leading to improved material durability. Moreover, the fiber content is limited to 1.5% by volume, which offers significant reduction in energy and carbon footprints. Because of the high durability and enhanced material greenness, the optimized EGC is promising for a broad range of civil infrastructure applications.

(iii) Characterization of durability properties of EGC

Fundamental durability properties of EGC have been experimentally investigated in this study. Particularly, crack patterns and water permeability of EGC studied in Chapter 5 are crucial for its transport properties, which govern many types of deterioration processes. The obtained experimental results will be useful in future studies on other durability properties of EGC. In addition, sulfuric acid resistance of EGC has been evaluated in Chapter 7, in comparison with OPC concrete and ECC. Those data can be used to estimate service life of EGC infrastructure under sulfuric acid attack, such as wastewater facilities.

(iv) Feasibility of self-healing EGC

The feasibility of achieving self-healing functionality in EGC has been demonstrated in Chapter 6. Only a handful of papers so far have reported self-healing phenomena in geopolymer materials. Experimental results in this study confirm slight but significant stiffness recovery in preloaded EGC due to self-healing of microcracks. Also, microstructure of healing products observed by SEM has been presented, with elemental analysis results by using EDS. While mechanisms behind the EGC self-healing have not been fully understood, this study will open a new window toward developing self-healing geopolymer materials.

(v) Feasibility of introducing EGC for sewer-pipe applications

Brief market research and technical-advantage analysis in Chapter 8 suggests that EGC is promising for large-diameter sewer pipe applications. In addition, a comparative environmental LCA shows lower life-cycle greenhouse gas emissions of the EGC pipe than RC and ECC pipes. The study also reveals dominant ingredients and LCA phases in their life-cycle environmental impacts, which provides valuable insights for developing a more sustainable EGC for those applications.

9.2 Research findings

Major research findings obtained during investigations are listed below;

(i) From Part II: Development of EGC

- The alkaline activator-to fly ash ratio has statistically insignificant effects on compressive strength of the EGC matrix. This is in contrast with many previous studies in the research community.
- EGC matrix has lower tensile strength and more brittle behavior than typical ECC matrix, which is however beneficial in achieving robust multiple microcracking and resultant high tensile ductility in the composite.
- Interface properties between EGC matrix and PVA fiber are significantly different from those for PVA-ECC; it is suggested that the stronger chemical bond, weaker frictional bond, and smaller slip-hardening coefficient of EGC contribute to the tighter crack with and higher tensile ductility.
- The developed EGC shows tensile strain-hardening behavior with high ductility of 3% even with a small fiber volume fraction of 1.0%. However, the performance variability is relatively large compared to that with 1.5 or 2.0% fiber content, which might be associated with the magnitude of PSH indices.
- GWI of the optimized EGC is roughly half that of normal cement concrete; conversely, the embodied energy of EGC is about 70% higher, which results from the use of energy-intensive PVA fiber.

(ii) From Part III: Characterization of EGC Durability

Chapter 5: Cracking Characteristics and Water Permeability of EGC

- Residual crack width of EGC is lognormally distributed as in ECC materials.

- Some EGC specimens under uniaxial tension showed suppressed propagation of localized cracking; a large localized crack initiated from the edge of the specimen (probably due to unintended poor compaction and fiber dispersion), but was confined to the near-edge area, not propagating through the matrix. A further research would be required to understand the mechanism behind this phenomenon.
- Multiple-point measurement is recommended to accurately characterize crack patterns of EGC; crack width is not constant along each crack, and the numbers of crack are different between the central area and near-edge sides of the specimen surface.
- When EGC and normal reinforced mortar/concrete are subjected to the same tensile strain, the cracked EGC shows a significantly lower permeability coefficient than the cracked reinforced mortar/concrete. This suggests better transport properties and related durability of EGC.
- Average crack width of EGC has a stronger correlation with permeability coefficient than maximum crack width; maximum crack width only represents the crack opening in a small area because of the nonuniform opening along each crack.
- White substance is formed on the surface of cracked EGC specimens during permeability testing. This seals some microcracks, reducing the permeability coefficient.

Chapter 6: Feasibility Study of Self-healing EGC

- The sealed microcracks also offer slight but significant stiffness recovery of EGC in uniaxial tension testing.
- However, the degree of EGC self-healing is limited compared to self-healing in ECC; some microcracks are completely sealed, while others are only partially sealed. The limited

formation of healing products would be a cause of the limited performance recoveries in water tightness and stiffness.

- EGC healing products are mostly angular, stone-like substance, and relatively rich in *Si* and *Al* but low in *Ca*. Unlike self-healing in cement-based materials, main healing products of EGC are neither calcite (CaCO_3) nor CSH.

Chapter 7: Sulfuric Acid Resistance of EGC

- Self-healing in EGC requires the presence of water; however, no healing is observed for EGC immersed in sulfuric acid solution. In contrast, most microcracks in ECC are completely sealed even in the acidic environment.
- Meanwhile, surface erosion of EGC due to the sulfuric acid exposure is limited compared to that of ECC and cement concrete; the rate of weight loss for acid-exposed EGC is roughly one third that of the cement-based materials. This verifies the high sulfuric acid resistance of EGC.
- In addition, no significant degradation in mechanical performances is observed for acid-exposed EGC, except in linear bending stiffness. However, the stiffness reduction is significantly lower than that for RC.

(iii) From Part IV: Application of EGC

- When equal service life is assumed for large-diameter EGC, ECC, and RC sewer pipes, a comparative LCA indicates the lowest GWI of the EGC pipe. On the other hand, the RC pipe has the lowest life-cycle energy use.

- If service life of the EGC pipe is more than 1.3 times that of the RC pipe, EGC performs best in both life-cycle energy consumption and GWI.
- Life-cycle energy consumption for large-diameter sewer pipes is highly dependent on the material-acquisition phase. Particularly, PVA fiber has high energy intensity and largely contributes to the energy use in EGC/ECC production.
- Similarly, life-cycle GWI is significantly affected by the amount of cement used in the pipe material. Since EGC incorporates no cement, the material acquisition is not the dominant phase. Instead, the pipe manufacturing has the largest contribution to the total GWP.
- For both life-cycle energy and GWI, transportation and installation phases have insignificant impacts. This suggests that the LCA result is not so sensitive to assumptions and simplifications in those phases.

9.3 Recommendations for future work

For continued development, characterization, and application of EGC, the following investigations are recommended for future work:

(i) Development of natural fiber-reinforced EGC

To drastically enhance the material greenness of EGC, PVA fiber should be replaced because of the high energy intensity. Specifically, use of natural fibers, instead of synthetic fibers produced from petroleum-based inputs, is promising. In recent years, much effort is being made in developing natural fiber-reinforced concrete. There is also ongoing research on natural fiber-reinforced ECC. Knowledge and findings from those studies will be useful in developing natural

fiber-reinforced EGC. Also, the integrated design method proposed in this doctoral research is applicable to the development.

(ii) Development of room temperature-cured EGC

The current EGC requires temperature curing to achieve good compressive strength. This is not suitable for cast-in-place applications. To make a broader range of EGC applications possible, development of room temperature-cured EGC is recommended. So far, various types of room temperature-cured geopolymer concrete have been developed. Particularly, slag-based geopolymers would be most promising.

(iii) Investigation on self-healing mechanisms in EGC

This doctoral research suggests that healing products of EGC are different from those of cement-based materials. As such, they might be produced through different mechanisms. To achieve better self-healing performance in EGC, those mechanisms should be first understood. Particularly, more detailed chemical compositions of healing products need to be studied by using advanced characterization techniques such as X-ray diffraction (XRD) and Fourier transform infrared spectroscopy (FTIR).

(iv) Characterization of other durability properties

To verify the enhanced material durability of EGC, other important durability properties should be investigated. Specifically, studies on the drying shrinkage, chloride-ion diffusivity, and fire and frost resistance would be recommended. Many previous studies on geopolymer concrete demonstrated comparable or better performances in such properties compared to cement concrete.

Thus, EGC is expected to have similar or even better performances. Verifying this hypothesis promotes introduction of EGC into a wider variety of civil infrastructure applications.

(v) Development of a more comprehensive LCA model for sewer pipes

First and foremost, the comparative LCA method used in this study has a great uncertainty in estimating service life of EGC pipes. Particularly, the high tensile ductility and multiple microcracking characteristics are not taken into account in the estimation. In addition, because of those unique characteristics, EGC pipes might be able to meet mechanical-performance requirements with a smaller wall thickness than RC pipes. It should be also mentioned that externalities associated with loss of use, repair, and replacement of sewer pipes might have significant impacts on the LCA result. Conducting further experimental and analytical investigations and data collection, a more comprehensive LCA model to account for the above aspects needs to be developed.

(vi) Cost analysis and minimization

No cost analysis has been conducted in this doctoral study. However, the material cost is one of the most important factors for introducing the new technology, especially into large-scale infrastructure applications. Since EGC uses no cement but utilizes fly ash (i.e. less expensive industrial byproduct), it has some advantage over cement concrete and ECC. On the other hand, the cost of alkaline solution could be a significant disadvantage of EGC. It is recommended to estimate the total material cost for EGC and compare it with those of competing materials. In addition, a further investigation will be required to minimize the EGC cost; using less expensive fibers or alkaline activators would be promising.

APPENDICES

APPENDIX A

Confounding of interaction effects

As an example, consider the simplest orthogonal array (OA), shown in Table A-1. For the L4 OA, up to three factors can be assigned to the columns, each of which has two factor levels. For simplicity, only an interaction effect between Factors A and B is considered. Then, the output performance can be expressed as the superposition of the factor effects and the interaction effect:

$$y_{ijk} = a_i + b_j + c_k + a_i b_j \quad (\text{A-1})$$

y_{ijk} is the output performance under i-, j-, and k-th levels of Factors A, B, and C, respectively; x_n represents the effect of Factor X at the n-th level; $a_i b_j$ represents the interaction effect between Factors A and B at the i-, and j-th levels of the factors.

Table A-1: L4 standard orthogonal array.

Trial No.	Column ID		
	A	B	C
1	<u>1</u>	<u>1</u>	<u>1</u>
2	<u>1</u>	<u>2</u>	<u>2</u>
3	<u>2</u>	<u>1</u>	<u>2</u>
4	<u>2</u>	<u>2</u>	<u>1</u>

The interaction effect can be measured by the difference between the averaged outputs at the A_1B_1 plus A_2B_2 levels and the A_1B_2 plus A_2B_1 levels. Namely, the following quantities are compared:

$$\bar{T}_{11+22} = \frac{y_{111} + y_{221}}{2} = \frac{(a_1 + a_2) + (b_1 + b_2)}{2} + c_1 + \frac{a_1b_1 + a_2b_2}{2} \quad (\text{A-2})$$

$$\bar{T}_{12+21} = \frac{y_{122} + y_{212}}{2} = \frac{(a_1 + a_2) + (b_1 + b_2)}{2} + c_2 + \frac{a_1b_2 + a_2b_1}{2} \quad (\text{A-3})$$

By subtracting Eq. A-3 from Eq. A-2:

$$\bar{T}_{11+22} - \bar{T}_{12+21} = (c_1 - c_2) + \frac{(a_1b_1 + a_2b_2) - (a_1b_2 + a_2b_1)}{2} \quad (\text{A-4})$$

Equation A-4 indicates that the interaction effect between Factors A and B is confounded with the main effect of Factor C, i.e. $(c_1 - c_2)$ in the equation. In other words, if no factor is assigned to the third column, the interaction effect between assigned Factors A and B can be quantified as the main effect of the third column. This is one way to deal with significant interaction effects in OAs.

Following the similar derivation to that above, it can be shown that, in L9 OA discussed in Chapter 3, the interaction effect between Factors A and B is confounded with both the third and fourth columns (Factors C and D). Further, many other interaction effects are also confounded with various main factor effects. This is a reason that the L9 OA is not suitable for evaluating factors that are expected to have significant interaction effects. Conversely, in L18 OA used in Chapter 4, all interaction effects are almost evenly confounded with main factor effects, and the influence on the evaluation of the main factor effects is minimal.

APPENDIX B

Derivation of P - u relations for debonding and pullout stages

(v) *Debonding stage*

Consider the fiber-debonding model shown in Fig. B-1; a single fiber with embedment length of L_e is loaded by external load P , and a portion of the fiber/matrix interface has been debonded due to the pullout load. Here, it is assumed that the tunnel-crack propagation initiates from the fiber exit point from the matrix, and that the length of the debonded zone is a .

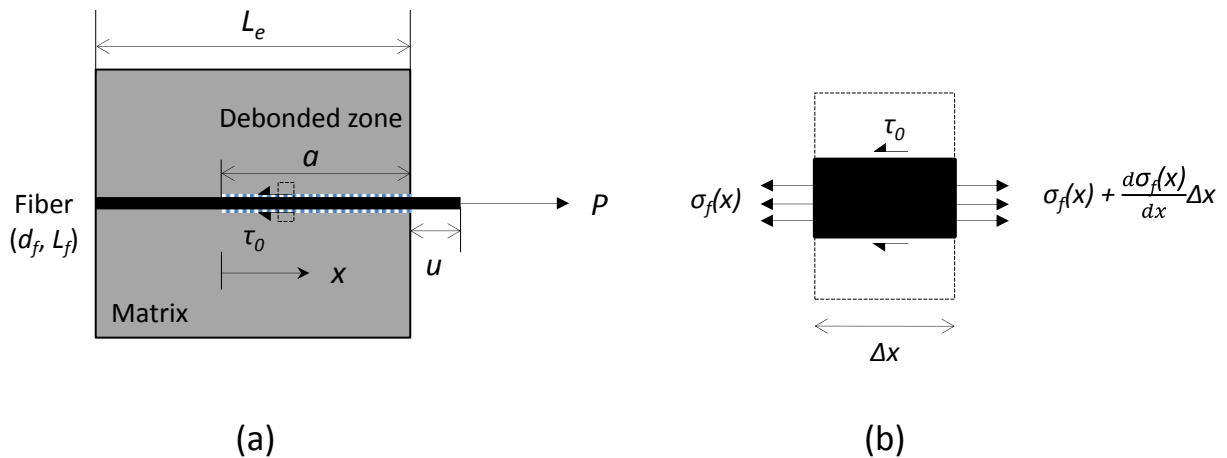


Fig. B-1: (a) Model of fiber debonding process; (b) a small fiber segment of the debonded zone.

In the debonded zone, only frictional bond resists the relative displacement between the fiber and matrix. Consider a small fiber segment at distance of x from the tunnel-crack front, illustrated in Fig. B-1(b). Then, if the frictional stress (τ_0) is constant in the debonded zone, the load balance in the small segment is given by:

$$\left\{ \sigma_f(x) + \frac{d\sigma_f(x)}{dx} \Delta x \right\} A_f = \sigma_f(x) A_f + \tau_0 (\pi d_f \Delta x) \quad (\text{B-1})$$

where $\sigma_f(x)$ is the stress in the fiber at distance x , Δx is the length of the segment, A_f is the fiber cross-sectional area, and d_f is the fiber diameter. Since A_f can be expressed as $\pi(d_f/2)^2$, Eq. B-1 can be rewritten as:

$$\frac{d\sigma_f(x)}{dx} = \frac{4\tau_0}{d_f} \quad (\text{B-2})$$

The boundary condition for the above differential equation is $\sigma_f(a) = \sigma = P/A_f$. Therefore, $\sigma_f(x)$ can be expressed as:

$$\sigma_f(x) = \frac{4\tau_0}{d_f} (x - a) + \sigma \quad (\text{B-3})$$

Next, the stress in the matrix, $\sigma_m(x)$, is considered. From the load balance in the debonded segment shown in Fig. B-2, the following equation is obtained:

$$\sigma_f(x) A_f + \sigma_m(x) A_m = \sigma A_f \quad (\text{B-4})$$

where A_m is the cross-sectional area of the matrix. Here, the fiber volume fraction V_f can be expressed as $A_f/(A_f + A_m)$. Therefore, dividing both sides of Eq. B-4 by $(A_f + A_m)$:

$$\sigma_f(x) V_f + \sigma_m(x) (1 - V_f) = \sigma V_f \quad (\text{B-5})$$

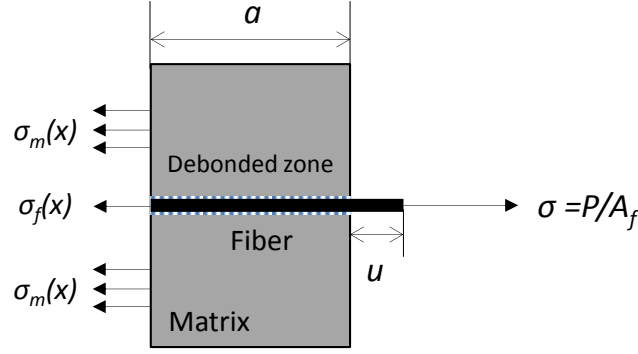


Fig. B-2: Force equilibrium in the debonded fiber and surrounding matrix.

By substituting Eq. B-3 into Eq. B-5, $\sigma_m(x)$ is expressed as:

$$\sigma_m(x) = \frac{V_f}{1-V_f} \frac{4\tau_0}{d_f} (a-x) \quad (\text{B-6})$$

Now, the displacement of the fiber (u_f) and that of the matrix (u_m) at distance x , caused by the external load are considered. It should be noted that the relative displacement between the fiber and matrix (γ) – i.e. interface slip – is given by $u_f - u_m$. Define ε_f and ε_m as the strains for the fiber and matrix, respectively. Then, from the definition of strain and stress-strain constitutive law, γ at distance x can be calculated as:

$$\gamma(x) = \int_0^x \varepsilon_f(x') - \varepsilon_m(x') dx' = \int_0^x \frac{\sigma_f(x')}{E_f} - \frac{\sigma_m(x')}{E_m} dx' \quad (\text{B-7})$$

where E_f and E_m are Young's modulus of the fiber and matrix. Substituting Eqs. B-3 and B-6 into Eq. B-7:

$$\gamma(x) = \frac{\sigma}{E_f} x + \frac{4\tau_0(1+\eta)}{E_f d_f} \left(\frac{x^2}{2} - ax \right) \quad (\text{B-8})$$

where η is defined as $V_f E_f / V_m E_m$ and V_m is the volume fraction of the matrix. It should be noted that, at $x = 0$ (i.e. the tunnel-crack front), γ is zero since there is no interface slip in the bonded zone. On the other hand, the interface slip at the fiber exit point ($x = a$) is given by:

$$\gamma(a) = \frac{\sigma}{E_f} a - \frac{2\tau_0(1+\eta)}{E_f d_f} a^2 \equiv u \quad (\text{B-9})$$

This is equivalent to the fiber pullout displacement u . Since a is an unknown variable, Eq. B-9 cannot be solved for the fiber pullout load P ; another condition to eliminate a from the equation is needed.

Here, an infinitesimal propagation of the tunnel crack is considered, assuming that the fiber and matrix comprise an elastic body. Based on the linear elastic fracture mechanics (LEFM), the energy balance in the system requires:

$$Pdu'_f = dU + dW_f + G_d dA \quad (\text{B-10})$$

Pdu'_f , dU , dW_f , and $G_d dA$ represent the work done by the external load, change in the stored strain energy of the elastic system, dissipated energy by the friction at the fiber/matrix interface, and fracture energy consumed to debond the interface, respectively. It should be noted that u'_f is the displacement of the fiber including not only the elastic stretch of the debonded zone but also that of the bonded zone. The force equilibrium of Eq. B-5 also holds in the bonded zone, while the elastic strains of the fiber and matrix are identical (i.e. $\varepsilon_f = \varepsilon_m$). Namely:

$$\sigma V_f = \sigma_f V_f + \sigma_m V_m = E_f \varepsilon_f V_f + E_m \varepsilon_m V_m = (E_f V_f + E_m V_m) \varepsilon_f \quad (\text{B-11})$$

Therefore, u'_f is expressed as:

$$u'_f = \int_0^a \frac{\sigma_f(x)}{E_f} dx + \frac{\sigma V_f}{E_f V_f + E_m V_m} (L_e - a) \quad (\text{B-12})$$

Meanwhile, regarding the friction term:

$$W_f = \int_0^a \tau_0 (\pi d_f dx) \gamma(x) \quad (\text{B-13})$$

From Eqs. B-8 and B-13:

$$W_f = \frac{\pi \tau_0 d_f \sigma}{2E_f} a^2 - \frac{4\pi \tau_0^2 (1+\eta)}{3E_f} a^3 \quad (\text{B-14})$$

For the strain energy term, a theory in LEFM that the change in elastic strain energy of the system is half the work done by external load is used. Considering the friction as surface traction, the work term minus the friction term can be regarded as the available energy for the strain-energy change. That is:

$$dU = \frac{1}{2} (P du'_f - dW_f) \quad (\text{B-15})$$

From Eqs. B-10 and B-15:

$$G_d dA = \frac{1}{2} (P du'_f + dW_f) \quad (\text{B-16})$$

where dA represents the area of the extended tunnel crack and can be expressed as $\pi d_f da$ where da is the length of the crack extension. Then, substituting Eqs. B-12 and B-14 into Eq. B-16, the following equation is obtained:

$$G_d = \frac{d_f}{8E_f(1+\eta)} \sigma^2 - \frac{\tau_0 a}{E_f} \sigma + \frac{2\tau_0^2(1+\eta)}{E_f d_f} a^2 \quad (\text{B-17})$$

Solve the above equation for $\sigma > 0$:

$$\sigma = \frac{4\tau_0(1+\eta)}{d_f} a + \sqrt{\frac{8G_d E_f (1+\eta)}{d_f}} \quad (\text{B-18})$$

By combining Eqs. B-9 and B-18, the following solution is obtained:

$$\sigma(u) = 2 \sqrt{\frac{2E_f(1+\eta)}{d_f} (\tau_0 u + G_d)}, \quad 0 < u \leq u_0 \quad (\text{B-19})$$

Or, by converting the stress σ into the force P , the equation can be rewritten as:

$$P(u) = \sqrt{\frac{\pi^2 E_f d_f^3 (1+\eta)}{2} \{ \tau_0 u + G_d \}}, \quad 0 < u \leq u_0 \quad (\text{B-20})$$

This is identical to the Eq. 3.27 in Chapter 3. Here, u_0 is the critical pullout displacement at which full-debonding is completed (i.e. $a = L_e$). Therefore, from Eq. B-18:

$$\sigma(u_0) = \frac{4\tau_0(1+\eta)}{d_f} L_e + \sqrt{\frac{8G_d E_f (1+\eta)}{d_f}} \quad (\text{B-21})$$

Also, from Eq. B-9:

$$u_0 = \gamma(L_e) = \frac{\sigma(u_0)}{E_f} L_e - \frac{2\tau_0(1+\eta)}{E_f d_f} L_e^2 \quad (\text{B-22})$$

By substituting Eq. B-21 into B-22:

$$u_0 = \frac{2\tau_0 L_e^2(1+\eta)}{E_f d_f} + \sqrt{\frac{8G_d L_e^2(1+\eta)}{E_f d_f}} \quad (\text{B-23})$$

This is identical to the Eq. 3.29 in Chapter 3.

(vi) *Pullout stage*

Consider the fiber pullout model shown in Fig. B-3; When no slip-dependent behavior is taken into account, the following force equilibrium is obtained:

$$\tau_0 \pi d_f \{L_e - (u - u_0)\} = P \quad (\text{B-24})$$

Then, to include the slip-hardening/softening effect, modify the friction by multiplying a factor that depends on the slip-hardening coefficient (β). The simplest model is given by:

$$P(u) = \pi \tau_0 d_f (L_e - u + u_0) \left(1 + \beta \frac{u - u_0}{d_f}\right), \quad u_0 \leq u \leq L_e + u_0 \quad (\text{B-25})$$

This is identical to the Eq. 3.28 in Chapter 3.

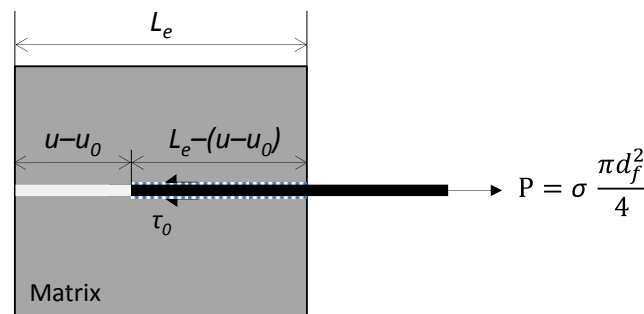


Fig. B-3: Model of fiber pullout process.

(vii) *Determination of G_d , τ_0 , and β from results of single-fiber pullout test*

First, since V_f is sufficiently small in the single-fiber pullout model, it can be assumed that η is negligible. Then, by converting the stress σ into the force P in Eq. B-21:

$$P_{debond}(u_0) = \pi\tau_0 d_f L_e + \pi\sqrt{\frac{G_d E_f d_f^3}{2}} \quad (\text{B-26})$$

Also, when $u = u_0$, Eq. B-25 gives:

$$P_{pullout}(u_0) = \pi\tau_0 d_f L_e \quad (\text{B-27})$$

From Eq. B-27, the Eq. 3.19 in Chapter 3 is obtained. In addition, by combining Eqs. B-26 and B-27, it can be shown that:

$$G_d = \frac{2}{\pi^2 E_f d_f^3} \{P_{debond}(u_0) - P_{pullout}(u_0)\}^2 \quad (\text{B-28})$$

This is identical to the Eq. 3.18 in Chapter 3.

Next, the Eq. 3.20 in Chapter 3 is derived, which gives the least square estimation (LSE) of β .

For the one-parameter LSE, the following equation needs to be solved:

$$\frac{d}{d\beta} \sum_i \{P_{ex}(u_i') - P_{pullout}(u_i')\}^2 = 0 \quad (\text{B-29})$$

where $P_{ex}(u_i')$ is the measured pullout load at the i -th data of the post-peak pullout displacement.

Then, from the chain rule in calculus:

$$\frac{d}{d\beta} \sum_i \{P_{ex}(u_i') - P_{pullout}(u_i')\}^2 = \sum_i 2\{P_{ex}(u_i') - P_{pullout}(u_i')\} \frac{d}{d\beta} \{P_{ex}(u_i') - P_{pullout}(u_i')\} = 0 \quad (\text{B-30})$$

It should be noted that

$$\frac{d}{d\beta} P_{ex}(u_i) = 0 \quad (\text{B-31})$$

Therefore, the following equation for β needs to be solved:

$$\sum_i \{P_{ex}(u_i) - P_{pullout}(u_i)\} \frac{d}{d\beta} P_{pullout}(u_i) = 0 \quad (\text{B-32})$$

By substituting Eq. B-25 into Eq. B-32:

$$\hat{\beta} = \frac{\sum_i P_{ex}(u_i) \cdot \frac{u_i(L_e - u_i)}{\pi\tau_0} - \sum_i d_f u_i (L_e - u_i)^2}{\sum_i \{u_i(L_e - u_i)\}^2} \quad (\text{B-33})$$

This is identical to the Eq. 3.20 in Chapter 3.

APPENDIX C

Derivation and analysis of the proposed hysteresis for fiber debonding load

Consider the pullout-debonding phase in single-fiber pullout shown in Fig. C-1. Suppose that the point A represents the current fiber pullout load and displacement of the short embedment side, and the points B and B_h indicate those of the long-embedment side for the original debonding-load model and the proposed hysteresis, respectively. Define u'_L as the maximum pullout displacement of the debonding side in the preceding loading history, and a' as the length of the debonded zone.

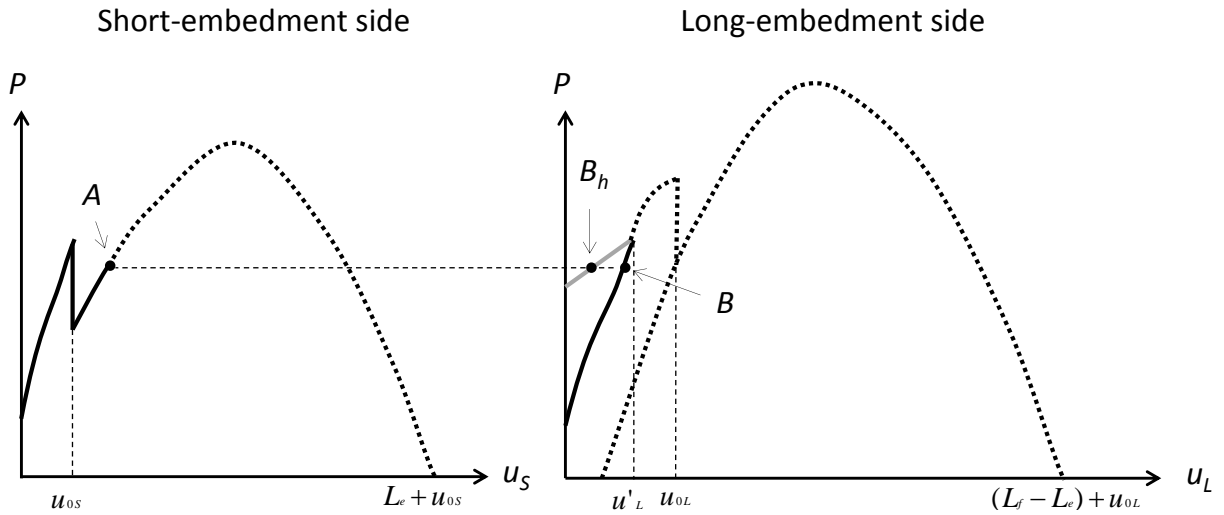


Fig. C-1: Pullout-debonding phase of single-fiber pullout.

For the debonding-side displacement u_L , further tunnel-crack propagation does not take place unless u_L is greater than u'_L . Thus, Eq. B-9 in Appedix B also holds for this case:

$$u_L = \frac{\sigma}{E_f} a' - \frac{2\tau_0(1+\eta)}{E_f d_f} a'^2 \quad (\text{C-1})$$

Also, it should be noted that

$$\sigma \frac{\pi d_f^2}{4} = P_{debond}^h(u_L) \quad (\text{C-2})$$

Then, by combining Eqs. C-1 and C-2:

$$P_{debond}^h(u_L) = \frac{\pi E_f d_f^2}{4a'} u_L + \frac{\pi \tau_0 d_f (1+\eta)}{2} a', \quad 0 < u_L < u'_L \quad (\text{C-3})$$

This is identical to the Eq. 3.33 in Chapter 3. In addition, by substituting $u_L = u'_L$ into Eq. C-3, the debonded length a' can be obtained by solving the following equation:

$$P_{debond}^h(u'_L) = \frac{\pi E_f d_f^2}{4a'} u'_L + \frac{\pi \tau_0 d_f (1+\eta)}{2} a' \quad (\text{C-4})$$

This is equivalent to the Eq. 3.34 in Chapter 3. The comparison between $P_{debond}(u_L)$ and $P_{debond}^h(u_L)$ has been shown in Fig. 3.9 in Chapter 3.

Now, the effect of this modification on the composite σ - δ relation is considered. As an example, the σ - δ curve of a standard ECC M45 is simulated by using the original and modified models. Three-dimensional random fiber distribution is assumed, but, for simplicity, both the matrix micro-spalling and Cook-Gordon effect (detailed in Section 3.3.2) are not taken into account.

Figure C-2 shows the simulation result. Significant difference cannot be seen between the two curves. This might be attributed to the fact that the pullout-debonding phase is not predominant in M45; as shown in Fig. C-3, most of fibers in the ECC are broken for large crack opening. As a

result, the model modification for the pullout-debonding phase has insignificant effect on the composite σ - δ relation.

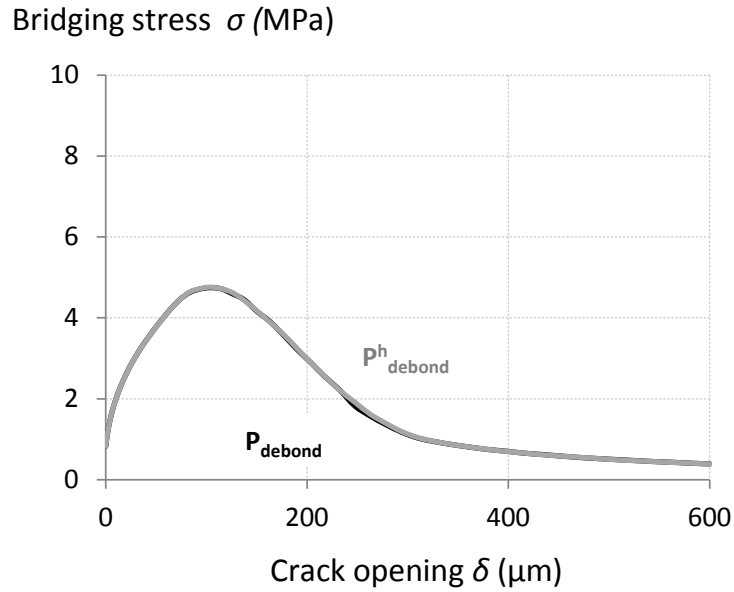


Fig. C-2: Simulated σ - δ relations of ECC M45 by using the original and modified models.

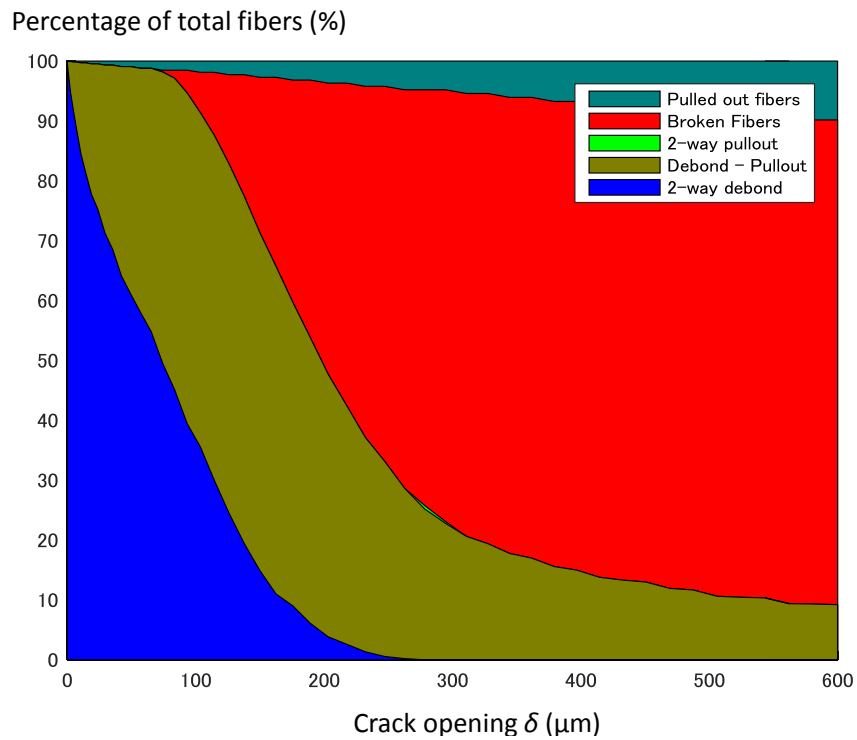


Fig. C-3: Simulated fiber status at each crack opening.

Conversely, if the pullout-debonding phase is predominant in a composite, there could be a significant effect of the modification. Here, to prevent the fiber rupture, a higher fiber nominal strength of 2000 MPa is used, instead of the original value of 1,060 MPa for M45. Also, from Eqs. B-20 and C-3, the difference between $P_{debond}(u_L)$ and $P^h_{debond}(u_L)$ can be larger when the composite has a higher chemical bond (G_d) on the fiber/matrix interface. Thus, G_d of 10 J/m² is used instead of the original value of 1.08 J/m².

Figure C-4 shows the σ - δ curve simulated with the high chemical bond and fiber strength. The difference between the original and modified models is now significant around the peak bridging stress. Indeed, the computed complementary energy J_b' is 766 J/m² for the original model, while that for the modified model is 790 J/m². Also, as expected, the pullout-debonding phase is predominant (Fig. C-5).

A further research would be required to verify this model modification.

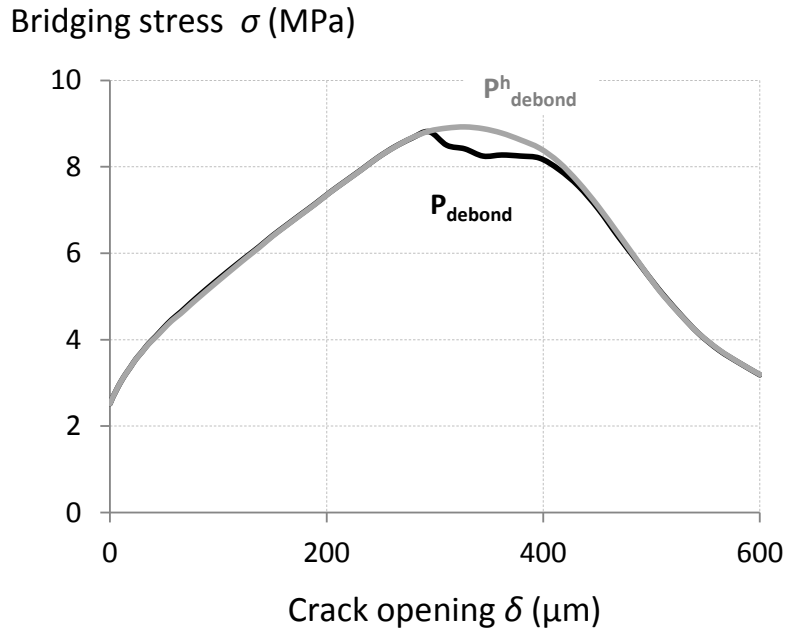


Fig. C-4: Simulated σ - δ relations with high chemical bond of 10 J/m² and fiber strength of 2000 MPa.

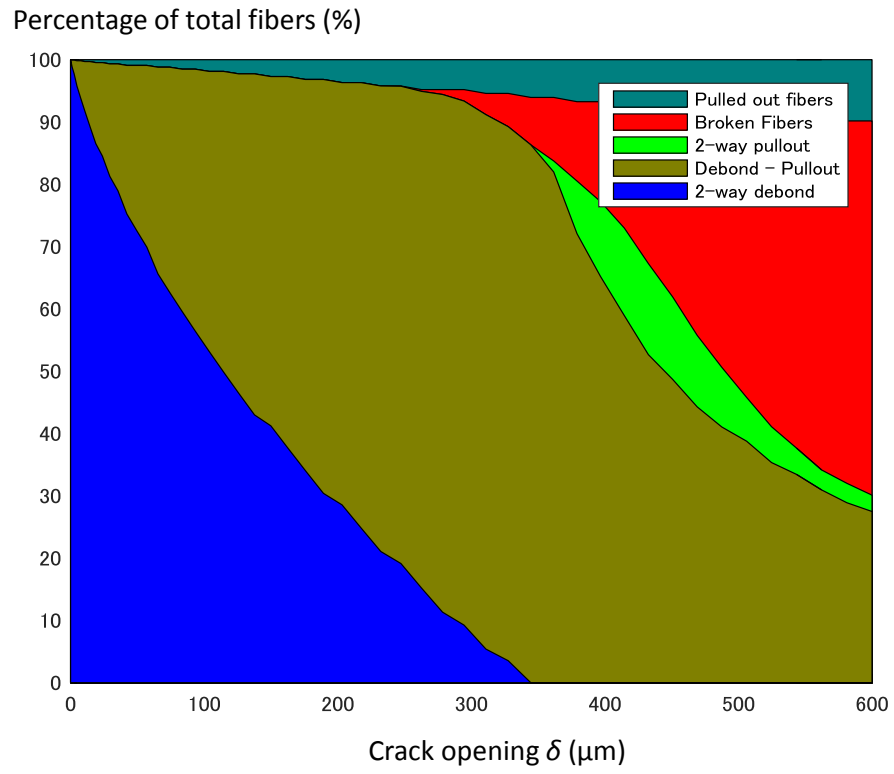


Fig. C-5: Simulated fiber status with high chemical bond and fiber strength.

APPENDIX D

Derivation of the modified formula for permeability coefficient

Consider the permeability-testing setup shown in Fig. D-1. Define water levels of the inflow and outflow pipes at time t as $h_{in}(t)$ and $h_{out}(t)$, respectively. Then, the hydraulic head $h(t)$ is given by

$$h(t) = h_{in}(t) - h_{out}(t) \quad (D-1)$$

Suppose that the water head changes from h_0 to h_f for the test duration of T .

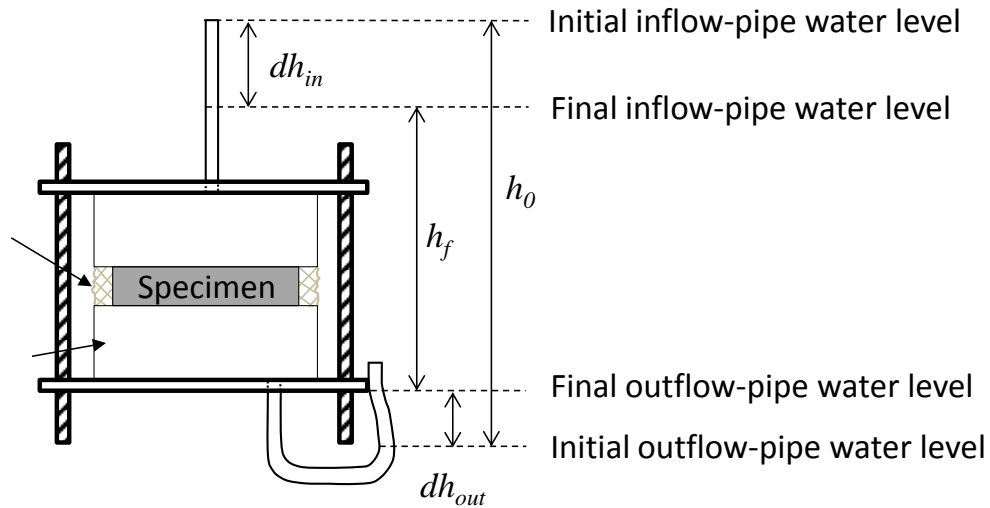


Fig. D-1: Modified permeability-testing setup used in this study.

From Darcy's law:

$$q(t) = k \frac{h(t)}{L} A \quad (D-2)$$

where $q(t)$ represents the volumetric flow rate of water (cm^3/s) permeating through the specimen with thickness of L (cm) and cross-sectional area of A (cm^2), and k is the corresponding permeability coefficient (cm/s). Also, from the mass conservation law, the following two equations are obtained:

$$q(t)\Delta t = -a_{in} \frac{dh_{in}(t)}{dt} \Delta t \quad (\text{D-3})$$

$$q(t)\Delta t = a_{out} \frac{dh_{out}(t)}{dt} \Delta t \quad (\text{D-4})$$

where Δt is an infinitesimal time increment, and a_{in} and a_{out} are the cross-sectional areas of the inflow and outflow pipes, respectively.

Taking the derivative of both sides in Eq. D-1 with respect to t :

$$\frac{dh(t)}{dt} = \frac{dh_{in}(t)}{dt} - \frac{dh_{out}(t)}{dt} \quad (\text{D-5})$$

Also, from Eqs. D-2 through D-4,

$$\frac{dh_{in}(t)}{dt} = -\frac{1}{a_{in}} k \frac{h(t)}{L} A \quad (\text{D-6})$$

$$\frac{dh_{out}(t)}{dt} = \frac{1}{a_{out}} k \frac{h(t)}{L} A \quad (\text{D-7})$$

Then, substitute Eqs. D-6 and D-7 into Eq. D-5:

$$\frac{dh(t)}{dt} = -\frac{1}{a_{in}} k \frac{h(t)}{L} A - \frac{1}{a_{out}} k \frac{h(t)}{L} A \quad (\text{D-8})$$

the above equation can be rewritten as

$$-\frac{1}{h(t)}dh(t) = \left(\frac{a_{in} + a_{out}}{a_{in}a_{out}} \right) \frac{kA}{L} dt \quad (D-9)$$

Integrating the above equation with respect to t from 0 to T and h from h_0 to h_f :

$$\ln\left(\frac{h_0}{h_f}\right) = \left(\frac{a_{in} + a_{out}}{a_{in}a_{out}} \right) \frac{kA}{L} T \quad (D-10)$$

Solving the above equation for k :

$$k = \frac{a_{in}a_{out}L}{(a_{in} + a_{out})AT} \ln\left(\frac{h_0}{h_f}\right) \quad (D-11)$$

This is equivalent to the Eq. 5.2 in Chapter 5.

It should be noted that, if a_{out} is sufficiently large, then dh_{out} becomes negligible. This ends up with the same testing condition as the original falling-head test setup (see Section 5.2.4), in which the outflow-pipe water level is constant during the test. Mathematically, Eq. D-11 is rewritten as

$$k = \lim_{a_{out} \rightarrow \infty} \left[\frac{a_{in}a_{out}L}{(a_{in} + a_{out})AT} \ln\left(\frac{h_0}{h_f}\right) \right] = \lim_{a_{out} \rightarrow \infty} \left[\frac{a_{in}L}{(a_{in}/a_{out} + 1)AT} \ln\left(\frac{h_0}{h_f}\right) \right] = \frac{a_{in}L}{AT} \ln\left(\frac{h_0}{h_f}\right) \quad (D-12)$$

This is identical to the original formula, Eq. 5.1, presented in Chapter 5.